Functional Polymer-Polymer Composites by Nano/Meso-Fiber Encapsulation: Applications in Drug Delivery Systems and Polymer Toughening

A Thesis

Submitted to the Faculty

of

Drexel University

by

Ya Liang

in partial fulfillment of the

requirements for the degree

of

Doctor of Philosophy

June 2010

Dedications

To

my parents, Yuxu Liang and Baoxin Xiang

and

my family, Paul Libbers, Nathan and Joshua

I could not do anything without your support and encouragement.

Acknowledgements

First of all I would like to give great thanks to my advisor, Dr. Giuseppe Palmese, for his mentoring and patience over the past six years. I enjoy the balance between freedom and instruction in this research. He always gives me valuable suggestions on my research and presentation skills. He also allows me to express different opinions and discusses them with me. He expresses his concern and care when I encounter difficulties in my personal life.

I would like to give thanks to my co-advisor, Dr. Anthony Lowman for his advice on the drug delivery work and kindness in giving me full access to the lab. I am thankful to have Dr. Robert Jensen from the Army Research Lab as my mentor since 2006. Dr. Robert Jensen gave me great assistance in understanding polymer toughening and composites in extreme detail as well as advice on writing style. I would like to extend my gratitude to the rest of my committee, Dr. Michele Marcolongo and Dr. Yossef Elabd, for their advice and time.

I would like to give special thanks to two fellow lab mates in the Palmese Research Group and Lowman Research Group, Aflal Rahmathullah and Noelle Comolli. They acted as mentors and gave me detailed directions when I started this research. I am also grateful to work with other graduate students and post doctoral fellows, such as Dr. Geng Xing, Dr. Erde Can, Mary Sullivan, Jackie Yim, Vivek Marella, Amutha Jeyarajasingam, Amy Peterson, Julianne Holloway, Brian Merritt, Don Campbell, James Throckmorton, Alex Grous and Arianna Watters in the Palmese Research Group and Tony Tuesca, Jonathan Thomas, Jennifer Vernengo, Sam Laurencin, Kara Spiller,

Vanessa Vardon, Jason Coleman and Erik Brewer in the Lowman Research Group. They either helped me with instrument operation and sample testing or provided a friendly environment in the lab.

I would like to express my appreciation to the following people. Dr. Daphne Pappas and Dr. Jason Robinette in the Army Research Lab have been gone out of their way to help me with research work such as plasma treatments, XPS analysis and fracture testing. Dan Luu in our department has provided technical assistant for the past six years. Dr. Hong Chen and Dr. Yuesheng Ye in the Elabd Research Group kindly offered their help on some research work. Dorothy Porter, Katie Brumbelow and Tracy McClure in our department have given tremendous help with administrative issues. Additionally, Thomas Measey and Tim Wade in the Chemistry Department provided me with NMR training and troubleshooting; Dee Breger and Edward Basgall in Drexel University Central Research Facility gave me SEM training and assisted with troubleshooting; Mark Shiber, Rich Miller, Earl Bolling and Paul Velez in Drexel University machine shop trained me in the use of band saws and helped with customizing machine parts.

I would like to express my deepest gratitude to my husband, Paul Libbers, for his support and sacrifices for me to finish my PhD work in Drexel. He has been helping me with written and spoken English since we knew each other. He encouraged me when I was frustrated. He helps to take care of kids and does more than his share of the house work to reduce my burden. I am so grateful that I have him in my life.

Finally I acknowledge the U. S. Army Research Laboratory for financial support under the Army Materials Center of Excellence Program, contract W911NF-06-2-0013.

Table of Contents

List of Tables xi

List of Figures xii

Abstract xix

Chapter 1: Introduction 1

1.1. Drug Delivery 1

1.1.1. Motivation 1

1.1.2. Research Objective 3

1.1.3. Contribution of this Research 4

1.2. Polymer Toughening 5

1.2.1. Motivation 5

1.2.2. Research Objective 7

1.2.3. Contribution of this Research 7

1.3. Structure of the Thesis 8

List of References 10

Chapter 2: Background 14

2.1. Drug Delivery Systems 14

2.1.1. Controlled Release Systems 15

2.1.2. Commercially Available Drug Delivery Systems 17

2.1.3. Drug Delivery Systems under Development 18

2.1.4. Drug Delivery Carriers Prepared via Nanotechnology 20

2.2. Polymeric Biomaterials for Drug Delivery....22

2.2.1. Non-degradable Hydrophobic Polymers....23

2.2.2. Biodegradable Polymers....24

2.2.2.1. PGA, PLA and PLGA – Most Widely Used Biodegradable Materials....24

2.2.2.2. Other Biodegradable Materials Used for Biomedical Applications....26

2.2.3. Hydrogels....28

2.2.3.1. Synthesis and Properties of Hydrogel Network....29

2.2.3.2. Applications of Hydrogels....31

2.2.3.3. Poly(Hydroxyethyl Methacrylate) (PHEMA)....31

2.2.3.4. Poly(Ethylene Glycol) (PEG)....32

2.2.3.5. Poly(Vinyl Alcohol) Hydrogels — Fabrication, Properties and Applications....32

2.2.3.6. Hydrogel Composites....37

2.3. Synthesis of Poly(lactone) — PLA, PGA, PCL and their Copolymers....37

2.4. Degradation of Poly(lactone) — PLA, PGA, PCL and their Copolymers....40

2.5.1. *In Vitro* Degradation Behavior....40

2.5.2. Factors Affecting Degradation....42

2.5. Electrospinning Techniques....46

2.6. Applications of Biodegradable Electrospun Micro- or Nanofibers in Tissue Engineering and Drug Delivery....49

2.7. Polymer Toughening....52

2.7.1. Molecular Origins of Toughness....52

2.7.2. Toughening of Thermoset Resins....53

2.7.2.1. Rubber-Modified Epoxies....54
2.7.2.2. Rigid Thermoplastics-Modified Epoxies....56
2.7.3. Interlayer Toughening in High Performance Composite Applications....58
2.8. Vinyl Ester Resins....60
2.8.1. Cure Kinetics of Vinyl Ester/Styrene System....60
2.8.2. Toughening of VE Resins....63
2.9. Polypropylene (PP)....65
2.9.1. Structure, Morphology and Properties....65
2.9.2. Crystallization Behavior....66
2.9.3. Surface Treatment....68
List of References....71
Chapter 3: PLGA Synthesis and Electrospun Fiber Fabrication....94
3.1. Experimental....94
3.1.1. Materials....94
3.1.2. PLGA Synthesis....95
3.1.3. Electrospun PLGA Fibers Fabrication....96
3.1.4. Characterization....96
3.2 Results and Discussion....97
3.2.1. PLGA Synthesis and Characterization....97
3.2.2. Fiber Morphology Control during Electrospinning....99
3.3 Chapter Summary....100
Chapter 4: *In vitro* Degradation of PLGA Fibers and PLGA-PVA Composites....113
4.1. Experimental....114

4.1.1. Materials 114

4.1.2. Sample Preparation 114

4.1.3. Characterization 116

4.2. Results and Discussions 117

4.2.1. *In vitro* Degradation Behavior of Electrospun PLGA Fibers 117

4.2.1.1. Degradation of Electrospun PLGA7 Fibers 118

4.2.1.2. Degradation of Electrospun PLGA4A Fibers 119

4.2.1.3. Glass Transition of PLGA 121

4.2.2. *In vitro* Degradation Behaviors of PLGA Fibers Embedded in PVA Hydrogels and Solvent-Cast PLGA Films 122

4.2.3. Modeling of PLGA Fiber Degradation 124

4.3. Chapter Summary 126

List of References 128

Chapter 5: Mechanical Properties of PLGA-PVA Composites during Incubation 148

5.1. Experimental 148

5.2. Results and Discussion 149

5.2.1. Influence of Testing Conditions and Processing History on Tensile Properties of PLGA4A Fiber Mats, PLGA4A-PVA Films and PVA Films 150

5.2.2. Tensile Properties of PLGA Fiber Mats, PVA Films and PLGA-PVA Films during Incubation 151

5.3. Chapter Summary 153

List of References 155

Chapter 6: Plasma-Based Surface Modification 169

6.1. Experimental 169

6.1.1. Materials 169

6.1.2. Procedure of Surface Treatment 169

6.1.3. Characterization 170

6.2. Results and Discussion 172

6.2.1. X-Ray Photoelectron Spectroscopy 173

6.2.2. Water Contact Angle Measurements 175

6.2.3. Morphology of Fiber Surface Analyzed with Environmental Scanning Electron Microscopy 176

6.2.4. Thickness of Grafted Layers Estimated from Thermogravimetric Analysis 176

6.2.5. Differential Scanning Calorimetry 177

6.3. Chapter Summary 178

List of References 179

Chapter 7: Toughening Vinyl Ester Resins with Polypropylene Fibers 190

7.1. Experimental 190

7.1.1. Materials 190

7.1.2. Surface Treatment of PP Fibers 191

7.1.3. Resin and Composite Fabrication 191

7.1.4. Composite Characterization 192

7.2. Results and Discussion 194

7.2.1. Toughening VE Resins Using Untreated and Oxygen-Treated PP Fibers 195

7.2.2. Toughening VE Resins using VTMS-Grafted PP Fibers 196

7.2.2.1. Thermal and Thermomechanical Properties 196

7.2.2.2. Mechanical Properties 199

7.2.2.3. Fracture Surface Morphology 201
7.3. Chapter Summary 202
List of References 204
Chapter 8: Polymer Toughening in High Performance Composite Applications 219
8.1. Experimental 219
8.1.1. Materials 219
8.1.2. Composite Fabrication and Testing Specimen Preparation 220
8.1.3. Interlaminar Fracture Toughness Measurements 221
8.2. Results and Discussion 222
8.2.1. Influence of Different Interlayers 222
8.2.2. Influence of Interlayer Thickness 223
8.2.3. Failure Mechanism 224
8.2.4. Using Freshly Received Glass Fiber Fabrics 225
8.3. Chapter Summary 226
List of References 227
Chapter 9: Conclusions and Recommendations 241
9.1. PLGA Fiber-PVA Hydrogel Composites 241
9.2. PP Fiber-VE Resin Composites 242
Vita 244

List of Tables

3.1 Summary of reaction conditions and polymer properties of PLGA synthesized 102

4.1 Electrospinning parameters and fiber sizes of electrospinning PLGA7 fibers 130

4.2 Electrospinning parameters and fiber sizes of electrospinning PLGA4A fibers 130

4.3 Comparison of rate constants k_d and k_e for fibers, fibers in PVA and films 130

5.1 Tensile strength, strain at maximum stress and Young's modulus of PLGA_45 fiber mats, PVA hydrogels and their composites in neutral PBS buffer tested at different crosshead speeds and temperatures 156

5.2 Tensile strength, strain at break and Young's modulus under incubation conditions for PVA, PLGA4A_45-PVA, PLGA4A_40-PVA and PLGA4A_35-PVA films during degradation 157

6.1 High resolution XPS carbon (C1s) peak deconvolution results.....180

7.1 Densities and volume fractions of VE systems.....205

7.2 Flexural properties of neat VE resin, PP-VE and OPP-VE composites 205

7.3 Thermal and thermomechanical properties of neat VE resin, PP-VE and VPP-VE composites.....206

7.4 Mechanical properties of neat VE resin, PP-VE and VPP-VE composites.....206

8.1 Mode II interlaminar fracture toughness of GF-VE composites with various interlayers.....228

8.2 Mode II interlaminar fracture toughness of GF-VE composites with different interlayer thickness 228

8.3 Mode II interlaminar fracture toughness of GF-VE composites using freshly received GF 228

List of Figures

1.1 A diagram illustrating the overall structure of the thesis 13

2.1 Chemical structures of PLA, PGA and PLGA polymers 85

2.2 (a) Chemical structure of PVA polymer and (b) PVA hydrogel network crosslinked via formation of crystallites 86

2.3 Synthesis of PLGA copolymer through ring-opening polymerization 87

2.4 Cationic octanoic acid co-initiated mechanism [63] ($A\Theta$ and $H^{\oplus}$ are from lactic acid or octanoic acid.) 88

2.5 Possible interactions between the stannous octoate and impurities in the polymerization mixture. Stannous hydroxide formed from reaction (a) and stannous alkoxide formed from reactions (b) and (c) [69] 89

2.6 Complexation or second-order insertion [53] 89

2.7 Hydrolysis of PLGA copolymers in water 90

2.8 Taylor cone formed in the electrospinning process 90

2.9 Instability region in an electrified PEO-water jet: (a) the whipping jet, (b) superposition of the whipping jet and the envelope, and (c) a trace of the jet in the entire instability region [80] 91

2.10 Three basic loading modes that give rise to different crack-tip displacements: Mode I (opening), Mode II (shearing) and Mode III (tearing) [143] 92

2.11 (a) The chemical structure of vinyl ester monomer derived from diglycidyl ether of bisphenol A (DGEBA) and methacrylic acid, and (b) a crosslinked network of the vinyl ester-styrene system created by free radical polymerization 93

3.1 Electrospinning apparatus set-up 103

3.2 A typical GPC plot of PLGA. The positive peak represents PLGA 104

3.3 Intrinsic viscosity calculation by extrapolating the inherent or reduced viscosities to the concentration approaching zero 105

3.4 ^{1}H NMR spectrum of PLGA in DMSO_d_6 solution 106

3.5 Concentration effect on morphologies of electrospun PLA (MW 20k-30k) membranes at a feeding rate of 1.2 ml/hr, tip-to-plate distance of 12.5 cm, and concentration of (a) 30wt% (11.2kV), (b) 40wt% (18.1kV) and (c) 50 wt% (11.9kV) 107

3.6 Concentration effect on morphologies of electrospun PLGA6 (LA/GA=85/15, Mw 69600) membranes at a feeding rate of 1.0 ml/hr, tip-to-plate distance of 21 cm, voltage of 14.4 kV and concentration of (a) 40% (b) 45 wt% 108

3.7 Tip-to-plate distance effect on morphologies of electrospun PLGA (LA/GA=65/35, MW 40k-75k) membranes at a feeding rate of 1.2 ml/hr, concentration of 35wt%, and distance of (a) 12.3 cm (11.5kV), (b) 13.5 cm (12kV) and (c) 15cm (14kV) 109

3.8 Tip-to-plate distance effect on morphologies of electrospun PLGA#2 (LA/GA=85/15, Mw 14500) membranes at a feeding rate of 1.2 ml/hr, concentration of 50wt%, and distance of (a) 8.5 cm (9.5kV) (b) 12.5 cm (12kV) and (c) 16.5 cm (12.5 kV) 110

3.9 Feeding rate effect on morphologies of electrospun PLGA4 (LA/GA= 85/15, Mw 89600) membranes at a distance of 21 cm, concentration of 40wt%, and feeding rate of (a) 0.8 ml/hr (V = 14.9 kV) (b) 1.6 ml/hr (V = 16.3 kV) 111

3.10 Feeding rate effect on morphologies of electrospun PLGA7 (LA/GA= 50/50, Mw 75700) membranes at a distance of 21 cm, concentration of 31wt%, and feeding rate of (a) 0.1 ml/hr (V = 12.5 kV) (b) 0.6 ml/hr (V = 19.7 kV) 112

4.1 Morphology of electrospun PLGA7 fibers used in the degradation study 131

4.2 Morphology of H20 fibers (a) before and (b) after one week or (c) two weeks of incubation in PBS buffer (pH=7.4) at 37°C 132

4.3 Normalized weight loss of all PLGA7 fiber mats during incubation in PBS buffer (pH=7.4) at 37°C 133

4.4 Morphology of electrospun PLGA4A fibers used in the degradation study. (a)-(c) before incubation, and (d)-(f) after incubation for one week. (a) and (d) 4A_35, (b) and (e) 4A_40, (c) and (f) 4A_45 134

4.5 Morphology of all PLGA4A fibers after (a)-(c) two weeks or (d)-(f) five weeks of incubation in PBS buffer (pH=7.4) at 37°C. (a) and (d) 4A_35, (b) and (e) 4A_40, (c) and (f) 4A_45 135

4.6 Normalized weight loss of PLGA4A fibers after up to eight weeks of incubation in PBS buffer (pH=7.4) at 37°C.....136

4.7 Molecular weight and polydispersity index of PLGA4A fibers after up to six weeks of incubation in PBS buffer (pH=7.4) at 37°C. (a) weight-average molecular weight (Mw), number-average molecular weight (Mn) and (b) polydispersity index (PI) of all fiber mats as a function of incubation time 137

4.8 4A-40 fibers (a) before and (b) after incubation for nine days 138

4.9 (a) Weight loss and (b) Lactic acid (LA) composition as a function of incubation time for PLGA7 fibers and PLGA4A fibers 139

4.10 DSC thermograms show the glass transition change under various conditions for PLGA4A.....140

4.11 Morphology of PLGA4A_40-PVA after (a) one week or (b) two weeks of incubation and (c) PLGA_35-PVA after two weeks of incubation in PBS buffer (pH=7.4) at 37°C.....141

4.12 Comparison of mat shrinkage of PLGA4A fibers and PLGA4A-PVA composites under incubation conditions. (a) Visual observation of PLGA4A_40 fiber mats and PLGA4A_40-PVA before and after incubation, and (b) plots of normalized shrinkage of three fiber mats and corresponding composites.....142

4.13 Normalized weight loss of PLGA4A fibers embedded in PVA hydrogels after up to eight weeks of incubation in PBS buffer (pH=7.4) at 37°C 143

4.14 Comparison of degradation of PLGA4A fibers, PLGA4A fibers inside PVA gels and PLGA4A films after up to eight weeks of incubation in PBS buffer (pH=7.4) at 37°C. (a) Normalized weight loss (b) weight-average molecular weight (Mw) and number-average molecular weight (Mn) of PLGA4A as a function of incubation time.....144

4.15 Morphology of PLGA4A films (a) before and (b) after one week of incubation in PBS buffer (pH=7.4) at 37°C.....145

4.16 Porous structure of the wet PLGA4A fiber-PVA composite. (a) Optical microscope image of 4A_45-PVA (fibers are shown in black and PVA is shown in white), and (b) ESEM image of 4A_40-PVA before incubation 146

4.17 (a) Number-average molecular weights were fit to the hydrolysis model for PLGA degradation, ln (Mn0/Mn) = kt, to get rate constants for hydrolysis; (b) Weight loss data were fit into the erosion model, ln (X/(1-X)) = -kt + m and X is % weight remaining, to get erosion rate constants 147

5.1 Instron setup for tensile testing of thin films in a PBS bath. 158

5.2 Comparison of tensile testing plots of PLGA_45 fiber mats, PVA hydrogels and their composites in neutral PBS buffer tested at 22°C using different crosshead speeds 159

5.3 Comparison of tensile testing plots of PLGA_45 fiber mats, PVA hydrogels and their composites in neutral PBS buffer tested at a crosshead speed of 10 mm/min at different temperatures.....160

5.4 Photos of tensile testing of PLGA_45-PVA composite tested in PBS bath at (a) 22°C or (b) 37°C.....161

5.5 Comparison of tensile testing curves of as-made and rehydrated PVA hydrogels and PLGA_45-PVA composites in neutral PBS buffer tested at a crosshead speed of 10 mm/min at 37 °C.....162

5.6 Tensile properties of rehydrated PVA hydrogel films during incubation tested at a crosshead speed of 10 mm/min in 37 °C neutral PBS buffer.....163

5.7 Tensile properties of rehydrated PLGA4A45-PVA films during incubation tested at a crosshead speed of 10 mm/min in 37 °C neutral PBS buffer 164

5.8 Tensile properties of rehydrated PLGA4A40-PVA films during incubation tested at a crosshead speed of 10 mm/min in 37 °C neutral PBS buffer 165

5.9 Tensile properties of rehydrated PLGA4A35-PVA films during incubation tested at a crosshead speed of 10 mm/min in 37 °C neutral PBS buffer 166

5.10 Tensile properties of PLGA fiber mat, rehydrated PLGA-PVA and PVA films before incubation tested at a crosshead speed of 10 mm/min in 37 °C neutral PBS 167

5.11 Tensile properties of all rehydrated PLGA4A-PVA and PVA films after 8-week incubation tested at a crosshead speed of 10 mm/min in 37 °C neutral PBS buffer.....168

6.1 The dielectric barrier discharge (DBD) plasma reactor used in this work 181

6.2 Reaction mechanism of surface modification to polypropylene using vinyltrimethoxysilane, a silane coupling agent. Adapted from reference [2].....182

6.3 XPS survey spectra of untreated PP, O_2-PP and VTMS-PP.....183

6.4 Atomic concentration ratios obtained from XPS analysis for —●— O:C of VTMS-PP, —▼— Si:C of VTMS-PP, —□— O:C of O_2-PP after 24 hours delay 184

6.5 High resolution XPS carbon spectrum of untreated and surface treated PP fibers. (a) untreated; (b) 15 s, (c) 30 s, (d) 60 s and (e) 90 s in O_2 plasma; (f) VTMS after 30 s O_2 plasma 185

6.6 Contact Angles of PP at various treatment conditions: —□— 10 minute delay after O_2 plasma treatment, —△— 30 minute delay after O_2 plasma treatment, —◆— 24 hour delay after O_2 plasma treatment, and —×— after VTMS treatment 186

6.7 ESEM micrographs showing difference in surface roughness of PP fibers (a) before treatment, after (b) 30 s, (c) 90 s and (d) 180 s plasma treatment in O_2, and after VTMS treatment following (e) 30 s and (f) 180 s O_2 plasma treatment 187

6.8 DSC thermograms of untreated PP, O_2 plasma treated PP and VTMS-grafted PP showed similar melting transitions 188

6.9 DSC thermograms of untreated PP, O_2 plasma treated PP and VTMS-grafted PP at the second heating ramp 189

7.1 Vacuum assisted resin transfer molding setup in composite fabrication 207

7.2 Density measurement setup 208

7.3 Instron setup for measuring tensile properties of rigid plastics 209

7.4 Load-deflection curves in flexural tests for neat VE resin and PP-VE composites using untreated PP or oxygen-treated PP fibers 210

7.5 ESEM micrographs of fracture surface of the PP-VE composites using (a) untreated PP and (b) oxygen-plasma treated PP 211

7.6 DMA temperature scan of (a) storage modulus and (b) loss modulus for neat VE resin and VE composites. —◇— VE, —+— PP-VE, —— VPP-VE 212

7.7 DSC thermograms of neat VE resin, PP-VE and VPP-VE composites at the first and second heating ramps and also at the first heating ramp after being tested in DMA. 213

7.8 DSC thermograms of untreated PP fibers, O_2-PP fibers and VTMS-PP fibers at the first and second heating ramps after isothermal annealing at 125°C under N_2 flow for three hours 214

7.9 ESEM micrographs of VE composites and PP fibers after DSC testing. (a) inside of PP-VE DSC specimen, (b) inside of VPP-VE DSC specimen, (c) outside of PP-VE DSC specimen, (d) outside of VPP-VE DSC specimen, (e) untreated PP fibers, and (f) VTMS-PP fibers 215

7.10 Multiple frequency sweep of VE, PP-VE and VPP-VE. For each material, curves shift from left to right when frequency increases from 0.1 Hz to 30 Hz..216

7.11 Load-deflection curves in tensile testing for neat VE resin, PP-VE and VPP-VE composites.....217

7.12 ESEM micrographs of fracture surface of (a, b) PP-VE and (c, d) VPP-VE 218

8.1 The layout of glass fiber-VE composite fabrication with an initial delamination and the sketch of the two interlaminar fracture modes 229

8.2 Mode I interlaminar fracture toughness testing using double cantilever beam (DCB) specimens 230

8.3 Mode II interlaminar fracture toughness testing using end notch flexural (ENF) specimens.....231

8.4 Hysteresis loop used to calculate friction energy in bending in mode II interlaminar fracture tests 232

8.5 Load-displacement curves in mode I interlaminar fracture tests using DCB specimens for GF-VE composites without PP, with one-ply PP or with one-ply VTMS-grafted PP (VPP) as the interlayer.....233

8.6 Mode I interlaminar fracture toughness as a function of delamination length **a** for GF-VE composites without PP, with one-ply PP or with 1-ply VPP as the interlayer 234

8.7 Load-displacement curves in mode II interlaminar fracture tests using ENF specimens for GF-VE composites without PP, with one-ply PP or with one-ply VPP as the interlayer.....235

8.8 Mode I interlaminar fracture toughness as a function of delamination length **a** for GF-VE composites with one-ply or two-ply PP interlayer 236

8.9 ESEM micrographs of fracture surface of GF-VE composites after mode I tests with (a) no PP, (b) 1-ply PP, (c) 2-ply PP, or (d) 1-ply VPP as the interlayer 237

8.10 ESEM micrographs of fracture surface of GF-VE composites after mode II tests with (a) 1-ply PP or (b) 2-ply PP as the interlayer.....238

8.11 Visual observation of fracture surface of GF-VE composites after (a) mode I tests and (b) mode II tests with various interlayer. The color of the glass fibers is lighter than that of the resin 239

8.12 ESEM micrographs of fracture surface of GF-VE composites after mode II tests with (a) no PP or (b) 2-ply PP as the interlayer using freshly received GF.....240

Abstract

Functional Polymer-Polymer Composites by Nano/Meso-Fiber Encapsulation: Applications in Drug Delivery Systems and Polymer Toughening

Ya Liang

Giuseppe R. Palmese, Ph.D.

Anthony M. Lowman, Ph.D.

This research focuses on developing functional polymer-polymer composites through fiber encapsulation. Two composite systems, poly(lactide-co-glycolide) (PLGA) – poly(vinyl alcohol) (PVA) and polypropylene (PP) – vinyl ester (VE), were investigated. The goal was to evaluate these systems for their potential applications in drug delivery and polymer toughening.

Sustained, controlled release of therapeutics and mechanical stability are desired in most drug delivery systems. This can be achieved by combining PLGA and PVA. The drug release rate mainly depends on the degradation rate of PLGA, while mechanical stability is maintained by PVA hydrogels. In this work, degradation behaviors of PLGA fibers and mechanical properties of PLGA-PVA composites were investigated during incubation in PBS (pH = 7.4) at 37°C. The size of nanofibers and the PVA matrix did not have a significant impact on the degradation rate. Degradation of PLGA fibers followed pseudo first-order kinetics. PVA matrix reduced mat shrinkage from 85% to 30% and maintained mechanical integrity of composites under incubation conditions. A gradual increase of tensile strengths and moduli of composites were observed after incubation for up to eight weeks, which was comparable to PVA hydrogels.

Thermosetting resins have good chemical and mechanical properties. However they are brittle, thus limiting their use in high performance composite materials. Rubber

particles are usually used to toughen thermosetting resins, but they also greatly reduce mechanical properties. Rigid thermoplastic polymers have been investigated as toughening materials while limiting the loss of mechanical properties. In this work, small diameter PP fibers were used to toughen VE resins. Results showed that PP greatly enhanced fracture toughness, but reduced mechanical strength of VE as voids were observed at the interface. Interfacial discontinuities of composites were improved after a plasma-based surface modification using vinyltrimethoxysilane (VTMS) was conducted on PP fibers. VTMS-grafting on PP did not significantly improve mechanical properties of the composite, but slightly increased fracture toughness by improving load transfer from VE to PP.

Overall, the PLGA-PVA system had a controllable degradation rate and desired mechanical stability for use in drug delivery systems, while the PP-VE system provided valuable information on toughening mechanisms of thermoplastic fibers and on toughening phase selection.

Chapter 1: Introduction

This research focused on developing functional polymer-polymer composites through fiber encapsulation. Each component possessed significantly different physical or chemical properties but remained separate and distinct on a macroscopic level within the finished structure. For the composites investigated in this work, random, continuous fibers were distributed in the continuous polymer matrix. Two composite systems were investigated in this work. One was a biodegradable polymer-hydrogel system designed for drug delivery applications. This system combined the biodegradability of poly(lactide-co-glycolide) (PLGA) and soft tissue resemblance of poly(vinyl alcohol) (PVA) hydrogel to design a controlled release device. The other was a thermoplastic fiber-thermoset resin system designed for polymer toughening applications. This system utilized the energy absorption and dissipation capability of thermoplastic fibers such as plastic deformation, fiber pullout and interfacial surface area to improve fracture toughness of brittle vinyl ester resins. Both composite systems were expected to have better mechanical properties than individual components and to have potential functionality. The overall goal was to evaluate such composite systems for their potential applications in drug delivery and polymer toughening.

1.1. Drug Delivery

1.1.1. Motivation

Traditional drug administration routes are simple and convenient, but they normally cause local or systemic toxicity, and have low bioavailability to the required

zone [1]. Implantable drug delivery devices can directly deliver the drugs to the target, which can reduce local and systemic toxicity, and improve bioavailability.

Drug delivery devices made with biodegradable materials can obtain sustained, controlled release. The release rate generally depends on the erosion rate. There is no surgery required to remove the device after drug release, so they are convenient for use as temporary drug delivery devices. For example, Gliadel® Wafers are temporary devices for delivering carmustine to treat brain tumors. However, it is impossible to remove the device if therapy needs to be terminated prematurely. The most commonly used biodegradable polymers are poly(lactide-co-glycolide) (PLGA) copolymers due to their excellent biocompatibility and non-toxic degradation products. These polymers are hydrolytically unstable and degrade *in vitro* and *in vivo* at very different rates. The degradation rates of copolymers can be modulated by varying the molar ratio of monomers, which is an advantage for controlled-release drug delivery systems. Unfortunately, these PLGA polymers usually go through bulk erosion [2], which causes the biodegradable devices to crumble into small pieces before most of the drugs are released. The fragments can move to other regions to cause local or systemic toxicity. When the devices are used to deliver growth factors in tissue engineering applications, the moving boundary due to degradation can result in shear stress in growing tissue, which is not good for cell differentiation.

Hydrogels have very good biocompatibility and resemble human soft tissues. Poly(vinyl alcohol) (PVA) is one of the hydrogels whose crosslinks can be formed physically through low temperature crystallization [3]. The most commonly used method is repeated cycles of freezing and thawing a PVA aqueous solution. This process can

eliminate the use of toxic crosslinking agents and organic solvents. Also, PVA hydrogels are bioadhesive in addition to having the properties common to all hydrogels [4]. They have been used in applications such as linings for artificial hearts, drug delivery, soft tissue replacements, articular cartilage, artificial skin, artificial pancreas, and hemodialysis membranes [4]. The potential problem for drug delivery applications is their fast release rate, which is controlled by drug diffusion through the swollen network. For many applications, drug concentration at the target depends on diffusion through the biological barrier [1], not the drug delivery device. Therefore, a slow but sustained release is normally preferred.

1.1.2. Research Objective

The goal was to evaluate whether this PLGA-PVA composite system was feasible for controlled-release drug delivery device applications regarding the controllable and predictable release rate and the required mechanical strength and stability. Specifically, three aims would be achieved through this work:

Aim 1: Control the molecular weight and copolymer composition of PLGA during synthesis; control the morphology of electrospun PLGA fibers.

Aim 2: Investigate *in vitro* degradation behavior of electrospun PLGA fibers; investigate influence of morphology and PVA hydrogels on PLGA fiber degradation; build a degradation model.

Aim 3: Investigate tensile properties of PVA hydrogels and PLGA-PVA composites during incubation.

1.1.3. Contribution of this Research

By combining biodegradable PLGA and PVA hydrogels, one can expect a drug delivery device having a sustained controlled release profile and good mechanical stability. Most research has been focused on PLGA microparticle - hydrogel systems from which a near linear or controlled release was obtained [5, 6]. The difficulty involved in developing those systems includes particle suspension and incorporation of large volume fraction. In this work random, continuous fibers were encapsulated in the PVA hydrogel matrix. These PLGA fibers had a predefined, even distribution and could be loaded in hydrogels at a much higher volume fraction than microparticles. Therapeutics were incorporated in PLGA fibers during the electrospinning process. This device could be used to deliver therapeutics to treat diseases or relieve pain. It could also be used to deliver growth factors for tissue growth between artificial tissues and the body. Physically crosslinked PVA hydrogels possess an interconnected porous structure which provides room for cell growth. Additionally, those biodegradable fibers can guide cell growth while releasing growth factors [7].

Research has shown that drug release depends on degradation when using PLGA as drug carriers, especially for macromolecules that diffuse very slowly in PLGA [8-10]. Therefore, understanding the degradation process will help one to predict the drug release rate. Many research groups have investigated the degradation and drug release of PLGA fibers. However, few studies have been done regarding the influence of the fiber morphology and PVA matrix on PLGA fiber degradation. Two research groups investigated the influence sample dimensions of PLGA spherical particles had on the degradation rate and found that the degradation rate increased with increasing sample

diameters in the range of 0.53 to 100 μm [11, 12]. However, if the dimension is so small that the intrinsic degradation rate can be obtained, the degradation will be independent of the sample dimensions. This may be achieved by using nano-scaled fibers. Therefore, this research investigated the *in vitro* degradation of PLGA fibers with a focus on factors that may affect the degradation in the fiber-hydrogel system, such as fiber morphology and PVA hydrogels. Mechanical stability of the fiber-hydrogel system during *in vitro* degradation was also addressed.

1.2. Polymer Toughening

1.2.1. Motivation

Vinyl ester (VE) resins are a class of thermoset polymers that possess high chemical and corrosion resistance, good thermal and mechanical properties, and are relatively easy to process. However, VE resins are brittle, thus limiting their use in high performance composite materials. Preformed rubber particles [13, 14], thermoplastic particles [15, 16] and thermoplastic fibers [17-19] have been developed for toughening VE resins. Rubber particles with diameters of 100 nm–5 μm provide excellent energy absorption capacity [20], but greatly reduce the mechanical strength. Rigid thermoplastics were used to toughen Epoxy resins in the early 1980s. The rigid thermoplastic phase was found to increase toughness without reduction in modulus or strength. Polyether sulfone, polysulfone, polyetherimide, polyphenylene ether and polybutylene terephthalate have been evaluated for toughening a variety of thermoset plastics and, in some cases, significant increases in toughness have been obtained [20]. High modulus thermoplastics have also been used to toughen VE resins [18, 19].

Compared to common particulate fillers, continuous polymeric fibers offer distinct toughening mechanisms such as fiber pullout, breakage and interfacial strength, while providing good physical properties.

Polypropylene is a tough, semicrystalline thermoplastic with a melting temperature of 161°C. In addition to the toughening properties of the PP fibers, the phase transition associated with melting could provide a new energy absorption mechanism. PP fibers with a nominal diameter of 50 μm were used to toughen glass fiber-thermoset (epoxy or isophthalic polyester) composites [21]. The laminates with thermoplastic fibers exhibited a considerable increase in energy absorption compared to laminates without thermoplastic fibers during impact and delamination propagation.

Most thermoplastics have low surface energy, which normally results in poor wettability and weak bonding at the interface. The discontinuities and void formation limit the interfacial strength and load transfer from the matrix to the toughening fibers. Surface treatments play an important role in improving interfacial bonding and preventing such discontinuities. Chemical functional groups have been added to the surface of polymeric fibers by techniques such as plasma treatment [18, 19, 22], UV/ Ozone [23] and the use of coupling agents [24, 25]. Such functional groups interact with the polymer matrix to enhance interfacial adhesion and mechanical properties of polymer-polymer composites. Gas plasma treatment is a commonly used technique because of the relatively low operation cost. Also, it is a fast process and affects the surface properties of the exposed material without altering its bulk. Chemical functional groups and minor surface etching are created during plasma treatment. Plasma-generated functional groups tend to reorganize in order to lower the surface energy during storage

[26], so stable functional groups grafted through coupling agents are preferred when an immediate follow-up process is unrealistic.

1.2.2. Research Objective

The goal was to evaluate if the PP-VE composite system could obtain better fracture toughness without sacrificing necessary mechanical properties when compared with neat VE resins. Three specific aims would be accomplished:

Aim 4: Study plasma-based surface modification to PP fibers; characterize functional groups created on the surface.

Aim 5: Evaluate toughening of brittle vinyl ester resins using thermoplastic PP fibers by characterizing thermal and mechanical properties of composites and analyzing the failure mechanism.

Aim 6: Investigate interlaminar fracture toughness of glass fiber-VE composites using thermoplastic fibers as interlayer.

1.2.3. Contribution of this Research

Thermoplastic particles and fibers have been used to toughen thermosetting resins. Those particles or fibers were normally in the tens of microns range in size. Most work focused on toughening epoxy resins. In this work, we focused on random, continuous, small-sized fibers in the submicron range. Commercial polypropylene (PP) fibers with small diameters (~1 μm) were chosen as the toughening agent for VE resins. The commercial availability could reduce cost as well. Small fibers provided a high surface-to-volume ratio, which could increase the total interfacial strength, enhance load transfer,

and improve energy absorbing capacity. Fracture toughness, tensile properties, flexural properties, thermal and thermomechanical properties were determined to evaluate the PP fibers as the toughening phase for VE resins. Influence of surface treatment of PP on interfacial strength, fracture toughness and mechanical properties of PP-VE composites was investigated. Fracture surface was used to analyze the failure mechanism of the composites with weak or strong interface. These PP fibers could also be used to toughen other thermosetting resins such as Epoxy. Furthermore, the toughened polymeric systems could be used in advanced composite applications to increase the interlaminar fracture toughness.

1.3. Structure of the Thesis

This thesis is divided into two parts according to the two applications. Chapter 2 gives some background related to PLGA-PVA and PP-VE systems, including drug delivery devices, biomedical materials, polymer toughening methods, surface treatments of polymers and major materials investigated in this work. Chapters 3-5 deal with the PLGA-PVA system while chapters 6-8 focus on the PP-VE systems. Chapter 9 summarizes the two composite systems and gives recommendations for future work.

Chapter 3 focuses on preparing PLGA nanofibers including controlling PLGA molecular weight and fiber morphology. Chapter 4 investigates degradation of PLGA fibers. Influence of fiber morphology and PVA matrix on PLGA degradation is studied and a degradation model is derived for the PLGA-PVA system. Chapter 5 studies the mechanical stability of the PLGA-PVA system during incubation. Chapter 6 investigates the surface modification of PP fibers, mainly with oxygen plasma and a silane coupling

agent (VTMS). Chapter 7 focuses on toughening VE resin using PP fiber mats, either untreated or surface treated PP. Fracture toughness and mechanical properties are used to evaluate the toughening capacity of PP fibers. Chapter 8 uses the PP-VE system in high-performance composites in an effort to increase interlaminar toughness. The overall structure of the thesis is shown in Figure 1.1.

List of References

1. Saltzman WM. Drug Delivery: Engineering Principles for Drug Therapy. New York: Oxford University Press US, 2001.

2. Burkersroda F, Schedl L, Gopferich A. Why degradable polymers undergo surface erosion or bulk erosion. Biomaterials 2002; 23: 4221-4231.

3. Peppas, NA. Infrared Spectroscopy of Semicrystalline PVA Networks. Makromol. Chemie. 1977; 178: 595-601.

4. Hassan CM, Peppas NA. Structure and applications of poly(vinyl alcohol) hydrogels produced by conventional crosslinking or by freezing/thawing methods. Advances in Polymer Science 2000; 153:37-65.

5. Liu X, Nakamura K, Lowman AM. Composite hydrogels for sustained release of therapeutic agents. Soft Materials 2003; 1(3): 393-408.

6. Galeska I, Kim TK, Patil SD, Bhardwaj U, Chatttopadhyay D, Papadimitrakopoulos F, Burgess DJ. Controlled release of dexamethasone from PLGA microspheres embedded within polyacid-containing PVA hydrogels. The AAPS Journal 2005; 7(1): E231-E240.

7. Li, W-J, Laurencin, C et al. Electrospun nanofibrous structure: A novel scaffold for tissue engineering. Journal of Biomed. Mater Res. 2002; 60: 613–621.

8. Shah SS, Cha Y, Pitt CG. Poly(glycolic acid-co-dl-lactic acid): diffusion or degradation controlled drug delivery? Journal of Controlled Release 1992; 18: 261-270.

9. Fitzgerald JF, Corrigan OI. Mechanisms governing drug release from poly-α-hydroxy aliphatic esters. In: Ei-Nokaly MA, Piatt DM, Charpentier BA, editors. Polymeric delivery systems, properties and applications. ACS Symposium Series No. 520. Washington DC: American Chemical Society, 1993: 311-326.

10. Zolnik BS, Burgess DJ. Effect of acidic pH on PLGA microsphere degradation and release. Journal of Controlled Release 2007; 122:338-344.

11. Siepmann J, Elkharraz K, Siepmann F, Klose D. How autocatalysis accelerated drug release from PLGA-based microparticles: a quantitative treatment. Biomacromolecules 2005; 6: 2312-2319.

12. Dunne M, Corrigan OI, Ramtoola Z. Influence of particle size and dissolution conditions on the degradation properties of polylactide-*co*-glycolide particles. Biomaterials 2000; 21: 1659-1668.

13. Gilbert EN, Hayes BS, Seferis JC. Interlayer toughened unidirectional carbon prepreg systems: effect of preformed particle morphology. Composites Part A: Applied Science and Manufacturing 2003; 34:245-252.

14. Johnsen BB, Kinloch AJ, Mohammed RD, Taylor AC, Sprenger S. Toughening mechanisms of nanoparticle-modified epoxy polymers. Polymer 2007; 48:530-541.

15. Groleau MR, Shi Y-B, Bertram JL, Sue HJ, Yang PC. Mode II fracture of composites interlayered with nylon particles. Composites Science and Technology 1996; 56:1223-1240.

16. Yun NG, Won YG, Kim SC. Toughening of epoxy composite by dispersing polysulfone particle to form morphology spectrum. Polymer Bulletin 2004; 52:365-372.

17. Hogg PJ. Toughening of thermosetting composites with thermoplastic fibres. Materials Science and Engineering A 2005; 412:97-103.

18. Moon SI, Jang J. Factors affecting the interfacial adhesion of ultrahigh-modulus polyethylene fibre-vinylester composites using gas plasma treatment. Journal of Materials Science 1998; 33:3419-3425.

19. Lin SP, Han JL, Yeh JT, Chang FC, Hsieh KH. Surface modification and physical properties of various UHMWPE-fiber-reinforced modified epoxy composites. J Appl Polym Sci 2007; 104:655-665.

20. Pearson RA. Introduction to the toughening of polymers. Pearson RA, Sue HJ, Yee AF, editor. Toughening of Plastics, Advances in Modeling and Experiments. ACS Symposium Series No. 759. Washington DC: American Chemical Society, 2000:1-12.

21. Hogg PJ. Toughening of thermosetting composites with thermoplastic fibres. Materials Science and Engineering A 2005; 412:97-103.

22. Brown JR, Mathys Z. Plasma surface modification of advanced organic fibres, Part V Effects on the mechanical properties of aramid/phenolic composites. Journal of Materials Science 1997; 32:2599-2604.

23. Khanchaitit P, Aht-Ong D. Continuous surface modification process with ultraviolet/ozone for improving interfacial adhesion of poly(ethylene terephthalate) /epoxy composites. Polym Compos 2006; 27:484-490.

24. Lu J, Askeland P, Drzal LT. Surface modification of microfibrillated cellulose for epoxy composite applications. Polymer 2008; 49:1285-1296.

25. Hashemi SA, Arabi H, Mirzaeyan N. Surface modification of bagasse fibers by silane coupling agents through microwave oven and its effects on physical, mechanical, and rheological properties of PP bagasse fiber composite. Polym. Compos 2007; 28:713-721.

26. Cui NY, Brown NMD. Modification of the surface properties of a polypropylene film using an air dielectric barrier discharge plasma. Applied Surface Science 2002; 189:31-38.

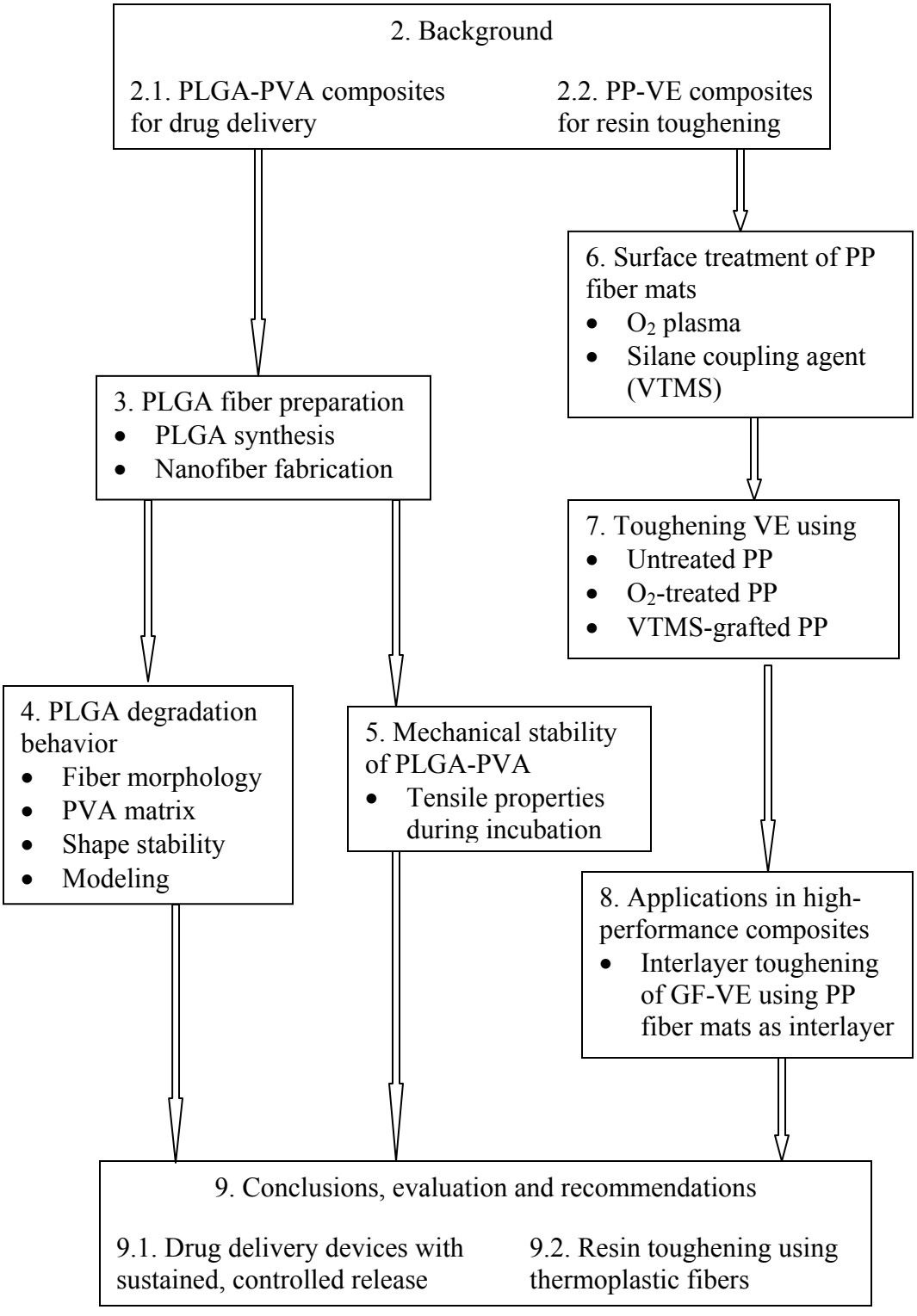

Figure 1.1. A diagram illustrating the overall structure of the thesis.

Chapter 2: Background

In this chapter, background for both applications will be covered. Existing and developing drug delivery systems will be discussed, followed by available polymeric biomaterials, nanotechnologies, and their applications. For the polymer toughening application, polymer toughening methods, surface modification techniques and applications in high performance composites will be discussed.

2.1. Drug Delivery Systems

Drugs/medicines have been administrated for centuries in the forms of pills, injections, lotions, and suppositories [1]. Traditional administration routes include oral, subcutaneous, intramuscular, intravenous, and topical delivery [2]. Traditional delivery systems include needles, syringes, fluted paper cups, intravenous bags and catheters [2]. Oral administration is usually preferred because it is easy, simple and convenient. However, many drugs are degraded within the gastrointestinal tract or not absorbed effectively through oral administration. Subcutaneous, intramuscular or intravenous injection can minimize the drug degradation. However, they may still destroy surrounding tissues, have minimum bioavailability to the required zone, or cause local or systemic toxicity. Intranasal delivery, such as calomist (cyanocobalarain, vitamin B_{12}) nasal spray and intranasal insulin, is an easy, patient-friendly administration route in the form of powders, drops, topical gels and sprays [2]. Nevertheless, topical delivery depends on the drug penetrating through the skin or mucous membranes, so the delivery

is very slow and even impossible for some macromolecules. Additionally, many topically administered drugs have systemic effects.

Proteins have been considered for therapeutic use due to the development of the recombinant protein technique. At present, proteins are administrated mainly by injection. However, proteins do not easily cross mucosal surfaces and biological membranes, are easily denatured or degraded, prone to rapid clearance in liver and other body tissues and require precise dosing [1]. Proteins are active in a variety of body parts, so administration of large quantities to treat disease in one organ can cause toxic effects in another [1].

Designing novel drug delivery systems should consider minimizing side effects and reducing damages to surrounding tissues by delivering medications only where needed. This can also improve drug bioavailability and subsequently reduce the cost by using fewer doses. Most importantly, some drugs have an optimun concentration range and can be toxic or have no therapeutic benefit outside the range. Therefore, the delivery of the proper amounts of therapeutics to targets in tissues or organs is highly desirable.

2.1.1. Controlled Release Systems

Controlled drug delivery systems can deliver drugs directly to the target, are more efficient than traditional systems, and can reach higher localized concentrations. Controlled release systems can be classified into diffusion-controlled, chemically-controlled, solvent-activated, or external force-induced release systems based on the release-triggering mechanism [3].

The most promising controlled release systems involve encapsulation or entrapment of therapeutics in polymeric devices or compartments. Polymeric delivery systems have been designed in different configurations such as reservoirs or matrices. The reservoir type is the earliest controlled delivery system and the polymer membrane surrounding drugs regulates the release rate through diffusion. Silicon elastomers or poly(ethylene-co-vinyl acetate) (EVAc) are usually used as membranes. The Norplant® contraceptive system, which delivers levonorgestrel for over five years, is a reservoir system. Potential problems of reservoir delivery systems include slow diffusion of large molecules and membrane failure. Matrix delivery systems are fabricated by dispersing drugs in a solid polymer matrix. Drugs are released by polymer erosion when using biodegradable polymers as the matrix or by polymer swelling or dissolution when using hydrophilic polymers such as hydrogels [4].

The field of controlled release mainly focuses on sustained release and pulsatile release. Sustained release normally involves drug release at a controlled rate due to diffusion out of polymers or polymer degradation over time [5]. The sustained release system can be in the form of oral tablets, polymer implants, polymer microspheres, and transdermal patches. Gliadel® and Lupron Depot® are two examples of commercially available polymeric sustained release devices [6]. Gliadel® Wafers are implantable polyanhydride wafers which release carmustine at a constant rate by polymer degradation into the surgical cavity created when a brain tumor is resected for malignant brain tumor treatments. Lupron Depot® consists of injectable polymer microspheres which can treat endometriosis, fibroids, precocious puberty, or cancer. Pulsatile release mimics the natural way the body produces hormones by using drug-carrying polymers that respond

to specific stimuli, such as changes of pH, temperature, electric or magnetic fields, exposure to light or ultrasound, or molecules in the human body [6]. The pulsatile release systems can be oral or implantable polymer devices, transdermal delivery, or a combination of pumps and catheters.

2.1.2. Commercially Available Drug Delivery Systems

Implantable pumps have been around for 30 years and are mainly used for cancer and post operative pain [7] by delivering drugs directly to the intrathecal or intracerebroventricular sites. For example, implantable intrathecal drug delivery systems for refractory cancer pain have been mainly used on patients who have more than a three-month life expectancy [8-9]. The Minimed Medtronic insulin delivery pump includes an insulin reservoir, a refilling port, a carbon monofluoride battery with lifetime of 6-7 years and safety features suitable for long-term usages [10]. It can be programmed with an external communicator. Implantable pumps may possess risks such as infection, pharmacological side effects, catheter dislodgment, and malfunction [2].

Surgically implanted medication delivery systems under the skin eliminate the frequent oral administration and improve adherence, especially for patients with serious psychiatric illnesses. Haloperidol implants in schizophrenic patients have shown advantages such as lower doses, consistent steady-state serum levels and fewer side effects [2].

The BioErodible MucoAdhesive (BEMA) delivery system is designed to deliver drugs across mucosal tissues locally or systemically. It provides rapid onset of action and improved bioavailability compared with the oral delivery. It has shown promise for

delivering pain medications, as well as antiemetics and antimigraine drugs [2]. The BEMA Fentanyl mouth patch from BioDelivery Sciences International (BDSI) is designed for breakthrough cancer pain in opioid-tolerant patients. It was approved by the U.S. FDA on July 16, 2009, and marketed as ONSOLIS®.

2.1.3. Drug Delivery Systems under Development

Ocular drugs have poor bioavailability, especially in the form of eyedrops. Contact lens sustain-release delivery systems use polymers which hold therapeutic agents in the matrices in contact lenses to increase drug bioavailability to the eye. Drug release is controlled by channels in the contact lenses which open upon contact with eyes. Potential applications include medication delivery for eye diseases such as glaucoma, wound-healing drug delivery for treating corneal wounds, and self-lubricating contact lenses for relieving discomfort [2].

Depot technology creates *in situ* drug-containing implants by subcutaneous or intramuscular injection of polymer solutions containing medications, which become solids or gels at the injection site. This technique can be used for local or systemic drug administration. It is an attractive delivery system for parenteral application due to its less invasive and painful features compared to traditional implants. Injectable *in situ* forming depot systems include thermoplastic pastes, *in situ* cross-linked polymers, *in situ* polymer precipitation, and thermally induced gelling systems [2, 5].

Microfabrication-based drug delivery systems generally consist of a microchip refillable drug reservoir, a battery, a mechanical pumping/valving mechanism, advanced electronics which control drug release and can be programmed from outside the body,

and catheters [10]. Implantable microchip drug delivery devices based on MEMS (microelectromechanical systems) technology are being developed by MicroCHIPs Inc [6, 11-13]. Potential advantages of the microchip-based drug delivery devices include releasing chemicals in any form, accuracy, complex release patterns, and drug stability enhancement [6]. Considerations have to be given in designing devices, including catheter kinks and disconnections, battery life, dead space, refilling failure and malfunction.

Nanotechnology has shown potential benefits in boosting drug delivery and drug targeting improvement in ways such as minimizing toxicity, improving efficacy, crossing particular physical barriers, and finding alternative and acceptable routes for protein delivery [5]. Drug carriers based on nanotechnology include micelles, vesicles, liquid crystals, dendrimers, nanospheres, nanocapsules, drug-loaded erythrocytes and nanoemulsion vaccines [2, 5]. Nanoscale drug carriers can potentially improve the drug delivery through nasal and sublingual routes so as to avoid first-pass metabolism, as well as delivering drugs to difficult-access ocular, brain, and intra-articular cavities [5]. Nanoparticles have been demonstrated to cross the blood brain barrier with little difficulty and Germany's nanoPharm has developed systems capable of reaching the brain for anesthesia, cancer drugs, and other therapeutics [14]. Estrasorb (FDA approval 2003) and Androsorb are two hormone replacement therapies for rapid topical delivery of active compounds through micellar nanoparticles developed by Novavax [14]. Elan's Nanocrystal technology has been used by Johnson and Johnson for an injectable formulation of paliperidone palmitate, a drug for schizophrenia, to enhance solubility by reducing the particle size to less than 200 nm (JNJ) [14].

Molecular imprinting technology (MIP) uses template molecules and functional monomers, oligomers, or polymers, which have specific chemical structures to interact with the template covalently or non-covalently, to form a pre-polymerization complex. The polymerization occurs in the presence of a cross-linking monomer and a selected solvent to control the morphology and macroporous structure. After removing the template, the resulting heteropolymer matrix will keep the specific recognition elements for the template molecule. MIP-based drug delivery systems can be used for rate-programmed, activation-modulated, or feedback-regulated drug delivery [5].

Conjugation of biological and synthetic polymers can improve drug bioavailability, drug targeting, and biocompatibility of drug delivery systems. For example, conjugation of biocompatible polymers to bioactive proteins or peptides can reduce toxicity, prevent immunogenic or antigenic side reactions, enhance blood circulation times and improve solubility. Modification of polymers with suitable oligopeptide sequences can improve active targeting. Polymers or polymer surfaces functionalized with peptide sequences derived from extracellular matrix proteins can mediate cell adhesion [5].

2.1.4. Drug Delivery Carriers Prepared via Nanotechnology

Micelles are formed by self-assembly of amphiphilic block copolymers in aqueous solutions. The drugs are entrapped in the core of micelles. The outer hydrophilic blocks and aqueous surroundings form a tight shell around the core, which protects the entrapped drugs against hydrolysis and enzymatic degradation. Drugs can be transported at concentrations higher than their intrinsic solubility in water. The corona

may prevent recognition by the reticuloendothelial system that will eliminate micelles from the bloodstream. The block copolymers can be functionalized to increase stability or selectivity [5].

Liposomes are a form of vesicles consisting of one or more phospholipid bilayers. Polar drugs are encapsulated in the polar core while amphiphilic and lipophilic molecules are soluble in the phospholipid bilayer. Drugs encapsulated in a nanocage functionalized with channel proteins are protected from premature degradation by proteolytic enzymes. The drug molecule can diffuse through the channel driven by the concentration gradient [5].

Dendrimers are highly branched macromolecules with symmetrical architecture and consist of a central core, branching units, and terminal functional groups. The external groups determine the solubility and chemical behavior of dendrimers. Targeting ligands are attached at the external surface. Functionalization of the dendrimers with polyethylene glycol can improve their stability and protect them from the mononuclear phagocyte system [5].

Nanoparticles (nanospheres and nanocapsules) can adsorb and /or encapsulate drugs and thus protect them from chemical and enzymatic degradation. Nanocapsules are vesicular systems, and drugs are surrounded by a polymer shell. Nanospheres are matrix systems, and drugs are physically and uniformly dispersed. Nanoparticles, particularly those made of biodegradable polymers, have potential applications in controlled release, targeting particular organs/tissues, gene therapy, and delivering proteins, peptides and genes through the peroral route [5]. Multilayered nanoparticles can be designed to penetrate the body's immune system. Each layer of the nanoparticle is designed to

overcome each physiologic barrier as the particle moves through the body. The outer layer is disposed once the nanoparticle moves through that barrier [2].

Liquid crystals can form different geometries with alternative polar and non-polar layers for encapsulating aqueous drug solution [5].

Erythrocytes can be split open and loaded with drugs. Glutaraldehyde, antibodies or specific carbohydrates can be grafted on the surface of the erythrocyte to increase the circulation half-life and allow for body barrier penetration and precise drug delivery [5].

A vaccine carrier system using nanoemulsions is a novel technique for vaccinating against a variety of infectious diseases [15]. The nanoemulsion vaccine is an oil-based emulsion administered in the nose and highly effective at penetrating the mucous membranes in the nose. This technique has proven to produce a strong immune response against smallpox [16] and HIV [17].

Electrospinning nanofibers are also used as drug carriers. These continuous fibers form a porous, predefined network. The drugs are dispersed in the polymer solution before electrospinning and then are uniformly distributed in the fibers upon solvent evaporation during electrospinning. Details of this technique will be discussed in section 2.5.

2.2. Polymeric Biomaterials for Drug Delivery

Biomaterials include metals, polymers, ceramics, glasses, natural materials and composites. The most important biomaterials used in drug delivery systems are polymers. Polymer delivery systems can provide localized delivery and long-term release. Some polymeric delivery systems can be designed to respond to environment or to stabilize

proteins. Depending on the applications, polymeric biomaterials can be classified into non-degradable hydrophobic polymers, biodegradable polymers and hydrogels.

2.2.1. Non-degradable Hydrophobic Polymers

Silicone elastomers are chemically inert, stable, and biocompatible. They were first used for controlled drug delivery systems in 1962 when Folkman and Long found that small molecules could diffuse through silicone membranes. Silicone has been approved by the FDA for many biomedical applications, such as breast prostheses and heart valve prostheses. Copolymerization of siloxanes with other polymers can enhance mechanical properties, improve adhesion to tissues, or control permeability [1].

Poly(ethylene-co-(vinyl acetate)) (EVAc) has excellent biocompatibility and has been approved by the FDA for use in implanted and topical devices. The most commonly used EVAc (ELVAX®-40, DuPont) contains 40% vinyl acetate with a low degree of crystallinity. EVAc is used in the Progestasert intra-uterine device to delivery contraceptive hormones. It is also used as a rate-controlling membrane in transdermal devices [1].

Several other common polymers have been used in biomedical devices and can be potentially used in drug delivery systems. For example, polyethylene is used to produce catheters and hip prostheses. Woven poly(ethylene terephthalate) fibers and poly(tetrafluoroethylene) are used in vascular grafts. Poly(methyl methacrylate) is used in orthopedic applications and in intraocular lenses [1].

2.2.2. Biodegradable Polymers

Biodegradable polymers are of great value in short-term applications such as temporary scaffolds, temporary barriers, drug delivery devices, and multifunctional devices. Absorbable sutures, used for surgery, are made from animal tissues, such as collagen. However, natural sutures have some disadvantages such as lacking uniformity of size, texture, strength and absorption rate, antigenetic characteristics, and short segments. Synthetic absorbable sutures, which would meet medical requirements for strength, handle-ability, non-toxicity, and predictable and uniform absorbability, are desirable [18]. Poly(glycolic acid) (PGA), the first synthetic absorbable suture, was developed in 1962 and then made commercially available as the surgical suture Dexon® in 1970 [19]. Then, a copolymer of 92wt% glycolic acid (GA)/ 8wt% lactic acid (LA), with limited application, was introduced as the competitive suture Vicry in 1975 [19]. Various biodegradable polymers, mainly linear aliphatic polyesters, have been studied as biomaterials for tissue engineering and drug delivery systems since then.

2.2.2.1. PGA, PLA and PLGA – Most Widely Used Biodegradable Materials

PGA is a hard, crystalline polymer and does not dissolve in most organic solvents [19], except in highly fluorinated organic solvents such as hexafluoroisopropanol (HFIP) [20]. The melting temperature of PGA is near 215-230°C and the glass transition temperature is about 35-40°C [21]. PGA is relatively hydrophilic and degrades in aqueous solutions, losing its mechanical integrity between two and four weeks [22].

Poly(lactic acid) can exist in two forms: optically active L-form or racemic D, L-form. Poly(l-lactic acid) (PLLA) is the naturally existing form. The semicrystalline

PLLA possesses about 37% crystallinity with a melting temperature of 170-180°C and a glass transition temperature of about 55-64°C [23]. Poly(d,l-lactic acid) (PLA) is amorphous with a glass transition temperature of 50-60°C [24]. PLLA is only soluble in halogenated solvents and HFIP while PLA can dissolve in many organic solvents [25]. PLA is more hydrophobic compared with PGA because the extra methyl groups reduce the molecular affinity to water. Thus, PLA has a slower hydrolysis rate and loses its mechanical integrity over many months or even years.

Poly(lactic-co-glycolic) acid (PLGA) copolymers with various LA/GA ratios can therefore be synthesized to obtain degradation rates in a broad range. PLGA prepared from l-lactic acid and containing 25 - 70% glycolic acid is amorphous, while PLGA prepared from d,l-lactic acid and containing less than 70% glycolic acid is amorphous [19]. There is no linear relationship between the copolymer composition and the physicomechanical properties of the copolymer. The 50:50 copolymers degrade more rapidly than either PGA or PLA due to the complete loss of crystallinity [26]. Chemical structures of PLA, PGA and PLGA are sketched in Figure 2.1. Because PLA, PGA, and PLGA combine many desirable properties and are approved by the U.S. FDA for medical applications, as well as a wide range of adjustable degradation rates, they have been of great interest for using in drug delivery systems [27].

PLGA has been modified to obtain desired properties. For applications of hydrophilic controlled-release systems, hydrophilic poly(ethylene glycol) (PEG) has been introduced into hydrophobic PLA or PLGA polymer chains to make diblock [28-30] or triblock [31-33] copolymers. PEG-modified surfaces are known to inhibit protein adsorption and possess superior biocompatibility with low immunogenicity and toxicity.

Therefore, the introduction of PEG segments not only enhances the water uptake capacity of PLA/PLGA but minimizes protein adsorption tendency [29]. NaOH-treated PLGA scaffolds have been studied for articular cartilage repair [34]. A more hydrophilic surface, increased surface area, nanoscale roughness, and altered porosity were observed after NaOH treatment. NaOH-treated PLGA scaffolds were shown to enhance chondrocyte functions such as adhesion, growth, differentiation and extracellular matrix synthesis. PLGA (10/90) electrospun membranes were post-drawn at a tensile speed of 4 mm/min at room temperature and then heated to 60, 70, 80 or 90°C at 5 °C/min under a constant stain for annealing [35]. Thermal annealing was found to increase the crystallinity but not the overall orientation, while drawing improved orientation. The degree of crystallinity of the stretched membrane decreased with increased annealing temperature. PLGA (8020) films were isothermally annealed at 115°C to increase the crystallinity [36]. The crystal size was found to increase with annealing time and the maximum crystallinity of 21% was achieved after 60 min of annealing. Voids formation was also observed during annealing.

2.2.2.2. Other Biodegradable Materials Used for Biomedical Applications

Poly(ε-caprolactone) (PCL) has excellent permeability, but biodegradation rate is significantly slower than PLA [37], which makes PCL more attractive for long-term implants and controlled release applications [27]. They are regarded as nontoxic and tissue-compatible materials, and have been used as a degradable staple for wound closure in Europe [26]. PCL-based copolymers, such as PCL/LA [37], PCL/GA [38], and

PCL/EEP (ethyl ethylene phosphate) [39], have been studied to improve degradation properties.

Polydioxanone (PDS) was produced as an absorbable suture material in 1980s. This polyester is highly flexible and can be used to make a variety of monofilament sutures. It is also used in orthopedic applications under the trade name Orthosorb® as a fixation element for bone repair [1].

Poly(hydroxy butyrate) (PHB), poly(hydroxy valerate) (PHV) and their copolymers are made by microorganisms via fermentation. Those polyesters can be degraded by soil bacteria but are relatively stable in ambient conditions. The degradation rate can be controlled by varying the copolymer composition. PHB degrades *in vivo* to D-3-hydroxybutyric acid, a normal constituent of human blood. They have been considered in applications such as controlled drug release, sutures and artificial skin [26].

Polyanhydrides are among the most reactive and hydrolytically unstable polymers used as biomaterials. Many polyanhydrides degrade by surface erosion. Surface erosion devices can maintain their structural integrity throughout the degradation process except that their dimensions are reduced. Aliphatic polyanhydrides degrade within days whereas some aromatic polyanhydrides degrade over several years. Therefore, aliphatic-aromatic copolymers are of great interest. They possess excellent biocompatibility and are used in drug delivery devices [26].

The first poly(ortho esters) for biomedical application was produced under the trade name Alzamer® at Alza Corporation in the 1970s. The ortho ester link is more stable in base than in acid, so the degradation rate can be controlled by incorporating acidic or basic additives. Poly(ortho esters) can be fabricated into surface eroding

devices. The properties of the polymers can be varied by changing diols in the synthesis. For example, the glass transition temperature can be reduced from 100°C to below 20°C by replacing *trans*-cyclohexanedimethanol with 1,6-hexanediol. [1, 26]

A copolymer of methyl vinyl ether and maleic anhydride was the first surface-eroding polymer produced at Alza Corporation in the 1970s. The rate of erosion increases as the pH drops. However, the erosion products are macromolecules so they are not easily metabolized or excreted by the body [1].

Poly(amino acids) degrade to naturally occurring amino acids, so they usually show a low level of systemic toxicity. Furthermore, the amino acid side chains offer sites for attaching drugs, pendent groups, or crosslinking agents. Copolymers of L-glutamic acid and γ–ethyl L-glutamate have been used to release a variety of drugs. However, they have few practical applications due to their highly insoluble and non-processible properties, as well as antigenicity and poor mechanical properties [1, 26].

Poly(propylene fumarate) (PPF) can degrade through the same hydrolysis mechanism as linear aliphatic polyesters and has been used for bone tissue engineering research [27]. Segmented polyurethanes can obtain a range of mechanical properties via structural variations, and biodegradable urethane-based polymers have been developed [27].

2.2.3. Hydrogels

Hydrogels are three-dimensional networked hydrophilic materials with water filling the space between the polymer chains. Hydrogels become soft and flexible without losing their shape or mechanical strength after absorbing water, and have

superficial resemblance to human soft tissues. Young's modulus of hydrogels is comparable to that of human soft tissues, which is in the range of 0.1 to 4 MPa [40]. The first hydrogel applied in surgery is poly(vinyl alcohol) (PVA) commercialized under the trade name Ivalon® [41]. It was crosslinked with formaldehyde and caused mild tissue reaction upon implantation, although shrinkage and calcification were observed after prolonged periods. Then, in the1950s, Wichterle and Lim synthesized poly(hydroxyethyl methacrylate) (PHEMA) and crosslinked the PHEMA with diesters of methacrylic acid and mono, di and triethylene glycols [41]. It later became a main component of contact lenses.

2.2.3.1. Synthesis and Properties of Hydrogel Network

The three-dimensional network of hydrogels is maintained by physical or chemical crosslinks. Chemical crosslinks are usually created by free-radical polymerizations using crosslinking agents. They can also be produced by ionizing radiation, which is a simple, efficient, clean, and environment-friendly process, accomplishing the synthesis and sterilization in one step [41]. Chemical crosslinks are permanent since chains are linked by covalent bonds. Physical crosslinks refer to chains connected by electrostatic forces, hydrogen bonds, hydrophobic interactions or chain entanglements. The physical crosslinks are non-permanent so the physical gels can be converted to polymer solutions by heating. For semicrystalline hydrogels, only amorphous regions swell in water while crystalline regions act as crosslinks [42]. These semicrystalline hydrogels can be prepared by freezing and thawing dilute polymer solutions. Bulk polymerization will result in non-porous hydrogels, which only permit

water and small solutes to diffuse through. Porous hydrogels are usually prepared by solution polymerization with the addition of porosigens such as water-soluble porosigens, water or organic solvents. Porous hydrogels possess less resistance to particle transfer but at the cost of reduced mechanical strength. The negative effect on mechanical properties can be minimized if the size of the porosigen is below 40 μm [41].

Swelling behavior of hydrogels in water is important in biomedical and pharmaceutical applications since the equilibrium degree of swelling influences the solute diffusion coefficient through hydrogels, surface properties and mobility, optical properties, and mechanical properties [26]. Highly swollen hydrogels include cellulose derivatives, PVA, poly(N-vinyl 2-pyrrolidone) (PNVP) and poly(ethylene glycol) (PEG). Moderately and poorly swollen hydrogels include PHEMA and its derivatives. Some hydrogels are sensitive to external stimuli, such as pH, temperature, ion concentration, osmotic pressure, electric field or magnetic field, and exhibit different properties including swelling behavior towards environmental changes [41].

Hydrogels exhibit good biocompatibility when contacting blood, body fluids and tissues due to their unique properties. Hydrogels resemble some hydrodynamic properties of natural biological gels, cells and tissues. Their soft, rubbery nature also minimizes mechanical and frictional irritation to the surrounding tissue. Moreover, the low interfacial tension between hydrogels and surrounding biological fluids and tissues minimizes the driving force for protein adsorption and cell adhesion [43].

2.2.3.2. Applications of Hydrogels

Hydrogels have been used in biomedical applications such as soft contact lenses, wound-healing bioadhesives, drug-delivery systems, and implants. For example, AQUA-GEL® is a wound care dressing mainly composed of polyvinylpyrrolidone (PVP), PEG and agar. Drug delivery systems based on hydrogels have been used for many years. Propess® is a prostaglandin delivery system using poly(ethylene oxide) (PEO). Transderm-Scop® is a transdermal delivery system of scopolamine for placing behind the ear, originally designed for astronauts who become sick in space. Ocusert® is a hydrogel strip containing pilocarpine for glaucoma patients for placing in the eye lid. Hydrogels have been used in plastic surgery to improve contour or to repair defects, such as breast implants, noses and chins. Potential implantation applications include artificial tendon, artificial kidney membranes, artificial cartilage, artificial skin, maxillofacial and sexual organ reconstruction materials, and vocal cord replacement materials [26, 41].

2.2.3.3. Poly(Hydroxyethyl Methacrylate) (PHEMA)

PHEMA is the most widely used hydrogel having similar water content to living tissue. It is easy and inexpensive to produce. This hydrogel is inert to normal biological processes, resistant to cell attachment, permeable to metabolites, resistant to degradation, non-absorbable by the body, and can withstand heat sterilization [26]. PHEMA has been used extensively in ophthalmic applications such as contact lenses and intraocular lenses. This hydrogel offers good mechanical stability, favorable refractive index and high oxygen permeability, so it is an ideal material for contact lenses. Because PHEMA has excellent biocompatibility but poor mechanical properties, hybrid materials have been

produced by grafting PHEMA to the surface of polymers with good mechanical properties for vascular graft applications [1, 41].

2.2.3.4. Poly(Ethylene Glycol) (PEG)

PEG is highly soluble in water and also soluble in some organic solvents. PEGs are liquid at room temperature when their molecular weights are less than 1000. PEG is referred to as PEO when the molecular weights is higher than 2×10^4. PEG is non-toxic and biocompatible, having large exclusion volume. Therefore, addition of PEG to protein or nucleic acid aqueous solutions induces crystallization and addition of high concentrations of PEG to cell suspensions induces cell fusion. Furthermore, PEG can be immobilized to polymer surfaces to reduce protein adhesion, or covalently coupled to proteins to decrease their immunogenicity and increase their half-life in plasma [1].

2.2.3.5. Poly(Vinyl Alcohol) Hydrogels — Fabrication, Properties and Applications

PVA polymers are generally prepared by the polymerization of vinyl acetate to poly(vinyl acetate) (PVAc), followed by hydrolysis of PVAc to PVA. The hydrolysis reaction does not reach completion, so PVA is actually a copolymer of PVA and PVAc. The degree of hydrolysis has an effect on the chemical properties, solubility and crystallization of PVA [44]. The solubility of PVA in water decreases with increasing degree of hydrolysis. As a result, PVA with a degree of hydrolysis above 90% can dissolve in water only after being heated above the glass transition temperature, which is near 80°C. The chemical structure of PVA is sketched in Figure 2.2a. PVA hydrogels can be formed by chemical or physical crosslinking. Difunctional crosslinking agents,

electron beam or γ–irradiation are common chemical crosslinking methods. For biomedical applications, residues of crosslinking agents are undesirable since they are toxic and hard to remove. Electron beam and γ–irradiation do not leave toxic agents but they cause a bubble formation in the hydrogel. Physical crosslinks are created by a crystallite formation, which does not require toxic crosslinking agents. These crystallites serve as crosslinking points to hold the hydrogel structure as shown in Figure 2.2b. Crystallites can be formed by annealing (fast drying), slow-drying dehydration at room temperature, repeated cycles of freezing-thawing PVA aqueous solution, low temperature crystallization of PVA in a mixed solvent, or aging. Hyon and Ikada proposed an explanation for the low temperature crystallization process. As the temperature of the homogeneous solution is lowered, the molecular motion is restricted. The enhanced intermolecular interaction, possibly due to hydrogen bonding, drives the formation of small crystalline nuclei. Crystallization proceeds further as the solution remains at a low temperature for a longer time. Low temperature crystallization results in larger free spaces between crystallites and larger sizes of crystallites than annealing. Aged hydrogels become denser due to phase separation, which results in the increased modulus and solvent exclusion. Stereo structure and molecular weight can affect the crystallization. Stereoregular structures do not favor crystallization, so the atactic PVA is the most crystallizable form. The isotactic form shows poor crystallinity. Physically crosslinked PVA hydrogels exhibit higher mechanical strength than chemically crosslinked PVA hydrogels because the mechanical load can be distributed on the crystallites. Additionally, physically crosslinked PVA hydrogels possess a high degree of

swelling in water, a rubbery and elastic nature, and close resemblance to human soft tissue [45].

PVA hydrogels formed by repeated freezing-thawing cycles is a preferred method for drug delivery applications because it is free of heat treatment and organic solvents. The properties of physically crosslinking PVA hydrogels depend on the molecular weight and degree of hydrolysis of PVA, concentration of the PVA solution, the temperature and time of freezing and thawing, and the number of freezing-thawing cycles. The bulky acetate groups can inhibit the gel formation, so a slight difference in the degree of hydrolysis can significantly impact the thermal behavior of PVA hydrogels. It has been shown that the viscoelasticity of PVA hydrogels showed little change between 15 and 50°C but a significant change above 50°C due to the irreversible physical change from gel to sol. The number and stability of crystallites increase with the number of freezing-thawing cycles. The crystallinity increases with increasing freezing time and increasing PVA concentration. The size of crystallites initially increases and then decreases with increasing thawing time. Modulus and strength increase with the number of freezing and thawing cycles, especially in the first several cycles, as well as increasing freezing time. Higher molecular weight or more cycles favor a denser structure. Stronger and denser hydrogels swell less in water and reach equilibrium faster. Swelling studies, with the help of DSC, have shown an initial decrease of crystallinity due to the melting out of smaller crystallites, followed by an increase of crystallinity at longer times due to additional crystallites formation through aging [45].

Modification of the repeated freezing-thawing technique can obtain PVA hydrogels with new or better properties. Addition of organic solvents using freezing-

thawing techniques can produce PVA hydrogels with high tensile strength, high water content and high light transmittance. Addition of triethylene glycols and higher oligomers of ethylene glycol can increase the strength and thermal stability of PVA hydrogels. Grafting PEG onto PVA can produce hydrogels with reduced protein adsorption and cell deposition. pH-sensitive hydrogels have been prepared with interpenetrating networks of PVA and poly(acrylic acid). The freezing-drying process also affects the tensile force, which increases with increasing evacuation time [45].

PVA hydrogels are non-toxic, non-carcinogenic, bioadhesive and easy processing, so they are excellent candidates for biomaterials. In addition, PVA hydrogels possess a high degree of swelling in water or biological fluids, a rubbery and elastic nature, a close resemblance to natural tissue and ready acceptance into the body. These characteristics do not change after long-term implantation. PVA hydrogels implanted subcutaneously or intramuscularly into rabbits showed no adhesion to surrounding tissues. PVA hydrogels annealed in the presence of glycerol showed reduced adsorption and platelet adhesion when contacting blood components [45].

Because of their excellent properties as a biomedical material, PVA hydrogels have been used in artificial organ and artificial tissue applications, such as artificial pancreas, linings of artificial hearts, biomembranes in artificial kidney, hemodialysis membranes, artificial skin, articular cartilage, catheters, and soft tissue replacements. PVA hydrogels have been investigated for artificial intervertabrate disc nuclei applications. Hydrogels having a water content of 30% or higher and a compressive strength 4 MPa or higher were produced. An overall conformation of natural disc nucleus can be obtained by combining various pieces with different properties. For

artificial articular cartilage applications PVA hydrogels were prepared with a mixed solvent of water and DMSO. Tensile strength and dynamic modulus, which are important to wear properties, can be increased by low temperature gelation followed by annealing at various temperatures. Hydrogel films cast with blends of collagen and PVA were studied for orthopedic applications. The physical crosslinkings were created via two dehydration steps followed by annealing. The resulting hydrogel films were successfully used as substrates to culture osteoblasts [45].

PVA hydrogels have been investigated in drug delivery applications. Mucoadhesive PVA hydrogels were investigated for use in epidermal bioadhesive systems for controlled release of epidermal growth factor or ketanserin for wound healing. Bioadhesion of PVA hydrogels was found to decrease with an increasing number of freezing-thawing cycles due to the increase of crystallinity. Bovine serum albumin release from PVA hydrogels was studied and the release was found to be diffusion controlled. Solute transport was a function of the crystalline fraction of PVA and the space between crystalline regions, although crystallinity change had little effect on the release mechanism. PVA hydrogels have also been investigated in transrectal drug delivery for hypertension treatments and buccal delivery systems for release of ergotamine tartrate for migraine treatment [45].

PVA hydrogels also show potential in contact lens applications. Transparent PVA hydrogels prepared by low temperature crystallization from PVA aqueous solutions with a water miscible organic solvent, such as DMSO, have higher tensile strength and less protein adsorption compared to conventional lens materials. The PVA lens did not affect the corneal epithelium of rabbit eyes [45].

2.2.3.6. Hydrogel Composites

Hydrogels can be incorporated with other materials to form composites. Hydrogel composites consisting of biodegradable polymers are the most promising systems in drug-delivery applications. In the system, micro- or nano-scaled drug carriers distribute in the continuous hydrogel matrix. The drug-release can be controlled via combined mechanisms, such as diffusion, degradation and stimuli. Sustained long-term release can be achieved through controlling the degradation rate of the drug carriers. In the meantime, hydrogels provide integrity and good mechanical support to the micro-scale components for implantation applications. Several studies have shown that a linear long-term releasing profile can be achieved when using PVA hydrogel composites embedded with PLGA microspheres [40, 46].

2.3. Synthesis of Poly(lactone) — PLA, PGA, PCL and their Copolymers

Synthesis of PLGA can be conducted either by polycondensation of lactic acid and/or glycolic acid or by ring-opening polymerization (ROP) of lactide and/or glycolide. Polycondensation has been known to obtain low molecular weight polymers [47-50] because of the equilibrium among free acids, water and polyester along with the formation of diester, although high molecular weight PLA by direct condensation polymerization has been studied [51, 52]. On the other hand, ROP of the cyclic diester can produce high molecular weight polymers and has been studied since the 1950s. Figure 2.3 gives the chemical reaction of PLGA synthesis via ROP using lactide and glycolide monomers. Two classes of catalysts — multivalent metal alkoxides (Al [53-55], Fe [56], Ti [57], Sn(IV) [58], Y [59]) and covalent metal carboxylates, particularly

tin(II) 2-ethylhexanoate (stannous octoate ($SnOct_2$)) — are mostly used. Kricheldorf and co-workers have studied various catalysts for ROP of polylactones and related polymerization mechanisms [38, 57, 58, 60-63]. They preferred $SnOct_2$ among all tested catalysts because it can act as a transesterification catalyst for alcohols and esters including lactones due to its energetically favorable free "d" orbital [62]. $SnOct_2$ is a highly efficient catalyst, offering high reaction rates, high conversion rates and high molecular weights, even at very high monomer/catalyst ratios. 99% optically pure PLLA can be prepared even at temperatures as high as 150^{o}C when using $SnOct_2$ as a catalyst. Most importantly, it is an approved food additive in many countries and its toxicity is extremely low compared to other heavy metal catalysts, which is desirable for biomedical applications.

Different techniques for the ring-opening polymerization of PLA/PLGA using $SnOct_2$ as a catalyst have been developed to get better control over polymer properties such as molecular weight, molecular weight distribution and reproducibility. ROP in bulk is a living polymerization and yields higher molecular weights than ROP in solvents [64, 65], which are normally used when monomers cannot be melted at interested polymerization temperatures. Bulk ROP under vacuum [19, 28, 66-72] or inert atmosphere [73, 74] at various polymerization temperatures and durations have been studied. Andreopoulos, et al., found that bulk ROP of lactide in vacuum resulted in better reproducibility and higher molecular weight than that under inert atmosphere [75]. Avgoustakis and Nixon's study showed that higher molecular weight polymers were obtained at lower temperatures (130^{o}C) [66]. Polymers decomposed at temperatures higher than 190^{o}C when the reaction was conducted for four hours, the optimum

polymerization time. As catalyst level increased, molecular weight initially increased and then decreased. Chain terminators such as lauryl alcohol [19] or 1-dodecanol [73] were normally added to further control the molecular weight.

Bulk ring-opening reaction mechanisms using $SnOct_2$ as a catalyst have been investigated and several authors have postulated possible mechanisms with $SnOct_2$ not being the real initiator [62, 71, 76-82]. Nijenhuis et al. suggested the possibility of co-initiation by monomers and initiator impurities and concluded that the polymerization proceeded through a Lewis acid catalyzed transesterification between an activated lactone and a hydroxyl group [76]. Schwach et al., proposed a cationic-type mechanism involving co-initiation by octanoic acid, an impurity in $SnOct_2$, as shown in Figure 2.4 [71]. They also claimed that hydroxytin(II) lactate (HTL), a side product formed during polymerization, could act simultaneously with $SnOct_2$ as an initiator. Because the polymerization of L-lactide using $SnOct_2$ as a catalyst led to almost 100% optically active PLLA, Zhang et al., believed that the initiation occurred by insertion coordination rather than ionic polymerization, which would cause racemization [77]. Based on their experimental results, they proposed a coordinative insertion mechanism as shown in Figure 2.5 [77], which stated that the polymerization of lactide was initiated by stannous alkoxide formed by $SnOct_2$ and alcohol. Kricheldorf et al., believed the polymerization did not follow a cationic, anionic, or pseudoanionic mechanism, but rather a second-order insertion or complexation mechanism [62]. Based on the end-group analysis using NMR spectroscopy, they concluded that the tin compound was first incorporated with an alcohol, an impurity in $SnOct_2$, as coinitiator and then interacted with lactide monomers (Figure 2.6 [62]). Several later papers [78-81] discussed the proposed mechanisms and

provided experimental data to support the coordination-insertion mechanism initiated by stannous alkoxide. They thought that the second-order insertion would block the active site of stannous alkoxide so that the ring-opening polymerization could not happen.

2.4. Degradation of Poly(lactone) — PLA, PGA, PCL and their Copolymers

PLA, PGA, PCL and their copolymers can go through hydrolytic degradation in aqueous medium. The hydrolysis reaction is given in Figure 2.7. It involves the polymer chains breaking down into smaller chains. The small polymer chains keep breaking down until water soluble oligomers are formed and released into the medium. The ultimate degradation products such as lactic acid and glycolic acid can enter the normal metabolic pathway of human beings and leave the body. Degradation of poly(lactone) in the forms of films, microparticles, pellets, fibers and sponges has been investigated by many research groups.

2.4.1. *In Vitro* Degradation Behavior

Most *in vitro* degradation studies were conducted at 37°C in a phosphate buffered solution (PBS) medium with pH maintained near 7.4. General observations include polymer swelling, molecular weight decrease, mass decrease, crystallinity increase, porous structure formation and physical disintegration.

Bulk water was found to depress the T_g of PLGA by 15°C reversibly regardless of incubation conditions [83]. T_g of PLGA was also depressed in humid environments, with the depression of T_g increasing with increasing relative humidity. It was proposed that the non-freezable (bound) water was responsible for plasticizing polymer and caused

polymer degradation. Water uptake from PLGA was found to increase steadily with time because the degradation resulted in a more hydrophilic matrix [84].

Yoon et al., [85] studied the degradation of PLGA (LA/GA of 75/25, 65/35 or 50/50) macroporous sponges with an average pore size of 200 μm and over 90% porosity. The mass loss showed a lag period at the beginning, during which hydrolyzed PLGA chains were retained within the matrix until water soluble oligomers were formed. The lag time of mass loss was found to be dependent on the molar ratio of PLGA copolymer. The degradation could be described by three consecutive events: hydrolytic chemical chain scission, water uptake and swelling, and physical disintegration. Significant swelling of the scaffolds during degradation was believed to contribute to the changed pore structure from macropores to micropores.

Zong et al., [86] investigated the structure and morphology change of electrospun PLGA (LA/GA of 10/90 or 75/25), PLA and PLLA fibrous membranes during degradation. These electrospun fibers were amorphous due to the retardation of crystallization of semicrystalline polymers during the electrospinning process [87]. A sudden increase in crystallinity and T_g was observed upon incubation. The crystallinity and apparent crystal size continuously increased at the beginning, but decreased after a long period. They thought the increased crystallinity was from the thermally-induced crystallization followed by the chain cleavage-induced crystallization. The electrospun fibers were highly oriented [87]. As a result, a large dimensional change was observed due to the relaxation of stretched amorphous chains near T_g in the aqueous medium. Electrospun crystallizable but amorphous PLGA (10/90) and PLLA membranes exhibited a very small shrinkage percentage (11% loss of the initial size for PLGA and 9% for

PLLA) compared with electrospun noncrystallizable PLGA (75/25) and PLA, which lost over 80% of their initial size. The porosity was found to decrease from 78% to 28% for PLGA (75/25) and from 75% to 52% for PLA. The small shrinkage was possibly associated with the significant crystallinity increase during incubation. The degradation was divided into four stages. Stage I involved a rapid thermally induced crystallization. In stage II, amorphous regions on the polymer chains were degraded, which enhanced the mobility of noncrystalline chains and led to cleavage-induced crystallization. In stage III, large mass loss from amorphous regions and increased water uptake were observed. Stage IV was marked by significant mass loss from the crystalline regions.

You et al., [88] studied the degradation of electrospun PGA, PLLA and PLGA (50/50) membranes. They found the degradation rates were in the order of PGA > PLGA >> PLLA. They observed a significant increase in crystallinity of PGA during the early degradation stage followed by a gradual decrease in crystallinity during the later degradation period. They proposed that hydrolytic degradation first occurred in the amorphous regions accompanied by the cleavage-induced crystallization, and then in the crystalline regions.

2.4.2. Factors Affecting Degradation

The degradation rate of PLA/PLGA depends on end groups [89], molecular weight [84], copolymer [85, 88, 90] molar ratio, polymer blend composition [31], morphological structure [91-94], crystallinity [35, 36] and incubation conditions [93, 95-99]. Lower molecular weight and higher glycolide content both favor water uptake so as to increase the degradation rates [84, 85, 88, 90].

Carboxyl end groups on the cleaved chains can catalyze the hydrolysis of other ester bonds to speed up the degradation. This mechanism is termed autocatalysis. Autocatalysis is frequently observed in thick biodegradable implants, which exhibit a slower degradation rate at the surface than in the bulk [100]. Sometimes a bimodal molecular weight distribution profile could be observed for the degraded PLGA [97]. Autocatalysis is negligible in the electrospun fibrous membranes because the small dimension of nanofibers creates a short diffusion path for the acidic degradation products [31]. Therefore, degradation of PLGA can be significantly affected by end groups on the polymer chain, specimen dimension and morphology.

Lee et al., [89] studied the end-group effect on degradation of polylactides. They found that mass loss and molecular weight decrease of COOH-terminated polylactides were much higher than those of Cl- and NH_2-terminated polylactides. They believed it was because NH_2 and Cl were less polar than COOH, while COOH could also catalyze the hydrolysis. Additionally, NH_2 was capable of complexing with acid groups that would otherwise accelerate the hydrolytic degradation.

Two research groups [91, 92] investigated the influence of sample dimension of PLGA (50/50) spherical particles on the degradation rate. Their results indicated that the degradation rate increased with increasing sample diameters in the range of 0.53 to 100 μm. The hydrolytic degradation of PGA melt-spun fibers (diameters of 155μm and 203μm) and pellets (about 17 mg per pellet) was investigated under various conditions by Ginde et al [93]. The degradation was found to be chemically controlled and independent of the fiber size. However, pellets degraded faster and showed more surface deterioration than fibers.

Porous PLGA (85/15) scaffolds in the range of 50-450 μm in pore size and 80-95% in porosity were investigated [94]. It was found that scaffolds with a higher porosity or a smaller pore size degraded slower than those with a lower porosity or a larger pore size, which was attributed to the wall effect and the surface area effect. Scaffolds with lower porosities or large pores possessed thicker walls between pores and smaller surface area, which could increase the diffusion path of acidic degradation products and result in stronger auto-catalysis effect on the degradation.

PLGA (10/90) electrospun membranes were post-drawn at room temperature and then annealed at elevated temperatures under a constant strain [35]. Post-drawn and annealed membranes exhibited a slower degradation rate at the beginning of incubation due to the increased crystallinity retarding the water diffusion. A faster degradation rate of the treated membranes was observed compared to as-spun membranes after two weeks of degradation, which was possibly due to the stringer autocatalysis by acidic oligomers entrapped in the denser microstructure of the drawn membranes. Isothermal annealing of PLGA (8020) films was investigated by Loo et al. [36]. Degradation rate was found to increase at higher crystallinity, which was related to the loss of amorphous materials and voids formation during annealing for a long time. T_g decreased and water uptake increased with increasing annealing time due to voids formation. The increased crystallinity and voids formation during annealing were found to be cooperative on changing the hydrolytic degradation rate. Higher crystallinity retarded degradation but void formation increased the degradation rate. The net change on degradation rate depended on which one was predominant under certain annealing conditions. The maximum retardation in hydrolytic degradation was achieved by annealing for 30 min.

Hydrolysis of PLGA (30/70) films was conducted at various pH levels of 5, 7 and 9 [95]. No significant change in degradation kinetics was observed due to the combined influence of crystallinity and hydrophobicity. However, degradation rate of PGA was found to be an order of magnitude faster in alkaline than in acidic medium [93]. Degradation of PLGA (50/50) and PLA in the form of pellets at pH 2, 7.4 and >13 was investigated [96]. It was noticed that PLGA and PLA exhibited bulk erosion profiles at pH 2 and 7.4. However, linear erosion profiles were observed at pH >13, which indicated the change of erosion profiles from bulk to surface erosion at high pH values. Degradation of PLGA (50/50 and 65/35) microspheres at pH 7.4 and pH 2.4 was investigated [97]. Degradation of polymer was found to be inside-out (bulk) at pH 7.4 but outside-in (surface) at pH 2.4. Surface pitting and pore formation were observed at pH 7.4. At pH 2.4 microspheres maintained smooth surfaces and were susceptible to fracture due to the crystallization of oligomers driven by their low solubility at the low pH. Additionally, the degradation occurred in a more homogeneous pattern at pH 2.4 than that at pH 7.4.

Temperature effect on degradation was also investigated. Reed and Gilding found that the glassy state protected PGA from hydrolysis at temperatures below T_g as all short-term chain motions were frozen. The rate of mass loss and threshold time before its onset depended on the temperature [95]. Incubation temperatures at 5, 25, 37 and 45°C were studied for their influence on the degradation of PLGA microspheres. In general, the degradation rate increased with increasing temperature. All microspheres exhibited a biphasic degradation profile and the induction period was prolonged with decreasing temperature. At 5°C, changes in molecular weight, mass, and morphology were

negligible even after 175 days incubation [92]. The degradation of PLA and PCL nanoparticles was significantly retarded at 5°C although rapid degradation happened at 37°C. A small change in molecular weight was observed after they were stored in unbuffered media for 350 days at 5°C. Furthermore, refrigeration stabilized PLA and PCL polymers even at a pH of 1.65 for up to 4 months [98].

Degradation of PLGA (50/50) films was compared in a static medium and a dynamic medium [99]. It was found that degradation was slower in the dynamic medium than in the static medium, possibly because water diffusing into polymer was slower in the dynamic medium where the simulated medium flow was perpendicular to the polymer surface.

2.5. Electrospinning Techniques

Electrospinning is a unique technique to fabricate micro- or nanofibers through electrostatic force. The resulting nonwoven fibers form a large, interconnected porous network. In this process, a polymer solution or melt is forced through a capillary and is charged by applying high voltage at the tip where a drop forms. When the electrostatic stress overcomes the surface tension of the charged droplet, a "Taylor cone" (Figure 2.8) is formed and a whipping liquid jet travels towards the grounded collection plate. The threads, which are split from the jet, repel and pile up parallel to each other while the solvent evaporates or the polymer cools down, and thus nonwoven fibers are collected on the plate.

Electrospinning was first introduced in the early 1930s by Formhals who reported the spinning of cellulose acetate fibers in acetone solution [105]. Then, Taylor led the

study of the jet forming process [106]. He described the shape of the viscous droplet at the tip of a tube when an electrical field was applied, and introduced the formation of a cone and the resulting jet on the apex. This conical shape of the jet was later referred to as the "Taylor cone". Taylor also determined that a 49.3^{o} semivertical angle was required to balance the surface tension with the electrostatic forces. Later, Baumgarten showed that the diameter of the jet first decreased to a critical value, and then increased with increasing electric fields [107]. Several authors [108-112] also studied the instability of the jet, also known as whipping as shown in Figure 2.9 [110]. They pointed out that the high electric field interacted with the surface charges of the jet, which resulted in the instability. This phenomenon caused bending and stretching of the jet and was suggested to be a key process in the formation of submicron-scale fibers [110, 111].

Most recent works focus on the effects of solution and process parameters on resulting fiber morphology. Larrondo and Mandley determined that the diameter of polyethylene and polypropylene fibers decreased with increasing melting temperature and applied voltage [113]. They also found that the diameter of melt-spun fibers was larger than solvent-spun fibers. Based on years of studies on electrospinning, Reneker and coworkers claimed that solution properties (viscosity, conductivity, and surface tension), controlled variables (hydrostatic pressure in the capillary, electric potential and distance between the tip and collection plate) and ambient parameters (temperature and humidity) are the major effects on the process and fiber morphology [114]. They studied electrospun poly(ethylene oxide) (PEO) fibers from aqueous solution and showed that fibers could be formed from solutions with a viscosity between 800 and 4000 centipoise (cp). The solution at a lower viscosity was too dilute to form a stable jet, while at a

higher viscosity it was too thick to form fibers. Jaeger et al., found that PEO fibers spun from aqueous solutions showed a "bead on a string" morphology, which could be avoided if PEO was spun from organic solvents [115]. Fong et al., proposed that beads were formed by the radial contraction of the fluid jet under surface tension [116]. Solution parameters such as viscosity, net charge density, and surface tension were also studied. They found that as the viscosity increased, the beads and the fiber diameters got bigger, the average distance between beads became longer, and the shape of the beads changed from spherical to spindle-like. The increase of net charge density had opposite effects on the diameters of beads and fibers but similar effects on the shape of beads comparing with increasing viscosity. The surface tension could be decreased by using a mixed solvent of water and methanol instead of water, which favored the formation of fibers without beads since the surface tension was the driving force for bead formation. Zong et al., investigated the effects of process parameters on the structure of electrospun fibers from PLA in N, N-dimethyl formamide (DMF) solution [87]. Similar conclusions about the effects of solution viscosity and charge density as Fong's study were obtained. The electric field and feeding rate were found to have less effect on fiber structures, although larger diameters of fibers and beads were formed at higher electric fields and feeding rates. Effect of incorporating drugs into electrospinning solutions on fiber structures was also reported. Kim et al., found that increasing the concentration of cefoxitin sodium, a hydrophilic drug, would favor fiber formation instead of beads, as well as decreasing the average fiber diameter and density [30]. However, Katti et al., showed that cefazolin - loaded nanofibers had larger diameters and smoother morphology than the unloaded

nanofibers [117]. Therefore, the effect of drugs on fiber morphology will depend on the properties of different drugs and electrospun solutions.

The electrospinning process has been modified to meet different purposes. To generate preferential orientation [87] or tubular [118] structures, a grounded rotating drum is used as the collection target instead of plates. Simultaneous electrospinning of two solutions using two sets of syringes and needles was developed to produce bicomponent fibers. Those syringes can have separate syringe pumps [119] or the two plastic syringes and needles can be adhered side by side to share a common pump [120]. A core-shell nanofiber structure has been introduced to embed drugs, growth factors or genes into the core of biodegradable polymer nanofibers [121, 122]. The special device is the nozzle with a coaxial opening structure which contains a core opening and a surrounding annular opening, where different solutions can be introduced into and electrospun into a core-shell-structure nanofiber.

Many biodegradable polymers, such as PLLA [123, 124], PLGA [87, 125] and PCL [126, 127], along with several water-soluble biomaterials, such as PEO [114-116] and polyvinyl alcohol (PVA) [128, 129], have been electrospun into fibers. Electrospun protein fibers, such as collagen [130] and fibrinogen [131], have been produced with retained bioactivity for use as tissue engineering scaffolds.

2.6. Applications of Biodegradable Electrospun Micro- or Nanofibers in Tissue Engineering and Drug Delivery

Electrospun biodegradable micro- or nanofiber meshes with high surface area-to-mass ratio and high porosity are highly suitable for tissue scaffolds. The dimensions and mechanical properties of these ultra-fine fibers can be fabricated to mimic those of

natural extracellular matrix (ECM). The high porosity of the scaffolds provides enough room for cell adhesion and proliferation, nutrient intake, and metabolic waste removal [132]. In addition, cells can maintain their phenotypic shapes and guided growth according to the fiber orientation [133]. Mesenchymal stem cells derived from bone marrow of neonatal rats were successfully seeded and proliferated on electrospun PCL scaffolds [126]. Electrospun PCL nanofibrous scaffolds were also used to support *in vitro* chondrogenesis of mesenchymal stem cells, and showed great potential for cartilage repair through cell-based tissue engineering approaches [127]. Human smooth muscle cells and endothelial cells were cultured on the electrospun nanofibrous scaffold of poly(L-lactide-co- ε -caprolactone) (PLLA-CL). A favorable interaction between cells and PLLA-CL fibers suggested that the synthetic scaffold is a potential blood vessel substitute [134]. Electrospun microfibers of PLGA/PLLA blends were used to culture primary cardiomyocytes for cardiac tissue engineering applications [125]. It was found that the more hydrophobic PLLA scaffolds promoted better cell adhesion and mature cytoskeleton structure with well-defined periodic units in the contractile machinery. PLGA nanofibers were fabricated in tubes on a rotating Teflon mandrel and implanted inside rat sciatic nerves to serve as nerve guidance channels [118]. Inflammatory response was devoid and successful nerve regeneration was observed.

Biodegradable micro- or nanofibers are also used as drug carriers for drug delivery systems. Luu et al., incorporated pCMVβ plasmids in biodegradable fiber meshes that were electrospun from a blend of PLGA and PLA-PEG using DMF as solvent for DNA delivery [32]. They found that DNA was predominantly distributed on the surface of the fibers, which caused the initial burst of released DNA, and the released

DNA was intact. A hydrophilic antibiotic, cefoxitin sodium, was electrospun with PLGA or a mixture of PLGA/PEG-b-PLA in DMF [30]. Initial burst of drug release was found when using PLGA, but amphiphilic PEG-b-PLA could reduce the initial cumulative amount of the released antibiotic and prolong the drug release period. The released antibiotic effectively inhibited the growth of the bacteria Staphylococcus aureus. Zeng et al., incorporated anti-tumor drugs such as paclitaxel, doxorubicin hydrochloride and doxorubicin base in PLLA electrospun fibers [124]. They found that near zero-order release without initial burst could be achieved for paclitaxel and doxorubicin base, which were compatible with PLLA and soluble in chloroform/acetone mixed solvent in electrospinning. However, an obvious initial burst of doxorubicin hydrochloride was observed due to the fact that the drugs were distributed on or near the surface. Another study conducted in this group incorporated doxorubicin hydrochloride in amphiphilic PEG-PLLA ultrafine fibers during electrospinning the water-in-oil emulsion [135]. The doxorubicin hydrochloride was entirely encapsulated inside the fibers and a reduced initial burst was achieved. The released doxorubicin hydrochloride maintained the same chemical structure and same antitumor activity against mice glioma cells as the original drug. Chew et al., encapsulated proteins, human β–nerve growth factor (NGF) stabilized in bovine serum albumin (BSA), in a copolymer of ε-caprolactone and ethyl ethylene phosphate (PCLEEP) via electrospinning [39]. The proteins were found to be randomly dispersed in the fibrous scaffold in aggregate forms. NGF was released at a time-independent rate for at least three months after a modest burst and proved to stimulate differentiation of PC12 (a rat pheochromocytoma cell line) cells into neurons. Jiang et al., fabricated biodegradable core-shell nanofibers using coaxial electrospinning for

controlled release study of two model proteins, BSA and lysozyme [122]. Proteins were contained in the PEG core and PCL composed the shell. The released lysozyme and BSA maintained their primary and secondary structures. In addition, the released lysozyme maintained comparable catalytic activity of its pristine counterpart.

2.7. Polymer Toughening

2.7.1. Molecular Origins of Toughness

The deformation of a specimen under a mechanical force is described by the stress-strain behavior. Small-strain behavior is mainly described by the moduli and Poisson's ratio, while large-strain behavior refers to failure mechanisms. Small-strain mechanical properties such as moduli and Poisson's ratio are affected by shape and orientation of the filler component, not by the sizes of the filler domains. Fracture occurs at the ultimate elongation. The total area under the stress-strain curve is used to describe the toughness, which refers to the total energy required to cause failure.

Toughness depends on molecular factors related to the nature of the materials, chemical crosslinks, anisotropy, thermal history, supramolecular organization as manifested by semicrystallinity and/or phase separation, temperature and deformation rate during testing, mode of deformation, variation in the specimen geometry, and factors related to fabrication parameters and/or end-use conditions [136]. For example, thick specimens are more likely to fail in a brittle manner than thin films, because of the triaxial stresses created as a result of the substantial thickness of a bulk specimen. At a given temperature and deformation rate, the tendency to fail in a brittle fashion is much greater in plane strain tension than it is in simple shear.

Three general failure modes for amorphous polymers include brittle fracture, shear yielding and crazing [136]. In brittle fracture, failure occurs in a brittle manner both at a microscopic (local) and a macroscopic (bulk) level. Brittle fracture involves breakage of covalent or Van der Waals bonds crossing the fracture surface. No plastic flow is involved in this cleavage process due to the low mobility of the polymer subunits. Crazing and shear yielding require sufficient mobility of chain segments for plastic flow to occur at a molecular level, so they can be considered to be ductile at a local level. At a macroscopic level, shear yielding is a homogeneous and continuous plastic deformation of the specimen while crazing is a heterogeneous process of cavitation, craze nucleation, propagation and breakdown, and crack propagation. Therefore, shear yielding is far more ductile than crazing at the macroscopic level. Local plastic flow processes (shear yield stress) and large-scale surface separation processes (surface tension) must be considered for crazing. Polymers that require a large stress (stronger) and more energy absorption (tougher) to fail are more useful. Failure by either crazing or shear yielding is favored over failure by brittle fracture. Many brittle polymers are toughened by modification to impart either the ability to craze more effectively or the ability to undergo shear yielding.

2.7.2. Toughening of Thermoset Resins

Thermoset resins are crosslinked polymer networks. When a polymer is crosslinked, the degree of freedom for motion of the chain segments is reduced because the weak physical interactions are replaced by strong chemical bonds. Large-scale plastic flow processes become very difficult. When the crosslink density is extremely high, a polymer will go through embrittlement. The mechanical performance of crosslinked

polymers is dependent on their crosslink density. The highly crosslinked thermoset resins are of great interest in developing high-performance composites. The high crosslink density can greatly reduce the local molecular mobility. Therefore, the dominant toughening mechanisms for highly crosslinked epoxies include crack deflection, crack bifurcation, crack pinning and crack bridging, which have low energy absorption capacity [137]. It is possible to toughen epoxies with a high crosslink density via shear yield-banding mechanisms, given that the toughening phase effectively alters the crack tip stress state from favoring brittle fracture to promoting shear yielding.

2.7.2.1. Rubber-Modified Epoxies

The first toughened polymer blends were binary mixtures of rubber and plastic. Factors that influence toughness include matrix properties, rubber particle size, rubber concentration, type of rubber, rubber particle-matrix interface, particle morphology, and blend morphology [138]. The presence of a dispersed inhomogeneity in an epoxy matrix can promote an extended damage zone when fracture occurs, which can effectively toughen the epoxy.

Kinloch et al., investigated the fracture behavior of the diglycidyl ether of bisphenol A (DGEBA) epoxy toughened by carboxyl-terminated butadiene nitrile (CTBN) liquid rubbers [139]. They obtained higher fracture toughness for the rubber-modified epoxy than the unmodified epoxy, although both epoxy systems exhibited essentially the same types of crack growth (brittle stable, brittle unstable and ductile stable crack growth.) The greater crack resistance in rubber-modified epoxies was believed to have resulted from the greater energy-dissipating deformation in the vicinity of the crack tip.

These deformations included localized cavitation in the rubber or at the interface along with plastic shear yielding in the matrix. The interaction between the stress field ahead of the crack and the rubber particles contributed to the enhanced energy dissipation capacity through shear yielding.

Toughening mechanisms in CTBN rubber-modified DGEBA epoxies were also investigated by Yee and Pearson [140, 141]. They found that the rubber particles simply enhanced shear deformation at low strain rates. At high strain rates the particles cavitated due to the triaxial stress associated with the crack tip and subsequently promoted further shear deformation. Cavitation relieved the triaxial tension at the crack tip, while shear band formation created a large plastic zone.

Pearson and Yee [142] also studied the effect of crosslink density on toughness and found that fracture toughness of epoxy is almost independent of the average molecular weight (Mc) between crosslinks in the range examined. After adding 10 v% elastomer, fracture toughness of the two-phase system increased rapidly with increasing Mc. The mechanism of failure of a multiphase system depends on the details of the morphology including the sizes of different components and the distances between them. Strength at the interface is important in determining the preferred failure mechanism. An order of magnitude increase in fracture toughness could only be obtained with epoxies having a low crosslink density and/or low T_g.

Material selection is critical for making tougher epoxy systems. The preferred choices for selecting an epoxy matrix for structural applications are low crosslink density and high local rigidity of the epoxy molecules [137]. Selecting a rubber toughener depends on the application because the type of rubber, size, and dispersion of particles

are all important in toughening epoxies. Soluble rubbers can lower T_g of the matrix, cause difficulty in morphology control, and result in poor reproducibility of product performance [137]. On the other hand, preformed rubber particles have controllable and reproducible particle sizes and shapes, and have been developed to toughen epoxies. The preformed CSR rubber particles were found to promote shear yielding in the epoxy matrix around the propagated crack tip even under the plane-strain mode-I loading condition [137]. However, CTBN and DAR rubber particles could not induce the extended shear yielding mechanism, nor could the poorly dispersed CSR rubber particles. Interfacial adhesion between the matrix and toughener phase is also critical in toughening. The proper amount of interfacial strength is necessary to relieve the triaxial tension and trigger localized shear banding. In general an intermediate interfacial bonding is believed to be beneficial for effective toughening.

2.7.2.2. Rigid Thermoplastics-Modified Epoxies

Applications of rubber particle toughening in high-temperature performance epoxies have been limited due to the great decrease in T_g and the low efficiency at promoting shear deformation in highly crosslinked epoxies when using rubbers. Tough rigid-rigid polymer alloys were developed in an effort to improve toughness without sacrificing strength. High-temperature thermoplastics can be incorporated in epoxies either as preformed, finely granulated particles or by phase separation from a homogeneous solution upon cure. The modulus and T_g of epoxies are generally maintained while the toughness increases in proportion to the amount of thermoplastics added. A co-continuous morphology, similar to the interpenetrated network, can be

formed at about 20% to 25% thermoplastic content. This system exhibited maximum fracture toughness [143].

Poly(arylene ether sulphone) modified epoxy networks via phase separation were investigated [144]. The bisphenol A-based polysulphones were compatible with the epoxy precursors over the entire range of compositions and molecular weights investigated. Polysulphone particles were precipitated and dispersed in the epoxy matrix upon phase separation during cure. When 15% polysulfone particles approximately 1 μm in diameter were incorporated in the network, a doubling of K_{1C} in epoxy with a T_g of 195°C was obtained with minimal sacrifice of the flexural modulus. It was found that the molecular weight of polysulfone had to be above a certain value in order to achieve such great toughness. The polysulfone particles improved fracture toughness, possibly by impeding the crack growth and absorbing energy through plastic deformation. Interfacial adhesion did not seem to influence the toughening efficiency of polysulfone particles although different interfacial morphologies were observed for the two systems.

A crystallizable thermoplastic, polyoxymethylene (POM), was used to toughen epoxy resins via reaction-induced phase separation [145]. Phase separation at curing temperatures above and below T_m of POM (168°C) was investigated. Phase separation occurred according to the spinodal decomposition mechanism at 180°C. Three morphologies were observed based on the compositions of the blends: particle dispersion in the matrix for 5 and 10 wt% POM in blends, a co-continuous morphology for 15 wt% POM, and a phase-inverted structure for 20 wt% up to 30 wt% POM. Secondary phase separation was believed to enhance the interfacial tension between the primary phases and lead to more rounded phase boundaries. At curing temperatures lower than 168°C,

isothermal crystallization interfered with reaction-induced phase separation. Phase separation occurred first, and then crystallization of POM started in the POM-rich phase at 150°C. While at 145°C, POM spherulites were formed in the blends before phase separation occurred. Phase separation then occurred in the amorphous zone between POM spherulites.

2.7.3. Interlayer Toughening in High Performance Composite Applications

Fiber-reinforced polymer composites have been widely used in high performance applications. In laminates, comprised of a number of plies with different orientations, the failure mode is a complex interaction. The types of failure mechanisms of composites include fiber debonding, interlaminar failure, fiber buckling, fiber pullout, fiber breakage, cracking of composites and micro-cracking of composites [146]. Interlaminar failure can occur when the interfacial strength between matrix and fibers is greater than the matrix cohesive strength. It is manifested in composites exhibiting excessively brittle behavior and having a high void content. The driving force for delamination is the mismatch in elastic constants between adjacent plies in a laminate. The composite laminates used in aerospace application are susceptible to internal delamination even under a relatively low impact, because there is no load-bearing fibers perpendicular to the lamination plane. The plies are bonded by thin layers of resin that constitute low energy fracture paths. Matrix toughening generally decreases the overall mechanical performance of the composites. Therefore, most interest has been directed towards toughening only the interlayers of the laminates.

The main types of crack loadings in determining the fracture toughness are termed mode I for crack opening, mode II for shearing and mode III for tearing as seen in Figure 2.10 [146]. Mode I tension fractures present smooth fracture surfaces resulting from brittle cleavage of the matrix and are characterized by 'river' patterns and minimum broken fibers. Mode II shear is a common type of shear failure in the composite and is characterized by 'hackles' and 'scallops'. Hackles are vertical and horizontal curved platelets which occur in the matrix between fibers, named after the patterns on crudely fashioned wood. Scallops are concave areas of the fracture surface with radiating striations. Cracks in isotropic materials tend to grow under mode I conditions. Mode II interlaminar fracture toughness can correlate well with the residual compressive strength. Mode III interlaminar fracture is important in assessing defect criticality for delamination between angle plies and for two-dimensional delamination in bending [147].

Polysulfone particles were dispersed in epoxy resin to toughen the carbon fiber-epoxy composite [148]. The mode I fracture toughness of the composite with 21 wt% large size particles was found to be 2.2 times higher than that of unmodified composite. This increase was attributed to the plastic deformation of the continuous polysulfone rich phase inside the swollen polysulfone particle. The toughening mechanisms of carbon fiber-epoxy composites containing nylon particles-incorporated interlays were investigated [149]. Mode II fracture toughness was found to increase linearly with interlayer thickness in a ductile epoxy matrix, regardless of particle incorporation. However, in the brittle epoxy systems particle toughening was realized by stress concentration-induced plastic deformation and particle bridging. An interlayer-toughened glass fiber-vinyl ester composite containing rubber particle-modified

interlayers was investigated under mode I and mode II fracture loading [150]. It was found that rubber particles did not promote yielding but inducing macro-cracking under both loading modes, which was thought to be the most dominant toughening mechanism within high particle content interlays.

2.8. Vinyl Ester Resins

Vinyl ester (VE) resins are a class of thermoset polymers that possess high chemical and corrosion resistance, and good thermal and mechanical properties. Vinyl ester monomers are generally diluted with a low molecular weight monomer such as styrene, to reduce their viscosity at room temperature for ease of processing. The styrene concentration is between 30 wt% and 55 wt% for most commercial VE resins. The molecular weight of the VE monomer and the percentage of styrene also vary with different commercial VE resins. VE resins are prime candidates for composites used in transportation and infra-structure due to the low viscous monomers at room temperature, rapid cure schedules and low cost. However, VE resins are brittle, thus limiting their use in high performance composite materials.

2.8.1. Cure Kinetics of Vinyl Ester/Styrene System

The chemical structure of a VE monomer obtained by reacting methacrylic acid with diglycidyl ether of bisphenol A (DGEBA) is shown in Figure 2.11a. The VE monomer can provide crosslinking capacity and branch points for the network because of the reactive vinyl groups at both ends of the molecule. The styrene monomer having only one vinyl group can provide linear chain extension. The vinyl groups of the VE

monomers can copolymerize with styrene to form a cross-linked network via a bulk free radical polymerization as sketched in Figure 2.11b. The reaction can either be carried out by thermal decomposition of the free radical initiators at temperatures higher than 70°C, or by redox decomposition of initiators using a metal catalyst at temperatures below 50°C. Cobalt naphthenate (CoNap) is a metal catalyst commonly used in conjunction with Trigonox, an organic hydroperoxide initiator. The cure kinetics of vinyl-ester resins is strongly dependent on initiator and catalyst concentrations, cure temperature and styrene concentration, which can affect diffusion, phase separation, and microgel formation. On the other hand, the development of the network can significantly affect physical, chemical and mechanical properties of the VE resin.

The curing process for the vinyl-divinyl system began with an induction period due to inhibitors and cage effects, followed by microgel formation at the early stages. Microgels are domains that have high crosslink density and are dispersed in a pool of unreacted monomers. Microgel formation was followed by their growth, coagulation into clusters, and linking of the clusters to form the final morphology. The microgel formation suggested that monomers were not converted homogeneously throughout the resin. [151]

Dua et al., [152] investigated the copolymerization kinetics at low temperature. It was found that alternating copolymerization was favored over homopolymerization at the early stage of cure. VE monomers reacted faster than styrene monomers during the initial stages. However, styrene could continue to react well after the VE reaction had ceased during the latter stages. The degree of polymerization for styrene and VE could be fit to an autocatalytic kinetic model. Effect of temperature, styrene concentration,

catalyst and initiator concentrations were studied in the same work. Temperature was found to have a positive effect on the reaction rates and final conversions of both monomers, with a greater influence on the styrene final conversion. When the styrene concentration increased, the reaction rates of both monomers decreased, but the final conversion of VE increased. The styrene concentration did not affect the styrene final conversion. When catalyst and initiator concentrations increased, the reaction rates and the final conversion of styrene increased, while no change was observed on the final conversion of VE double bonds.

Ziaee and Palmese [151] investigated temperature effects on cure kinetics and mechanical properties of the VE/styrene system. They found that the overall conversions of VE and styrene, along with the T_g of the postcured resins, were independent of their initial cure temperatures. A higher VE-to-styrene ratio was detected in the network at 30°C cure than at 90°C cure during the initial stages when microgels were formed. However, this ratio was not correlated to the crosslink density of the network. The early network structure had a significant effect on the final morphology of the postcured VE. Larger characteristic dimensions of the nodular morphology were observed for VE cured at 30°C compared to VE cured at 90°C using atomic force microscopy. The mechanical strength and fracture toughness of postcured VE resins were significantly higher for samples precured at 30°C than those precured at 90°C. The different mechanical properties could be attributed to the size and composition of the heterogeneities of cured VE/styrene systems. Phase separation of the mixture into polymer-rich and monomer-rich phases possibly happened during microgel formation and could be affected by the cure temperature.

The cure behavior of these systems could be affected by the presence of reinforcement. Brill and Palmese [153] investigated the cure behavior of VE/styrene resins near untreated and silane-treated IRE crystal surfaces. They found that VE possessed a slightly lower conversion but styrene showed a slightly higher conversion near an untreated interface compared to the bulk. A more rapid consumption of styrene compared to VE near a silane-treated crystal surface was determined, which resulted in a greatly reduced final conversion of VE monomers near the interface compared to the bulk, as low as 20% in many cases. This behavior was possibly due to the altered copolymerization behavior and molecular mobility constraints. This investigation suggested that sizings of glass fibers could significantly alter the composition of the crosslinked network near a fiber surface in glass fiber–reinforced VE systems. A lower T_g interphase that was rich in styrene homopolymers could be formed.

2.8.2. Toughening of VE Resins

Liquid rubber modifiers, such as carboxyl-terminated butadiene nitrile (CTBN), vinyl terminated butadiene-acrylonitrile (VTBN) and epoxy terminated butadiene-acrylonitrile (ETBN), have been used to toughen VE resins [154, 155]. In these systems a suitable liquid rubber is usually dissolved in the uncured resin to form a one-phase system that phase separates upon reaction to form rubber domains within a continuous hard matrix. The formation of a second, rubber-rich phase within a brittle thermoset matrix can greatly improve fracture toughness if the second phase meets certain criteria relative to size, shape, volume fraction, dispersion, and adhesion [154]. Good phase separation obtained by controlling the polymerization reaction can limit plasticization and

add energy dissipating mechanisms so as to improve fracture toughness [139]. If a significant portion of the liquid rubber cannot precipitate from the monomers during cure, the trapped rubber will plasticize the VE matrix phase. Therefore, rubber modified VE resin systems should be formulated as close to the miscibility curve as possible so the maximum phase separation during cure can be achieved [155]. This is particularly important for VE systems since they generally react rapidly and gel at lower conversion. As a comparison, the phase separation is easier to control for step polymerizing systems such as amine-cured epoxies.

Ullett and Chartoff [154] noticed a significant improvement in fracture toughness, up to 116% increment, with modest rubber additions, but almost no change in Young's modulus or T_g in rubber-toughened VE. It was found that the fracture toughness increased with increased volume fraction of second-phase rubber particles. In addition, VE systems with two-phase particles exhibited better fracture toughness than those with single-phase particles, possibly due to a different failure mechanism. Two-phase particles appeared to fail by cavitation, while single-phase particles seemed to fail by tearing from the outside in.

Robinette et al., [155] found that the modified VE systems exhibited a significant increase in fracture toughness with some losses in modulus and T_g. VE systems toughened by ETBN achieved a higher toughness than those toughened by VTBN due to the difference in rubber particle formation and resulting morphology. The chemical linkage of VTBN to the vinyl ester matrix was believed to hinder the complete phase separation, but assisted the retention of mechanical properties when compared to ETBN.

It is worth mentioning that poor compatibility of liquid rubbers with the VE monomers is often a significant problem which can hinder their application in VE systems [154, 155]. Compatibilizing agents can be added to improve the rubber solubility in the VE monomers, but they can also hinder the phase separation during cure. Molecular weight of commercial vinyl ester monomers is therefore often reduced to obtain better miscibility [155].

Preformed fibers that did not require phase separation were investigated for toughening VE resins. Robinette [156] had encapsulated electrospun polysulfone fibers in VE systems after applying silane-based surface treatment to fibers. The resulting composites exhibited no loss in modulus, higher thermal stability and a three-fold increase in fracture toughness.

2.9. Polypropylene (PP)

2.9.1. Structure, Morphology and Properties

Polypropylene (PP) can exist in three typical stereo-configurations: isotactic, snydiotactic, and atactic. These stereo-isomeric configurations induce stable specific overall conformations of the polymer chain. Isotactic PP (i-PP) is a 2 × 3/1helix, syndiotactic PP (s-PP) is a 4 × 2/1 helix, and atactic PP (a-PP) has a random conformation [157]. The stable regular conformations of isotactic and syndiotactic chains promote crystallization by a parallel organization of chain segments from the same chain or from chains in the vicinity [157]. i-PP and s-PP cannot be dissolved in any solvent at room temperature due to their high crystallinity whereas a-PP can be easily dissolved in various solvents. Dissolution of i-PP is usually conducted at high

temperatures in the range of 130-170°C with halogenated aromatic compounds (mono-, di-, or trichlorobenzene) or decaline [157]. However, high temperature can promote thermo-oxidative degradation that mainly acts on tertiary carbons.

The majority of commercial PP polymers are isotactic. i-PP backbone adopts a helical configuration with the pendant methylene groups fitting closely together, so the chain rotation is restricted. The most recognizable feature in the IR spectrum of i-PP is the strong methyl absorption band at 1378 cm^{-1} and the characteristic doublet at 1155 and 970 cm^{-1}[158]. The bands used to determine the crystallinity of i-PP appear at 1166, 998 and 840 cm^{-1} [158]. Internal reference peaks for PP are used to compensate for variations in sample thickness. The most reliable peak is at 2720 cm^{-1} [158] since it is not sensitive to changes in sample crystallinity.

PP-PE copolymers can be synthesized to obtain special properties. For example, PP-PE random copolymer is more flexible and tough than PP homopolymer, but less rigid [158]. PP-PE block copolymer has a superior impact resistance to PP homopolymer without sacrificing any rigidity [158]. Elastomeric PP homopolymers can be synthesized using metallocene catalysts. Metallocene PP has good elastimeric performance with high elastic recovery (>90%), high elongation to break (1000-2000%), good tensile strength (3-34 MPa) and low modulus [159].

2.9.2. Crystallization Behavior

i-PP has four crystal structures: monoclinic α form, hexagonal β form, triclinic γ form and quenched form [160]. The α form is the most commonly formed in normal melt-crystallized and solution-crystallized i-PP. Equilibrium melting temperature (T_m^o)

of α form crystals is between 185-209°C. α i-PP can be recrystallized and/or annealed from a less ordered α1 form to a more ordered α2 form. α i-PP spherulitic textures are classified into four distinct types, I to IV. A rich or even pure β form in i-PP can be prepared through rapid quenching, zone solidification, crystallization in a temperature gradient, or use of selective nucleating agents. β form is thermodynamically less stable than α form under normal crystallization conditions and can be transformed into α form during drawing at high temperature. T_m^o of β -form crystals vary from 170-200°C. γ form is normally observed in low molecular weight i-PP or crystallization of i-PP at elevated pressure above 200 MPa. Rapid quenching of i-PP fails to produce a totally amorphous structure. The structure of the quenched form is described as smectic. The smectic structure is composed of parallel 2 × 3/1 helices with disorder existing in the packing of the chains perpendicular to their axes.

The further the crystallization conditions are from the equilibrium, the less perfect is the structure produced, such as a lower degree of crystallinity, smaller size crystallites, or a lower melting temperature. This imperfection also implies a lower structural stability. Peak multiplication and duplication are normally observed on the melting curves of PP [161]. Separate melting of crystallite fractions of α i-PP gives individual peaks. Peak duplication is due to recrystallization superimposed on melting. Recrystallization is a polymer isothermally crystallized from the melt during melting, giving rise to melting endotherms with typical double peak shapes. The recrystallization can be eliminated by rapid heating, partial cross-linking or destruction of chain folds [161]. Crystalline supermolecular structures caused by oriented growth from heterogeneous surfaces are designated transcrystalline structures. Transcrystallization

appears when the density of the crystal nuclei is much higher on a solid surface in contact with a polymer melt than in the melt bulk [161]. The crystallites are allowed to grow only perpendicular to the solid surface, so a transcrystalline front is formed parallel to the surface. No β- form trans-crystallites have been observed.

2.9.3. Surface Treatment

PP has low surface energy so it has to be treated for applications in coatings, bonding, printing and metallization. The frequently used surface treatments for PP include plasma, corona and flame treatment, among which plasma treatment has the most promise for application in PP treatment. The modification with plasma is typically limited to the surface without affecting the bulk. More uniform surfaces are introduced by plasma than by flame and corona treatments [162]. Various chemical functionalities can be introduced on the surface by using different gases in the plasma treatment.

Plasma can be defined as a gas containing charged and neutral species, including electrons, positive ions, negative ions, radicals, atoms and/or molecules [162]. Functional groups are produced by reactions between gas and surface species, while crosslinks are formed between surface species. Characterization involves surface-sensitive techniques, such as X-ray photoelectron spectroscopy (XPS), secondary ion mass spectrometry, contact angle measurement and atomic force microscopy.

Air, oxygen, nitrogen, argon, water, carbon dioxide, CF_4, CF_3H, CF_3Cl, CF_3Br, SF_6 and SOF_2 plasma have been used to modify PP surfaces to provide the required surface properties for various applications [162]. Oxygen and oxygen-containing plasma such as air and water can produce a variety of oxygen functional groups, including C-O,

C=O, O-C=O, C-O-O and CO_3 at the surface [162]. PP treated with air, O_2/Ar, or water/Ar plasma showed significant improvement in adhesion with mild steel [162]. A low pressure O_2/N_2 plasma treatment on polypropylene (PP) was found to quickly functionalize the PP surface with O- and N-containing chemical groups within a few seconds; while surface roughening happened at a significantly longer time [163]. Roughening of the PP surface is possibly due to preferential attack on the amorphous region by plasma [162]. The rough surface was reported to have a negative contribution on adhesion of polymer coatings due to the weak bond of the surface layer to the bulk [163]. Kowalonek et al., studied air plasma treatment to PP and found the optimal treatment time is 75 s [164]. They thought hydrophilic functional groups were formed only after side chains were oxidized, given that methyl groups were easily oxidized to form CO_2. Cui et al., [165] treated PP films with an air dielectric barrier discharge plasma and found the treatment modified both morphology and composition of the PP surface. The spherulitic feature of the PP surface changed into randomly-shaped surface protrusions, surface toughness increased with increasing treatment time, heavily oxidized carbon species were detected on the treated surface and contact angles were largely reduced. Wang et al., [166] developed a surface modification model in an atmospheric pressure dielectric barrier discharge based on statistical theory and an orthogonal experimental design method. The model could predict the influence of different discharge parameters on water contact angle and oxygen concentration. Surface reactions, etching, and plasma polymerization can occur simultaneously in a fluorine-containing plasma. Polymerization is dominant in CF_3H plasma, which leads to a polymer coating on the surface [162].

Aging of plasma-treated PP has been studied. Contact angle measurement is a very surface-sensitive technique, and can be used to study the dynamic characteristics of polymer surfaces in various environments. Polar groups formed in oxygen-containing plasma can increase surface energy. When O_2-treated PP is stored in a low-energy medium such as air or vacuum, its surface energy decreases. This decrease may be due to rotation of polar groups in the bulk or migration of low molecular weight fragments to the surface in order to reduce the interfacial energy [162]. A fluorine-containing plasma can decrease the surface energy. When such a low-energy surface is placed in a high-energy medium such as water, nonpolar groups on the surface tend to move to the bulk in order to minimize the interfacial energy [162].

List of References

1. Saltzman WM. Drug Delivery: Engineering Principles for Drug Therapy. New York: Oxford University Press US, 2001.

2. Berkowitz, AC, Goddard, DM. Novel drug delivery systems: future directions. Journal of Neuroscience Nursing April 1 2009.

3. Swami SN. Radiation Synthesis of Polymeric Hydrogels for Swelling-controlled Drug Release Studies. PhD Dissertation, University of Western Sydney, New South Wales, Australia, 2004.

4. Baldwin SP, Saltzman WM. Materials for protein delivery in tissue engineering. Advanced Drug Delivery Reviews 1998; 33: 71-86.

5. Kaparissides C, Alexandridou S, Kotti K, Chaitidou S. Recent advances in novel drug delivery systems. Journal of Nanotechnology Online 2006; 2.

6. Santini, JT Jr, Richards AC, Scheidt R, Cima, MJ, Langer R. Microchips as controlled drug-delivery devices. Angew. Chem. Int. Ed. 2000; 39: 2396-2407.

7. Asher A. What are implantable drug pumps? September 18, 2008. http://backandneck.about.com

8. Smith TJ, Coyne PJ. How to use implantable intrathecal drug delivery systems for refractory cancer pain. The Journal of Supportive Oncology 2003; 1(1):73-76.

9. Smith TJ, Coyne PJ, Staats PS, Deer T, Stearns LJ, Rauck RL, Boortz-Marx RL, Buchser E, Catala E, Bryce DA, Cousins M, Pool GE. An implantable drug delivery system (IDDS) for refractory cancer pain provides sustained pain control, less drug-related toxicity, and possibly better survival compared with comprehensive medical management (CMM). Annals of Oncology 2005, 16: 825-833.

10. Mhatre AA. Implantable Drug Delivery System with an In-Plane Micropump. Master's Thesis, University of Texas at Arlington, 2006.

11. Elman NM, Ho Duc HL, Cima MJ. An implantable MEMS drug delivery device for rapid delivery in ambulatory emergency care. Biomed Microdevices 2009; 11:625-631.

12. Maloney JM, Santini JT Jr. Implantable microchips for controlled drug delivery. Proceedings of the 26th IEEE EMBS annual international conference. San Francisco, CA, USA. Sept 1-5, 2004. 2668-2669.

13. Sbiaa Z. MEMS fabricated chip for an implantable drug delivery device. Proceedings of the 28th IEEE EMBS annual international conference. New York City, USA. Aug 30-Sept 3, 2006. 5621-5624

14. Nanotechnology to revolutionise drug delivery. 2005. Technologist.com

15. Baker JR Jr., Hamouda, T. Nanoemulsion vaccines. U.S. patent 7,314,624. January 3, 2008.

16. Bielinska AU, Chepurnov AA, Landers JJ, Janczak KW, Chepurnova TS, Luker GD, Baker JR Jr. A novel, killed- virus nasal vaccinia virus vaccine. Clinical and Vaccine Immunology, February 2008; 15(2): 348-358.

17. Bielinska AU, Janczak KW, Landers JJ. Nasal immunization with a recombinant HIV gp120 and nanoemulsion adjuvant produces Th1 polarized responses and neutralizing antibodies to primary HIV type 1 isolates. AIDS Research Human Retroviruses 2008; 24: 271-81.

18. Schmitt E, Polistina R. Surgical Sutures. US Patents 3,297,033. Jan. 10, 1967.

19. Gilding DK, Reed AM. Biodegradable polymers for use in surgery—Polyglycolic/poly(lactic acid) homo- and copolymers: 1. Polymer 1979; 20: 1459–1464.

20. Pinkus, AG, Subramanyam R. New high-yield, one-step synthesis of polyglycolide from haloacetic acids. Journal of Polymer Science, Polymer Chemistry Edition 1984; 22: 1131-1140.

21. Varma-Nair M, Pan R, Wunderlich B. Heat capacities and entropies of linear, aliphatic polyesters. Journal of Polymer Science, Part B: Polymer Physics 1991; 29: 1107-1115.

22. Bourne RB, Bitar H, Andreae PR, Martin LM, Finlay JB, Marquis F. *In vivo* comparison of four absorbable sutures: Vicryl, Dexon Plus, Maxon and PDS. Canadian Journal of Surgery 1998; 31: 43-45.

23. Hoogsteen W, Postema AR, Pennings AJ, Brinke GT, Zugenmaier P. Crystal structure, conformation and morphology of solution-spun poly(L-lactide) fibers. Macromolecules 1990; 23 (2): 634-642.

24. Jamshidi K, Hyon SH, Ikada Y. Thermal characterization of polylactides. Polymer 1988; 29 (12): 2229-2234.

25. Schindler A, Harper D. Polylactide II. Viscosity-molecular weight relationships and unperturbed chain dimensions. Journal of Polymer Science, Polymer Chemistry Edition 1979; 17: 2593-2599.

26. Alexander H, Brunski JB, Cooper SL, Hench LL, et al. Chapter 2: Classes of materials used in medicine. In: Ratner BD, et al. editors. Biomaterials Science: An Introduction to Materials in Medicine, second edition. London: Elsevier Academic Press, Inc. 2004: 67-236.

27. Ma P. Scaffolds for Tissue Fabrication. Materials Today, May 2004.

28. Beletsi A, Leontiadis L, et al. Effect of preparative variables on the properties of poly(*dl*-lactide-*co*-glycolide)-methoxypoly(ethyleneglycol) copolymers related to their application in controlled drug delivery. International Journal of Pharmaceutics 1999; 182: 187–197.

29. Jeong J, Lim D, et al. Synthesis, characterization and protein adsorption behaviors of PLGA/PGA di-block co-polymer blend films." Colloids and Surfaces B. Biointerfaces 2000; 18: 371–379.

30. Kim K, Luu Y, et al. Incorporation and controlled release of a hydrophilic antibiotic using poly(lactide-*co*-glycolide)-based electrospun nanofibrous scaffolds. Journal of Controlled Release 2004; 98: 47–56.

31. Kim K, Yu M, Zong X, Chiu J, Fang D, Seo Y-S, Hsiao BS, Chu B, Hadjiargyrou M. Control of degradation rate and hydrophilicity in electrospun non-woven poly(dl-lactide) nanofiber scaffolds for biomedical applications. Biomaterials 2003: 24: 4977–4985.

32. Luu Y, Kim K, et al. Development of a nanostructured DNA delivery scaffold via electrospinning of PLGA and PLA-PEG block copolymers. Journal of Controlled Release 2003; 89: 341–353.

33. Qiao M, Chen D, Ma X, Liu Y. Injectable biodegradable temperature-responsive PLGA-PEG-PLGA copolymers: synthesis and effect of copolymer composition on the drug release from the copolymer-based hydrogels. International Journal of Pharmaceutics 2005; 294: 103-112.

34.27. Park G, Pattison M, et al. Accelerated chondrocyte functions on NaOH-treated PLGA scaffolds." Biomaterials 2005; 26: 3075–3082.

35. Zong X, Ran S, Fang D, Hsiao BS, Chu B. Control of structure, morphology and property in electrospun poly(glycolide-co-lactide) non-woven membranes via post-draw treatments. Polymer 2003; 44: 4959-4967.

36. Loo S, Ooi C, et al. Effect of isothermal annealing on the hydrolytic degradation rate of poly(lactide-*co*-glycolide) (PLGA). Biomaterials 2005; 26: 2827–2833.

37. Feng X, Song C, Chen W. Synthesis and evaluation of biodegradable block copolymers of e-caprolactone and dl-lactide. Journal of Polymer Science: Polymer Letters Edition 1983; 21: 593–600.

38. Kricheldorf H, Jonté J, Berl M. Polylactones 3. Copolymerization of glycolide with l,l-lactide and other lactones. Makromol. Chem., Supplement 1985;12: 25–38.

39. Chew SY, Wen J, Yim EKF, Leong KW. Sustained release of proteins from electrospun biodegradable fibers. Biomacromolecules 2005; 6: 2017–2024.

40. Galeska I, Kim TK, Patil SD, Bhardwaj U, Chatttopadhyay D, Papadimitrakopoulos F, Burgess DJ. Controlled release of dexamethasone from PLGA microspheres embedded within polyacid-containing PVA hydrogels. The AAPS Journal 2005; 7(1): E231-E240.

41. Rosiak JM, Janik I, Kadlubowski S, Kozicki M, Kujawa P, Stasica P, Ulans P. Radiation formation of hydrogels for biomedical applications. The International Atomic Energy Agency's report, 2002. Centre of Excellence "Lasers & Biomaterials in Medicine" report, 2002: 1-50. http://mitr.p.lodz.pl/biomat/raport/book_index.html

42. Peppas NA. Infrared spectroscopy of semicrystalline PVA networks. Makromol. Chemie 1977; 178: 595-601.

43. Park K, Shalaby WSW, Park H. Chapter 1: Introduction. In: Biodegradable Hydrogels for Drug Delivery. Pennsylvania: Technomic publishing company, Inc., 1993:1-12.

44. Friedlander HN, Harris HE, Pritchard JG. Structure-property relations of poly(vinyl alcohol). 1. Influence of polymerization solvents and temperature on the structure and properties of poly(vinyl alcohol) derived from poly(vinyl acetate). Journal of Polymer Science, Polymer Chemistry Edition 1966; 4: 649-664.

45. Hassan CM, Peppas NA. Structure and applications of poly(vinyl alcohol) hydrogels produced by conventional crosslinking or by freezing/thawing methods. Advances in polymer science 2000; 153:37-65.

46. Liu X, Nakamura K, Lowman A. Composite hydrogels for sustained release of therapeutic agents. Soft Materials 2003; 1: 393–408.

47. Asano M, Yoshida M, et al. Biodegradability of a hot-pressed poly(lactic acid) formulation with controlled release of LH-RH agonist and its pharmacological influence on rat prostate. Makromol. Chem., Rapid Commun. 1985; 6: 509–513.

48. Beck M. Process for preparing condensation polymers of hydroxyacetic acid. US Patent 2,585,427. Feb. 12, 1952.

49. Higgins N. Condensation polymers of hydroxyacetic acid. US Patent 2,676,945. Apr. 27, 1954.

50. Nevin R. Polymerization process and product. US Patent 4,273,920. Jun. 16, 1981.

51. Moon S, Lee C, et al. Melt polycondensation of l-lactic acid with Sn(II) catalysts activated by various proton acids: A direct manufacturing route to high molecular weight Poly(l-lactic acid). Journal of Polymer Science: PartA: Polymer Chemistry 2000; 38: 1673–1679.

52. Ajioka M, Enomoto K, et al. Basic properties of polylactic acid produced by the direct condensation polymerization of lactic acid. Bull. Chem. Soc. Jpn. 1995; 68: 2125–2131.

53. Dubois PH, Jacobs C, et al. Macromolecular engineering of polylactones and polylactides. 4. Mechanism and kinetics of lactide homopolymerization by aluminum isopropoxide. Macromolecules 1991; 24: 2266–2270.

54. Kowalski, A., Duda, A. and Penczek, S. Polymerization of l,l-lactide initiated by aluminum isopropoxide trimer or tetramer. Macromolecules 1998; 31: 2114–2122.

55. Montaudo, G., Montaudo, M. et al. Evidence for ester-exchange reactions and cyclic oligomer formation in the ring-opening polymerization of lactide with aluminum complex Initiators. Macromolecules 1996; 29: 6461–6465.

56. Chujo K, Hobayashi H, et al. Ring-opening polymerization of glycolide. Die Makromolekulare Chemie 1967; 100: 262–266.

57. Kricheldorf H, Berl M, Scharnagl N. Poly(lactones): 9. Polymerization mechanism of metal alkoxide initiated polymerizations of lactide and various lactones. Macromolecules 1988; 21: 286–293.

58. Kricheldorf H, Boettcher C, Tönnes K-U. Polylactones: 23. Polymerization of *racemic* and *meso* d,l-lactide with various organotin catalysts—Stereochemical aspects. Polymer 1992; 33 (13): 2817–2824.

59. Stevels W, Ankoné M, et al. Kinetics and mechanism of l-lactide polymerization using two different yttrium alkoxides as initiators. Macromolecules 1996; 29: 6132–6138.

60. Kricheldorf H, Dunsing R. Polylactones: 8. Mechanism of the cationic polymerization of l,l-dilactide. Makromol. Chem. 1986; 187: 1611–1625.

61. Kricheldorf H, Kreiser-Saunders I. Polylactones: 19. Anionic polymerization of l-lactide in solution. Makromol. Chem. 1990; 191: 1057–1066.

62. Kricheldorf H, Kreiser-Saunders I, Boettcher C. Polylactones: 31. Sn(II) octoate-initiated polymerization of l-lactide: A mechanistic study. Polymer 1995; 36 (6): 1253–1259.

63. Kricheldorf H, Lee S-R, Bush S. Polylactones: 36. Macrocyclic polymerization of lactides with cyclic Bu_2Sn initiators derived from 1,2-ethanediol, 2-mercaptoethanol, and 1,2-dimercaptoethane. Macromolecules 1996; 29 (5): 1375–1381.

64. Duda A, Penczek S. Thermodynamics of l-lactide polymerization. Equilibrium monomer concentration. Macromolecules 1990; 23: 1636–1639.

65. Kowalski A, Libiszowski J, et al. Polymerization of l,l-dilactide initiated by tin (II) butoxide. Macromolecules 2000; 33: 1964–1971.

66. Avgoustakis K, Nixon J. Biodegradable controlled release tablets I: Preparative variables affecting the properties of poly(lactide-*co*-glycolide) copolymers as matrix forming material. International Journal of Pharmaceutics 1991 ; 70: 77–85.

67. Degée PH, Dubois PH, et al. Beneficial effect of triphenylphosphine on the bulk polymerization of l,l-lactide promoted by 2-ethylhexanoic acid tin (II) salt. Journal of Polymer Science: Part A: Polymer Chemistry 1999; 37: 2413–2420.

68. Eling B, Gogolewski S, Pennings A. Biodegradable materials of poly(l-lactic acid): 1. Melt-spun and solution-spun fibres." Polymer 1982; 23: 1587–1593.

69. Kim S, Han Y-K, et al. Multifunctional initiation of lactide polymerization by stannous octoate/pentaerythritol. Makromol. Chem. 1992; 193: 1623–1631.

70. Schindler A, Gaetano K. Poly(lactate) III. Stereoselective polymerization of meso-dilactide. Journal of Polymer Science: Part C: Polymer Letters 1988; 26: 47–48.

71. Schwach G, Coudane J, et al. More about the polymerization of lactides in the presence of stannous octoate. Journal of Polymer Science: Part A: Polymer Chemistry 1997; 35: 3431–3440.

72. Zhang X, Wyss U, et al. An investigation of the synthesis and thermal stability of poly(d,l-lactide). Polymer Bulletin 1992; 27: 623–629.

73. Kenley RA, Lee MO, Mahoney TR II, Sanders LM. Poly(lactide-*co*-glycolide) decomposition kinetics *in vivo* and *in vitro*. Macromolecules 1987; 20: 2398–2403.

74. Wasserman D, Versfelt C. Use of stannous octoate catalyst in the manufacture of poly l(-)lactide/coglycolide sutures. US Patent 3,839,297. Oct. 1, 1974.

75. Andreopoulos A, Hatzi E, Doxastakis M. Synthesis and properties of poly(lactic acid). Journal of Materials Science: Materials in Medicine 1999; 10: 29–33.

76. Nijenhuis A, Grijpma D, Pennings A. Lewis acid catalyzed polymerization of l-lactide. Kinetics and mechanism of the bulk polymerization. Macromolecules 1992; 25: 6419–6424.

77. Zhang X, Maconald D, et al. Mechanism of lactide polymerization in the presence of stannous octoate: The effect of hydroxy and carboxylic acid substances. Journal of Polymer Science: Part A: Polymer Chemistry 1994; 32: 2965–2970.

78. Kowalski A, Duda A, Penczek S. Mechanism of cyclic ester polymerization initiated with tin(II) octoate. 2. Macromolecules fitted with tin(II) alkoxide species observed directly in MALDI-TOF spectra. Macromolecules 2000; 33: 689–695.

79. Kowalski A, Duda A, Penczek S. Kinetics and mechanism of cyclic esters polymerization initiated with tin(II) octoate. 3. Polymerization of l,l-dilactide. Macromolecules 2000; 33: 7359–7370.

80. Storey R, Sherman J. Kinetics and mechanism of the stannous octoate-catalyzed bulk polymerization of –caprolactone. Macromolecules 2002; 35: 1504–1512.

81. Ryner M, Stridsberg K, et al. Mechanism of ring-opening polymerization of 1,5-dioxepan-2-one and l-lactide with stannous 2-ethylhexanoate. A theoretical study. Macromolecules 2001; 34: 3877–3881.

82. Kricheldorf H, Kreiser-Saunders I, Stricker A. Polylactones 48. $SnOct_2$-initiated polymerizations of lactide: A mechanistic study. Macromolecules 2000; 33: 702–709.

83. Blasi P, D'Souza SS, Selmin F, DeLuca PP. Plasticizing effect of water on poly(lactide-co-glycolide). Journal of Controlled Release 2005; 108: 1-9.

84. Avgoustakis K, Nixon JR. Biodegradable controlled release tablets II: Preparation and properties of poly(lactide-*co*-glycolide) powders. International Journal of Pharmaceutics 1993; 99: 239–246.

85. Yoon JJ, Park TG. Degradation behaviors of biodegradable macroporous scaffolds prepared by gas foaming of effervescent salts. Journal of Biomedical Material Research 2001; 55: 401-408.

86. Zong X, Ran S, Kim K-S, Fang D, Hsiao BS, Chu B. Structure and morphology changes during *in vitro* degradation of electrospun poly(glycolide-co-lactide) nanofibers membranes. Biomacromolecules 2003; 4: 416-423.

87. Zong X, Kim K, Fang D, Ran S, Hsiao BS, Chu B. Structure and process relationship of electrospun bioabsorbable nanofiber membranes. Polymer 2002; 43: 4403–4412.

88. You Y, Min B-M, Lee SJ, Lee TS, Park WH. *In vitro* degradation behavior of eletrospun polyglycolide, polylactide, and poly(lactide-*co*-glycolide). Journal of Applied Polymer Science 2005; 95: 193–200.

89. Lee S-H, Kim SH, Han YK, Kim YH. Synthesis and degradation of end-group-functionalized polylactide. Journal of Polymer Science: Part A: Polymer Chemistry 2001; 39: 973-985.

90. Zhang H, Cui W, Bei J, Wang S. Preparation of poly(lactide-co-glycolide-co-caprolactone) nanoparticles and their degradation behavior in aqueous solution. Polymer Degradation and Stability 2006; 91: 1929-1936.

91. Siepmann J, Elkharraz K, Siepmann F, Klose D. How autocatalysis accelerated drug release from PLGA-based microparticles: a quantitative treatment. Biomacromolecules 2005; 6: 2312-2319.

92. Dunne M, Corrigan OI, Ramtoola Z. Influence of particle size and dissolution conditions on the degradation properties of polylactide-*co*-glycolide particles. Biomaterials 2000; 21: 1659-1668.

93. Ginde RM, Gupta RK. *In vitro* chemical degradation of poly(glycolic acid) pellets and fibers. Journal of Applied Polymer Science 1987; 33: 2411-2429.

94. Wu L, Ding J. Effects of porosity and pore size on *in vitro* degradation of three-dimensional porous poly(d,l-lactide-co-glycolide) scaffolds for tissue engineering. Journal of Biomedical Material Research 2005; 75A: 767-777.

95. Reed AM, Gilding DK. Biodegradable polymers for use in surgery—Polyglycolic/poly(lactic acid) homo and copolymers: 2. *In vitro* degradation. Polymer 1981; 22: 494–498.

96. Burkersroda F, Schedl L, Gopferich A. Why degradable polymers undergo surface erosion or bulk erosion. Biomaterials 2002; 23:4221-4231.

97. Zolnik BS, Burgess DJ. Effect of acidic pH on PLGA microsphere degradation and release. Journal of Controlled Release 2007; 122:338-344.

98. Coffin MD, McGinity JW. Biodegradable pseudolatexes: the chemical stability of poly(dl-lactide) and poly(ε-caprolactone) nanoparticles in aqueous medium. Pharmaceutical Research 1992; 9 (2): 200-205.

99. Huang Y, Qi M, Zhang M, Liu H, Yang D. Degradation mechanisms of poly(lactic-co-glycolic acid) films *in vitro* under static and dynamic environment. Trans Nonferrous Met.Soc. China 2006; 16: s293-s297.

100. Vey E, Roger C, Meehan L, Booth J, Claybourn M, Miller AF, Saiani A. Degradation mechanism of poly(lactic-co-glycolic) acid block copolymer cast films in phosphate buffer solution. Polymer Degradation and Stability 2008; 93: 1869-1876.

101. Fitzgerald JF, Corrigan OI. Mechanisms governing drug release from poly-α-hydroxy aliphatic esters. In: Ei-Nokaly MA, Piatt DM, Charpentier BA, editors. Polymeric delivery systems, properties and applications. ACS Symposium Series No. 520. Washington DC: American Chemical Society, 1993: 311-326.

102. Prout EG, Tompkins FC. The thermal decomposition of potassium permanganate. Trans Faraday Soc 1944; 40:488-498.

103. Shah SS, Cha Y, Pitt CG. Poly(glycolic acid-co-dl-lactic acid): diffusion or degradation controlled drug delivery? Journal of Controlled Release 1992; 18: 261-270.

104. Avgoustakis K, Nixon JR. Biodegradable controlled release tablets III: Effect of polymer characteristics on drug release from heterogeneous poly(lactide-*co*-glycolide) matrices. International Journal of Pharmaceutics 1993; 99: 247–252.

105. Formhals A. Process and apparatus for preparing artificial threads. US Patent 1,975,504. Oct. 2, 1934.

106. Taylor G. Electrically driven jets. Proc. R Soc. London, Ser. A 1969; 313: 453.

107. Baumgarten P. Electrostatic spinning of acrylic microfibers. Journal of Colloid and Interface Science 1971; 36 (1): 71–79.

108. Hohman M, Shin M, et al. Electrospinning and electrically forced jets. I. Stability theory. Physics of Fluids 2001; 13 (8): 2201–2220.

109. Reneker D, Yarin A, et al. Bending instability of electrically charged liquid jets of polymer solutions in electrospinning. Journal of Applied Physics 2000; 87: 4531-4547.

110. Shin Y, Hohman M, et al. Electrospinning: A whipping fluid jet generates submicron polymer fibers. Applied Physics Letters 2001; 78 (8): 1–3.

111. Shin Y, Hohman M, et al. Experimental characterization of electrospinning: The electrically forced jet and instabilities. Polymer 2001; 42: 9955–9967.

112. Spivak A, Dzenis Y, Reneker D. A Model of steady state jet in the electrospinning process. Mechanics Research Communications 2000; 27 (1): 37–42.

113. Larrondo L, Manley R. Electrostatic fiber spinning from polymer melts. I. Experimental observations on fiber formation and properties. Journal of Polymer Science: Polymer Physics Edition 1981; 19: 909–920.

114. Doshi J, Reneker D. Electrospinning process and applications of electrospun fibers. Journal of Electrostatics 1995; 35: 151–160.

115. Jaeger R, Bergshoef M, et al. Electrospinning of ultra-thin polymers fibers. Macromol. Symp. 1998; 127: 141–150.

116. Fong H, Chun I, Reneker D. Beaded nanofibers formed during electrospinning. Polymer 1999; 40: 4585–4592.

117. Katti DS, Robinson KW, Ko FK, Laurencin CT. Bioresorbable nanofiber-based systems for wound healing and drug delivery: Optimization of fabrication parameters. J Biomedical Materials Research Part B: Applied Biomaterials 2004; 70B: 286–296.

118. Bini T, Goa S, et al. Electrospun poly(l-lactide-*co*-glycolide) biodegradable polymer nanofibre tubes for peripheral nerve regeneration. Nanotechnology 2004; 15: 1459–1464.

119. Min B-M, You Y, et al. Formation of nanostructured poly(lactic-*co*-glycolic acid)/chitin matrix and its cellular response to normal human keratinocytes and fibroblasts. Carbohydrate Polymers 2004; 57: 285–294.

120. Gupta P, Wilkes G. Some investigations on the fiber formation by utilizing a side-by-side bicomponent electrospinning approach. Polymer 2003; 44: 6353–6359.

121. Sun Z, Zussman E, Yarin AJ, Wendorff JH, Greiner A. Compound core-shell polymer nanofibers by co-electrospinning. Advanced Materials 2003; 15 (22): 1929–1932.

122. Jiang H, Hu Y, Li Y, Zhao P, Zhu K, Chen W. A facile technique to prepare biodegradable coaxial electrospun nanofibers for controlled release of bioactive agents. Journal of Controlled Release 2005; 108: 237-243.

123. Zeng J, Xu X, Chen X, Liang Q, Bian X, Yang L, Jing X. Biodegradable electrospun fibers for drug delivery. Journal of Controlled Release 2003; 92: 227-231.

124. Zeng J, Yang L, Liang Q, Zhang X, Guan H, Xu X, Chen X, Jing X. Influence of the drug compatibility with polyer solution on the release kinetics of electrospun fiber formulation. Journal of Controlled Release 2005; 105: 43-51.

125. Zong X, Bien H, Chung CY, Yin L, Fang D, Hsiao BS, Chu B, Entcheva E. Electrospun fine-textured scaffolds for heart tissue constructs. Biomaterials 2005; 26: 5330-5338.

126. Yoshimoto H, Shin YM, Terai H, Vacanti JP. A biodegradable nanofiber scaffold by electrospinning and its potential for bone tissue engineering. Biomaterials 2003; 24: 2077–2082.

127. Li WJ, Tuli R, Okafor C, Derfoul A, Danielson KG, Hall DJ, Tuan RS. A three-dimensional nanofibrous scaffold for cartilage tissue engineering using human mesenchymal stem cells. Biomaterials 2005; 26: 599-609.

128. Ding B, Kim H-Y, et al. Preparation and characterization of nanoscaled poly(vinyl alcohol) fibers via electrospinning. Fibers and Polymers 2002; 3 (2): 73–79.

129. Koski A, Yim K, Shivkumar S. Effect of molecular weight on fibrous PVA produced by electrospinning. Materials Letters 2004; 58: 493-497.

130. Matthews JA, Wnek GE, Simpson DG, Bowlin GL. Electrospinning of collagen nanofibers. Biomacromolecules 2002; 3: 232–238.

131. Wnek GE, Carr ME, Simpson DG, Bowlin GL. Electrospinning of nanofiber fibrinogen structures. Nano Letters 2003; 3 (2): 213–216.

132. Karande TS, Ong JL, Agrawal CM. Diffusion in musculoskeletal tissue engineering scaffolds: Design issues related to porosity, permeability, architecture and nutrient mixing. Annals of Biomedical Engineering 2004; 32 (12): 1728-1743.

133. Li WJ, Laurencin CT, Caterson EJ, Tuan RS, Ko FK. Electrospun nanofibrous structure: A novel scaffold for tissue engineering. Journal of Biomedical Materials Research 2002; 60: 613–621.

134. Xu C, Inai R, Kotaki M, Ramakrishna S. Electrospun nanofiber fabrication as synthetic extracellular matrix and its potential for vascular tissue engineering. Tissue Engineering 2004; 10 (7/8): 1160–1168.

135. Xu X, Yang L, Xu X, Wang X, Chen X, Liang Q, Zeng J, Jing X. Ultrafine medicated fibers electrospun from W/O emulsions. Journal of Controlled Release 2005; 108: 33-42.

136. Bicerano J, Seitz JT. 1. Molecular origins of toughness in polymers. Arends CB, editor. Polymer Toughening. New York: Marcel Dekker, Inc., 1996: 1-60.

137. Sue H-J, Garcia-Meitin EI, Pickelman DM. 5. Fracture behavior of rubber-modified high performance epoxies. In: Arends CB, editor. Polymer Toughening. New York: Marcel Dekker, Inc., 1996: 131-174.

138. Pearson RA. 1. Introduction to the toughening of polymers. In: Pearson RA, Sue H-J, Yee AF, editors. Toughening of Plastics, Advances in Modeling and Experiments. ACS Symposium Series No. 759. Washington DC: American Chemical Society, 2000: 1-12.

139. Kinloch AJ, Shaw SJ, Tod, DA, Hunston DL. Deformation and fracture behaviour of a rubber-toughened epoxy: 1. Microstructure and fracture studies. Polymer 1983; 24:1341-1354.

140. Yee AF, Pearson RA. Toughening mechanisms in elastomer-modified epoxies, Part 1 Mechanical studies. Journal of Materials Science 1986; 21:2462-2474.

141. Pearson RA, Yee AF. Toughening mechanisms in elastomer-modified epoxies, Part 2 Microscopy studies. Journal of Materials Science 1986; 21:2475-2488.

142. Pearson RA, Yee AF. Toughening mechanisms in elastomer-modified epoxies, Part 3 The effect of cross-link density. Journal of Materials Science 1989; 24:2571-2580.

143. McGarry FJ. 6. Rubber-toughened thermosets. In: Arends CB, editor. Polymer Toughening. New York: Marcel Dekker, Inc., 1996: 175-188.

144. Hedrick JL, Yilgor I, Jurek M, Hedrick JC, Wilkes GL, McGrath JE. Chemical modification of matrix resin networks with engineering thermoplastics: 1. Synthesis, morphology, physical behaviour and toughening mechanisms of poly(arylene ether sulphone) modified epoxy networks. Polymer 1991, 32(11): 2020-2032.

145. Goossens S, Goderis B, Groeninckx G. Reaction-induced Phase separation in crystallizable micro- and nanostructured high melting thermoplastic/epoxy resin blends. Macromolecules 2006; 39: 2953-2963.

146. Scheirs J. 15. Failure of fibre-reinforced composites. In: Compositional and Failure Analysis of Polymers – A Practical Approach. Chichester: John Wiley & Sons, Ltd., 2000: 449-481.

147. Gillespie JW, Carlsson LA. 6.3. Interlaminar fracture of laminated composite materials. In: Gillespie JW, Carlsson LA, editors. Delaware Composites Design Encyclopedia, Volume 6: Test Methods. Pennsylvania: Technomic, 1990: 113-160.

148. Yun NG, Won YG, Kim SC. Toughening of epoxy composite by dispersing polysulfone particle to form morphology spectrum. Polymer Bulletin 2004; 52:365-372.

149. Groleau MR, Shi Y-B, Bertram JL, Sue HJ, Yang PC. Mode II fracture of composites interlayered with nylon particles. Composites Science and Technology 1996; 56:1223-1240.

150. Stevanovic D, Kalyanasundaram S, Lowe A, Jar PYB. FEA of crack-particle interactions during delamination in interlayer toughened polymer composites. Engineering Fracture Mechanics 2005; 72: 1738-1769.

151. Ziaee S, Palmese GR. Effects of temperature on cure kinetics and mechanical properties of vinyl-ester resins. Journal of Polymer Science: Part B: Polymer Physics 1999; 37: 725-744.

152. Dua S, McCullough RL and Palmese GR. Copolymerization kinetics of styrene/vinyl-ester systems: low temperature reactions. Polymer Composites 1999; 20 (3): 379-391.

153. Brill RP, Palmese GR. Cure behavior of DGEBA vinyl-ester-styrene resins near silane-treated interfaces. Journal of Applied Polymer Science 2006; 101: 2784-2792.

154. Ullett JS, Chartoff RP. Toughening of unsaturated polyester and vinyl ester resins with liquid rubbers. Polymer Engineering and Science 1995; 35(13):1086-1097.

155. Robinette EJ, Ziaee S, Palmese GR. Toughening of vinyl ester resin using butadiene-acrylonitrile rubber modifiers. Polymer 2004; 45:6143-6154.

156. Robinette EJ. Toughening Vinyl Ester Matrix Composites by Tailoring Nanoscale and Mesoscale Interfaces. PhD Dissertation, Drexel University, Pennsylvania, USA, 2005.

157. Monasse B, Haudin JM. 1. Molecular structure of polypropylene homo- and copolymers. In: Karger-Kocsis J, editor. Polypropylene: Structure, Blends and Composites. Volume 1 Structure and Morphology. London: Chapman & Hall, 1995: 3-30.

158. Scheirs J. 5. Thermal analysis of polymers. In: Compositional and Failure Analysis of Polymers – A Practical Approach. Chichester: John Wiley & Sons, Ltd., 2000: 175-177.

159. Gauthier WJ. Elastomeric polypropylene homopolymers using metallocene catalysts. In: Karger-Kocsis J, editor. Polypropylene: An A-Z Reference. Springer-Verlag, 1999: 178-185.

160. Cheng SZD, Janimak JJ, Rodriguez J. 2. Crystalline structures of polypropylene homo- and copolymers. In: Karger-Kocsis J, editor. Polypropylene: Structure, Blends and Composites. Volume 1 Structure and Morphology. London: Chapman & Hall, 1995: 31-55.

161. Varga J. 3. Crystallization, melting and supermolecular structure of isotactic polypropylene. In: Karger-Kocsis J, editor. Polypropylene: Structure, Blends and Composites. Volume 1 Structure and Morphology. London: Chapman & Hall, 1995: 56-115.

162. Chan C-M. Surface modification of polypropylene by plasma. In: Karger-Kocsis J, editor. Polypropylene: An A-Z Reference. Springer-Verlag, 1999: 794-799.

163. Harth K, Hibst H. Surface modification of polypropylene in oxygen and nitrogen plasmas. Surface and Coatings Technology 1993; 59:350-355.

164. Kaminska A, Kaczmarek H, Kowalonek J. The influence of side groups and polarity of polymers on the kind and effectiveness of their surface modification by air plasma action. European Polymer Journal 2002; 38:1915-1919.

165. Cui NY, Brown NMD. Modification of the surface properties of a polypropylene film using an air dielectric barrier discharge plasma. Applied Surface Science 2002; 189:31-38.

166. Wang C, He X. Polypropylene surface modification model in atmospheric pressure dielectric barrier discharge. Surface & Coatings Technology 2006; 201:3377-3384.

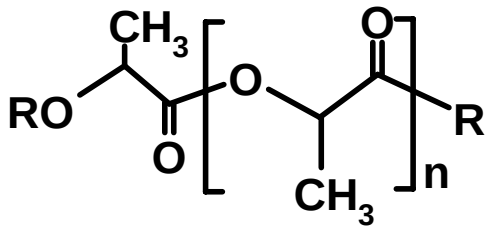

Poly(Lactide) (PLA)

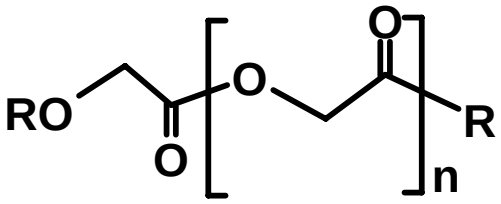

Poly(Glycolide) (PGA)

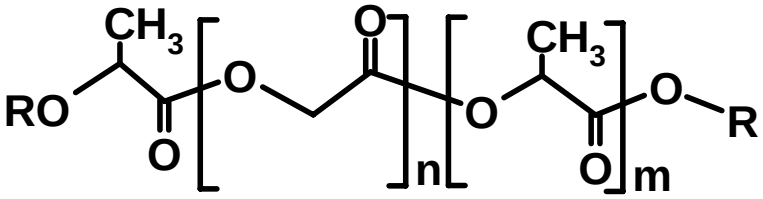

Poly(Lactide-co-Glycolide) (PLGA)

Figure 2.1. Chemical structures of PLA, PGA and PLGA polymers.

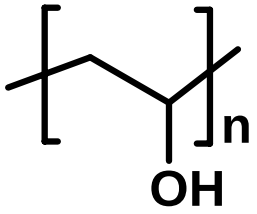

(a)

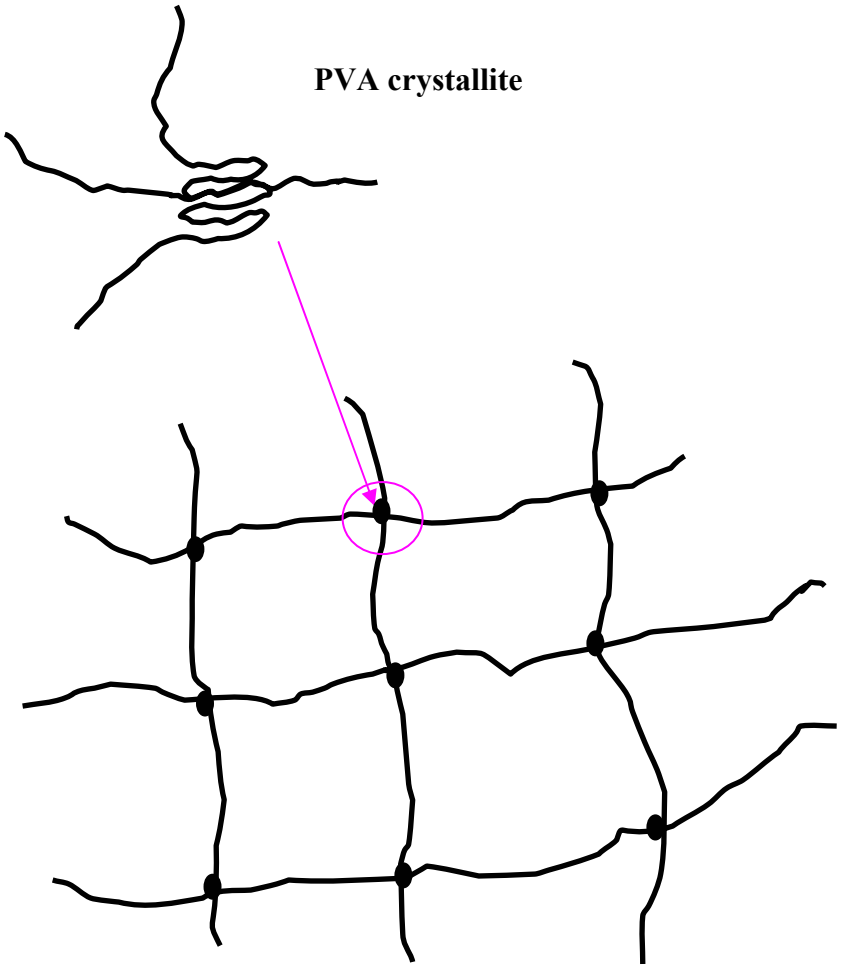

(b)

Figure 2.2. (a) Chemical structure of PVA polymer and (b) PVA hydrogel network crosslinked via formation of crystallites.

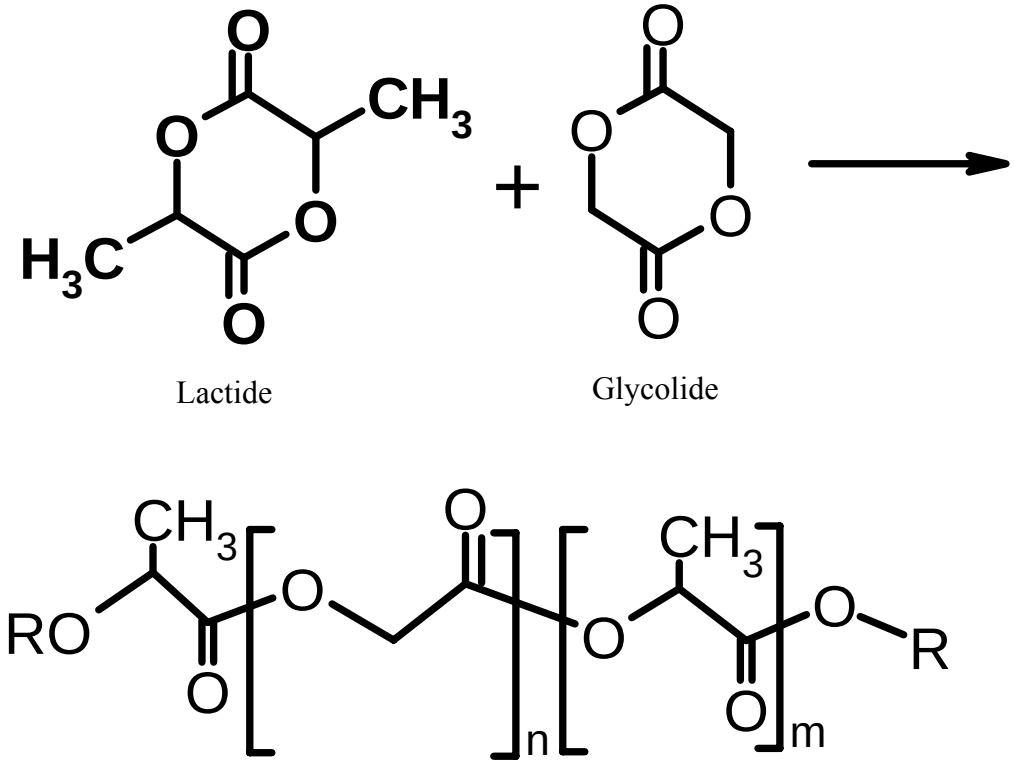

Figure 2.3. Synthesis of PLGA copolymer through ring-opening polymerization.

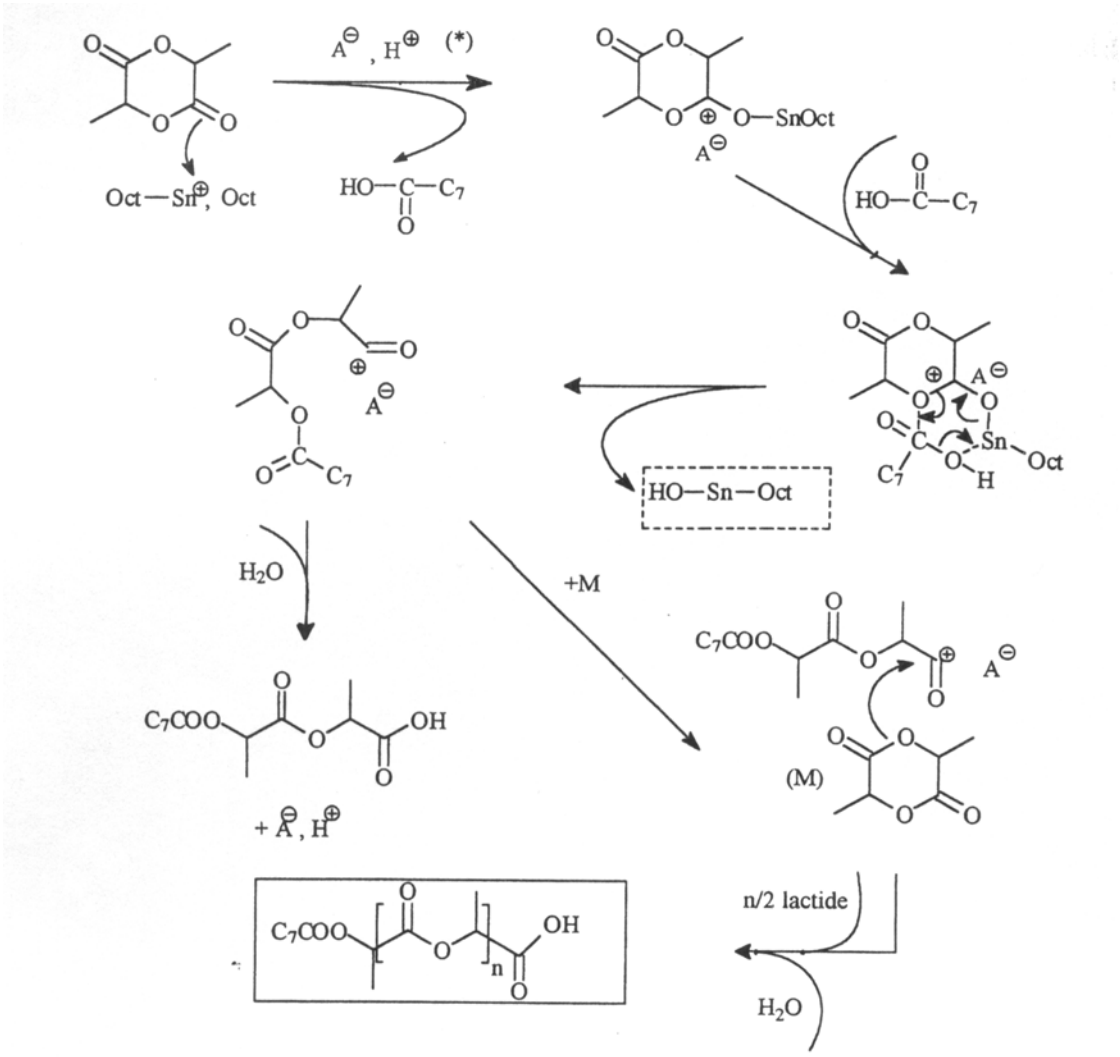

Figure 2.4. Cationic octanoic acid co-initiated mechanism [63] (AΘ and $H^{\oplus}$ are from lactic acid or octanoic acid.)

$$C_7H_{15}COO–Sn–OOCC_7H_{15} + H_2O \leftrightarrow C_7H_{15}COO–Sn–OH + C_7H_{15}COOH \quad \textbf{(a)}$$

$$C_7H_{15}COO–Sn–OOCC_7H_{15} + HO–R \leftrightarrow C_7H_{15}COO–Sn–OR + C_7H_{15}COOH \quad \textbf{(b)}$$

$$C_7H_{15}COO–Sn–OH + HO–R \leftrightarrow RO–Sn–OH + C_7H_{15}COOH \quad \textbf{(c)}$$

Figure 2.5. Possible interactions between the stannous octoate and impurities in the polymerization mixture. Stannous hydroxide formed from reaction (a) and stannous alkoxide formed from reactions (b) and (c) [69].

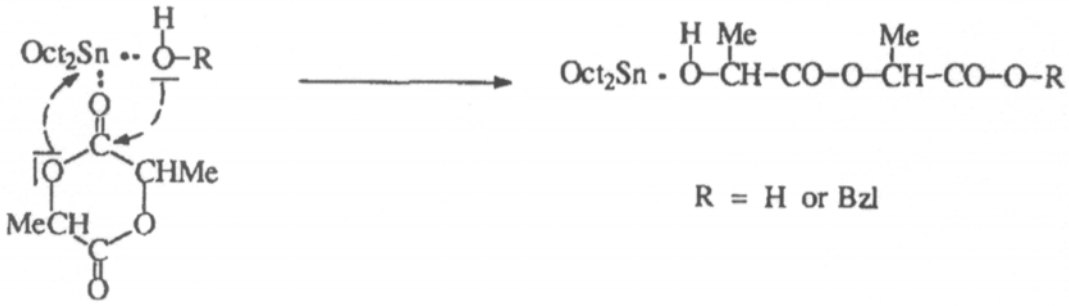

Figure 2.6. Complexation or second-order insertion [53].

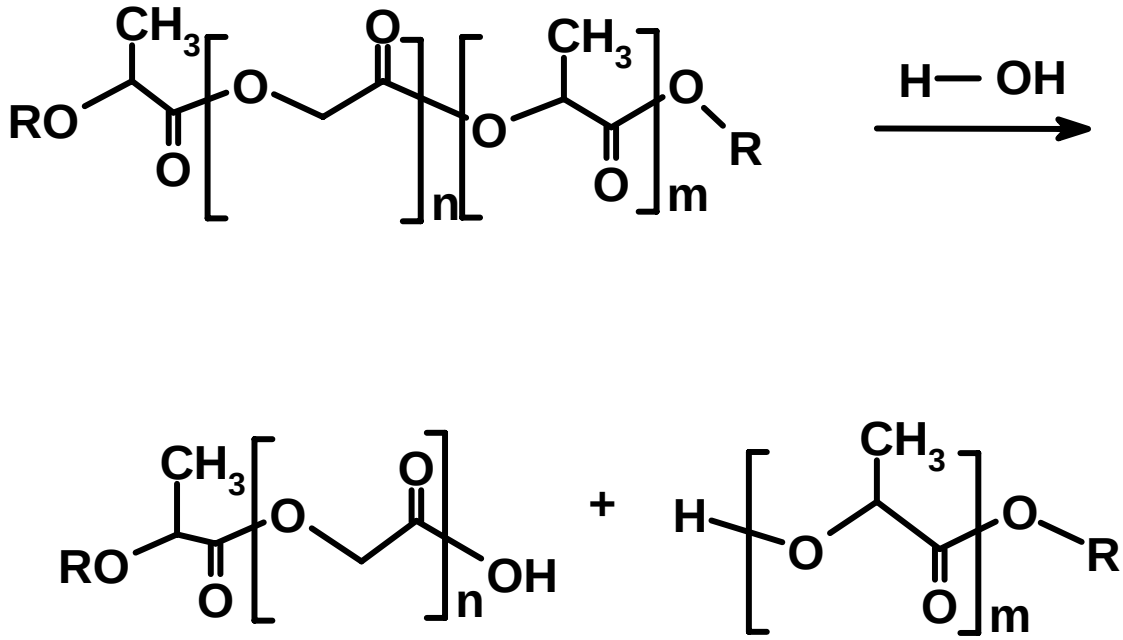

Figure 2.7. Hydrolysis of PLGA copolymers in water.

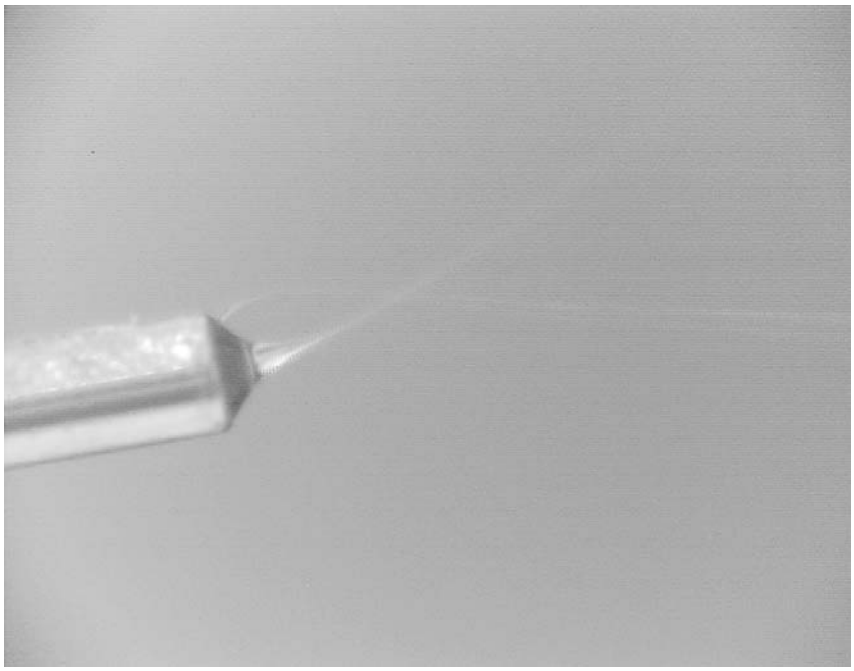

Figure 2.8. Taylor cone formed in the electrospinning process.

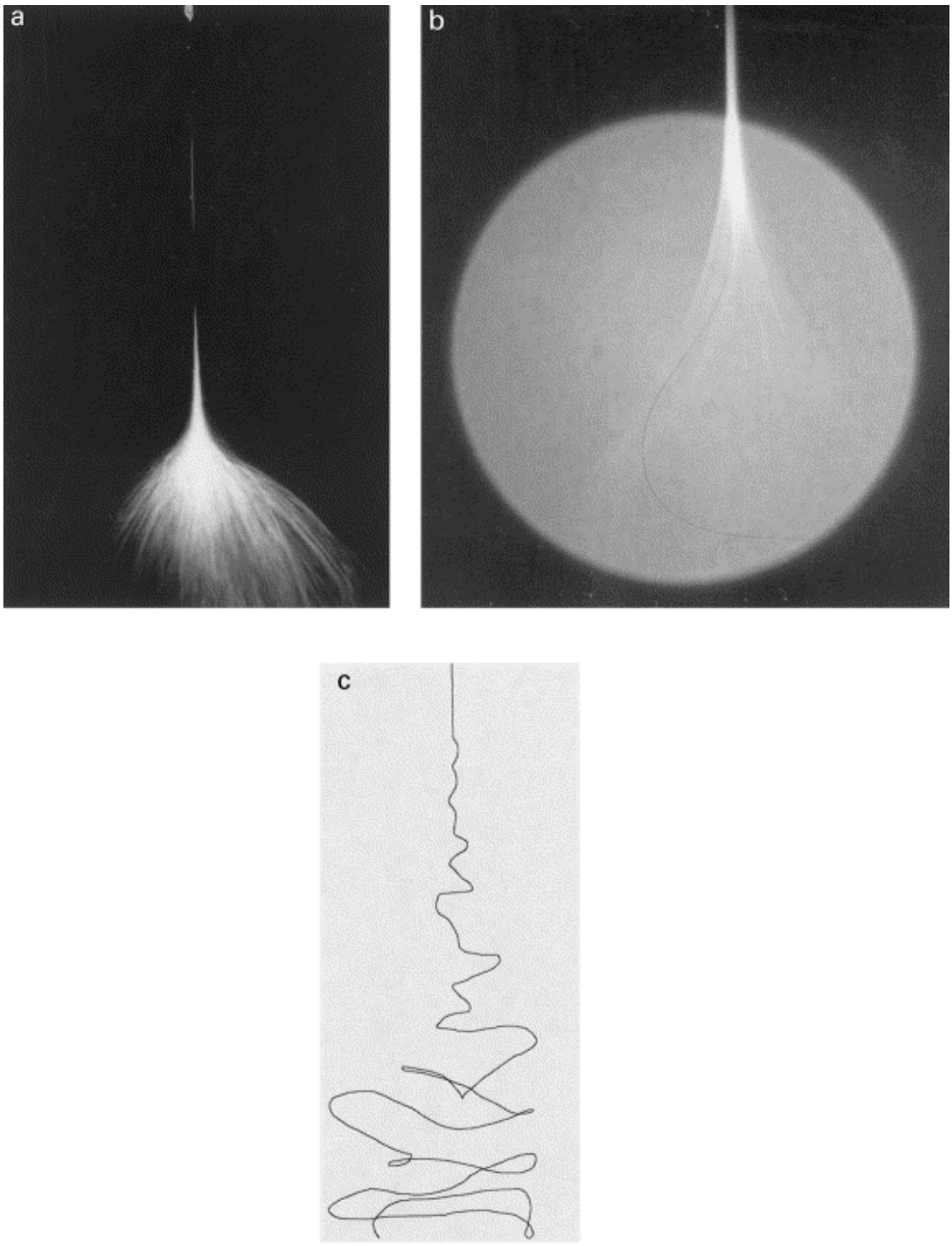

Figure 2.9. Instability region in an electrified PEO-water jet: (a) the whipping jet, (b) superposition of the whipping jet and the envelope, and (c) a trace of the jet in the entire instability region [80].

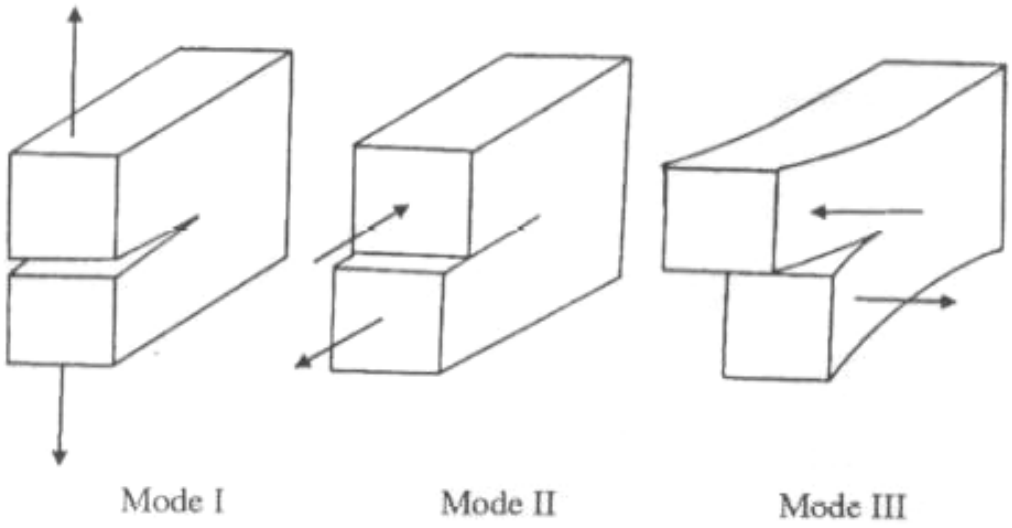

Figure 2.10. Three basic loading modes that give rise to different crack-tip displacements: Mode I (opening), Mode II (shearing) and Mode III (tearing) [143].

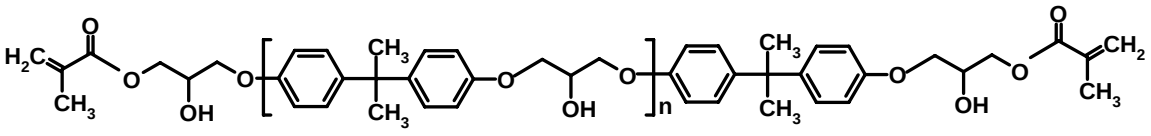

(a) vinyl ester monomer

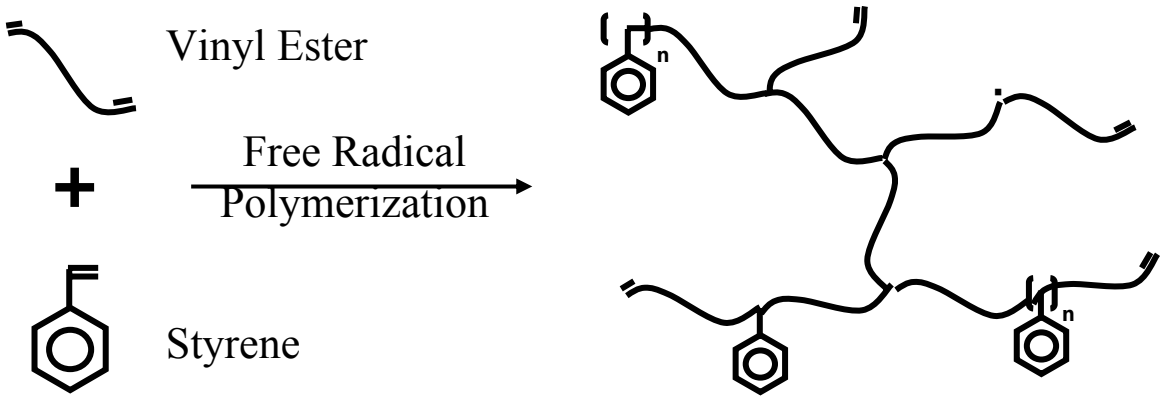

(b) cure chemistry of the vinyl ester-styrene system

Figure 2.11. (a) The chemical structure of vinyl ester monomer derived from diglycidyl ether of bisphenol A (DGEBA) and methacrylic acid, and (b) a crosslinked network of the vinyl ester-styrene system created by free radical polymerization.

Chapter 3: PLGA Synthesis and Electrospun Fiber Fabrication

The degradation rate of PLGA depends on molecular weight, copolymer composition, morphology, dimensions, processing history and environmental conditions. The environmental conditions normally cannot be adjusted for a particular application, but one can vary the properties of PLGA to obtain the desired degradation rate. A bulk ring-opening polymerization under a high-vacuum atmosphere is the preferred synthesis method due to its good reproducibility. Polymerization conditions, such as temperature, duration and additives, will be investigated for controlling the molecular weight and copolymer composition. Electrospun fibers were fabricated through the charged polymer solution traveling from the tip of a stainless steel needle to an aluminum collection plate in a high electrical field. Solvent, solution viscosity, traveling distance, polymer solution feeding rate, intensity of the electric field, humidity and needle gauge can affect fiber morphology. These electrospinning parameters will be investigated for controlling morphologies of electrospun fibers.

3.1. Experimental

3.1.1. Materials

Monomers, L-lactide and glycolide, PLA and polystyrene standards were purchased from Polysciences Inc. All other reagents were purchased from Sigma-Aldrich. Tin(II) 2-ethylhexanoate (stannous octoate ($SnOct_2$), 95%) was diluted in hexane to make an 8wt% solution for use as a catalyst. D,L-lactic acid (85wt% aqueous solution) was added as a chain terminator/initiator to control the molecular weight. Chloroform and methanol were used in the purification process. Tetrahydrofuran (THF) was the mobile

phase in a gel permeation chromatography and anhydrous deuterated dimethyl sulfoxide (DMSO_d_6) was the solvent in solution nuclear magnetic resonance (NMR) spectroscopy. N, N-dimethylformamide (DMF) was used as the electrospinning solvent. Commercial PLA (MW 20k-30k) and PLGA (LA/GA=65/35, MW 40k-75k) were used in the morphology study of electrospun fibers.

3.1.2. PLGA Synthesis

PLGA polymers were synthesized via bulk ring-opening polymerizations under a high-vacuum atmosphere. First, 20g of monomers having a certain molar ratio of lactide to glycolide were well-mixed in a round-bottom flask. After adding lactic acid and $SnOct_2$ solutions to the monomers, a magnetic stirring bar was added. The well mixed reactants were dried under a high vacuum (30mmHg) for at least 30 min before polymerization. Then, the reaction flask was sealed under vacuum and immersed in a silicon oil bath in which the temperature was controlled by a stirring hotplate with an external probe. After several hours of polymerization under constant temperature, the sealed reaction vessel was taken out of the oil bath and allowed to cool at room temperature. 200ml chloroform was then added into the flask to dissolve the polymerization products. The resulting homogeneous solution was poured into 1000ml of cold methanol to precipitate and purify the PLGA. Then, the purified PLGA was dried in a vacuum oven at 40^{o}C for 48 hours.

3.1.3. Electrospun PLGA Fibers Fabrication

The solution electrospinning technique was used to generate micro- or nanoscale fibers. A high voltage power supply provided high electrical fields between the tip of a stainless steel needle (18-gauge, 0.84mm in diameter) and an aluminum collection plate. The travel path was in a chamber with flowing air to keep an optimum humidity (%RH~10-15%) and humidity in the chamber was monitored by a traceable® hygrometer. The needle and syringe were connected via Teflon tubing. A syringe pump was used to precisely feed the polymer solution. The liquid droplet on the tip was observed through a PIXERA 1.2 million pixel digital camera system. Small amount of fibers were collected on the aluminum foil for studying fiber structures under different parameters. When the electrospun fibers were used in the subsequent degradation study or mechanical tests, releasable cloth was used to collect large amount of fibers. The typical electrospinning set-up is shown in Figure 3.1.

3.1.4. Characterization

Characterization of PLGA polymers was focused on the intrinsic viscosity of PLGA in chloroform solution, molecular weight (MW), polydispersity index (PI) and copolymer compositions. A Cannon Ubbelohde viscometer (size 0C) suspended in a water bath was used to measure the viscosity of PLGA in chloroform solution at room temperature. Concentrations used for viscosity measurements were 0.25, 0.5, and 1.0g/dl. Measurements of the MW and PI were performed on a gel permeation chromatography (GPC) using a Waters apparatus equipped with two styrene-divinylbenzene packing columns. A refractive index detector was used to analyze data. The mobile phase was

THF, and the polystyrene standards were used to generate the calibration curve. A PLGA solution with a concentration of 1mg/ml in THF solvent was normally used in GPC tests. GPC tests were conducted at a flow rate of 1 ml/min at 30°C. Copolymer compositions were determined by ^{1}H NMR on a Varian Unity Inova 300 Mhz instrument. Approximately 15 mg of PLGA polymers were dissolved in 1 ml DMSO_d_6. NMR spectra were acquired at 25°C using 64 scans and analyzed using Vnmr 6.1b software (Varian, Inc., Palo Alto,CA).

Fiber morphologies were studied using an environmental field emission scanning electron microscope (ESEM), Model XL30 ESE FEG, in high vacuum mode. An acceleration voltage of 1 keV was used in most cases. Samples were sputter-coated with platinum for 30 seconds prior to ESEM evaluation. XLDocu software was used to capture high-resolution ESEM pictures.

3.2 Results and Discussion

3.2.1. PLGA Synthesis and Characterization

PLGA polymers with different molecular weight and different copolymer compositions were synthesized by varying the amount of the chain terminator and the catalyst, the monomer ratio, polymerization temperature and duration. Polymerization temperature and duration need to be considered together for avoiding PLGA degradation during synthesis or prolonged reaction time. When the reaction temperature is too low, the polymerization is very slow or incomplete; when the reaction temperature is too high, polymers may degrade during synthesis. Therefore, we selected an intermediate reaction temperature of 160ºC for most of the polymerization study. There is also an optimum for

polymerization time. For a certain polymerization temperature, the molecular weight of polymer first increases with reaction time and then decreases due to the degradation becoming the dominant determining factor on the molecular weight. The amount of chain terminators added was based on the theoretical calculation of the desired molecular weight, such as 50,000 for PLGA 5-7. The amount of catalysts was chosen so we could accelerate the reaction.

Figure 3.2 gives an example of the typical GPC plot, differential refractive index as a function of retention time. The retention time can be converted to the molecular weight based on the calibration curve of polystyrene standards. Number-average molecular weight (Mn), weight-average molecular weight (Mw), and molecular weight distribution (MWD) or polydispersity index (PI) can be calculated from the converted GPC plot, differential refractive index as a function of molecular weight. Intrinsic viscosity of PLGA in chloroform solution at 22^{o}C water bath is extrapolated from the plot of the inherent or reduced viscosity *vs.* concentration as shown in Figure 3.3. The intrinsic viscosity is the inherent or reduced viscosity when the concentration approaches 0. A typical NMR spectrum of PLGA is given in Figure 3.4. The peak at a chemical shift of 2.5 is from protons on DMSO and the peak at 3.35 is contributed from H_2O. The peak at 5.2 is from protons on -CH, the peak at 4.9 represents protons on -CH_2, and the peak at 1.45 is contributed from protons on the side chain -CH_3. The composition of each group can be obtained from integrating the area under the peak.

Reaction conditions and properties of polymers are summarized in Table 3.1. It is obvious that more lactic acids or a shorter reaction time lead to lower molecular weights in the investigated range when comparing reaction conditions and polymer properties for

PLGA4-7. Copolymer compositions of synthesized polymers mainly depended on the molar ratio of monomers added to the reactants. The slightly lower LA composition in the polymer may be due to the higher solubility of PLA in the mixed solvent of chloroform and methanol, which may result in oligomers with high LA composition being washed out more than oligomers with lower LA composition during the purification step. The polymerization in the absence of lactic acids resulted in polymers that were not soluble in any solvents as in the case of PLGA1. Therefore, the molecular weight of PLGA should be within certain range in order to have practical usage. Results from PLGA2 and PLGA3 are not consistent with PLGA5, which might be due to the poorly controlled reaction conditions for PLGA2 and PLGA3.

3.2.2. Fiber Morphology Control during Electrospinning

Morphologies of electrospinning fibers can be affected by solution parameters or operation parameters. Solution parameters include viscosity, conductivity and surface tension while operation parameters include electric potential, feeding rate and distance between the tip and collection plate. Different morphologies, such as beads, beads-on-strings, or fibers, can be obtained by varying these electrospinning parameters. DMF was chosen as the electrospinning solvent because of its good electron conductivity, suitable vapor pressure at room temperature and high solubility for PLGA. Intensity of the electric field was chosen so that a stable Taylor cone was formed at the tip of the needle.

As the solution viscosity increases, by increasing polymer molecular weight or concentration, morphology can change from beads, to beads on strings, to thin fibers, then to thicker fibers as seen in Figures 3.5 and 3.6. The bead formation is due to the

surface tension contracting the fibers into spheres if the fibers are still wet when they reach the collection plate. The viscosity of polymer solution has upper and lower bounds for fiber formation. If the viscosity is too low, a continuous polymer stream in the electrical field cannot be formed. If the viscosity is too high, the repelling force of the static electrical charges cannot overcome the surface tension of the polymer droplet at the needle tip to form submicron-sized fibers.

Shorter traveling (tip-to-plate) distances favor bead formation, but longer traveling distances favor fiber formation. Intermediate distances can lead to beads-on-strings morphology (Figure 3.7). Distances within the investigated range do not have significant influence on the diameter of fibers as long as fibers are completely dry before they reach the collection plate, i.e. free of beads formation (Figure 3.8).

Theoretically, the faster the polymer is fed, the thicker the fibers should be. The voltage has to be increased to maintain a stable Taylor cone when the feeding rate is increased. The increased voltage may cause the fibers to be thinner due to the increased repelling force of the static electrical charge, so the effect of the feeding rate is not as obvious as the viscosity change as seen in Figure 3.9. If the feeding rate is so fast that fibers are not dry when they deposit on the collection plate, fibers may become beads under surface tension. Figure 3.10 shows that bigger spindles are formed under faster feeding rates.

3.3 Chapter Summary

PLGA copolymers were synthesized via a bulk ring-opening polymerization under a high-vacuum atmosphere for better reproducibility and higher molecular weight

polymer formation. A polymerization temperature of 160^{o}C was chosen to avoid the possible degradation of synthesized polymers but still complete the reaction in a reasonable time. In general, reducing lactic acid or slightly extending the reaction time can obtain higher molecular weight. However, if the reaction time is too long at a high polymerization temperature, synthesized polymers start to degrade. Copolymer compositions mainly depend on the initial ratio of monomers, but LA composition is slightly lower than the initial value.

The electrospinning technique is a simple and unique technique for fabricating submicron fibers, which are formed by the repelling force of the static electrical charges on the polymer droplet traveling in a high electrical field. Lower molecular weights or lower glycolic acid contents make polymer processing easier because of their higher solubility in solutions. In order to form fibers, the molecular weight has to be high enough to provide suitable viscosity. Furthermore, higher molecular weight can produce more uniform fibers when the polymer solution is within a suitable viscosity range for electrospinning. Longer distance is preferred for fiber formation, but space limitation or the output voltage of the power supply is also a consideration. Slower feeding rates can produce thinner and more uniform fibers at the expense of time. The best combination to obtain uniform fibers is to use a PLGA polymer with medium molecular weight (20000~50000) but a polymer concentration close to the upper limit.

Table 3.1: Summary of reaction conditions and polymer properties of PLGA synthesized.

	LA/GA molar ratio	$SnOct_2$ wt % of total monomers	Lactic acid mol % total monomers	Reaction condition ^oC, hours	Intrinsic viscosity dl/g	Mw	Mn	PI
PLGA1	50/50	0.03	0	180, 4.5	—	—	—	—
PLGA2	85/15	0.1	0.28	160, 5	0.43	14300	4900	2.9
PLGA3	85/15	0.1	0.3	160, 5	0.31	11800	3600	3.3
PLGA4	85/15 (83/17)*	0.1	0.14	160, 5	0.81	89600	36000	2.49
PLGA5	85/15 (83/17)*	0.1	0.28	160, 5	0.55	59900	25300	2.37
PLGA6	85/15 (83/17)*	0.1	0.28	160, 6	0.68	69600	27600	2.52
PLGA7	50/50 (45/55)*	0.1	0.26	160, 6	—	75700	22500	3.37

* molar ratio of LA/GA obtained from NMR

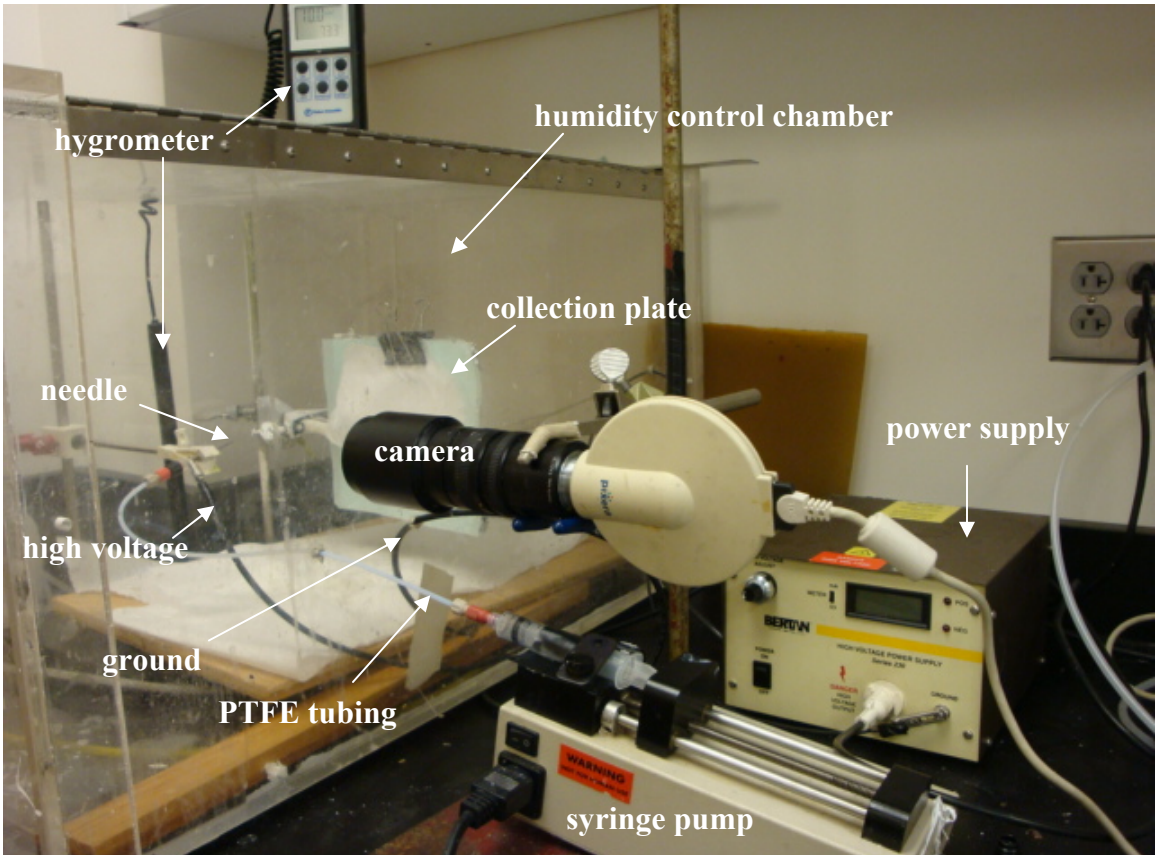

Figure 3.1. Electrospinning apparatus setup.

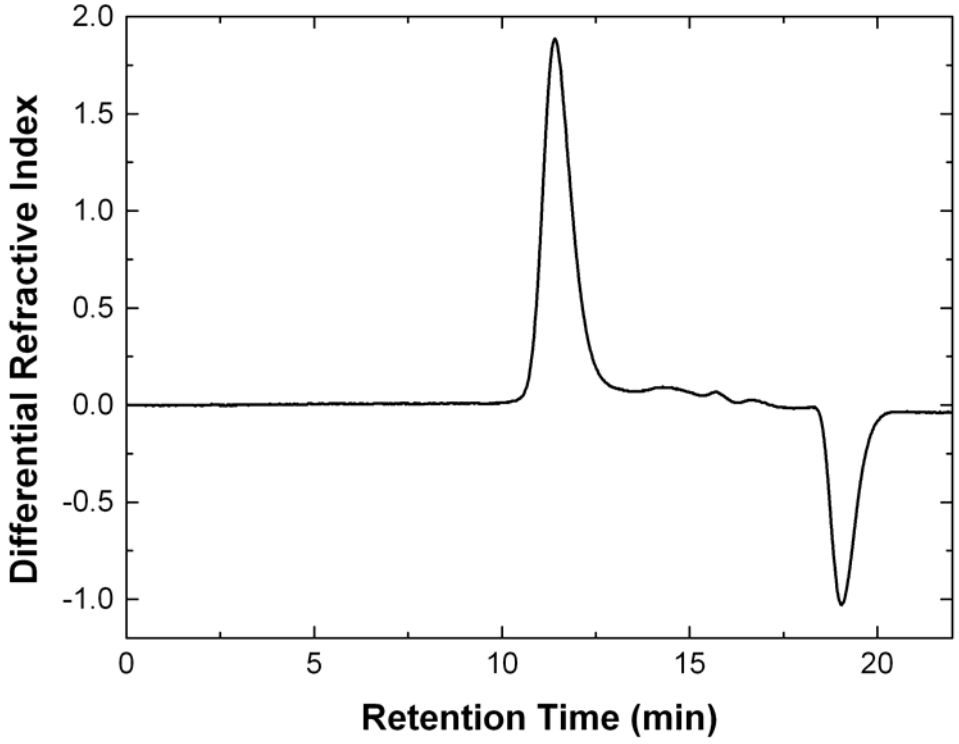

Figure 3.2. A typical GPC plot of PLGA. The positive peak represents PLGA.

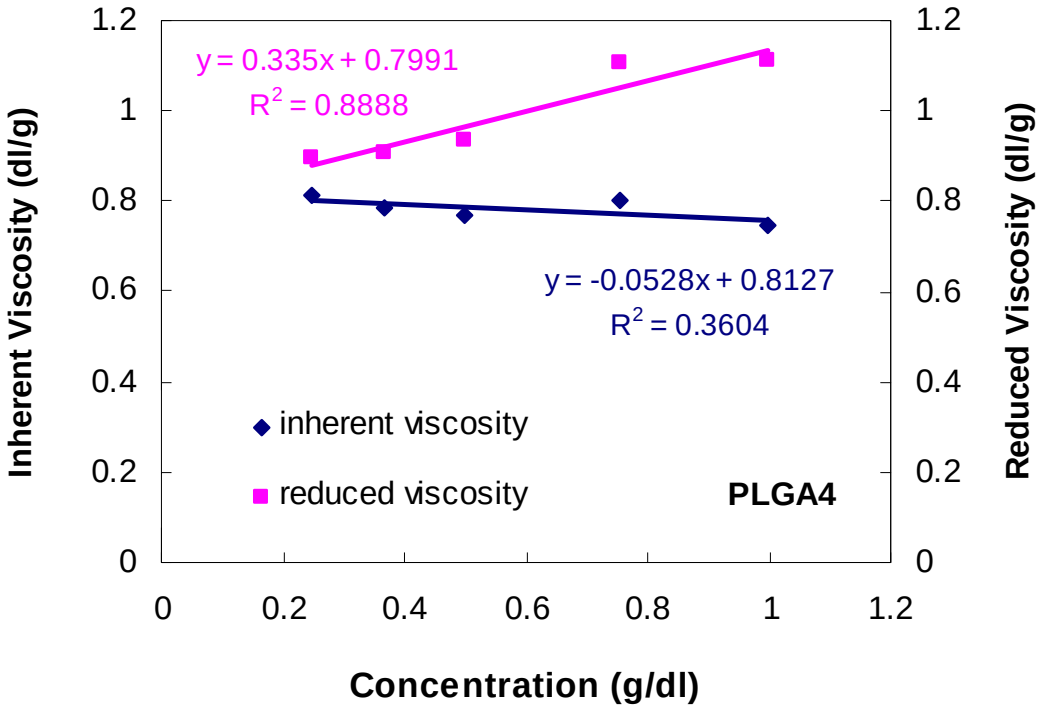

Figure 3.3. Intrinsic viscosity calculation by extrapolating the inherent or reduced viscosities to the concentration approaching zero.

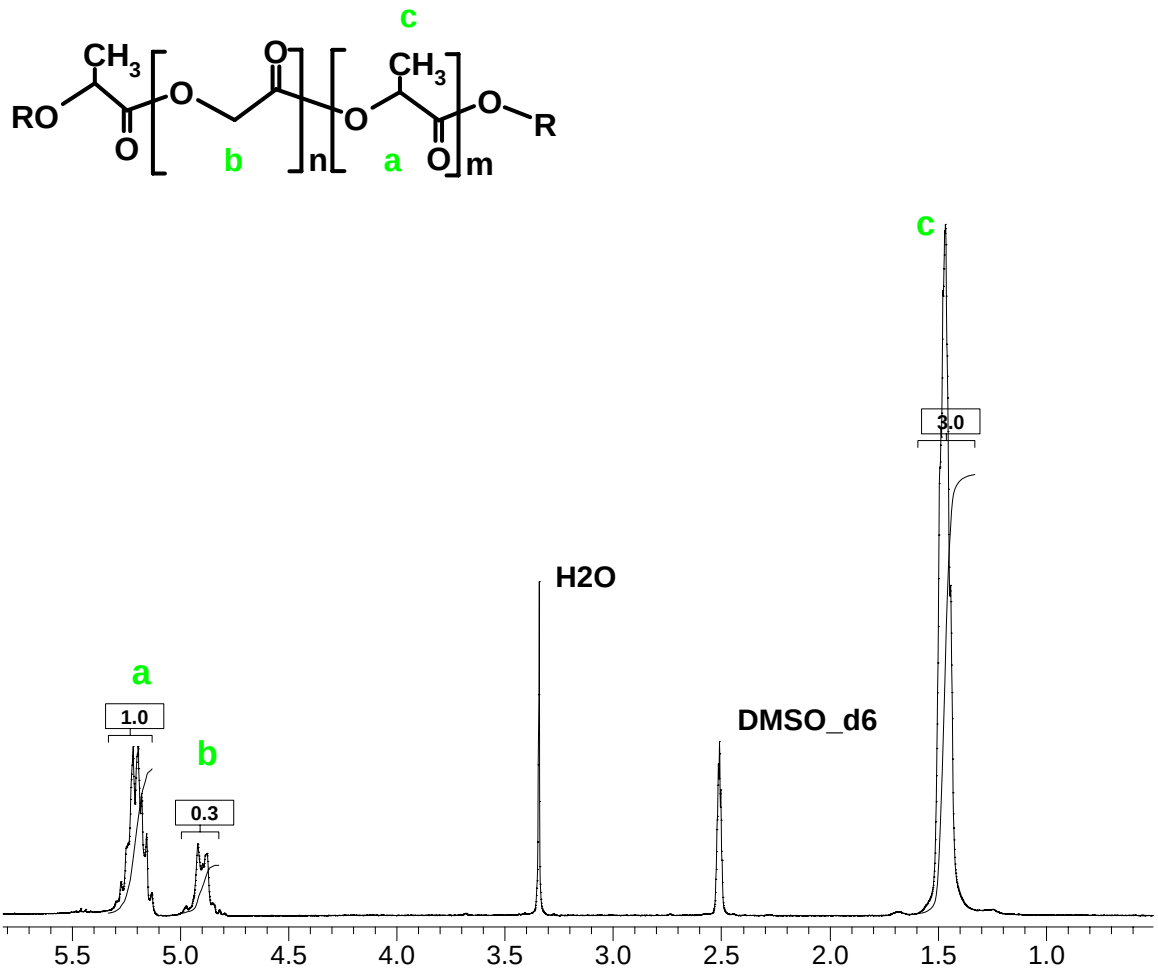

Figure 3.4. ^{1}H NMR spectrum of PLGA in DMSO_d_6 solution.

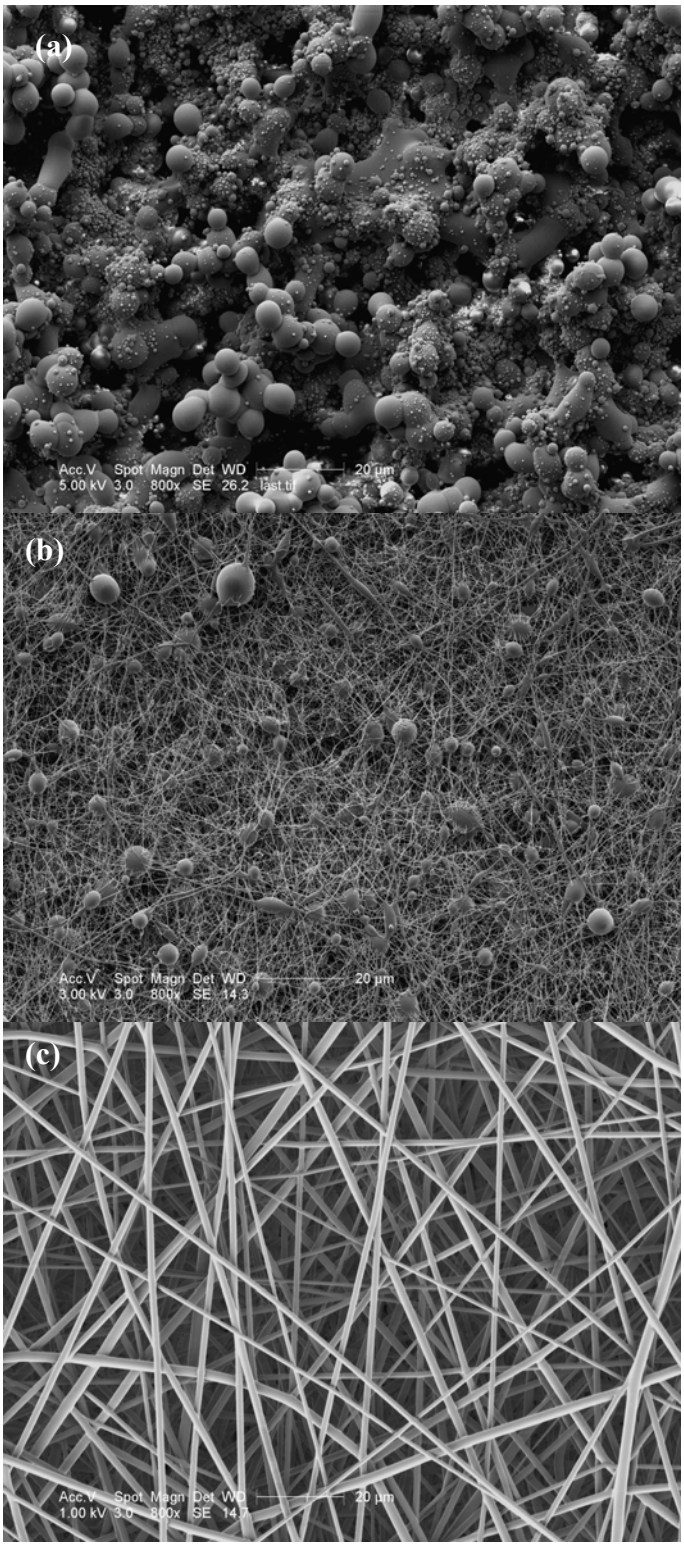

Figure 3.5. Concentration effect on morphologies of electrospun PLA (MW 20k-30k) membranes at a feeding rate of 1.2 ml/hr, tip-to-plate distance of 12.5 cm, and concentration of (a) 30wt% (11.2kV), (b) 40wt% (18.1kV) and (c) 50 wt% (11.9kV).

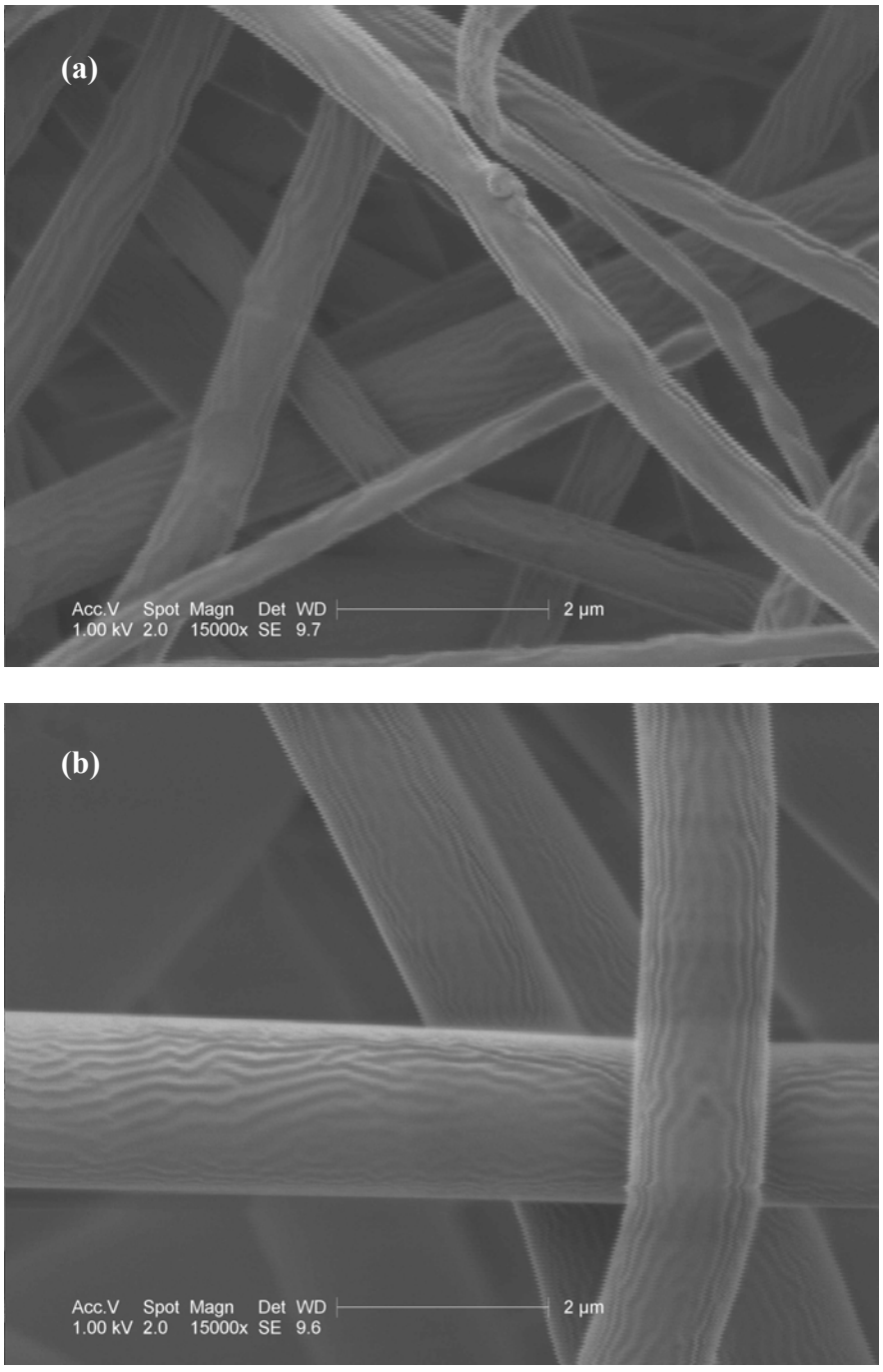

Figure 3.6. Concentration effect on morphologies of electrospun PLGA6 (LA/GA=85/15, Mw 69600) membranes at a feeding rate of 1.0 ml/hr, tip-to-plate distance of 21 cm, voltage of 14.4 kV and concentration of (a) 40% (b) 45 wt%.

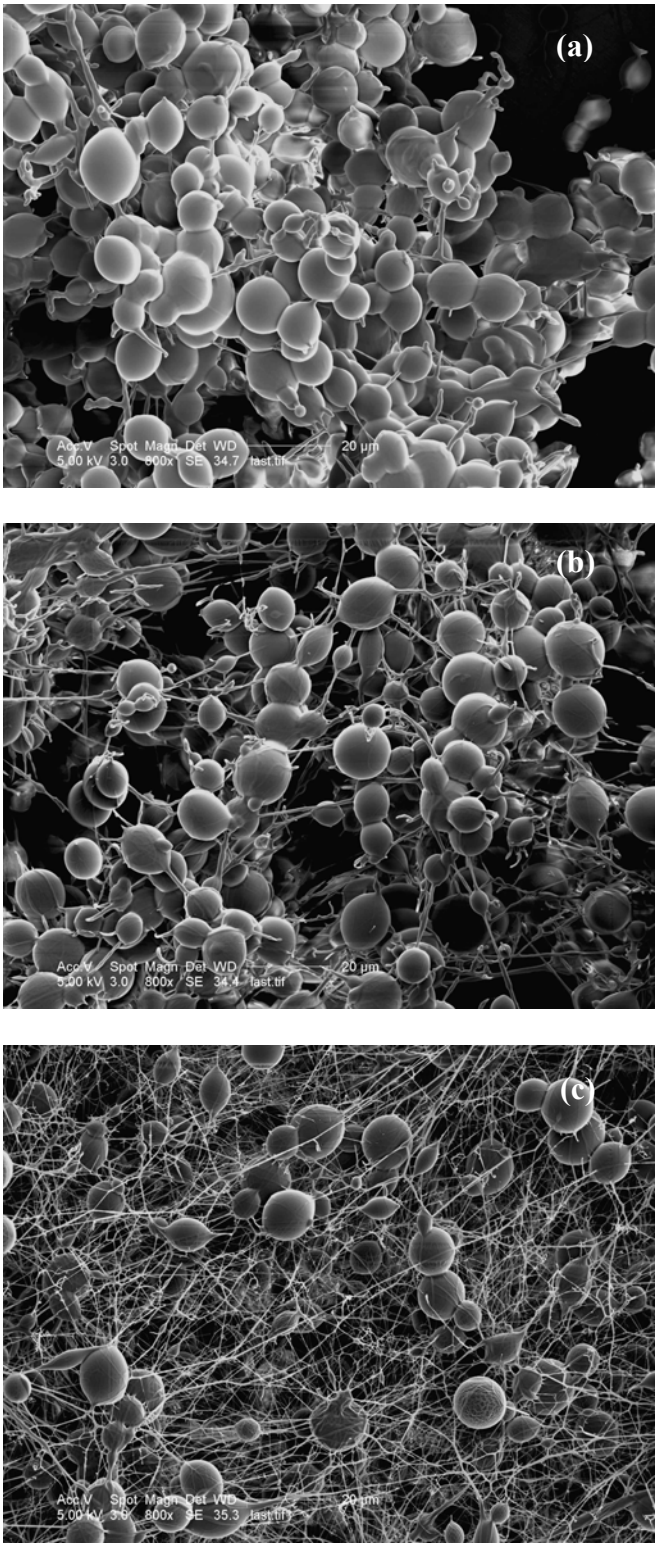

Figure 3.7. Tip-to-plate distance effect on morphologies of electrospun PLGA (LA/GA=65/35, MW 40k-75k) membranes at a feeding rate of 1.2 ml/hr, concentration of 35wt%, and distance of (a) 12.3 cm (11.5kV), (b) 13.5 cm (12kV) and (c) 15cm (14kV).

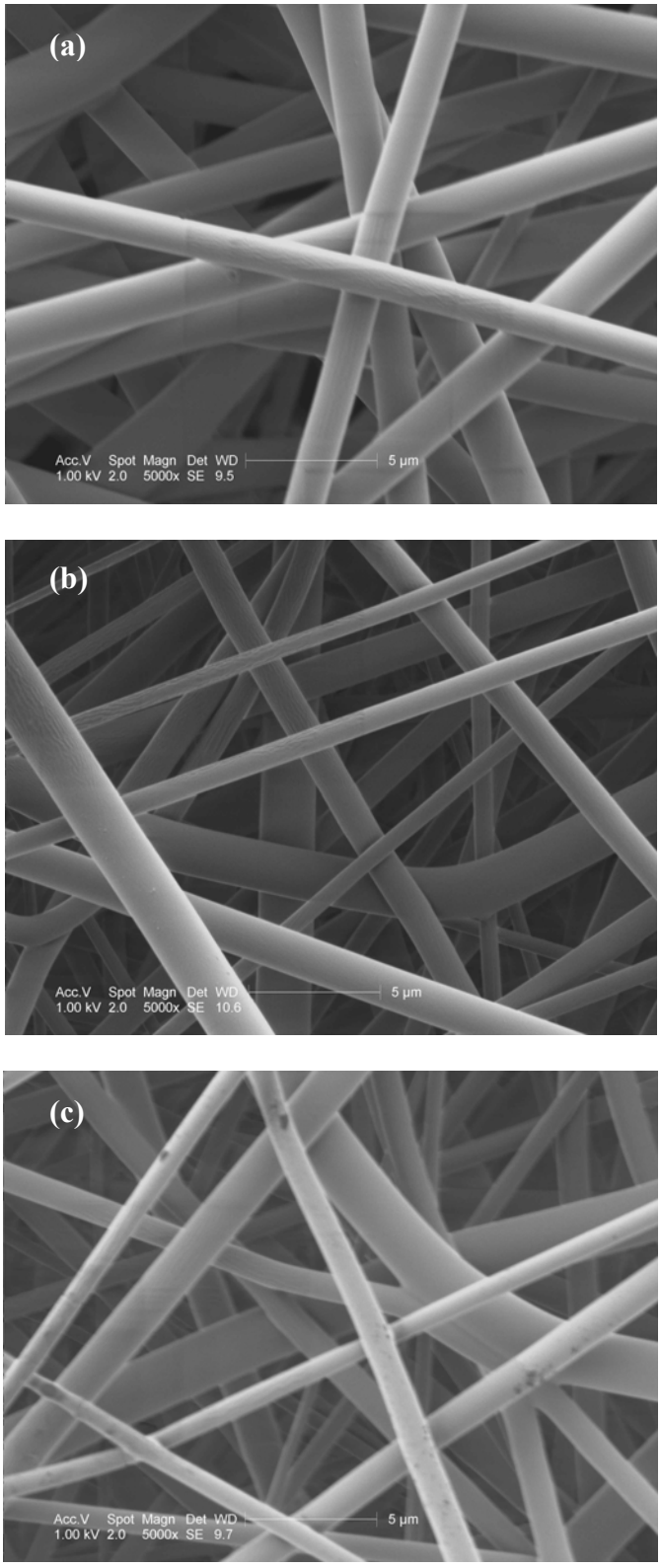

Figure 3.8. Tip-to-plate distance effect on morphologies of electrospun PLGA#2 (LA/GA=85/15, Mw 14500) membranes at a feeding rate of 1.2 ml/hr, concentration of 50wt%, and distance of (a) 8.5 cm (9.5kV) (b) 12.5 cm (12kV) and (c) 16.5 cm (12.5 kV).

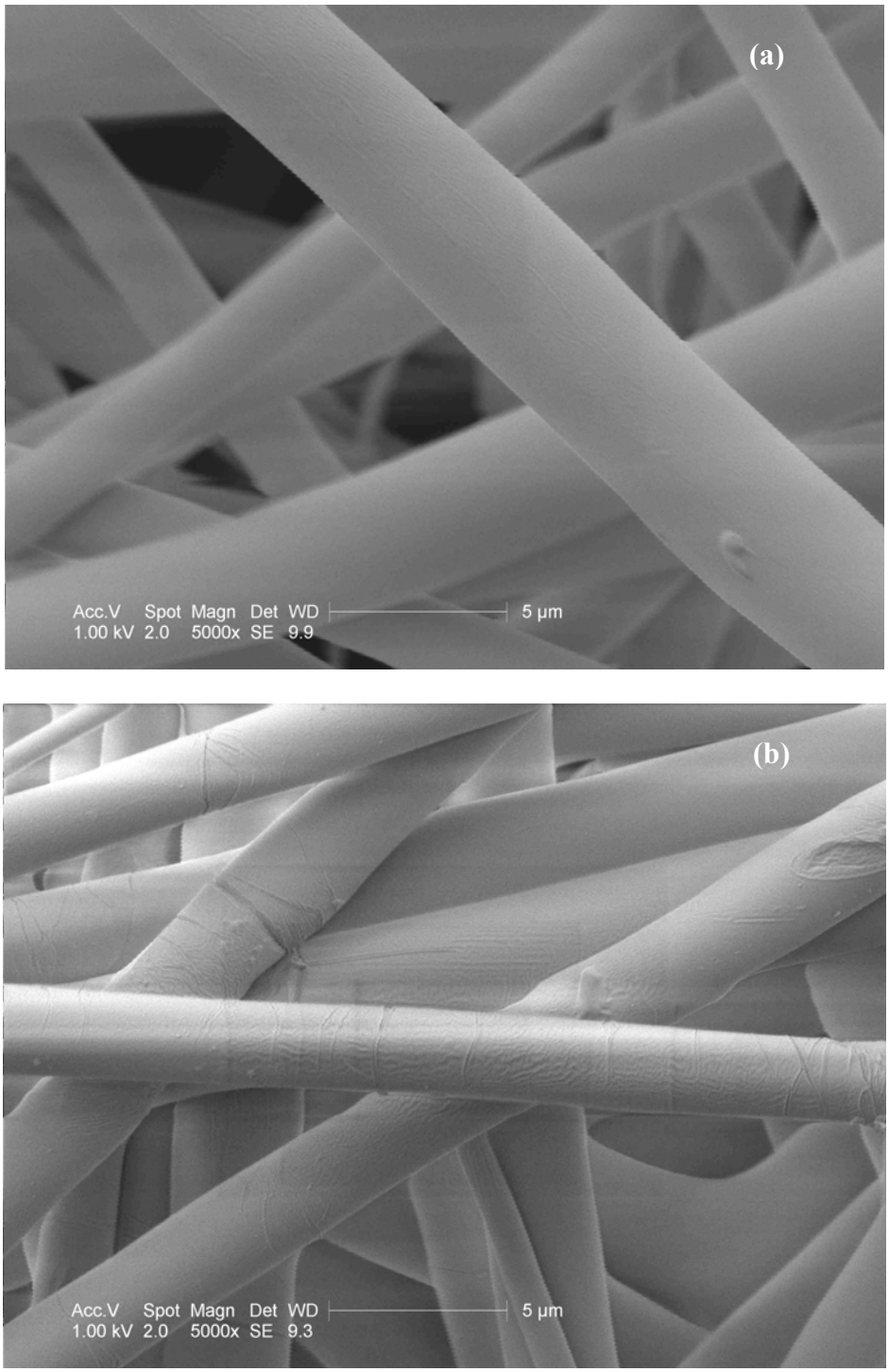

Figure 3.9. Feeding rate effect on morphologies of electrospun PLGA4 (LA/GA= 85/15, Mw 89600) membranes at a distance of 21 cm, concentration of 40wt%, and feeding rate of (a) 0.8 ml/hr (V = 14.9 kV) (b) 1.6 ml/hr (V = 16.3 kV).

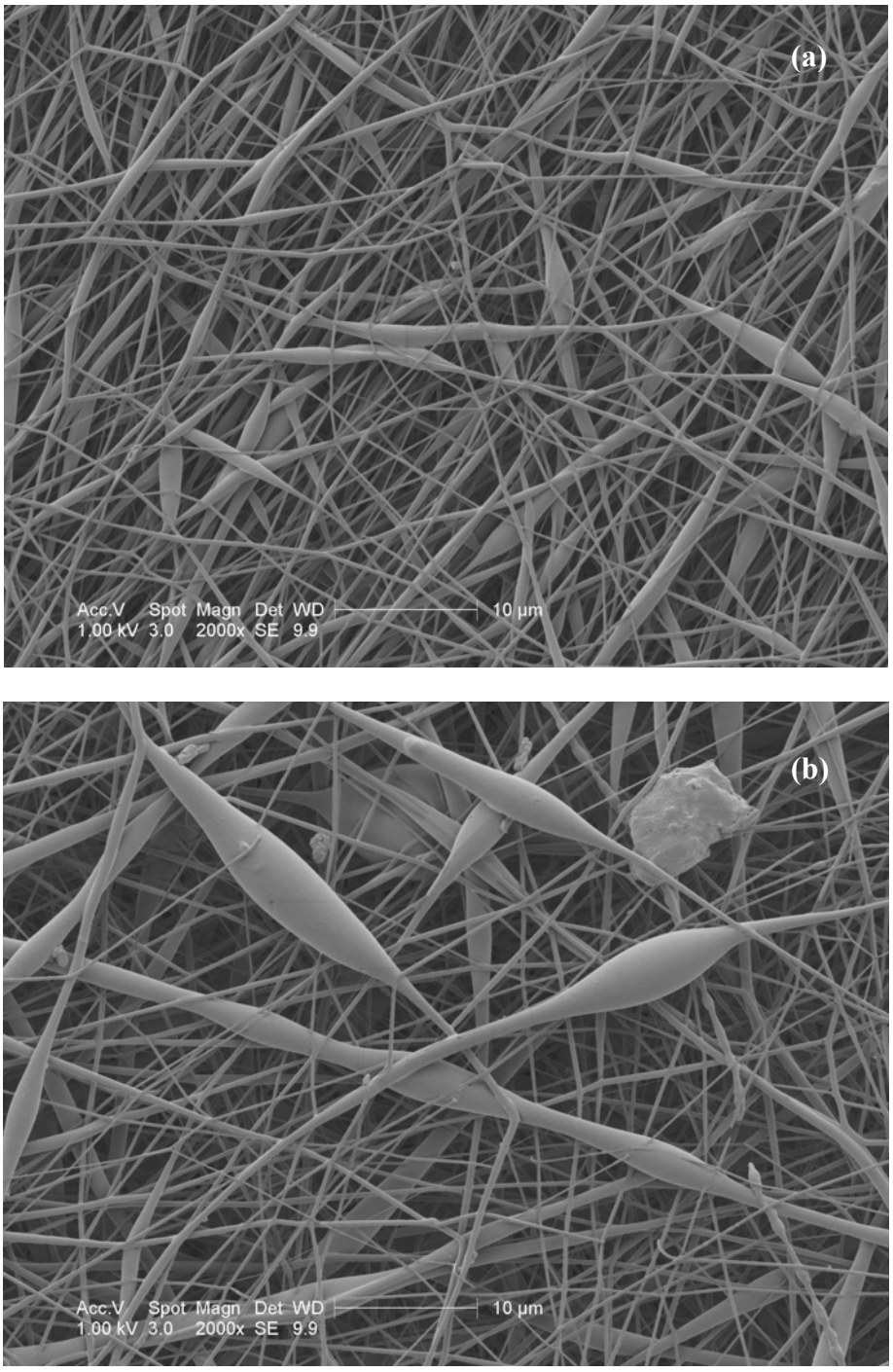

Figure 3.10. Feeding rate effect on morphologies of electrospun PLGA7 (LA/GA= 50/50, Mw 75700) membranes at a distance of 21 cm, concentration of 31wt%, and feeding rate of (a) 0.1 ml/hr (V = 12.5 kV) (b) 0.6 ml/hr (V = 19.7 kV).

Chapter 4: *In vitro* Degradation of PLGA Fibers and PLGA-PVA Composites

Release of therapeutic drugs, especially macromolecules such as proteins, from biodegradable polymers strongly depends on the erosion rate. Therefore, it is important to understand the degradation behavior of PLGA at body conditions. Degradation of PLGA depends on molecular weight, copolymer composition, dimension, crystallinity, morphological structure and incubation conditions (temperature, humidity, pH, solutes and macromolecules such as enzymes.

You et al. found that hydrolytic degradation first occurred in the amorphous regions and then in the crystalline regions [1]. Lower molecular weights and higher glycolide compositions favor water uptake for amorphous PLGA, which increases the degradation rate [2]. Autocatalysis of ester bonds by the degraded byproducts is negligible in the electrospun fibrous membranes because the small dimensions of nanofibers create a short diffusion path for degraded byproducts [3]. When PLGA fibers degrade slower than their water uptake rate, the intrinsic degradation kinetics is obtained. This can be satisfied when we have nanoscale fibers. The intrinsic degradation rate is independent of sample dimensions. A study on PLGA spherical particles showed that the degradation rate increased with increasing sample diameters in the range of 0.53-43 μm [4]. For sample dimensions in the submicron range, the influence of dimensions or morphologies on the degradation behavior has not been reported. It is also beneficial if a cutoff dimension for the intrinsic degradation rate can be determined.

To maintain the mechanical integrity of the drug delivery device, we proposed to embed the electrospun PLGA fibers in the PVA matrix. The matrix may affect the drug

release rate and degradation byproducts removal. Therefore, it is important to study how the degradation behavior of PLGA fibers changes after being incorporated in the PVA matrix.

In this chapter the *in vitro* degradation study is mainly conducted in the phosphate buffered saline (PBS) solution at 37^{o}C and pH 7.4. Factors such as the molecular weight, copolymer composition, fiber diameter, sample dimensions and PVA matrix, are investigated. Morphology change during the degradation is also studied. Finally, a degradation model is developed for the fiber system and the fiber-hydrogel composite system.

4.1. Experimental

4.1.1. Materials

A commercial PVA, Elvanol grade 71-30 (DuPont), was used in this work. It is 99% hydrolyzed and molecular weight is 113,000. PLGA synthesized in the lab and a commercial PLGA were used in the degradation study. The commercial PLGA, 5050 DLG 4A (Lakeshore Biomaterials), has a LA/GA ratio of 50/50 and an inherent viscosity of 0.35-0.45 dl/g with acid end groups. PLGA4A was used to refer to this commercial PLGA. Dulbecco's phosphate buffered saline (PBS), dichloromethane (DCM) and dimethyl sulfoxide (DMSO) were purchased from Sigma-Aldrich.

4.1.2. Sample Preparation

In the *in vitro* degradation study, electrospun mats were cut into small pieces that weighed about 20mg. After the dry weight for each piece was measured, the individual

samples were put in vials containing 30 ml PBS solution and incubated in a water bath. The temperature of the water bath was controlled to 37^{o}C and the pH of the buffer was kept near 7.4 by refreshing the PBS every two days. At scheduled time intervals, triplicate samples for each condition were removed from the buffer, rinsed with deionized water, and dried in a freeze dryer for two days. The dry weights of hydrolyzed samples were recorded.

The PVA aqueous solution of each desired concentration was prepared at 120^{o}C in an autoclave for half an hour and then allowed to cool at room temperature. Electrospun fibrous mats were cut into small pieces similar to what were used in the fiber degradation study, and their dry weights were measured. The PLGA mats were pre-wet with PVA solutions by using compression to drive the air out. Then the wet mats were placed between two glass slides with Teflon spacers, and the PVA solution was added between the slides using a disposable pipette. The mixture in the mold was sealed and exposed to five cycles of freezing at -20^{o}C for 24 hours followed by thawing at room temperature for one hour. The resulting hydrogel composites were frozen at -20^{o}C and dried in a freeze dryer for 48 hours. After the dry weights of composites were measured, they were used in the degradation study following the same procedure as for the fiber mats.

PLGA films were cast by dissolving PLGA in DCM, allowing the DCM to evaporate under a nitrogen blanket overnight, and then drying the films by compressing them between two glass slides at ambient temperature under vacuum for two days. The thickness of the PLGA film was about 1-2mm. A degradation study of PLGA films was conducted using the same procedure as for the fiber mats.

4.1.3. Characterization

The dry weights before and after degradation of incubated samples were used to calculate the percent dry weight loss of PLGA. Percent shrinkage of samples was calculated according to the reduction of the 2-D surface area of the mat using the following equation:

$$\%shrinkage = \frac{(initial\_surface\_area) - (surface\_area\_after\_incubation)}{(initial\_surface\_area)} \times 100\%$$

Molecular weights and molecular weight distributions of the intact and hydrolyzed samples were measured using GPC. Because the PVA hydrogel did not swell or dissolve in THF, PLGA-PVA composites were dissolved in a small amount of DMSO and then excess THF was added to precipitate PVA. The filtrated THF solution containing PLGA was used in GPC tests. Change of copolymer compositions during degradation was analyzed with NMR using DMSO_d_6 as a solvent. Morphological change of fibers, composites and films during degradation were observed under ESEM. Detailed descriptions of GPC, NMR and ESEM are found in Chapter 3.

A TA Instruments DSC Q2000 differential scanning calorimeter (DSC) was used to determine the glass transition temperature (T_g) under N_2 flow. Sample sizes were about 3 mg. Temperature scans were performed from -50°C to 200°C at a heating/cooling rate of 10°C/min.

ESEM micrographs of dry samples were obtained using the procedure described in Chapter 3. Wet PLGA-PVA samples were observed under wet mode using ESEM at an acceleration voltage of 15 KeV. A cooling stage was used to keep the sample cool and wet.

Optical microscope images were taken using a thin slice of PLGA-PVA composites for better light transmission. The composites were frozen and sliced into 20 μm thicknesses using a cryo-microtome.

4.2. Results and Discussions

4.2.1. *In vitro* Degradation Behavior of Electrospun PLGA Fibers

Degradation of PLGA depends on molecular weight, copolymer composition, temperature, humidity, pH, dimension and morphology. In the preliminary study, fibers electrospun from PLGA polymers with a LA/GA molar ratio of 85/15 were used. Because of the slow degradation rate at that copolymer composition, approximately 2-3% weight loss was observed after those PLGA fiber mats were incubated in water at 37°C for 10 weeks. PLGA7 was then synthesized and used for the degradation study. The molar ratio of 50/50 and the theoretical molecular weight of 50,000 were chosen so that the polymer would offer a faster degradation rate but still have good solubility in common solvents. The preliminary study on PLGA7 fibers showed about 80% weight loss after 5 weeks of incubation in water at 37°C. When the same PLGA7 fibers were soaked in an acidic solution (0.1 M HCl aqueous solution), the degradation significantly slowed down. Other research groups also found that PLGA degrades faster in a basic environment than in an acidic environment [5-6]. Burgess et.al. thought that the low solubility of acidic oligomers at pH lower than the pKa value of lactic acid, 3.8, drove the formation of crystalline oligomeric units and slowed down the erosion rate [6]. Since the application is in a neutral environment, the rest of the degradation study was conducted in a PBS buffer with a constant pH of 7.4 at body temperature.

4.2.1.1. Degradation of Electrospun PLGA7 Fibers

Five fiber mats electrospun from PLGA7, labeled from H16 to H20 as shown in Figure 4.1, were used in the degradation study to investigate if the size and morphology of fibers would have any influence on the degradation rate. Details of electrospinning parameters and corresponding fiber diameters are listed in Table 4.1. Diameters of fibers and spindles became smaller in the order of H16 to H20 when the polymer concentration or feeding rate used in the electrospinning process was reduced. PLGA7 electrospinning solutions with concentrations higher than 35 wt% could not be obtained due to the solubility limitation.

Morphology of PLGA7 fibers changed under incubation conditions. ESEM images of dried fiber mats showed that individual fibers swelled and relaxed, which reduced voids and resulted in the mat shrinking as seen in Figure 4.2b-c. Significant amounts of Nano-pits appeared on the fibers after incubation for two weeks as shown in Figure 4.2c, which indicated that erosion had begun. The weight loss of each of the five fiber mats during degradation is compared in Figure 4.3, and no significant difference in the degradation rate was observed for different fiber morphologies. Additionally, significant weight losses were observed starting from two weeks of incubation. Unfortunately, molecular weights of degraded PLGA7 fibers couldn't be obtained because they only partially dissolved in THF, possibly due to the crystallite formation from the short polymer chains having high GA compositions during degradation.

4.2.1.2. Degradation of Electrospun PLGA4A Fibers

PLGA4A was used for the remainder of the study. Three electrospun PLGA4A fibers were obtained by varying the polymer concentration of the electrospinning solution as shown in Figure 4.4a-c. Each fiber is labeled according to its PLGA concentration during electrospinning, i.e. 4A_45, 4A_40 and 4A_35. Details of electrospinning parameters and corresponding fiber sizes are listed in Table 4.2.

Similar to PLGA7 fibers, swollen dry fibers and reduced voids were observed under incubation conditions (Figure 4.4d-f). Nano-pits started to appear at some fiber surfaces after one week of degradation. By the end of two weeks nano-pits almost covered the entire fiber surface as shown in Figure 4.5 a-c. The pits increased in size, and the fiber mats got more and more fragile as degradation proceeded. PLGA fibers showed larger pits and a clear sign of surface erosion after five weeks of incubation (Figure 4.5 d-f).

Weight loss of all PLGA4A fibers showed a similar trend. Significant weight loss happened after two weeks of incubation as seen in Figure 4.6. The weight-average molecular weight (Mw), number-average molecular weight (Mn) and polydispersity index (PI) of different fibers were also similar during degradation as shown in Figure 4.7a-b. Molecular weight decreased quickly during the first two weeks but then slowed down thereafter. Polydispersity index increased with incubation time due to the random breakdown of polymer chains. This degradation profile is probably due to the auto-catalysis by the accumulated acidic degradation products inside fibers and the percolation phenomena [5]. Hydrolysis rate is slower than the water uptake rate at the studied sample dimension so the PLGA polymers go through bulk erosion, given that the critical

diffusion length for bulk erosion changing into surface erosion is 10^{-1}m [5]. The degradation is then accelerated by the acidic end groups of broken ester chains inside fibers. The fiber surface has a lower degradation rate because the incubation buffer can quickly neutralize the acidic groups [7]. Thus monomers and oligomers accumulate inside fibers, greatly increasing the hydrolysis rate (molecular weight decreases) but limiting the erosion rate (weight loss). When a critical osmotic pressure from the accumulated degradation products builds up inside the fiber, the surface layer breaks. According to the percolation phenomena, release of monomers and oligomers happens only after a network of pores forms. The porous network allows faster diffusion of neutral PBS buffer into the fibers to neutralize the acidic groups, so hydrolysis gradually slows down. As a result, significant weight loss is observed and the molecular weight of the remaining polymer changes very slowly after the critical period, about two weeks in our study. This hypothesis is confirmed by the morphologies of the fiber surface and fiber cross section shown in the ESEM images in Figure 4.8. PLGA fibers before incubation exhibit smooth surfaces and solid cross sections (Figure 4.8a). After nine days of incubation, a highly porous structure is observed at the fiber cross section but the fiber surface shows signs of surface etching with much lower porosity (Figure 4.8b).

One difference between PLGA7 and PLGA4A is that PLGA7 degrades faster than PLGA4A, with 90% weight loss after six weeks for PLGA7 but only 65% weight loss after eight weeks for PLGA4A as shown in Figure 4.9a. This is mainly due to a higher LA composition of PLGA4A (0.53) than that of PLGA7 (0.45) (Figure 4.9b). Figure 4.9b also shows that LA composition increases with degradation extent for both PLGAs, which indicates that the GA component degrades faster than the LA component.

4.2.1.3. Glass Transition of PLGA

Glass transition of PLGA changes with processing history, humidity and degradation as shown in the DSC thermograms in Figure 4.10. As-received PLGA4A powders have a glass transition temperature (T_g) near 50°C and the small endothermal peak at T_g indicates some extent of orientation. T_g of the electrospun fibers is almost the same except that the endothermal peak becomes sharper and larger, indicating an increased orientation after electrospinning. After two weeks of incubation, the endothermal peak becomes smaller due to relaxation under incubation conditions but T_g stays almost the same. After three weeks of incubation, the glass transition becomes very broad, possibly due to the broadening of molecular weight distribution and loss of orientation. The reduced onset T_g may be attributed to the increased free volume of the porous matrix and increased amount of low molecular weight degradation products. When water is added into the PLGA4A fibers, the glass transition of PLGA is overlapped with a wide water evaporation peak and T_g is reduced to near 30°C indicated by the shoulder at the wide peak. This can explain the relaxation of fibers and shrinking of mats under the incubation temperature, which is higher than the T_g of wet PLGA. The reduced T_g during incubation may facilitate the release of degradation products into the incubation medium by increasing their mobility inside PLGA. The glass transition of solvent-cast PLGA films is shown as a step without the endothermal peak, and the corresponding T_g is near 12°C. The lower T_g and lack of orientation may affect the degradation behavior.

4.2.2. *In vitro* Degradation Behaviors of PLGA Fibers Embedded in PVA Hydrogels and Solvent-Cast PLGA Films

PLGA fibers are embedded in PVA hydrogels in the potential drug delivery application, so the degradation of PLGA can be affected by hydrogels. The same degradation study was performed on PLGA4A fibers encapsulated in hydrogels to investigate the influence of the hydrogel matrix on the degradation behavior. .

PLGA4A fibers encapsulated in PVA matrices show little swelling, relaxation or void reduction under incubation conditions, to a much lesser extent than fibers without PVA as seen in Figure 4.11 a-b. Nano-pits can be observed on the fibers not being covered by PVA after two weeks of incubation (Figure 4.11c). The dimension of the fiber mat did not change after encapsulation in PVA gels (Figure 4.12a). After being incubated in PBS buffer at 37°C for two days, the composite was slightly wrinkled and its dimension was reduced a little. On the other hand, the PLGA fiber mat showed greatly reduced dimensions and uneven surfaces at the same incubation conditions. Shrinkage of all fiber mats and composite films is compared quantitatively in Figure 4.12b. It is obvious that the size of fibers has little influence on the mat shrinkage, but PVA matrices greatly reduce the shrinkage from 85% to 30% by anchoring fibers in the matrix.

PVA hydrogels can lose up to 10% of their original dry weight during incubation and the amount of weight loss is random depending on the individual sample, which makes it difficult to obtain weight loss from PLGA alone. It is found that weight loss of PVA hydrogel happens mostly on the first day of incubation at 37°C. Therefore in the weight loss study, dry weights of the composites after one day of incubation were measured. Those values were taken as the initial weights of the composites. Here we

assume that all weight loss from the PVA hydrogel happens after one day and no weight loss is contributed by PLGA in the first day of incubation. Figure 4.13 represents the normalized weight loss of three PLGA4A fibers embedded in PVA hydrogels during *in vitro* degradation in PBS buffers up to eight weeks. Again, all three fibers exhibit similar weight loss curves.

Average weight loss of PLGA4A after up to eight weeks of incubation for three fiber mats, three fiber-PVA composites and PLGA films are compared in Figure 4.14a. The thick PLGA film was investigated to provide evidence that the dimensions of PLGA will affect degradation behavior if they are significantly larger than the nanofibers. Fibers in their free form have similar erosion curves but slightly slower weight loss rates from the second week compared to fibers inside the PVA. Nevertheless, films exhibit a much faster erosion rate from the first week, which is also confirmed by nano-pits appearing on degraded films during the first week as shown in Figure 4.15. The molecular weight change for fibers both with and without a PVA matrix is similar, but films show a faster decrease in molecular weight as shown in Figure 4.14b. PVA may add a diffusion barrier to the PBS buffer and degradation products, so the fiber surface cannot be neutralized as fast as when they are in direct contact with the buffer. The decreased pH at the surface may be contributed to the faster erosion rate. When the wet composites were examined under a microscope, there were 10-20μm interconnected pores in the PVA phase (Figure 4.16a) and in the fiber-PVA phase (Figure 4.16b). This porous structure may contribute to the significant increase of the erosion rate after fibers are embedded in PVA. On the other hand, the thick films degrade much faster than the other two fiber systems and erosion starts one week earlier compared to fibers. This

difference would be mainly attributed to the larger dimension (2mm vs. 1 μm) and lower surface area-to-volume ratio of films compared to small fibers. The auto-catalysis by the accumulated degradation products inside films has a predominant effect on the overall hydrolysis rate. Degradation of films slows down after four weeks when a highly porous network is formed. Therefore, hydrolysis of PLGA, either fiber or film, is affected by auto-catalysis but to a different extent. The extent of auto-catalysis depends on diffusion of accumulated degradation products and diffusion of the neutral buffer or pH gradient in the PLGA.

4.2.3. Modeling of PLGA Fiber Degradation

Degradation of PLGA can be diffusion controlled, kinetics controlled or a mixed mechanism, depending on the water diffusivity, hydrolysis rate and sample dimension. We can estimate the characteristic time for water diffusing through PLGA using the literature value of water diffusivity in amorphous PLA, 10^{-7} cm^2/s at 37ºC [8]. The characteristic time for water diffusing through 1μm distance at 37ºC is about 0.025 s, which becomes 6.94 hrs for a 1 mm diffusion length. The characteristic time for hydrolysis can be derived from our experimental data. We can assume that the rate constant of small fibers is close to the intrinsic rate constant (without auto-catalysis effect). Degradation of small fibers follows pseudo-first-order kinetics [9-11] and the characteristic time is the inverse of the rate constant k_d. k_d derived from first-order kinetics is 2.4×10^{-7} s^{-1}, so the characteristics time τ_k is 1158 hours. It is obvious that the hydrolysis is kinetic controlled at the beginning even for samples as thick as 2 mm after comparing the characteristic times for water diffusion and PLGA hydrolysis. As the

hydrolysis goes on, diffusion will affect removal of degradation products and pH gradient inside PLGA, therefore affecting the kinetics, especially true for bigger dimensions. The hydrolysis rate increases when there is a significant amount of accumulated degradation products, but decreases as the PLGA becomes highly porous after extended erosion.

Factors such as surface area-to-volume ratio, accumulated degradation products, pH gradient and PVA barriers all end up affecting the auto-catalysis, so we can simplify the degradation model by using one kinetic model with different rate constants for different systems. The hydrolysis model is based on the pseudo-first-order kinetics. The kinetics is expressed by the differential equation below [9].

$$d[COOH]/dt = k'[PLGA][H_2O][COOH] = k_d[COOH]$$

After assuming [COOH] = 1/Mn and integrating the differential equation, we can get the integrated expression.

$$\ln (Mn_0/Mn) = k_d t + m$$

where Mn is the number-average molecular weight at time t and Mn_0 is the number-average molecular weight at time t = 0. The rate constant k_d for the three systems was obtained from the number-average molecular weight data during the first three weeks of degradation (two weeks for films).

The erosion model is based on a model used for a polymer-decomposition-dependant drug release [12], which is analogous to an original model used for the thermal decomposition of potassium permanganate crystals [13]. The erosion kinetics can be expressed as

$$\ln (X/(1-X)) = -k_e t + m$$

where X is % weight remaining. The detailed derivation can be found in reference [12]. The rate constant k_e was obtained from the weight loss data. The hydrolysis model and erosion model were applied to the hydrolysis and weight loss data to derive the rate constants for the three systems, PLGA fibers, fiber-PVA composites and PLGA films, in Figure 4.17a, b. Both k_d and k_e for three systems are listed in Table 4.3.

It is clear that the PLGA fibers both with and without a PVA matrix possess similar k_d and k_e, while k_d and k_e of PLGA films are about three times as much as those of PLGA fibers. The erosion rate of PLGA films greatly decreases to almost 20% of the initial value after three weeks of degradation.

4.3. Chapter Summary

In vitro degradation studies were conducted in pH = 7.4 PBS buffer at 37ºC. The degradation behavior of electrospun PLGA fibers was investigated under various conditions. Factors studied include copolymer composition, morphology, dimension, and PVA hydrogels.

It seems that the two-week incubation at body conditions is a transition point for studied PLGA fibers with a LA/GA ratio of 50:50. By the end of two weeks, nanopits completely covers the fiber surface, weight loss starts increasing greatly, and molecular weight decrease slows down. The glycolide component degrades faster than the lactide component in PLGA copolymers. Copolymers with higher glycolide content degrade faster if their molecular weights are similar. Fiber diameter does not have significant influence on the degradation rate, while PVA matrix has slightly positive effect on the degradation rate. Hydrolysis of PLGA in all morphologies is accelerated by auto-

catalysis of the acidic degradation products, but to a different extent. Thick PLGA films possess the fastest degradation rate due to their large dimensions, which results in a significant pH gradient inside PLGA. Swollen fibers and shrunken mats are observed under incubation conditions due to the relaxation of softened fibers above T_g of wet PLGA, which is near 30ºC. PVA can reduce shrinking of PLGA fiber mats by anchoring fibers in the matrix.

PLGA undergoes bulk erosion within the dimensions studied no matter whether it is film or fibers. Degradation of PLGA fibers with or without the PVA matrix is kinetic controlled as the water diffusion can be ignored due to the small dimension of nanofibers and the porous structure of fiber mats and composites. The PLGA hydrolysis model is based on the pseudo-first-order kinetics and all factors such as local pH, accumulated degradation products and diffusion are incorporated into a rate constant. The PLGA erosion model is based on a polymer-decomposition-dependant drug release model. The PLGA fibers with or without a PVA matrix possess similar k_d and k_e, while k_d and k_e of PLGA films are about three times as much as those of PLGA fibers.

List of References

1. You Y, Min B-M, Lee SJ, Lee TS, Park WH. *In vitro* degradation behavior of eletrospun polyglycolide, polylactide, and poly(lactide-*co*-glycolide). Journal of Applied Polymer Science 2005; 95: 193-200.

2. Avgoustakis K, Nixon J. Biodegradable controlled release tablets 3: Effect of polymer characteristics on drug release from heterogeneous poly(lactide-*co*-glycolide) matrices. International Journal of Pharmaceutics 1993; 99: 247-252.

3. Kim K, Yu M, Zong X, Chiu J, Fang D, Seo Y-S, Hsiao BS, Chu B, Hadjiargyrou M. Control of degradation rate and hydrophilicity in electrospun non-woven poly(D,L-lactide) nanofiber scaffolds for biomedical applications. Biomaterials 2003; 24: 4977-4985.

4. Dunne M, Corrigan OI, Ramtoola Z. Influence of particle size and dissolution conditions on the degradation properties of polylactide-co-glycolide particles. Biomaterials 2000; 21: 1659-1668.

5. Burkersroda F, Schedl L, Gopferich A. Why degradable polymers undergo surface erosion or bulk erosion. Biomaterials 2002; 23:4221-4231.

6. Zolnik BS, Burgess DJ. Effect of acidic pH on PLGA microsphere degradation and release. Journal of Controlled Release 2007; 122:338-344.

7. Vey E, Roger C, Meehan L, Booth J, Claybourn M, Miller AF, Saiani A. Degradation mechanism of poly(lactic-co-glycolic) acid block copolymer cast films in phosphate buffer solution. Polymer Degradation and Stability 2008; 93:1869-1876.

8. Yoon JS, Jung HW, Kim MN, Park ES. Diffusion coefficient and equilibrium solubility of water molecules in biodegradable polymers. Journal of Applied Polymer Science 2000; 77:1716-1722.

9. Loo SCJ, Ooi CP, Wee SHE, Boey YCF. Effect of isothermal annealing on the hydrolytic degradation rate of ply(lactide-co-glycolide) (PLGA). Biomaterials 2005; 26:2827-2833.

10. Kenley RA, Lee MO, Mahoney TR II, Sanders LM. Poly(lactide-co-glycolide) decomposition kinetics *in vivo* and *in vitro*. Macromolecules 1987; 20: 2398-2403.

11. Siepmann J, Elkharraz K, Siepmann F, Klose D. How autocatalysis accelerates drug release from PLGA-based microparticles: a quantitative treatment. Biomacromolecules 2005; 6:2312-2319.

12. Fitzgerald JF, Corrigan OI. Mechanisms governing drug release from poly-α-hydroxy aliphatic esters. In: Ei-Nokaly MA, Piatt DM, Charpentier BA, editors. Polymeric delivery systems, properties and applications. ACS Symposium Series No. 520. Washington DC: American Chemical Society, 1993: 311-326.

13. Prout EG, Tompkins FC. The thermal decomposition of potassium permanganate. Trans Faraday Soc 1944; 40:488-498.

Table 4.1. Electrospinning parameters and fiber sizes of electrospinning PLGA7 fibers.

ID	Concentration in DMF	Feeding Rate	Voltage	Tip-to-Plate Distance	Fiber Size
	wt %	ml/hr	kV	cm	nm
H16	34.7	0.8	17.3	21	642±298 (fibers) 2908±2127 (spindles)
H17	34.95	0.6	18.7		436±221 (fibers) 1592±371 (spindles)
H18	34.95	0.2	15.7		406±159 (fibers) 1112±236 (spindles)
H19	31	0.6	19.7		255±125 (fibers) 1533±799 (spindles)
H20	31	0.1	12.5		261±259 (fibers) 1142±21 (spindles)

Table 4.2. Electrospinning parameters and fiber sizes of electrospinning PLGA4A fibers.

ID	Concentration in DMF	Feeding Rate	Voltage	Tip-to-Plate Distance	Fiber Size
	wt %	ml/hr	kV	cm	nm
4A_35	35	0.1	11	21	138±42 (fibers) 3174±1160 (beads)
4A_40	40				660±258 (fibers)
4A_45	45				808±152 (fibers)

Table 4.3. Comparison of rate constants k_d and k_e for fibers, fibers in PVA and films.

	Fibers	Fibers in PVA	Films
Degradation: k_d, week^{-1}	0.2311	0.2609	0.8021
Erosion: k_e, week^{-1}	0.5251	0.5515	1.5188 0.3398

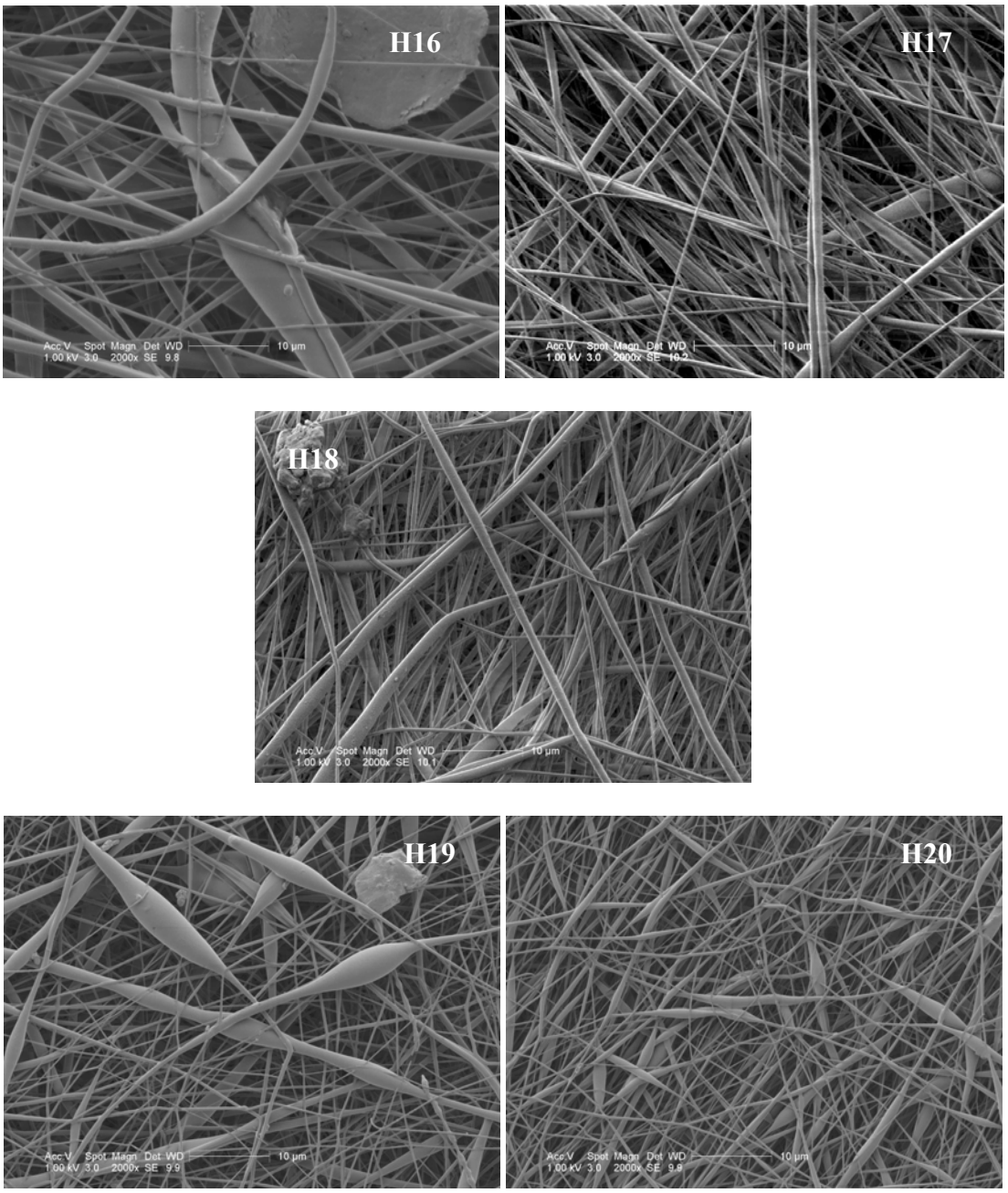

Figure 4.1. Morphology of electrospun PLGA7 fibers used in the degradation study.

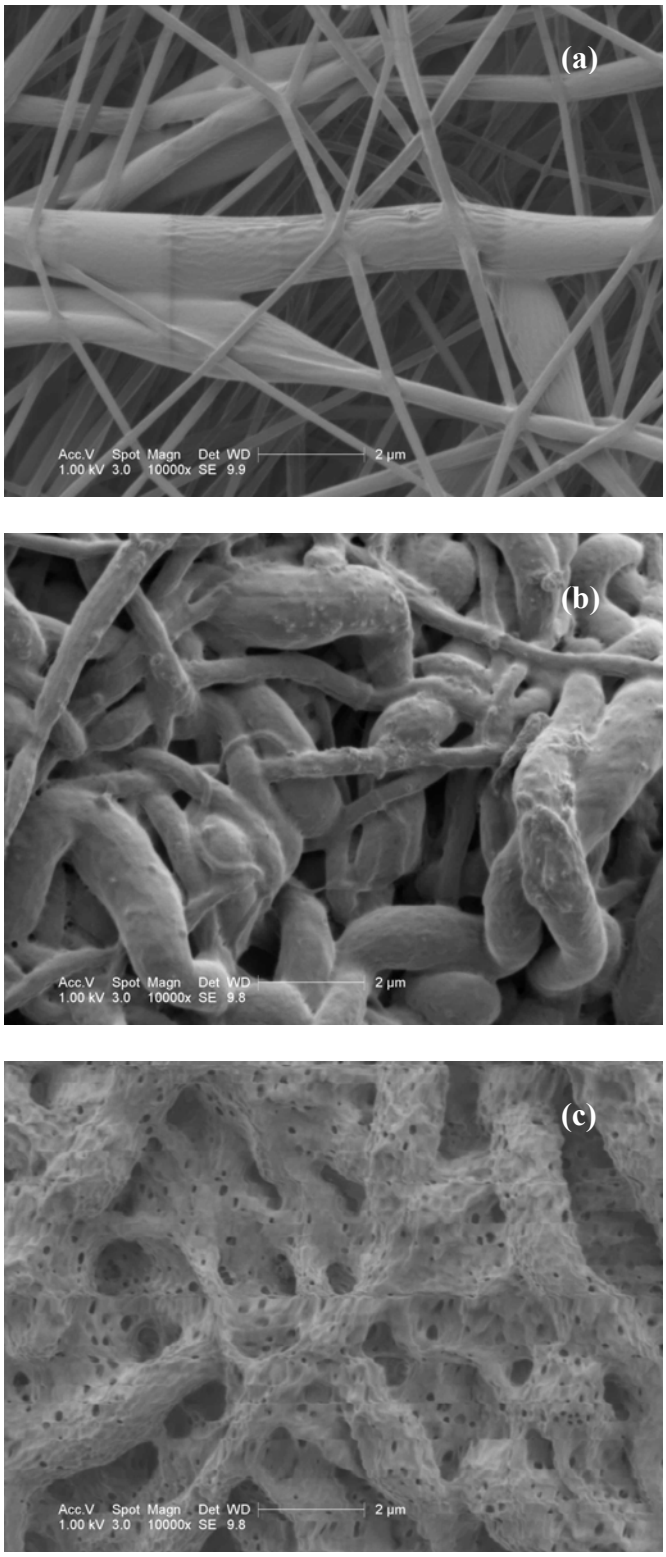

Figure 4.2. Morphology of H20 fibers (a) before (b) after one week or (c) two weeks of incubation in PBS buffer (pH=7.4) at 37°C.

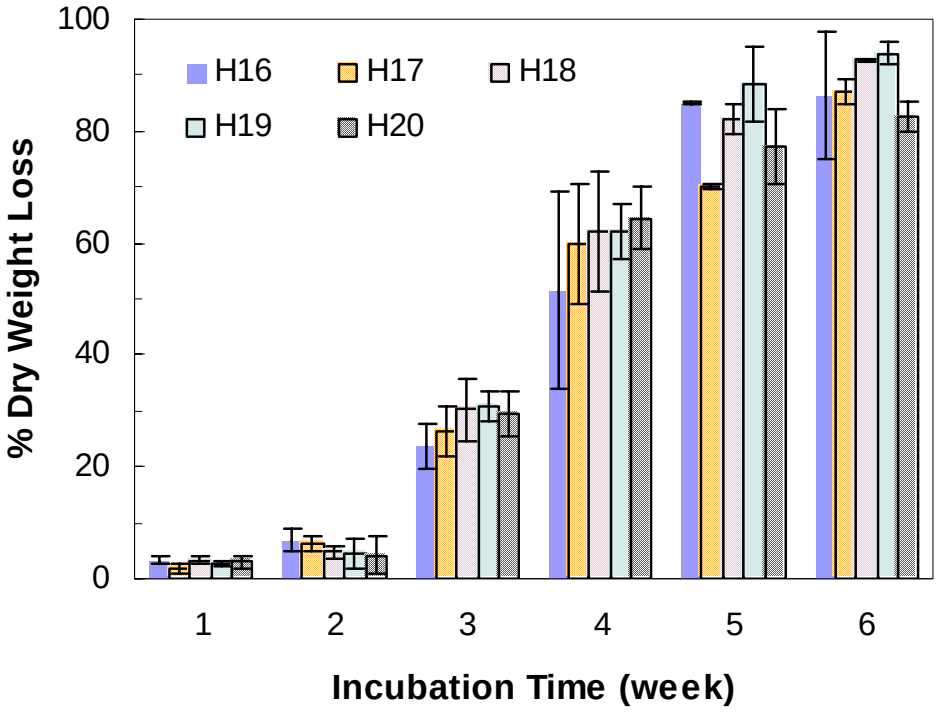

Figure 4.3. Normalized weight loss of all PLGA7 fiber mats during incubation in PBS buffer (pH=7.4) at 37°C.

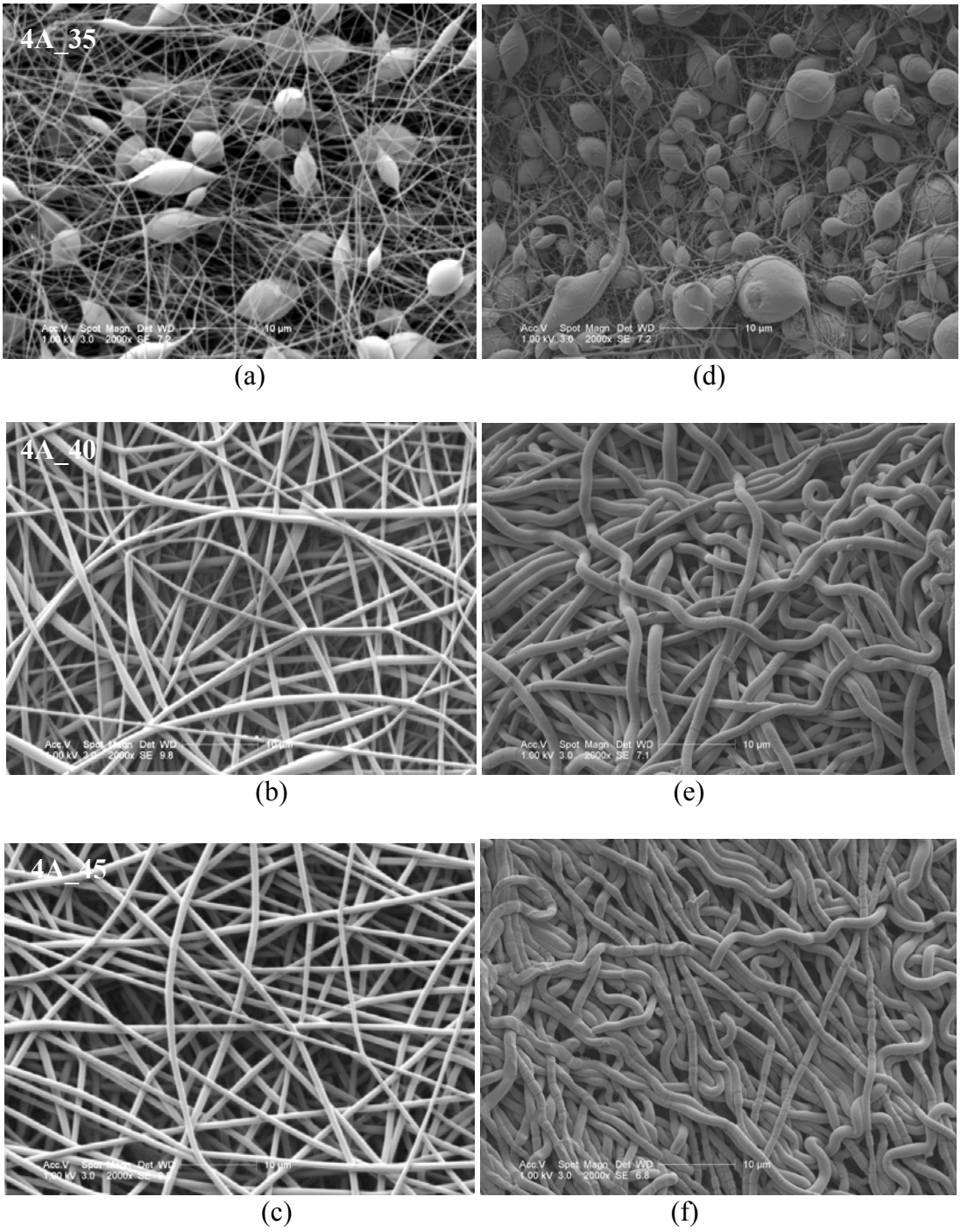

Figure 4.4. Morphology of electrospun PLGA4A fibers used in the degradation study. (a)-(c) before incubation, and (d)-(f) after incubation for one week. (a) and (d) 4A_35, (b) and (e) 4A_40, (c) and (f) 4A_45.

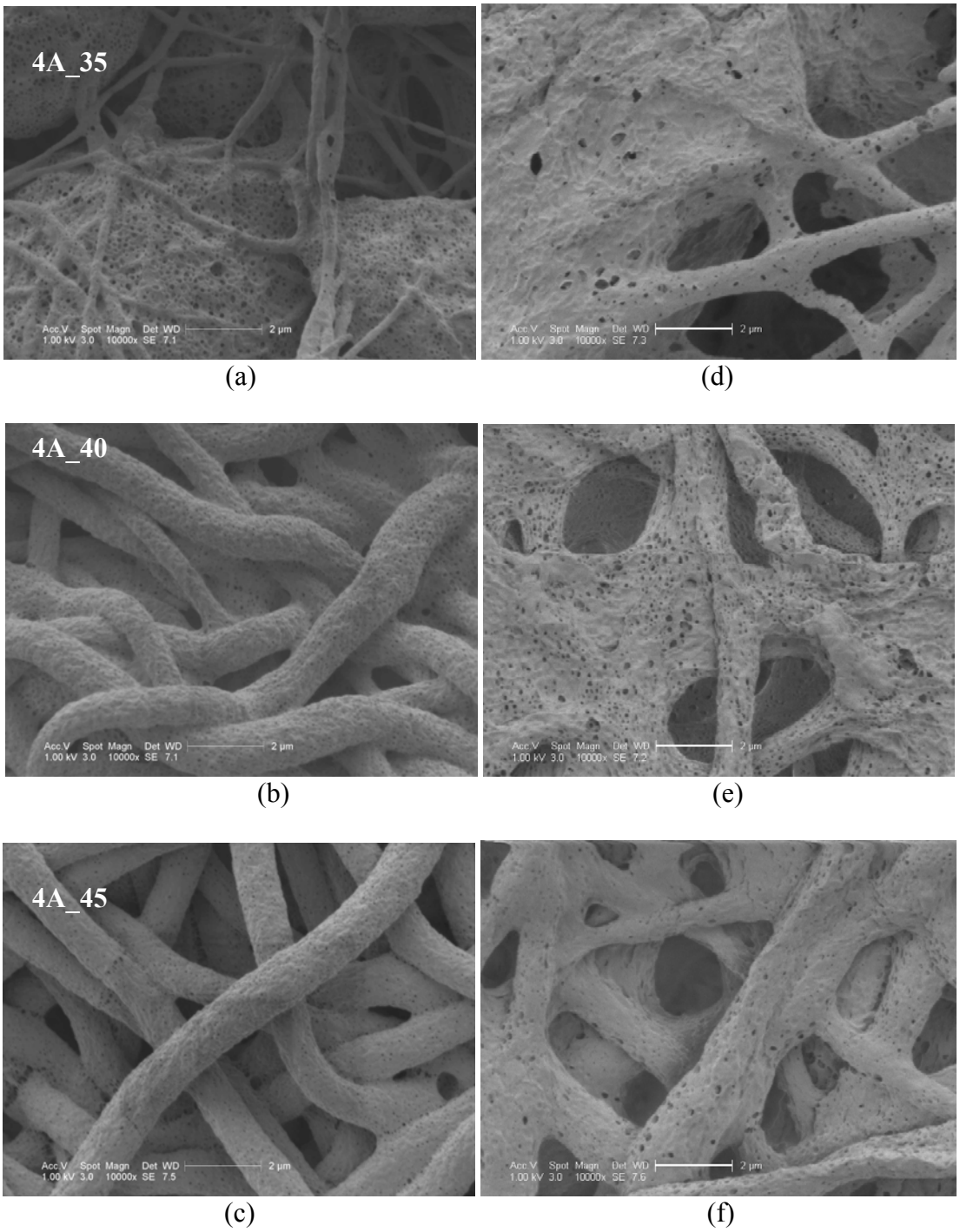

Figure 4.5. Morphology of all PLGA4A fibers after (a)-(c) two weeks or (d)-(f) five weeks of incubation in PBS buffer (pH=7.4) at 37°C. (a) and (d) 4A_35, (b) and (e) 4A_40, (c) and (f) 4A_45.

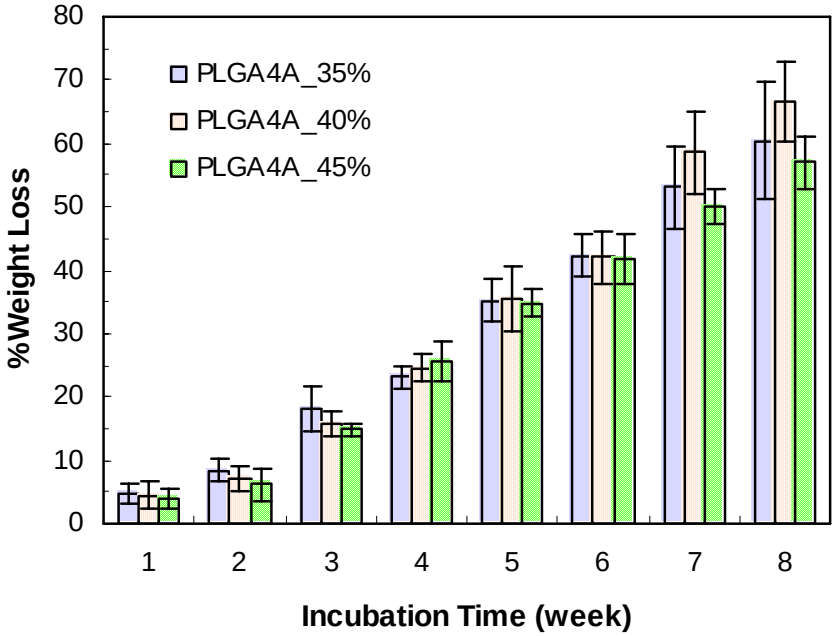

Figure 4.6. Normalized weight loss of PLGA4A fibers after up to eight weeks of incubation in PBS buffer (pH=7.4) at 37°C.

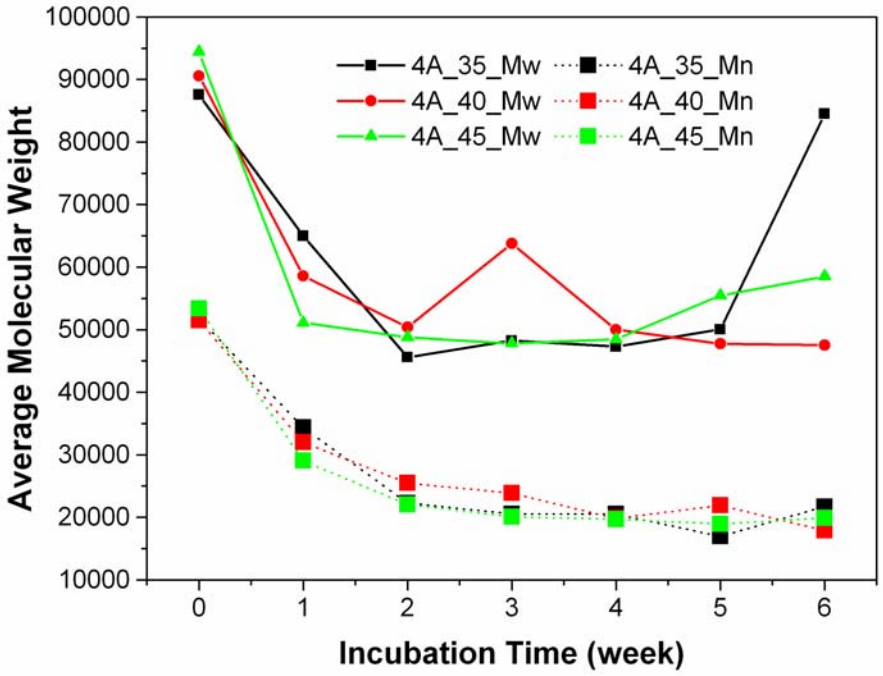

(a)

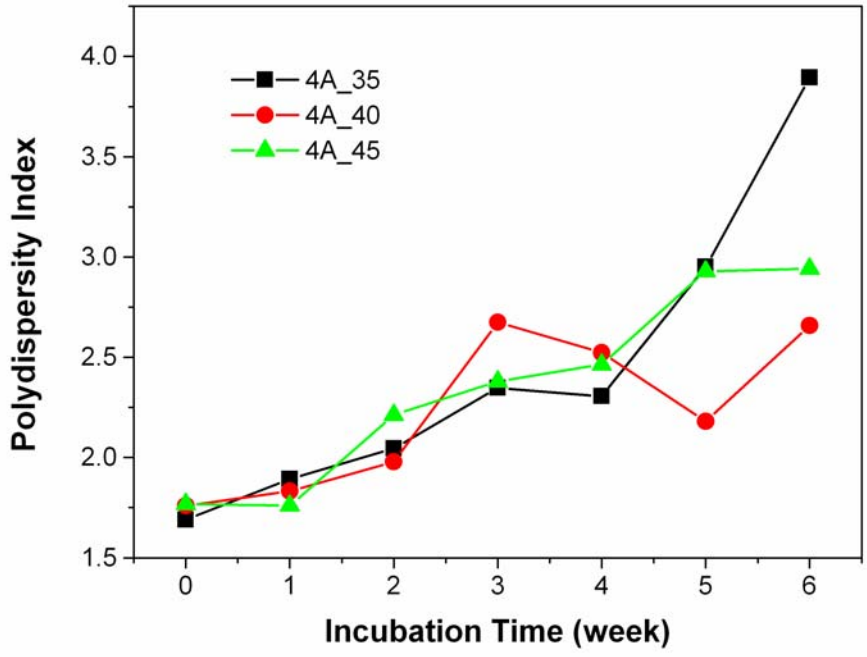

(b)

Figure 4.7. Molecular weight and polydispersity index of PLGA4A fibers after up to six weeks of incubation in PBS buffer (pH=7.4) at 37°C. (a) weight-average molecular weight (Mw), number-average molecular weight (Mn) and (b) polydispersity index (PI) of all fiber mats as a function of incubation time.

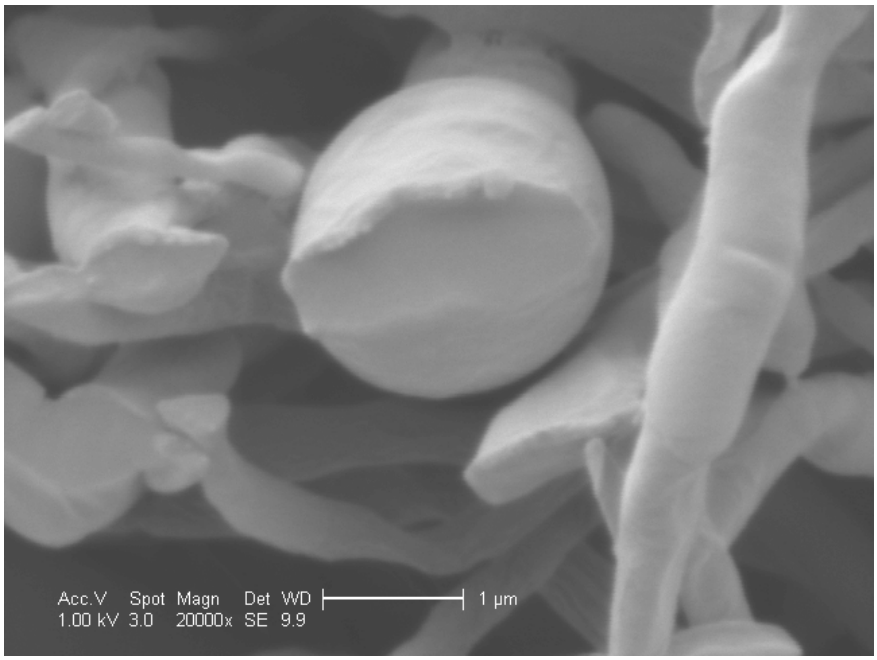

(a)

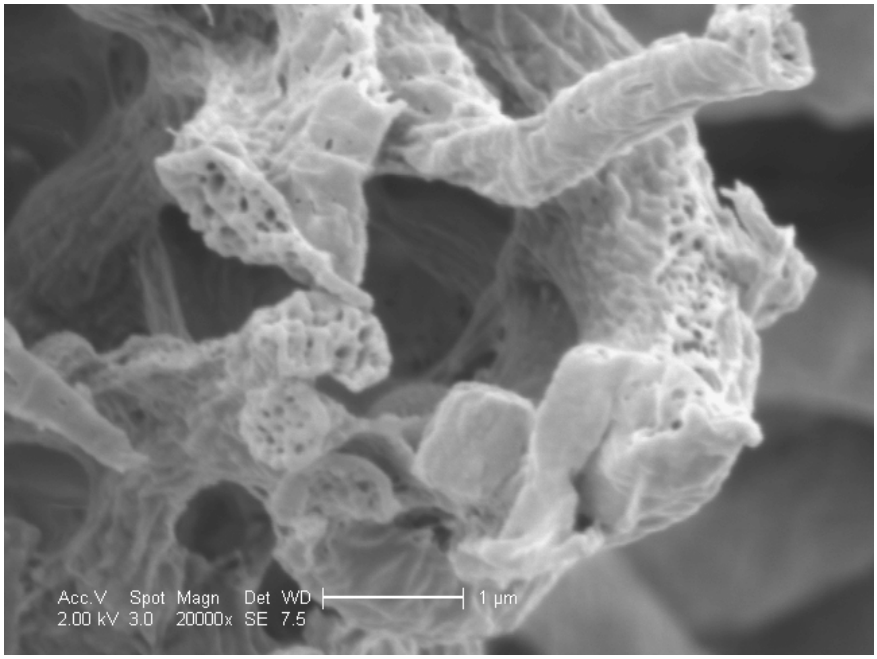

(b)

Figure 4.8. 4A-40 fibers (a) before and (b) after incubation for nine days.

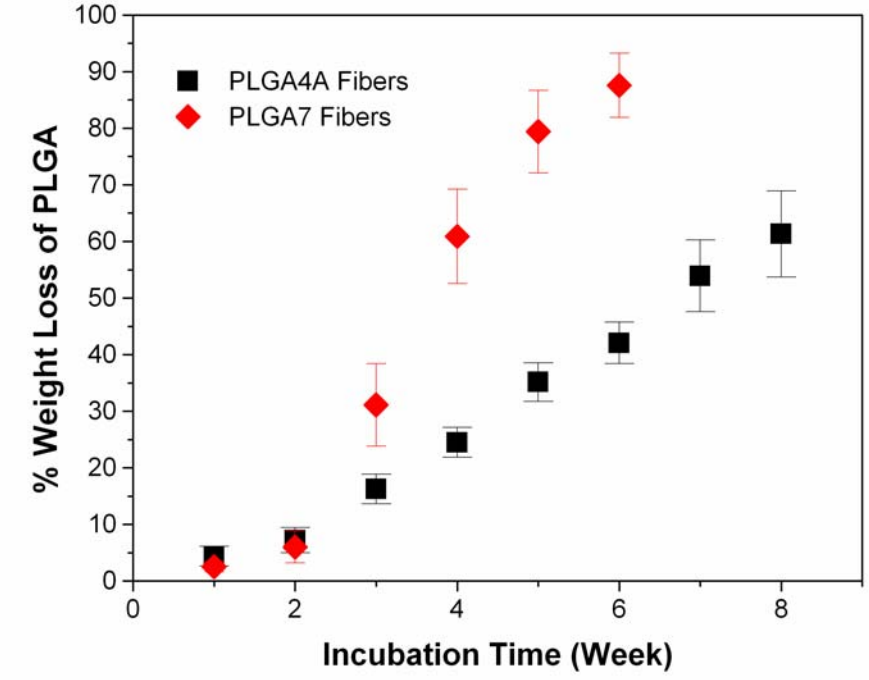

(a)

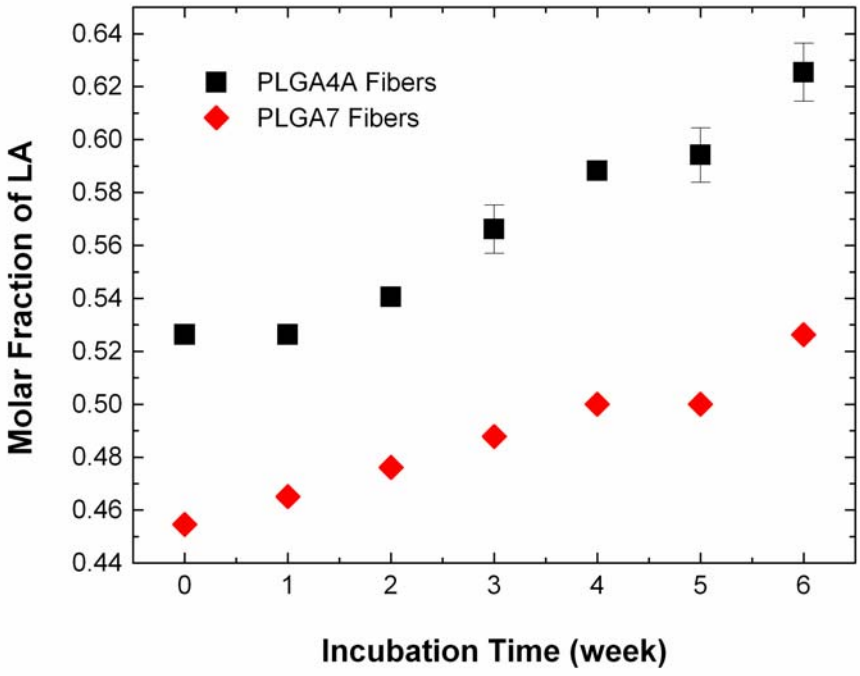

(b)

Figure 4.9. (a) Weight loss and (b) Lactic acid (LA) composition as a function of incubation time for PLGA7 fibers and PLGA4A fibers.

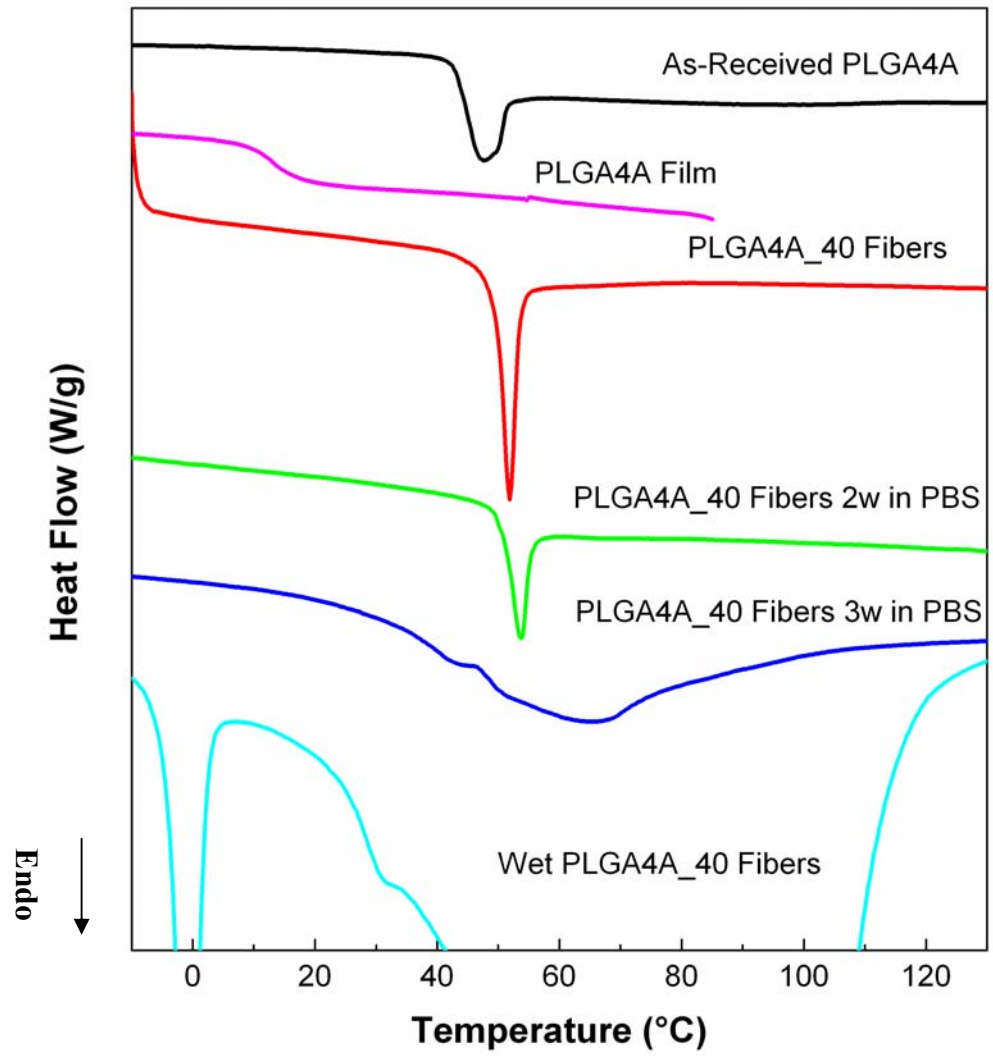

Figure 4.10. DSC thermograms show the glass transition change under various conditions for PLGA4A.

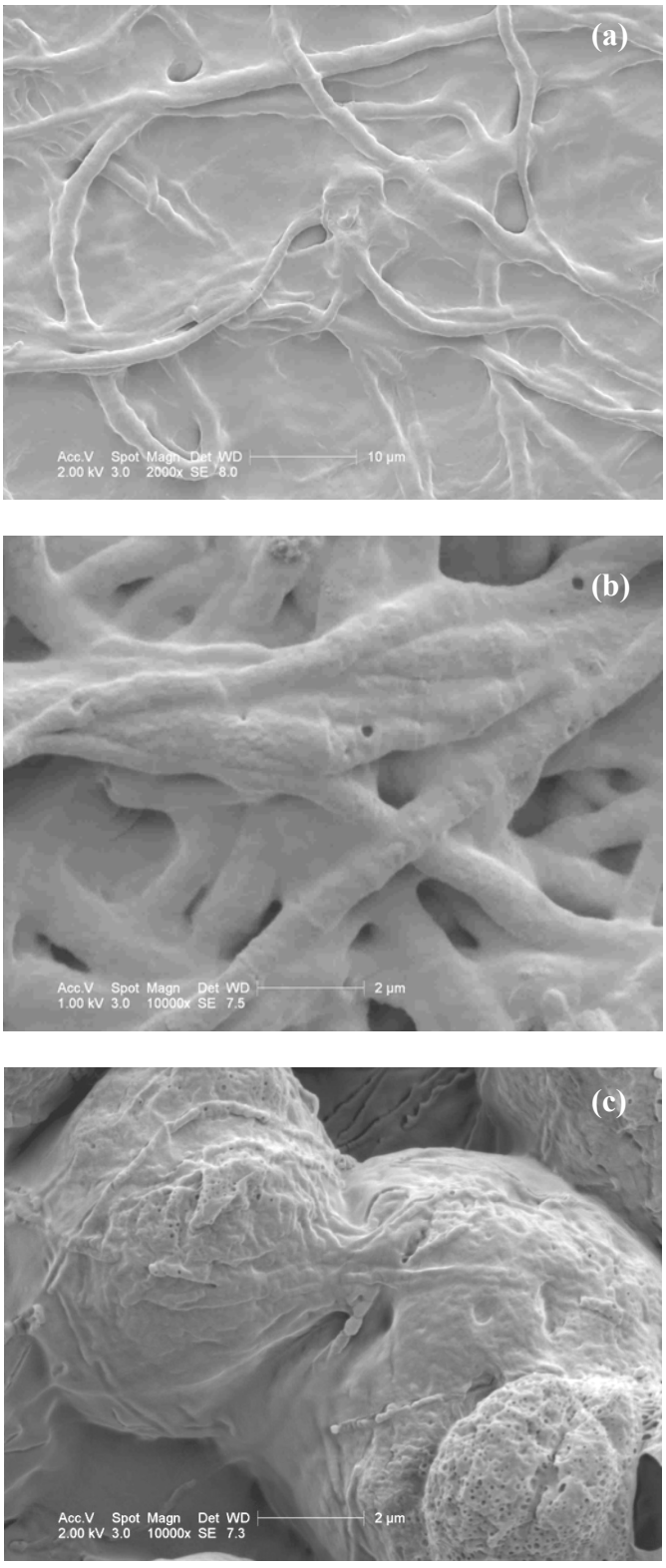

Figure 4.11. Morphology of PLGA4A_40-PVA after (a) one week or (b) two weeks of incubation and (c) PLGA_35-PVA after two weeks of incubation in PBS buffer (pH=7.4) at 37°C.

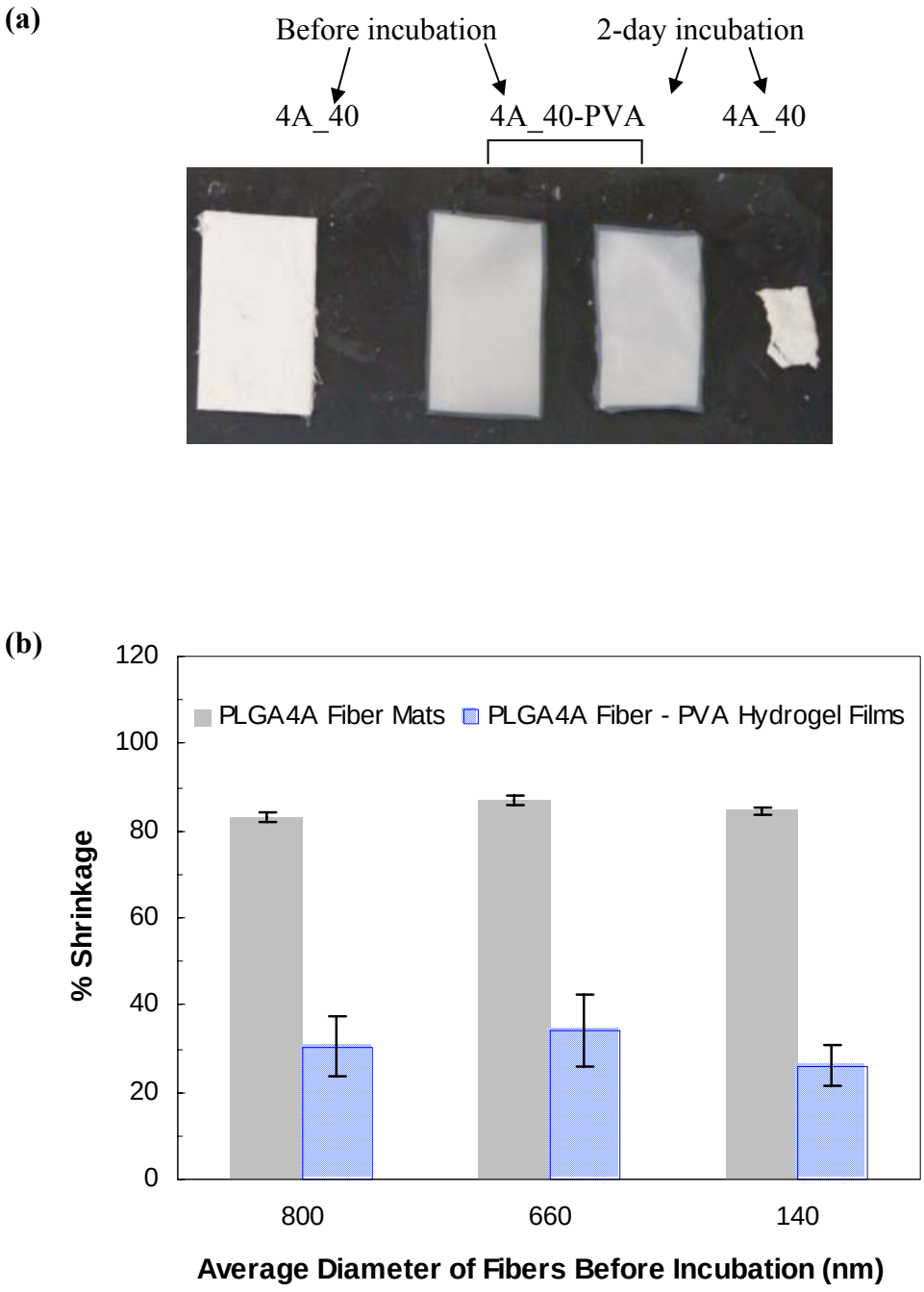

Figure 4.12. Comparison of mat shrinkage of PLGA4A fibers and PLGA4A-PVA composites under incubation conditions. (a) Visual observation of PLGA4A_40 fiber mats and PLGA4A_40-PVA before and after incubation, and (b) plots of normalized shrinkage of three fiber mats and corresponding composites.

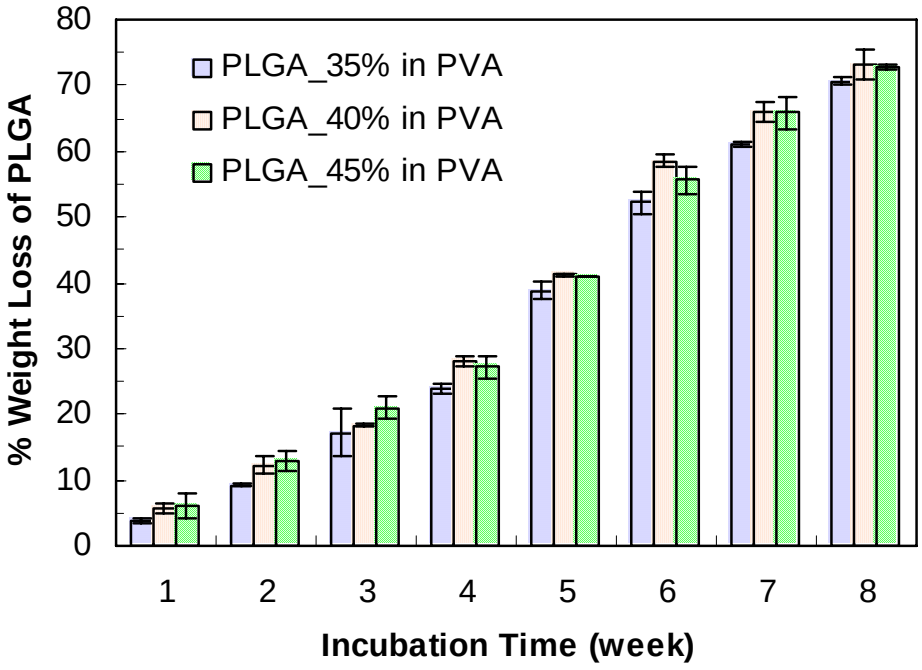

Figure 4.13. Normalized weight loss of PLGA4A fibers embedded in PVA hydrogels after up to eight weeks of incubation in PBS buffer (pH=7.4) at 37°C.

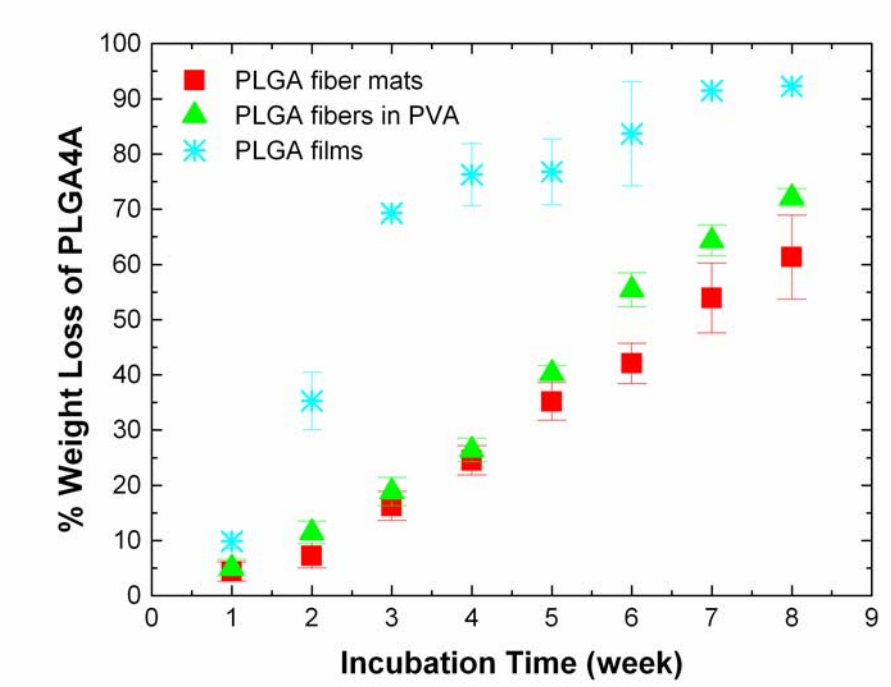

(a)

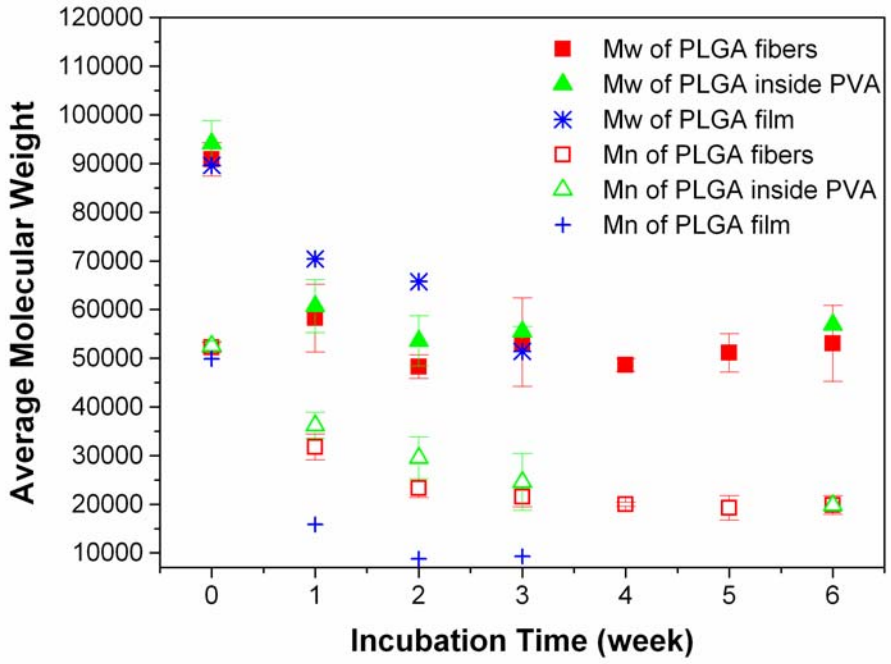

(b)

Figure 4.14. Comparison of degradation of PLGA4A fibers, PLGA4A fibers inside PVA gels and PLGA4A films after up to eight weeks of incubation in PBS buffer (pH=7.4) at 37°C. (a) Normalized weight loss (b) weight-average molecular weight (Mw) and number-average molecular weight (Mn) of PLGA4A as a function of incubation time.

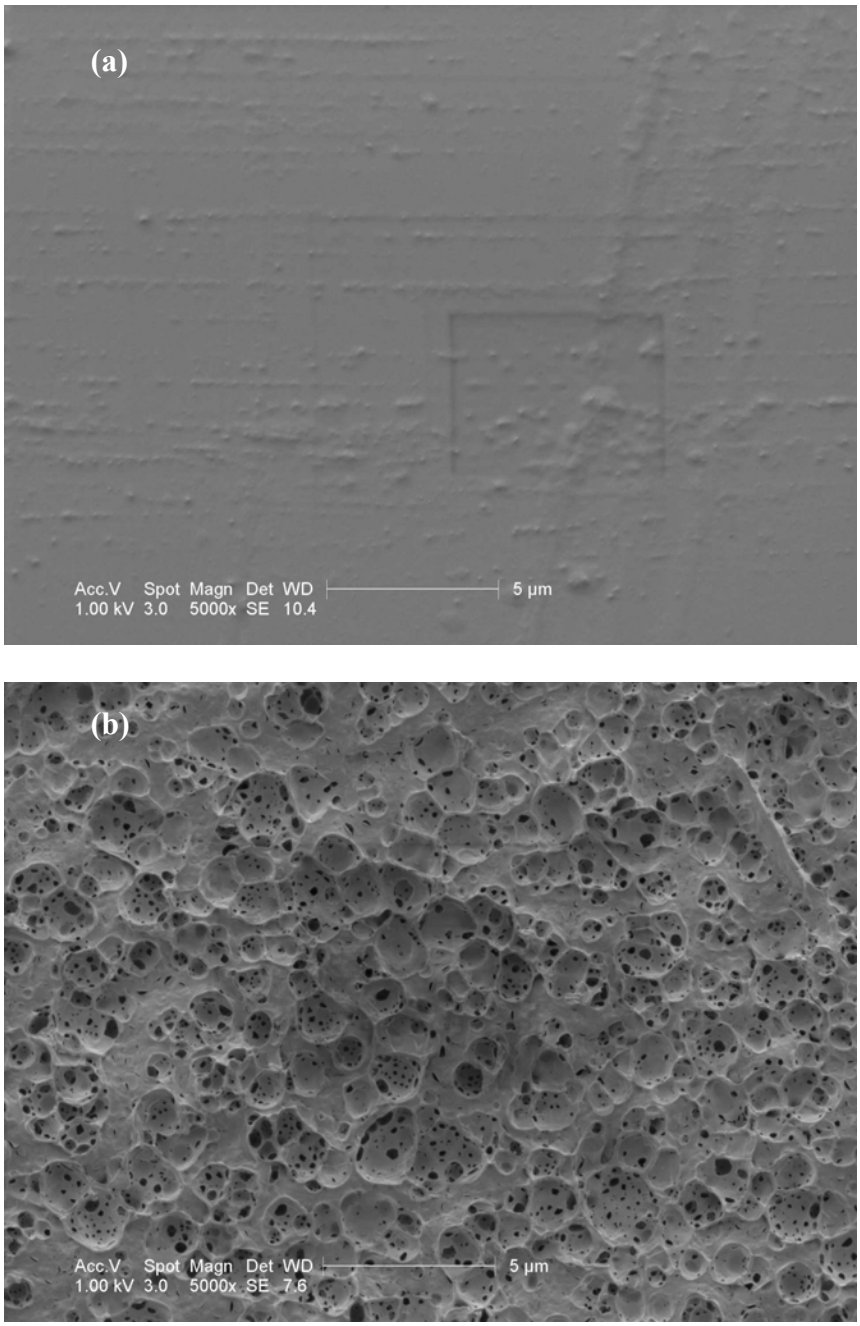

Figure 4.15. Morphology of PLGA4A films (a) before and (b) after one week of incubation in PBS buffer (pH=7.4) at 37°C.

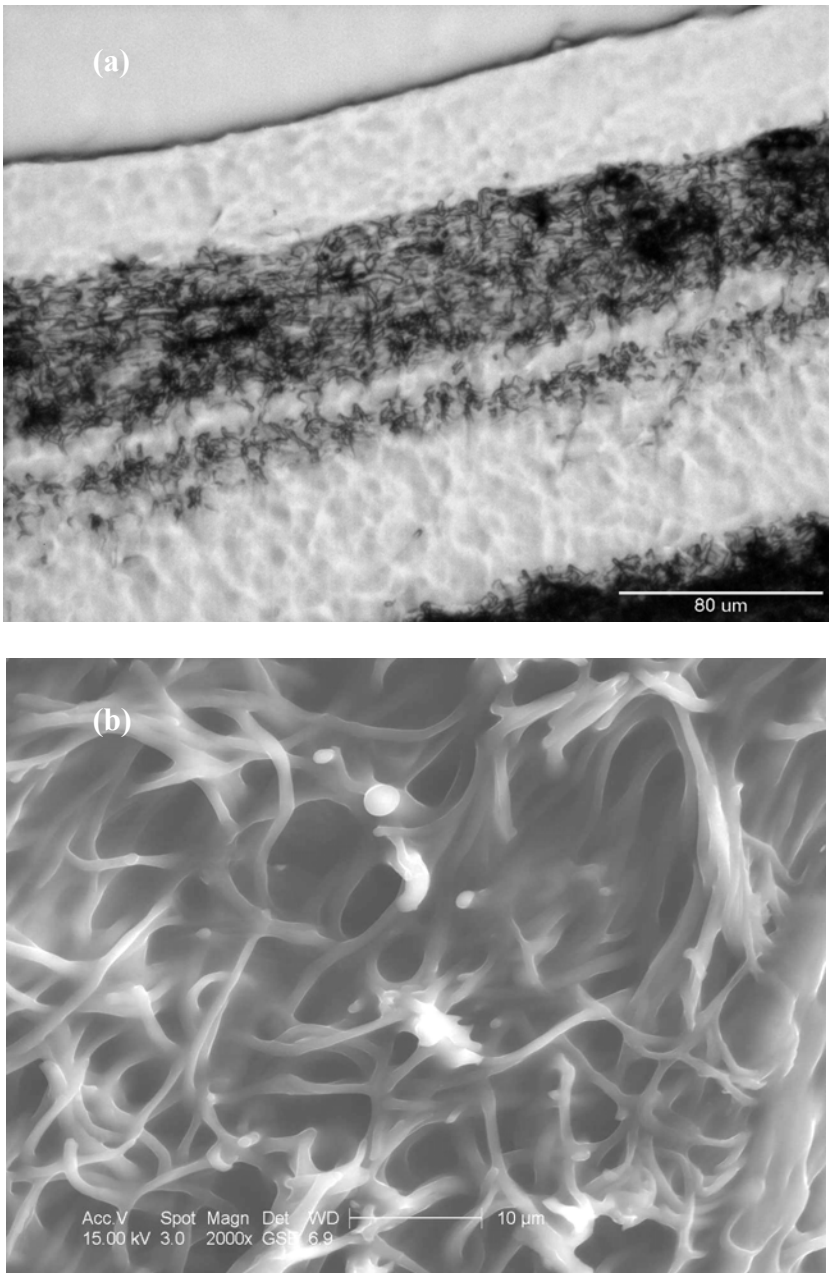

Figure 4.16. Porous structure of the wet PLGA4A fiber-PVA composite. (a) Optical microscope image of 4A_45-PVA (fibers are shown in black and PVA is shown in white), and (b) ESEM image of 4A_40-PVA before incubation.

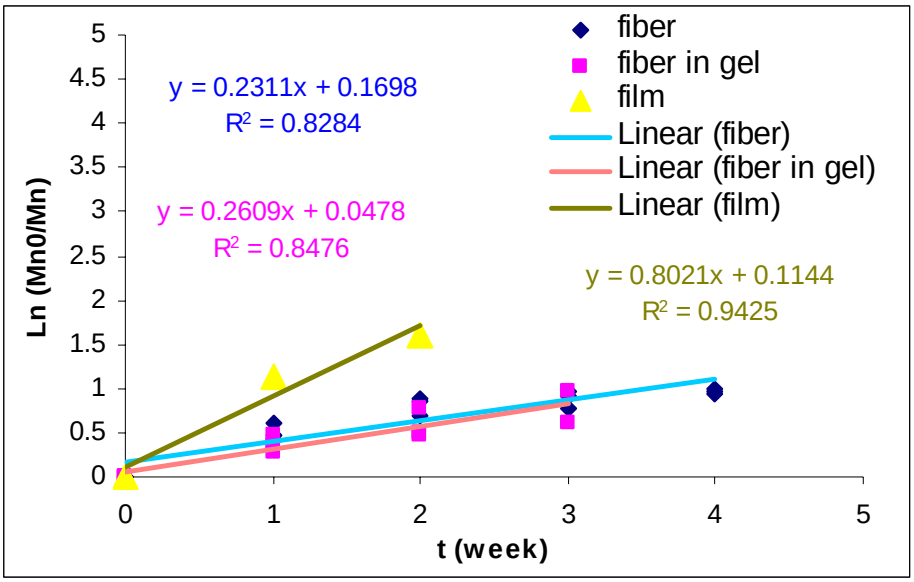

(a)

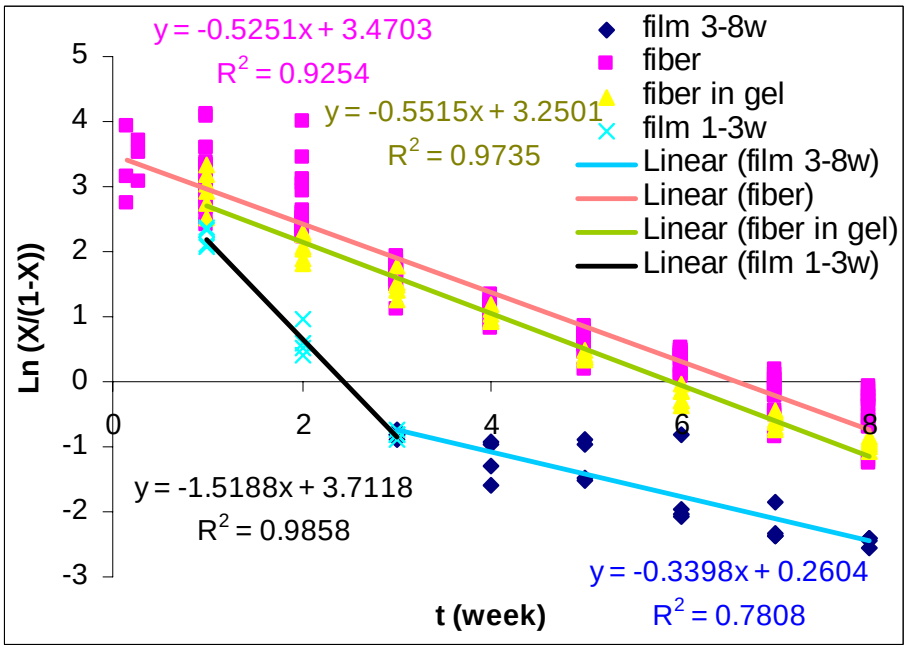

(b)

Figure 4.17. (a) Number-average molecular weights were fit to the hydrolysis model for PLGA degradation, ln (Mn0/Mn) = kt, to get rate constants for hydrolysis; (b) Weight loss data were fit into the erosion model, ln (X/(1-X)) = -kt + m and X is % weight remaining, to get erosion rate constants.

Chapter 5: Mechanical Properties of PLGA-PVA Composites during Incubation

The PLGA-PVA composites should have the mechanical strength required for use in drug delivery devices. The change in the mechanical properties should be within a reasonable range during the use of the device. In Chapter 2, it was mentioned that PVA hydrogels have similar mechanical properties to natural human tissues. In this chapter, tensile properties of PLGA-PVA composite films will be compared to those of PVA hydrogel films before and during incubation in PBS at 37°C.

5.1. Experimental

Tensile properties of PLGA4A fiber mats, PVA hydrogel films and PLGA4A-PVA composite films were tested under the tensile mode in a PBS bath using an Instron 4442 universal testing instrument. The data acquisition software used was Bluehill. The setup is shown in Figure 5.1. Rectangular specimens were prepared according to ASTM D882-02 [1] with some adjustment on the dimension to accommodate the size of the PBS bath. The gauge length was set at 20 mm, specimen thickness was 0.10-0.25 mm, and specimen width was about 6-7 mm. PVA hydrogels and PLGA-PVA composites not being incubated were equilibrated in the PBS buffer at ambient temperature (~22°C) for at least one hour before testing. All PLGA fibers were pre-wet before testing. Two crosshead speeds, 2 mm/min and 10 mm/min, were used to investigate if the strain rate had any influence on the results. The tensile testing was performed at two bath temperatures, 22°C or 37°C, to examine the tensile properties below or above T_g of wet PLGA, which is near 30°C. Rehydrated specimens of PVA hydrogels and composites

were also tested at 10 mm/min in 37°C PBS. Rehydrated specimens were prepared by soaking the freeze-dried specimens in PBS at ambient temperature for an hour before testing. The rehydrated samples were used in the incubation study and the incubation conditions were the same as those in the degradation study. The tensile testing of incubated samples was conducted in 37°C PBS using a crosshead speed of 10 mm/min. At least five specimens were tested for each sample.

5.2. Results and Discussion

Tensile properties of PLGA-PVA composites at body conditions were obtained to compare with those of PVA hydrogels before and after incubation in 37°C PBS. Since the application is at the body temperature, mechanical properties at 37°C are desired. In order to limit variability of the PBS bath temperature during the tensile testing, the testing speed should be as high as possible without introducing artifacts to the results. The tensile properties may be affected by the testing speed or by the testing temperature. Two testing speeds, 2 mm/min and 10 mm/min, were used in the tensile testing at ambient temperature (about 22°C). Tensile properties were also obtained at 37°C using a testing speed of 10 mm/min. Rehydrated specimens of PVA hydrogels and composites were tested as a comparison to the freshly made specimens since the dry form was preferred for the long term storage. Since those PVA hydrogels are physically crosslinked through crystallites, the processing history is expected to have significant influence on the tensile properties.

5.2.1. Influence of Testing Conditions and Processing History on Tensile Properties of PLGA4A Fiber Mats, PLGA4A-PVA Films and PVA Films

Tensile stress-strain plots of PLGA4A_45 fiber mats, PVA hydrogels and their composites at 22°C using two testing speeds are compared in Figure 5.2. It is clear that the two crosshead speeds did not result in significantly different results. PLGA4A_45 fiber mats had the highest tensile strength and the lowest strain at break at 22°C.

Tensile stress-strain curves of the three systems at different testing temperatures and a testing speed of 10 mm/min are compared in Figure 5.3. Tensile strength, strain at break and modulus are listed in Table 5.1. PVA hydrogels exhibited similar stress-strain curves at the two temperatures, except for a slightly higher strain at break. The PLGA-PVA composite had similar tensile strength at the two temperatures but a higher strain at break at 37°C. The tensile stress of the composite at 22°C was higher than that at 37°C at the same strain. The testing temperature had the most significant influence on PLGA fiber mats because the T_g of the wet PLGA fiber is near 30°C. Fiber mats are more flexible (lower modulus) but weaker at 37°C than at 22°C. Stress-strain curves of the PLGA fiber mat, PVA hydrogel and their composite had similar shapes at 37°C, but the PVA hydrogel was stronger than the other two. On the other hand, the PLGA-PVA composite films were more rigid and easier to handle than PVA hydrogel films at ambient temperature.

The PLGA fiber mats and PLGA-PVA composites exhibited a jump at a strain near 0.1 at 22°C as shown in Figure 5.2 and 5.3. The jump is probably due to the formation of cracks on the PLGA mats due to their low flexibility at 22°C as seen in Figure 5.4a. The white part is PLGA and the translucent part is PVA on the tensile specimens in Figure 5.4. The initial modulus is used to represent the linear portion

before the jump while Young's modulus is used to represent the initial linear portion after the jump. Those data are listed in Table 5.1. The initial modulus was much higher than the Young's modulus for PLGA fiber mats and PLGA-PVA composites. This is because the moduli of fiber mats and composites were greatly decreased after PLGA mats were broken under tension. When the same sample was tested at 37°C, the crack was not observed as shown in Figure 5.4b. The reason is that the PLGA became more flexible at 37°C.

Rehydrated and freshly made testing specimens of PVA hydrogels and PLGA-PVA composites are compared in Figure 5.5. Tensile strength, strain at break and Young's modulus are summarized in Table 5.1. Rehydrated PVA hydrogels and composites showed higher tensile strength and modulus than freshly made samples. The stronger PVA hydrogel may be attributed to the increased crystallinity of PVA during drying.

5.2.2. Tensile Properties of PLGA Fiber Mats, PVA Films and PLGA-PVA Films during Incubation

Tensile stress-strain curves of PVA hydrogels before incubation and after two weeks, four weeks and eight weeks of incubation are compared in Figure 5.6. The slopes of these curves showed a faster increase after strains exceeded about 0.4. Therefore, two moduli were reported for each curve in the linear portion at strains less than 0.4 and at strains between 0.4 and 1. The tensile strength, strain at break and modulus are listed in Table 5.2. The modulus and strength of PVA hydrogels gradually increased, but the strain at break decreased during incubation. The slopes of those stress-strain curves increased quickly at the beginning of the incubation, and then slowed down with longer

incubation time. These changes may be associated with the aging process of PVA hydrogels and de-swelling behavior of hydrogels in the PBS buffer.

Tensile stress-strain curves of the three PLGA-PVA composites during incubation are shown in Figure 5.7, Figure 5.8 and Figure 5.9, respectively. The stress-strain curves of the composites exhibit a linear increase at strains between 0 and 1 before incubation, so only one modulus was reported for each curve. However, after incubation the shape change of the stress-strain curves for the composites is similar to that of PVA hydrogel. The slope change during incubation for the composites was different compared with PVA hydrogels, which may have resulted from the mechanical property change associated with the degradation of PLGA fibers. The slopes of the stress-strain curves for PLGA4A_45-PVA and PLGA4A_40-PVA increased slowly in the first four weeks of incubation, but then increased faster during the remaining four weeks. However, the slopes of the stress-strain curves of PLGA4A_35-PVA did not change much during incubation. The tensile properties of the four PVA systems during incubation are included in Table 5.2. In general, all composites exhibited similar trends to the PVA hydrogels. The modulus and strength gradually increased, while the strain at break decreased during incubation. The only exception is that the tensile strength of the PLGA4A_35-PVA composite gradually decreased during incubation. This is possibly due to the beads-on-strings fiber morphology of PLGA4A_35 fibers. These very thin strings about 100 nm in diameter became very weak during degradation, so their tensile properties decreased faster than the bigger fibers with diameters near 1 μm. Therefore the increase of the tensile strength contributed from PVA hydrogels was overacted by the great decrease of tensile strength contributed from PLGA4A_35 fibers.

Those tensile results are also plotted to compare the four hydrogel systems before (Figure 5.10) and after eight weeks of incubation (Figure 5.11). Before incubation, PLGA4A_45-PVA, PLGA4A_40 and PVA had similar tensile stress-strain curves, but PLGA4A_35-PVA possessed the highest tensile properties. This is possibly due to the higher volume fraction of the PLGA4A_35 fiber (9 v%) in the composite than those of the other two fibers in their composites (7 v%). The big beads of several microns in diameters may also offer better plastic deformation to withstand higher stress. After eight weeks of incubation, all hydrogel systems exhibited similar tensile properties. These results indicate that incorporation of PLGA nanofibers in PVA has little influence on the tensile properties of PVA hydrogel films during incubation in PBS. Therefore, the PLGA fiber-PVA composite is expected to have the desired mechanical stability in many applications where PVA hydrogels have been used.

5.3. Chapter Summary

Tensile properties of PLGA fiber mats, PVA hydrogels and their composites were investigated under different testing conditions and during incubation. The two different crosshead speeds, 2 mm/min and 10 mm/min, did not result in significantly different results for any of the three systems. The two testing temperatures were found to affect the tensile results of PLGA mats and the composites due to the reduced glass transition temperature of PLGA from 50ºC in a dry environment to 30ºC in a wet environment. PVA hydrogels were stronger than either PLGA fiber mats or composites above 30ºC. Below 30ºC, the stress-strain curves of PLGA mats and composites exhibited a different shape compared with those of PVA hydrogels. PLGA fiber mats showed the highest

tensile strength and the lowest strain at break below 30ºC. Drying the PVA hydrogel or composite improved their tensile properties. In general, the modulus and strength gradually increased, while the strain at break decreased during incubation for all PLGA-PVA composites and PVA hydrogels. Incorporation of PLGA nanofibers in PVA had little influence on the tensile properties of PVA hydrogel films during long-term incubation.

List of References

[1] Standard Test Method for Tensile Properties of Thin Plastic Sheeting. Annual Book of ASTM Standards, Designation: D 882 – 02. ASTM International, June 2002.

Table 5.1. Tensile strength, strain at maximum stress and Young's modulus of PLGA_45 fiber mats, PVA hydrogels and their composites in neutral PBS buffer tested at different crosshead speeds and temperatures.

Testing Conditions	Speed (mm/min)	2	10	10	10
	Temperature of PBS Bath (°C)	22	22	37±2	37±2 (Rehydrated samples)
PVA	Strength (MPa)	1.02±0.25	1.00±0.12	1.01±0.31	1.52±0.36
	Strain	2.35±0.31	2.26±0.23	2.31±0.57	2.39±0.38
	Modulus (MPa)	0.34±0.04	0.36±0.02	0.31±0.06	0.49±0.07
PLGA4A_45	Strength (MPa)	3.00±0.98	3.12±0.58	1.37±0.42	—
	Strain	1.29±0.49	1.85±0.57	3.43±0.16	—
	Modulus (MPa)	0.55±0.20	0.52±0.06	0.21±0.05	—
	Initial Modulus (MPa)	151.8±73.9	133.2±54.9	—	—
PLGA4A_45-PVA	Strength (MPa)	0.84±0.19	0.68±0.19	0.77±0.16	1.10±0.17
	Strain	2.57±0.40	2.47±0.28	2.94±0.63	3.09±0.21
	Modulus (MPa)	0.09±0.03	0.11±0.02	0.22±0.03	0.29±0.02
	Initial Modulus (MPa)	14.06±5.44	11.40±3.58	—	—

Table 5.2. Tensile strength, strain at break and Young's modulus under incubation conditions for PVA, PLGA4A_45-PVA, PLGA4A_40-PVA and PLGA4A_35-PVA films during degradation.

Testing Conditions	Testing Speed (mm/min)		10		
	Temperature of PBS Bath (°C)		37±2		
Degradation Time		0 Week	2 Weeks	4 Weeks	8 Weeks
PVA	Strength (MPa)	0.91±0.09	1.09±0.15	1.10±0.11	1.25±0.13
	Strain at Break	2.87±0.08	2.72±0.28	2.35±0.13	2.10±0.13
	Modulus at Strain < 1 (MPa)	0.22±0.04	0.40±0.07	0.50±0.09	0.63±0.08
	Modulus at Strain < 0.4 (MPa)	0.13±0.03	0.17±0.03	0.20±0.04	0.26±0.04
PLGA4A_45-PVA	Strength (MPa)	0.92±0.11	0.94±0.11	0.75±0.18	1.03±0.27
	Strain at Break	—	3.15±0.41	2.61±0.56	2.05±0.38
	Modulus at Strain < 1 (MPa)	0.19±0.02	0.29±0.04	0.28±0.08	0.52±0.07
	Modulus at Strain < 0.4 (MPa)	—	0.23±0.02	0.24±0.06	0.27±0.04
PLGA4A_40-PVA	Strength (MPa)	0.81±0.02	0.84±0.10	0.92±0.07	1.20±0.21
	Strain at Break	—	3.08±0.14	3.60±0.00	2.11±0.24
	Modulus at Strain < 1 (MPa)	0.23±0.01	0.29±0.04	0.32±0.02	0.58±0.05
	Modulus at Strain < 0.4 (MPa)	—	0.25±0.04	0.28±0.03	0.31±0.03
PLGA4A_35-PVA	Strength (MPa)	1.62±0.13	1.23±0.18	1.12±0.28	1.04±0.15
	Strain at Break	—	2.69±0.76	2.69±0.62	1.98±0.54
	Modulus at Strain < 1 (MPa)	0.47±0.04	0.56±0.14	0.61±0.09	0.75±0.09
	Modulus at Strain < 0.4 (MPa)	—	0.44±0.08	0.51±0.10	0.29±0.02

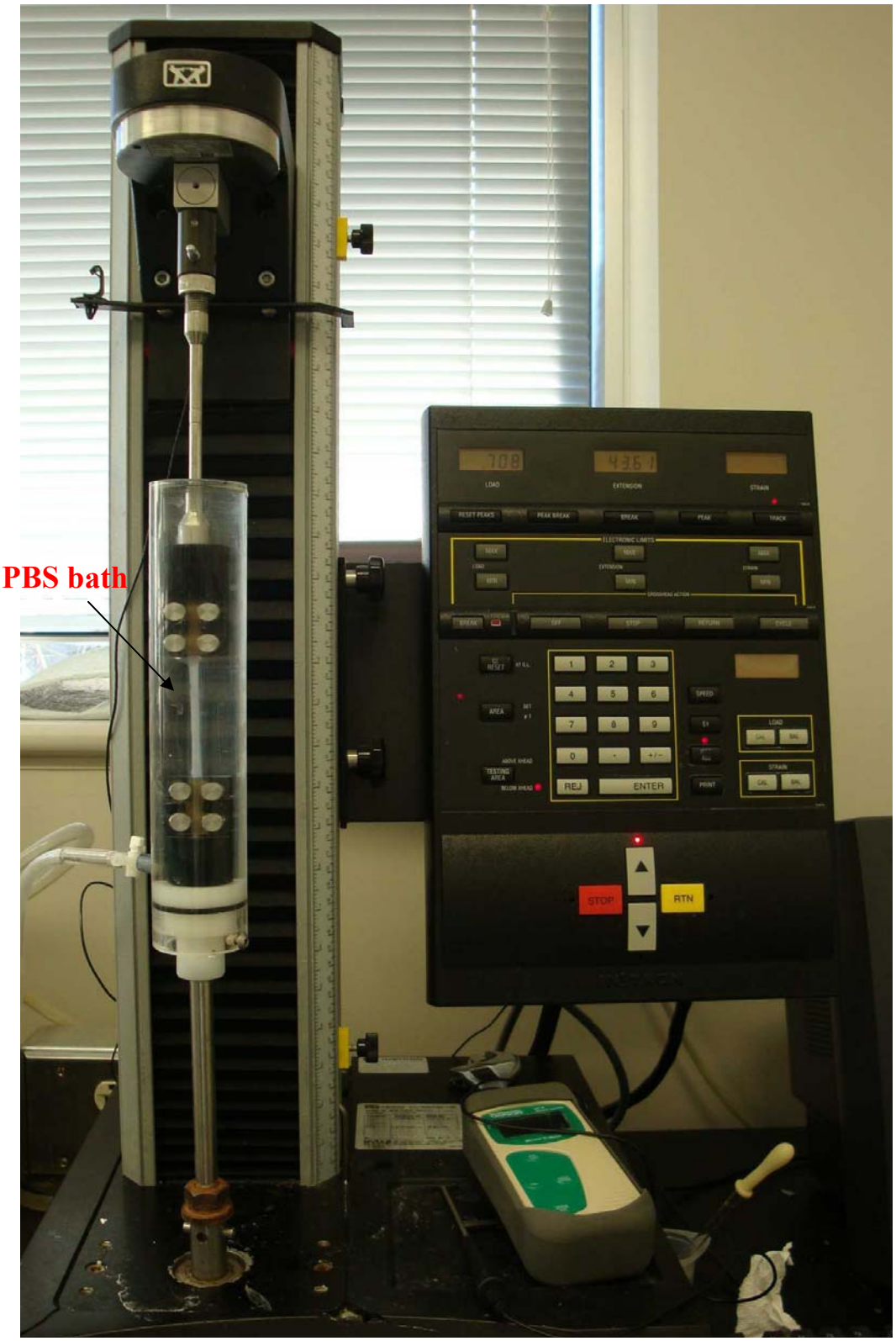

Figure 5.1.Instron setup for tensile testing of thin films in a PBS bath.

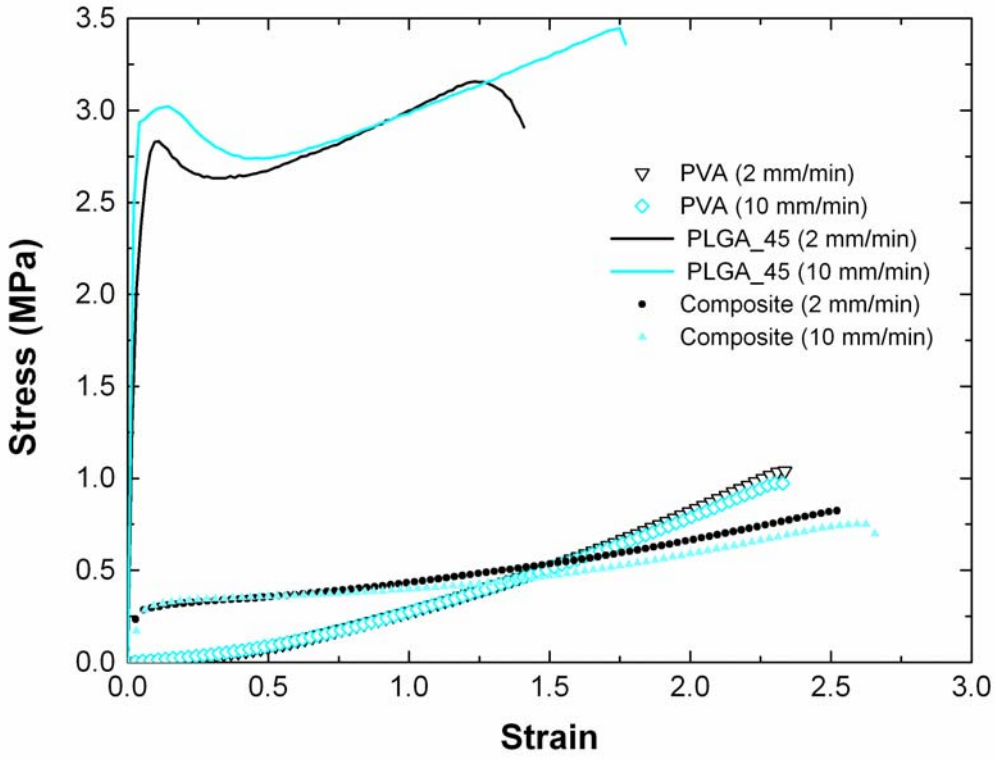

Figure 5.2. Comparison of tensile testing plots of PLGA_45 fiber mats, PVA hydrogels and their composites in neutral PBS buffer tested at 22°C using different crosshead speeds.

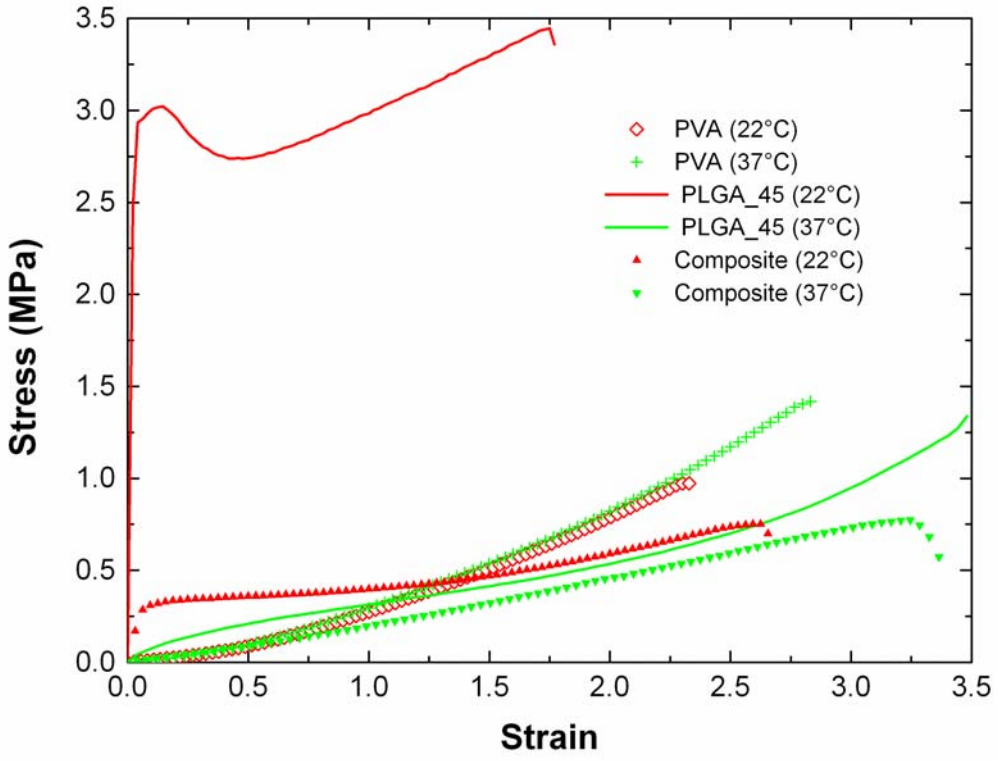

Figure 5.3. Comparison of tensile testing plots of PLGA_45 fiber mats, PVA hydrogels and their composites in neutral PBS buffer tested at a crosshead speed of 10 mm/min at different temperatures.

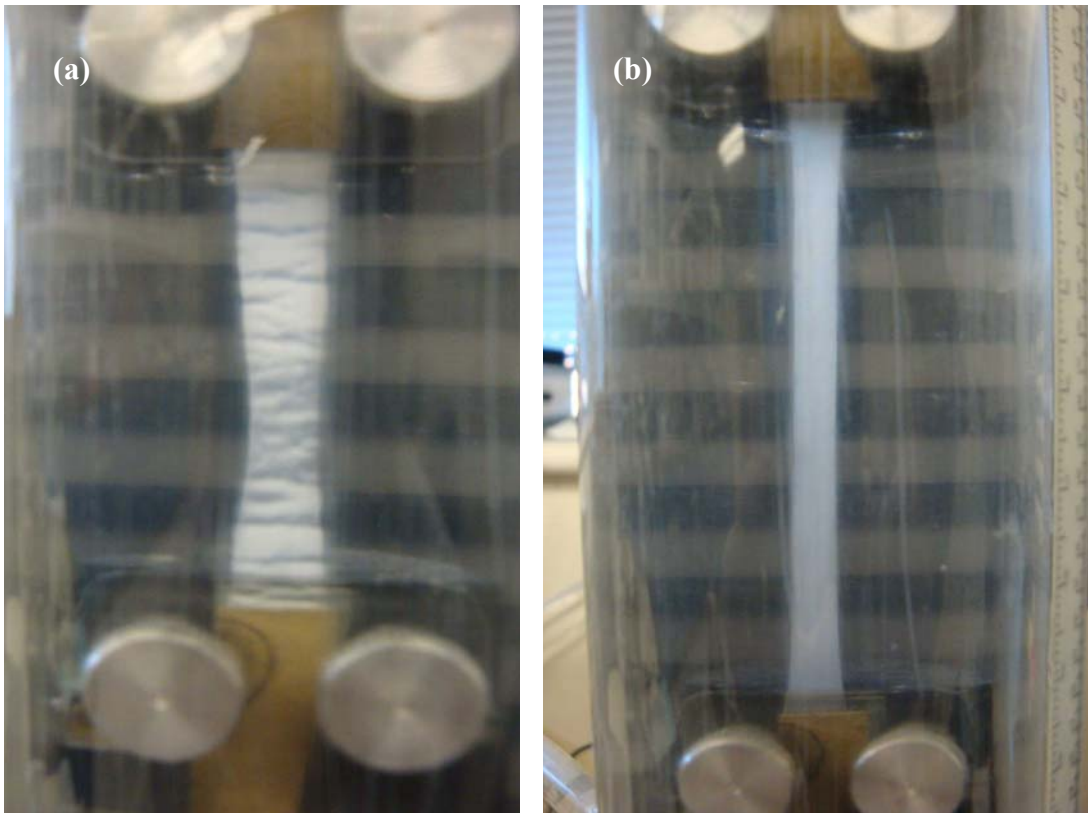

Figure 5.4. Photos of tensile testing of PLGA_45-PVA composite tested in PBS bath at (a) 22°C or (b) 37°C.

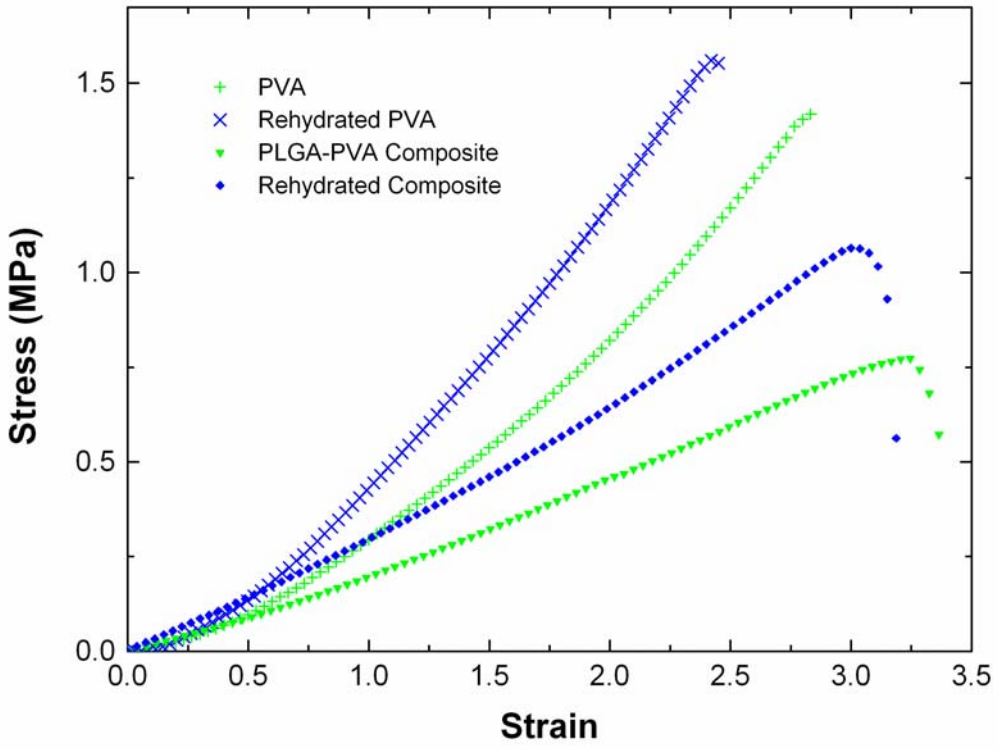

Figure 5.5. Comparison of tensile testing curves of as-made and rehydrated PVA hydrogels and PLGA_45-PVA composites in neutral PBS buffer tested at a crosshead speed of 10 mm/min at 37 °C.

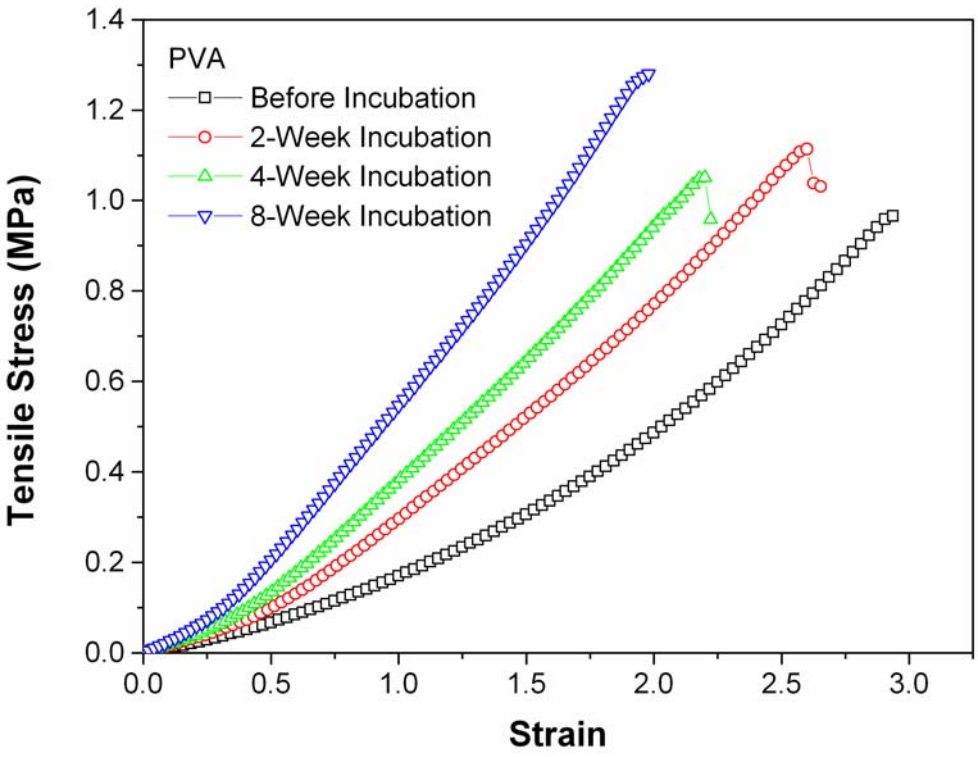

Figure 5.6. Tensile properties of rehydrated PVA hydrogel films during incubation tested at a crosshead speed of 10 mm/min in 37 °C neutral PBS buffer.

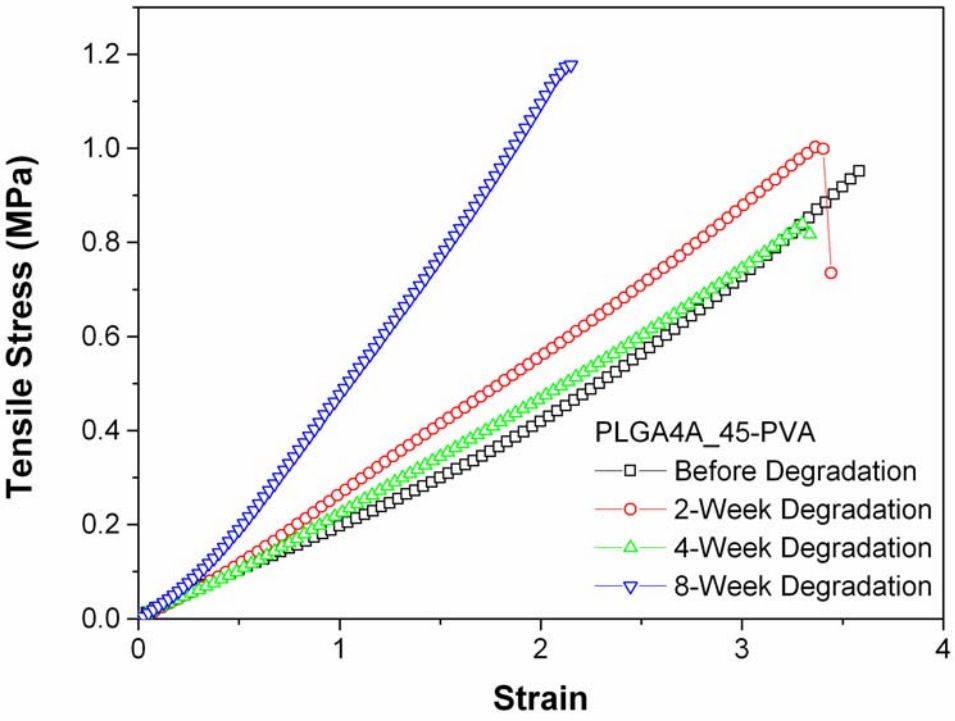

Figure 5.7. Tensile properties of rehydrated PLGA4A45-PVA films during incubation tested at a crosshead speed of 10 mm/min in 37 °C neutral PBS buffer.

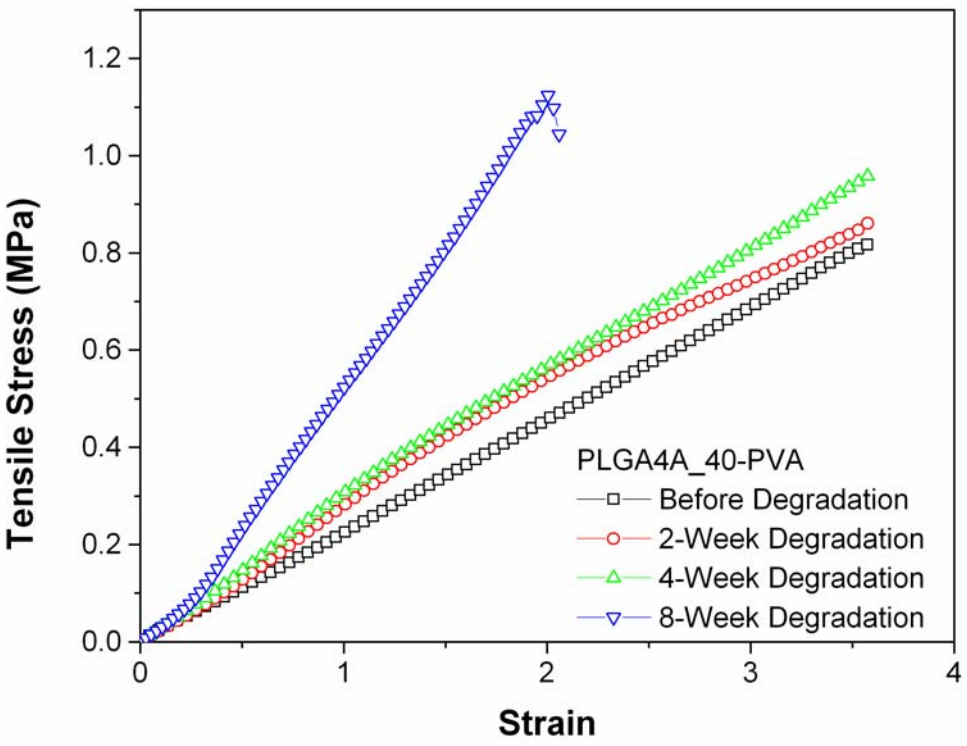

Figure 5.8. Tensile properties of rehydrated PLGA4A40-PVA films during incubation tested at a crosshead speed of 10 mm/min in 37 °C neutral PBS buffer.

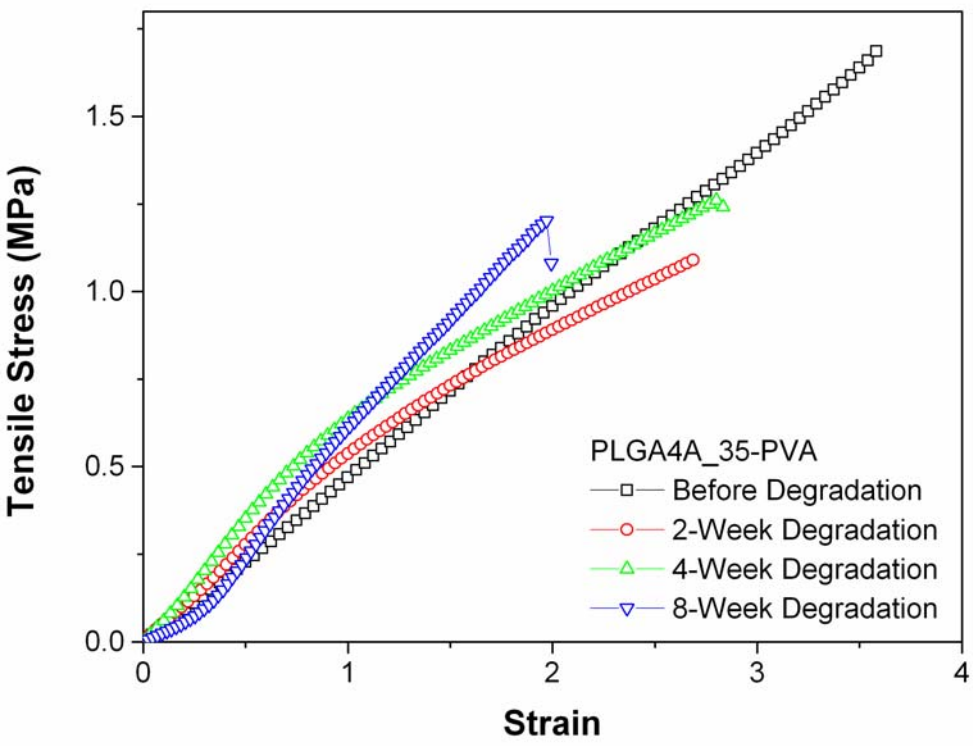

Figure 5.9. Tensile properties of rehydrated PLGA4A35-PVA films during incubation tested at a crosshead speed of 10 mm/min in 37 °C neutral PBS buffer.

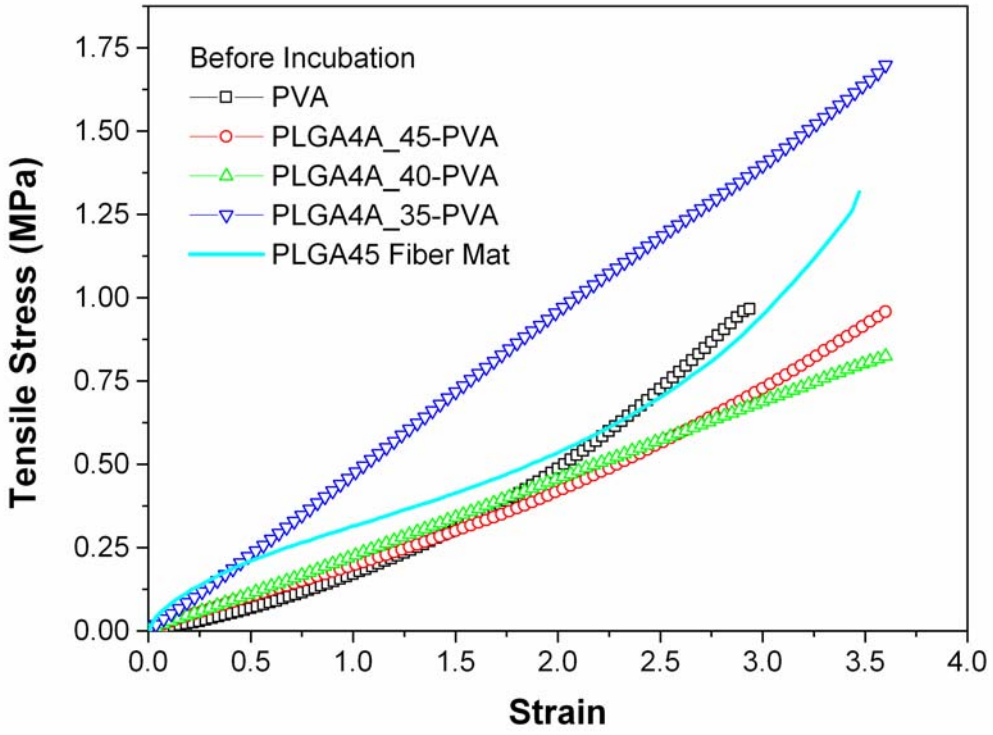

Figure 5.10. Tensile properties of PLGA fiber mat, rehydrated PLGA-PVA and PVA films before incubation tested at a crosshead speed of 10 mm/min in 37 °C neutral PBS.

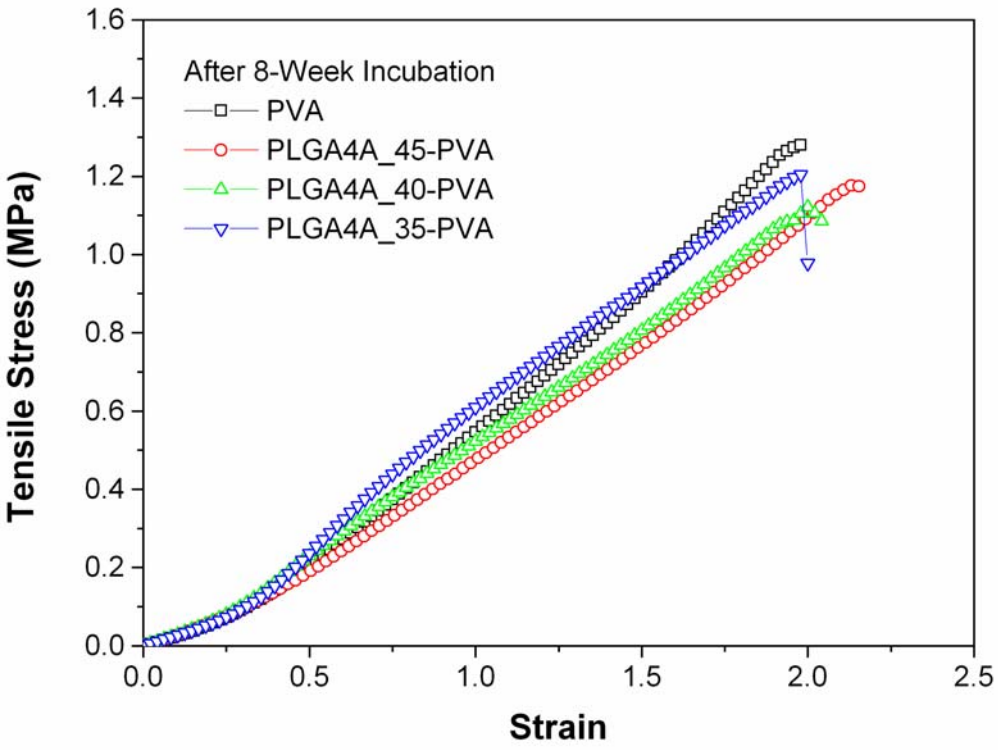

Figure 5.11. Tensile properties of all rehydrated PLGA4A-PVA and PVA films after 8-week incubation tested at a crosshead speed of 10 mm/min in 37 °C neutral PBS buffer.

Chapter 6: Plasma-Based Surface Modification

Surface modification creates chemical functional groups that interact with the polymer matrix to enhance interfacial adhesion and mechanical properties of polymer-polymer composites. Gas plasma treatment affects the surface properties of the exposed material without altering its bulk. Chemical functional groups and minor surface etching are created during plasma treatment. The improved wettability through chemical bonding and mechanical interlocking due to the rough surface have potential for improving interfacial adhesion of polyethylene fiber-VE composites. In this chapter, oxygen plasma will be applied on polypropylene fibers to increase the hydrophilicity of the surface. Silane coupling agents will be added immediately after oxygen plasma treatment in order to graft stable functional groups.

6.1. Experimental

6.1.1. Materials

Polypropylene (PP) fibers (Hills Inc.) were melt-blown using ExxonMobil PP3746G granular homopolymer with a melt flow index (MFI) of 1500. Vinyltrimethoxysilane (VTMS) (Aldrich) was used as a silane coupling agent. Acetic acid (Sigma-Aldrich) was used to adjust the pH of VTMS aqueous solution.

6.1.2. Procedure of Surface Treatment

A planar Dielectric Barrier Discharge (DBD) plasma system was used for the surface treatment with desired gases. The construction of the DBD reactor is shown in

Figure 6.1. The distance between the electrodes was 3 mm and the power output during plasma treatment was approximately 0.1 W/cm^2 with a frequency of 165 Hz. The area of each electrode was approximately 225 cm^2. Oxygen (O_2) was used as the desired treatment gas. A flow rate of 1 L/min pure O_2 was injected into the space between two electrodes at atmospheric pressure for more than 2 minutes before discharge to allow a uniform glow discharge. Treatment time varied from 15 to 180 seconds and both sides of PP fiber meshes were exposed to oxygen plasma for the same period. VTMS, a silane coupling agent with a vinyl functional group, was dissolved in deionized water to make a 0.3wt% solution. Its pH was then adjusted to 3.5 by drop-wise addition of acetic acid [1]. The solution was prepared one hour prior to use to allow complete hydrolysis and then used within two hours to limit condensation in the solution. No more than one hour after oxygen-plasma treatment, PP meshes were soaked in the VTMS solution for 10 minutes and then dried in a vacuum oven at 60°C for at least 40 hours to allow for condensation of the siloxane linkages and subsequent removal of water. The reaction mechanism is described in Figure 6.2, which is adapted from Rahmathullah et al. [2]. The suggested VTMS polycondensation temperature of 125°C was decreased to 60°C because plasma-treated PP was found to degrade during polycondensation of silane coupling agents at 125°C. Interestingly, untreated PP exhibited resistance to degradation during polycondensation of VTMS at 125°C.

6.1.3. Characterization

Elemental composition and chemical functional groups on the fiber surface were analyzed by X-Ray photoelectron spectroscopy (XPS). XPS spectra were obtained using

a Kratos Axis Ultra 165 spectrometer equipped with a hemispherical analyzer. The X-ray was generated with an Aluminum Kα (1486.7eV) monochromatic source energized at 20 kV and 100 W, and irradiated at a 1 mm × 0.5 mm area. The takeoff angle was adjusted to 90° with respect to the sample surface. The pressure in the analysis chamber was $<10^{-9}$ mbar. Surface charge effects were neutralized by using a flood gun. A value of 285.0 eV for the hydrocarbon C1s core level was used as the calibration energy for the binding energy scale.

While XPS functional group analyses provide information from a surface layer about 10nm in depth, contact angle measurement can give true surface information [3]. Static contact angle measurements using the sessile drop method were performed on a modular CAM200 Optical Contact Angle and Surface Tension Meter (KSV Instruments, Ltd., Finland), by dispensing a drop of deionized water with known volume from a microliter syringe onto the sample surface at ambient conditions. A monochromatic LED light source was used to image the water drops and the images captured were used to measure contact angles (θ) using Young - Laplace curve fitting. At least ten measurements were made for each sample.

The amount of VTMS grafted on PP fibers was determined by heating the treated PP fiber mats to 800°C in N_2 flow at a rate of 10°C/min using a TA Instruments TGA Q50 thermogravimetric analyzer. Since crosslinked siloxanes are stable at a temperature as high as 800°C, but PP decomposes at a much lower temperature, the weight remaining at 800°C was taken as the weight of grafted VTMS. Samples weighing approximately 20 mg were used.

A TA Instruments DSC Q2000 differential scanning calorimeter (DSC) was used to determine the melting temperature (T_m) and heat of melting (ΔH_m) of untreated and treated PP fibers under N_2 flow. Sample sizes were about 3 mg. Temperature scans were performed from -70°C to 200°C at a heating/cooling rate of 10°C/min.

Fiber surface morphologies were studied using ESEM with an acceleration voltage of 3 keV in high vacuum mode. Details are described in Chapter 3.

6.2. Results and Discussion

The surface treatment followed in this study involved a two step process. Theoretically, plasma treatment with O_2 can add functional groups such as hydroxyl, ether, carbonyl, and carboxyl groups to the surface [3-5]. Silane coupling agents covalently graft to the polymer surface via functional groups such as hydroxyl groups and polymerize by condensation reactions to form a crosslinked network [1-2]. Generally a shorter plasma treatment time is favored for adding functional groups to the surface. Kowalonek et al. studied the influence of side groups and polarity of polymers on surface modification by air plasma and found that PP had an optimal treatment time of 75 s while PE was optimal at 15 s [6]. They proposed that methyl groups on the side chains of PP were easily oxidized to form CO_2 and therefore hydrophilic functional groups were formed only after side chains were oxidized. In our study, we used treatment times ranging from 15 s to 180 s in an attempt to determine the optimal treatment time. Oxygen plasma treated PP (O_2-PP) and VTMS grafted PP (VTMS-PP) fibers were analyzed using untreated PP fibers as a control.

6.2.1. X-Ray Photoelectron Spectroscopy

The XPS survey spectrum of VTMS-PP in the range of 0-1200 eV given in Figure 6.3 clearly showed peaks corresponding to C at 285 eV, O at 532.5 eV, and Si at both 153.5 and 102.6 eV. Also in Figure 6.3, the XPS survey spectrum of O_2-PP shows two peaks corresponding to C and O while untreated PP only had one peak at 285 eV corresponding to C. Atomic ratios of O:C and Si:C for O_2-PP, VTMS-PP and untreated PP were compared as a function of the treatment time in Figure 6.4. It is clear that 30 s and 180 s plasma treatment gave the highest Si:C ratio, while 15 s plasma treatment resulted in the lowest O:C and Si:C ratios. Oxygen concentrations of O_2-PP samples showed similar trends as those of VTMS-PP samples. Oxygen concentration increased with longer treatment times, but the plasma-induced hydrophilic functional groups reached equilibrium at an O:C ratio of approximately 0.3, which was also noticed by Cui and Brown [3]. They explained that the methyl groups on the polymer chains oxidize during plasma treatment so that the backbone carbons remain relatively unaffected. Therefore, the oxidation reached equilibrium when 1/3 of the surface carbons, i.e. those from methyl groups, were oxidized. The XPS results for O_2-PP were obtained one day after the treatment. However, Cui and Brown discovered that plasma-treated PP films do not show significant changes in surface composition obtained from XPS after being stored in air at room temperature for eight days [3].

Figure 6.5 shows the high resolution XPS carbon (C1s) spectrum of a PP fiber surface before and after processing for 15 s to 90 s in the oxygen plasma, as well as after VTMS grafting. Chemical components and their concentrations of the C1s peak can be obtained by deconvolution using Gaussian-Lorentzian fit, and the peak positions and the

types of functional groups are based on literature values [3-4, 7]. C1s spectrum of untreated PP can be well fitted with one peak at binding energy E_b = 285 eV, which represents the hydrocarbon [-(C-C)-] and [-(C-H)-]. After plasma treatment, the C1s peak broadens towards higher energy values in the form of a long tail extending up to 292 eV. This indicates that oxidized carbon species at higher binding energy appear. C1s spectrum of oxidized PP can be well fitted by introducing four oxidized carbon peaks, i.e. alcohol [-(C-O-H)-] and/or ether [-(C-O-C)-] at 286.3 eV, carbonyl [-(C=O)-] and/or acetal [-(O-C-O)-] at 287.2 eV, carboxyl [-(C=O)-O-] at 288.7 eV, and carbonate [-O-(C=O)-O-] at 290.1 eV. Following VTMS treatment, the C1s peak becomes narrower and the tail shortens to 287.5 eV. C1s spectrum of VTMS-PP can be deconvoluted with three peaks associated with hydrocarbon, alcohol/ether, and carbonyl/acetal, respectively. Since all high resolution C1s spectra of VTMS-PP samples were found to be similar, only the results of VTMS-PP after 30s oxygen plasma treatment is shown in Figure 6.5. The atomic concentration of each component for all samples discussed above is listed in Table 6.1. It is clear that the concentration of the hydrocarbon component decreases with increasing plasma treatment time. C-OH or C-O-C is formed at a short treatment time, but the concentration decreases as further oxidization occurs. The atomic concentrations of more oxidized carbon species increase as the treatment time increases, except for (C=O)-O concentration that undergoes almost no change. We can assume that the alcohol or ether group is created as soon as enough discharge energy is applied. As the discharge energy increases, the oxidized carbon species oxidize further and more hydrocarbon bonds are oxidized, until the oxidization process reaches equilibrium. After VTMS treatment, the concentration of hydrocarbon greatly increases, as only 5%

alcohol/ether carbon and less than 1% carbonyl/acetal carbon are present. This may be attributed to the fact that –OH groups reacted with VTMS and highly oxidized carbon species are fully oxidized to CO_2 during the VTMS grafting process. It is worth mentioning that a takeoff angle of 90° was used on the fibers to obtain higher intensity at the expense of a larger penetration depth. This may result in an altered distribution of carbon functional groups from a more precise distribution obtained using angle resolved XPS, which can provide depth distribution of chemical composition on a smooth surface [8-9].

6.2.2. Water Contact Angle Measurements

Water contact angle (CA) measurements were used to evaluate the influence of time delay between plasma conditioning and the subsequent silane treatment. The changes to surface chemistry after the plasma treatment are potentially complex as the hydrophilic functional groups can reorganize to reduce surface energy while, conversely, free radicals can continue to create additional hydrophilic surface functionality through further reaction with atmospheric oxygen. Contact angles as a function of both treatment time and delay time are compared in Figure 6.6. The significant standard deviation of contact angle measurements of O_2-PP mats indicates that the surface treatment was not uniform. Nevertheless, a slight decrease of CA for treatment times of 15 s, 90 s and 120 s is observed but almost no change for treatment times of 30 s, 60 s and 180 s after a delay time of approximately 30 minutes. After 24 hours, CA for treatment times of 15 s, 90 s, 120 s and 180 s approach values found right after treatment, but CA for 30 s and 60 s treatment times significantly increase. This indicates that reorganization and

generation of hydrophilic groups were in equilibrium during short delay time for 30 s and 60 s plasma treatment. While for treatment times of 15 s, 90 s and 120 s, a net increase of hydrophilic ether, carbonyl, and carboxyl functional groups might contribute to the decreased CA observed during short delay times. After a 24 hour delay, plasma treatment times of 15 s to 60 s showed large recovery of CA. However, the 180 s treatment did not seem to be affected by delay time. After VTMS grafting, the CA was significantly increased in comparison to the O_2-PP, and became very close to that of untreated PP.

6.2.3. Morphology of Fiber Surface Analyzed with Environmental Scanning Electron Microscopy

ESEM micrographs of treated and untreated fiber surfaces are given in Figure 6.7 and clearly show that treated fibers possessed rougher surfaces than untreated fibers and that roughness increases with treatment time. After the VTMS was crosslinked on the surface, the surface was still rougher than that of untreated PP. These results suggest that 15 s of plasma exposure is too short to greatly oxidize the methyl groups of PP, while more than 60s of plasma exposure significantly etches the polymer surface.

6.2.4. Thickness of Grafted Layers Estimated from Thermogravimetric Analysis

Based on both XPS and CA results, 30 s was selected as the optimal treatment time and was used as the baseline for this study. TGA results indicated approximately 1 wt% VTMS grafted onto PP after 30 s of plasma treatment. This corresponds to a grafted layer about 2nm in thickness if it is assumed that the crosslinked VTMS covers the fiber surface uniformly.

6.2.5. Differential Scanning Calorimetry

Although ESEM analysis showed clear signs of surface degradation, no appreciable differences in the melting transition temperature and heat of melting (ΔH_m) were observed in DSC thermograms for treated and untreated fibers as shown by Figure 6.8. T_m for all untreated and treated PP was about 161°C and ΔH_m at the corresponding melting transition was approximately 90 J/g. It is interesting that all PP fibers showed different thermal properties at the melting transition in the second heating ramps given in Figure 6.9, although ΔH_m was about 80 J/g for all samples. The decreased crystallinity might be attributed to different crystalline structures formed during cooling. Untreated PP had four distinct melting peaks at 144, 150, 157 and 164°C, but O_2-PP only had two peaks at 156 and 163°C. After VTMS treatment the peak at 163°C reduced to a shoulder. The two peaks at 144 and 150°C for untreated PP are not common, and small crystallites or imperfections associated with amorphous regions may be formed at the cooling rate (10°C/min) that was selected. After increasing the cooling rate to 40°C/min or decreased to 2°C/min, the two peaks at lower temperatures disappeared. The typical DSC thermogram of PP has two melting peaks because of the semi-crystalline nature of PP. At most processing conditions, crystallites formed during cooling are not perfect. Therefore, the melting process is accompanied by recrystallization and increased crystal ordering. The overall peak is superimposed with melting of original crystallites, reorientation of imperfect structures, recrystallization, and melting of newly formed crystallites [10]. The peak at the highest melting temperature represents the melting of crystallites formed through recrystallization during melting. The recrystallization during melting can be eliminated by increasing the heating rate to 20°C/min. Slow cooling

(2°C/min) or crystallizing isothermally at higher temperature will reduce the imperfection so that no noticeable recrystallization peaks in the DSC thermogram can be seen, as this may also be the case for the as-received PP fiber which only showed a small shoulder at 160°C on the melting peak without obvious split. The two lower T_m for O_2-PP were not observed. We think that O_2 plasma caused scission of polymer chains, possibly in the amorphous region, which eliminated the small crystallite formation at the cooling rate of 10°C/min. As for the reduced recrystallization capacity during melting for VTMS-PP, we believe that the VTMS linkages functioned as crosslinks on PP, which hindered recrystallization [10].

6.3. Chapter Summary

Surface modification was applied to polypropylene fibers via two methods: a single-step oxygen plasma treatment and a two-step silane treatment. Oxygen plasma can add hydrophilic functional groups, but also roughen the surface without affecting the bulk properties. Longer treatment time generally creates more oxidized groups and a rougher surface, but causes little increase in total functional groups. Hydrophilicity of oxygen plasma treated polypropylene fibers decreases after long-term storage. Optimum plasma treatment time for silane grafting is 30s. Surface modification changes recrystallization behavior of PP fibers. PP fibers coated with VTMS linkages showed significantly different thermal behavior compared to unrestrained PP fibers.

List of References

1. Almanza-Workman AM, Raghavan S, Deymier P, Monk DJ, Roop R. Aqueous silane-surfactant co-dispersions for deposition of hydrophobic coatings onto pre-oxidized polysilicon. Colloids and Surfaces A: Physicochem Eng Aspects 2004; 232:67-75.

2. Rahmathullah AM, Robinette EJ, Chen H, Elabd YA, Palmese GR. Plasma assisted synthesis of hollow nanofibers using electrospun sacrificial templates. Nuclear Instruments and Methods in Physics Research B 2007; 265:23-30.

3. Cui NY, Brown NMD. Modification of the surface properties of a polypropylene film using an air dielectric barrier discharge plasma. Applied Surface Science 2002; 189:31-38.

4. Wang C, He X. Polypropylene surface modification model in atmospheric pressure dielectric barrier discharge. Surface & Coatings Technology 2006; 201:3377-3384.

5. Harth K, Hibst H. Surface modification of polypropylene in oxygen and nitrogen plasmas. Surface and Coatings Technology 1993; 59:350-355.

6. Kaminska A, Kaczmarek H, Kowalonek J. The influence of side groups and polarity of polymers on the kind and effectiveness of their surface modification by air plasma action. European Polymer Journal 2002; 38:1915-1919.

7. Borcia G, Chiper A, Rusu I. Using a He + N_2 dielectric barrier discharge for the modification of polymer surface properties. Plasma Sources Sci Technol 2006; 15:849-857.

8. Gries WH. A general procedure for extracting quantitative depth information from take-off-angle-resolved XPS and AES. Applied Surface Science 1996; 100/101: 41-46.

9. Hamamura N, Yumoto M, Sakai T. Depth dependence of modified bond on surface processed PTFE using high E/n discharge. 1998 International Symposium on Electrical Insulating Materials Conference Proceedings, Toyohashi, Japan; IEEE Xplore, 1998. p. 163-168.

10. Karger-Kocsis J, editor. Polypropylene: Structure, Blends and Composites, Volume 1: Structure and Morphology. London: Chapman & Hall, 1995.

Table 6.1. High resolution XPS carbon (C1s) peak deconvolution results.

E_b	Functional groups	Atom %					
(eV)		untreated	15s	30s	60s	90s	VTMS+30s
285.0	C-H, C-C	100	56.23	54.86	50.70	41.36	94.30
286.3	C-OH, C-O-C	—	27.68	20.09	26.28	22.85	5.00
287.2	C=O, O-C-O	—	8.68	14.84	12.55	22.06	0.60
288.7	O-C=O	—	6.14	6.07	6.22	6.72	—
290.1	O-(C=O)-O	—	1.26	4.12	4.88	7.02	—

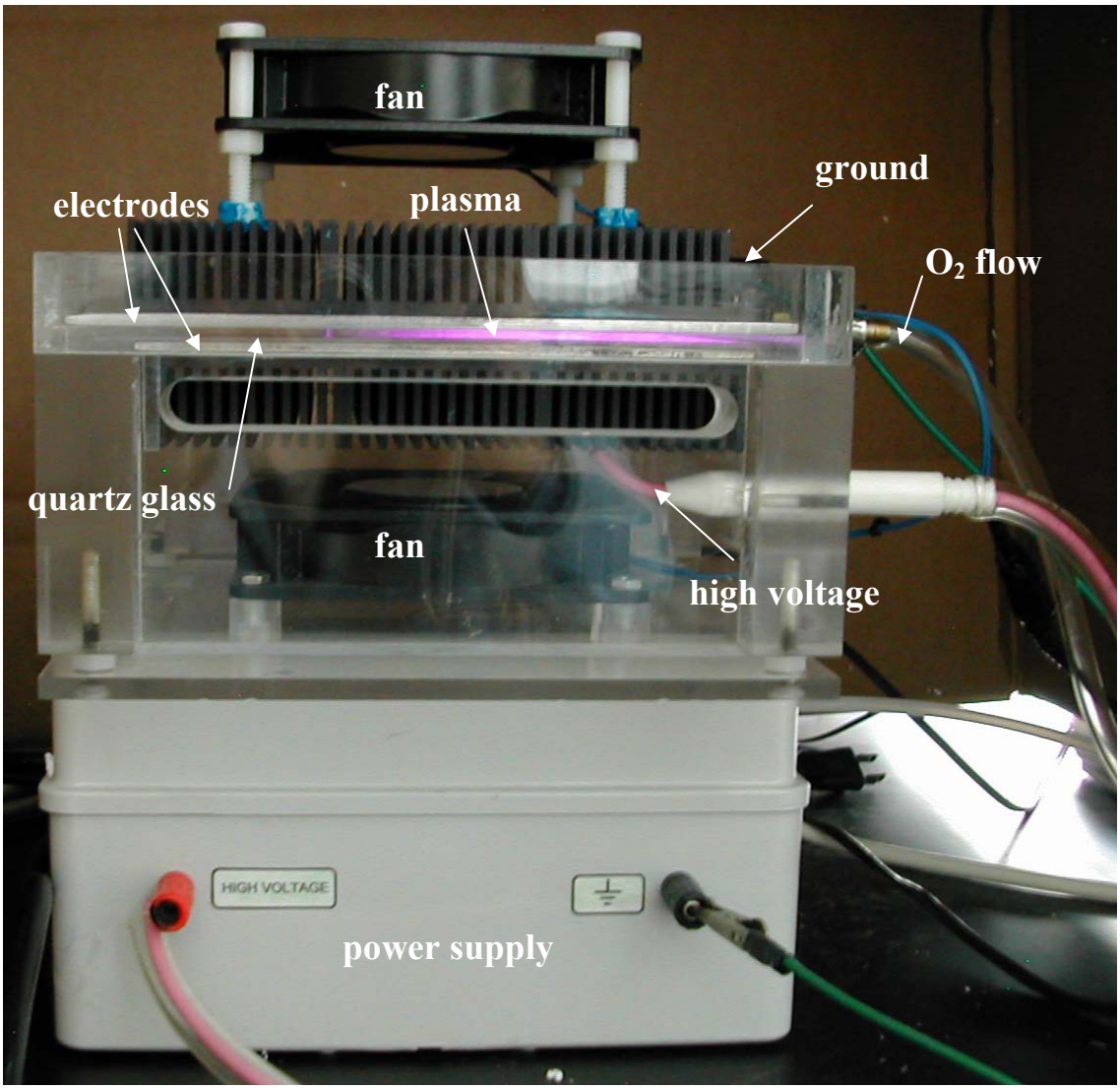

Figure 6.1. The dielectric barrier discharge (DBD) plasma reactor used in this work.

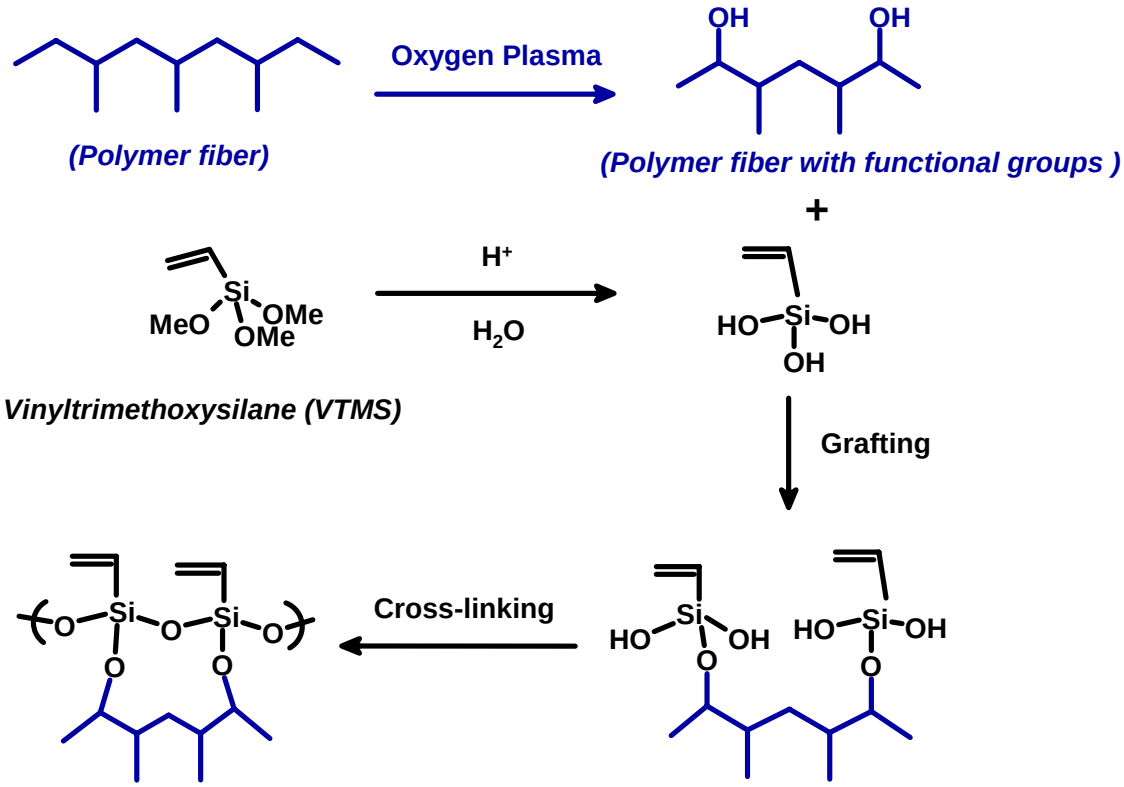

Figure 6.2. Reaction mechanism of surface modification to polypropylene using vinyltrimethoxysilane, a silane coupling agent. Adapted from reference [2].

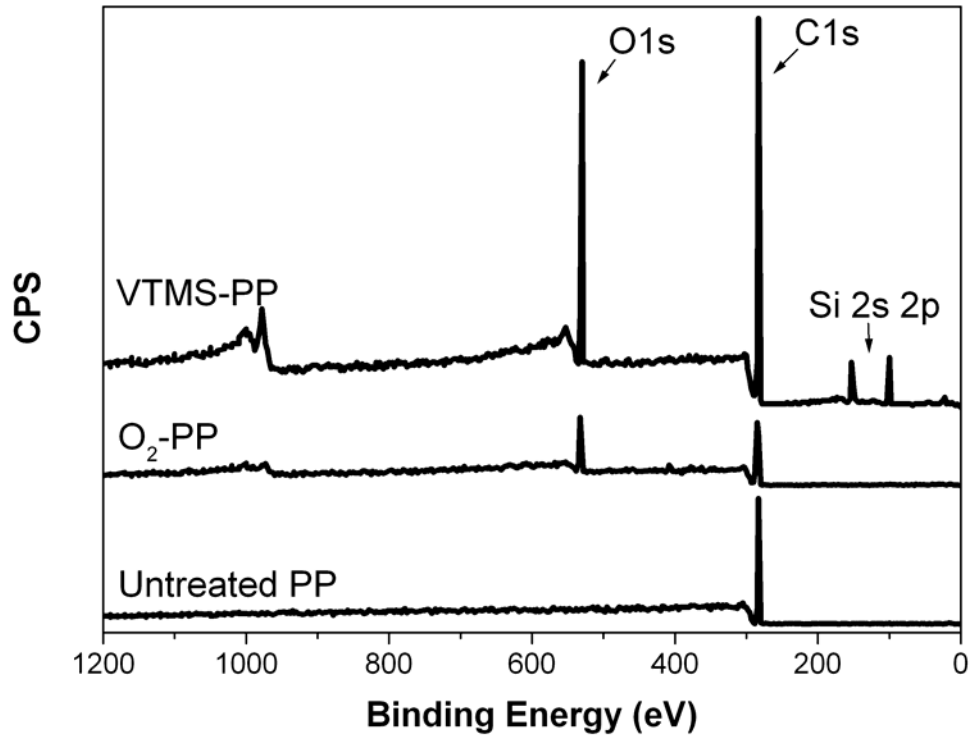

Figure 6.3. XPS survey spectra of untreated PP, O_2-PP and VTMS-PP.

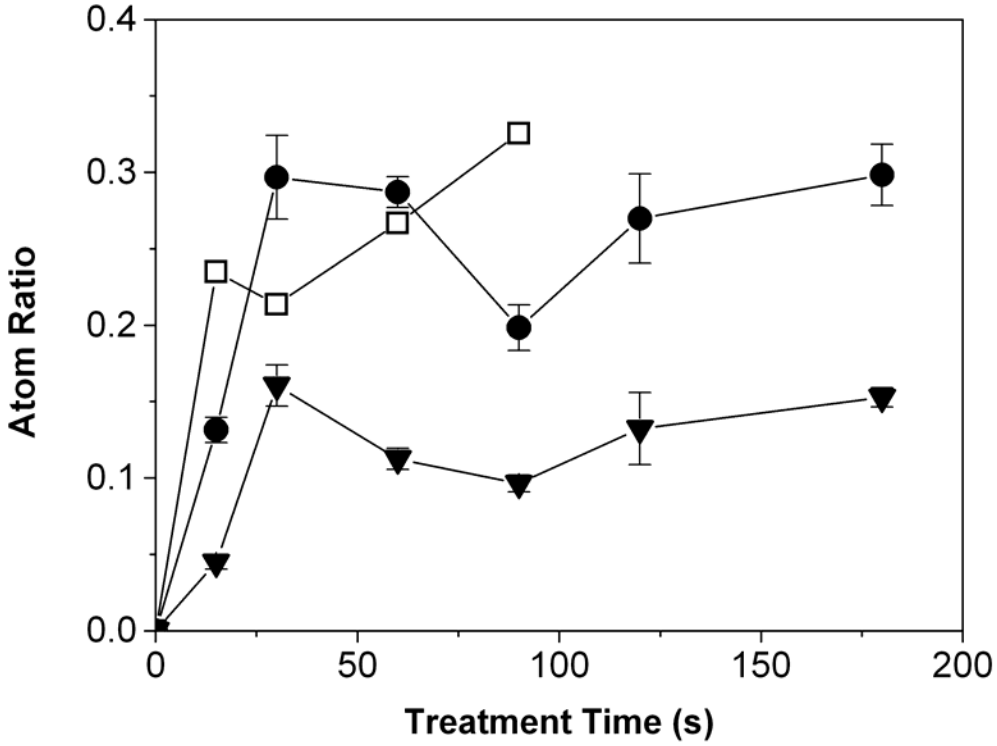

Figure 6.4. Atomic concentration ratios obtained from XPS analysis for —●— O:C of VTMS-PP, —▼— Si:C of VTMS-PP, —□— O:C of O_2-PP after 24 hours delay.

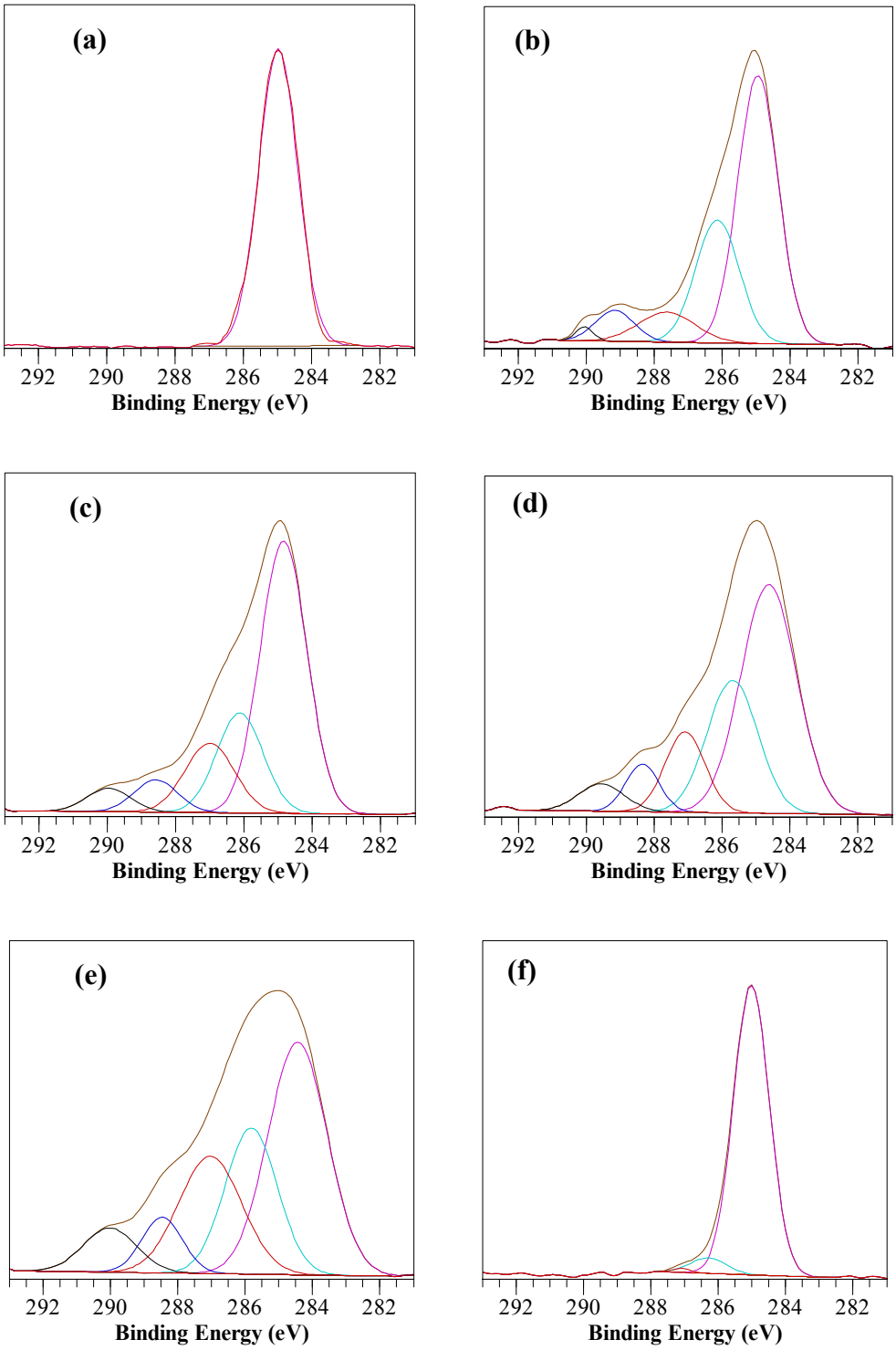

Figure 6.5. High resolution XPS carbon spectrum of untreated and surface treated PP fibers. (a) untreated; (b) 15 s, (c) 30 s, (d) 60 s and (e) 90 s in O_2 plasma; (f) VTMS after 30 s O_2 plasma.

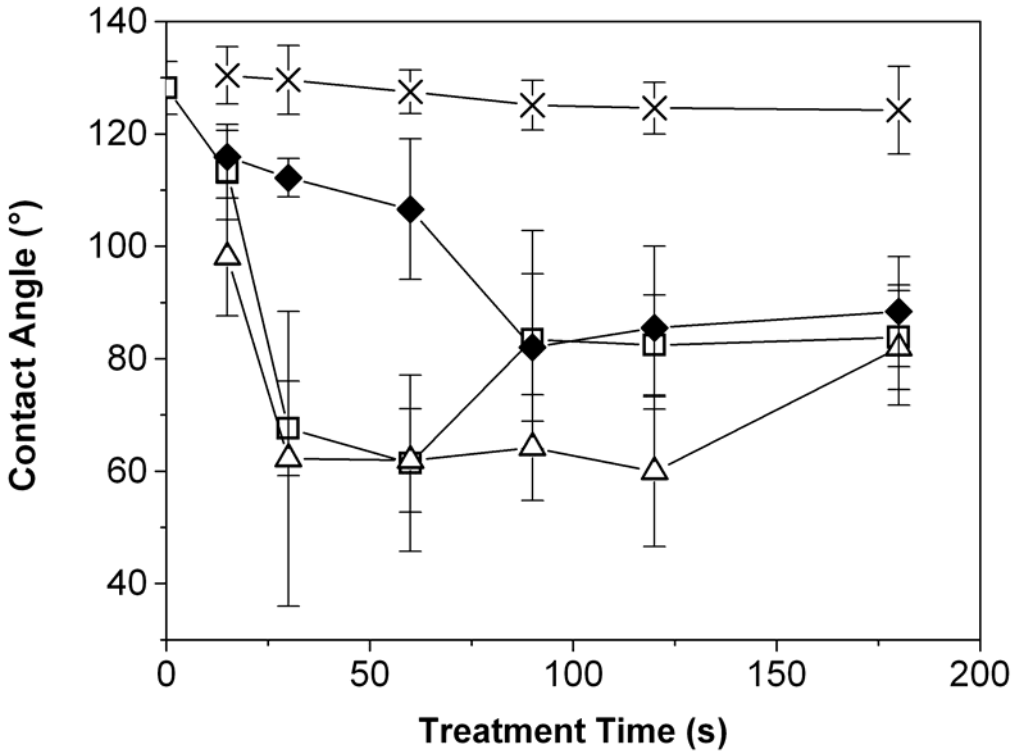

Figure 6.6. Contact Angles of PP at various treatment conditions: —□— 10 minute delay after O_2 plasma treatment, —△— 30 minute delay after O_2 plasma treatment, —◆— 24 hour delay after O_2 plasma treatment, and —×— after VTMS treatment.

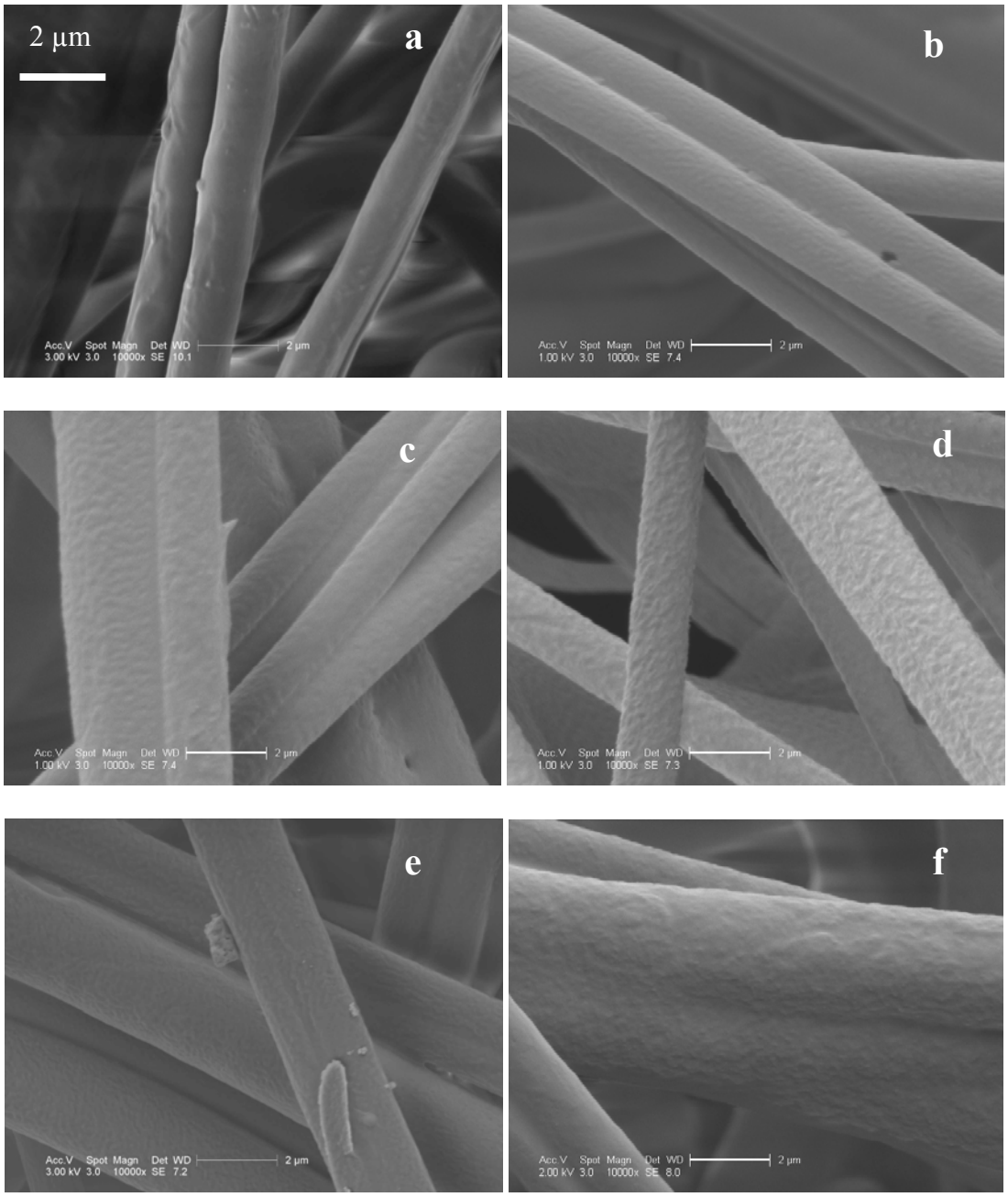

Figure 6.7. ESEM micrographs showing difference in surface roughness of PP fibers (a) before treatment, after (b) 30 s, (c) 90 s and (d) 180 s plasma treatment in O_2, and after VTMS treatment following (e) 30 s and (f) 180 s O_2 plasma treatment.

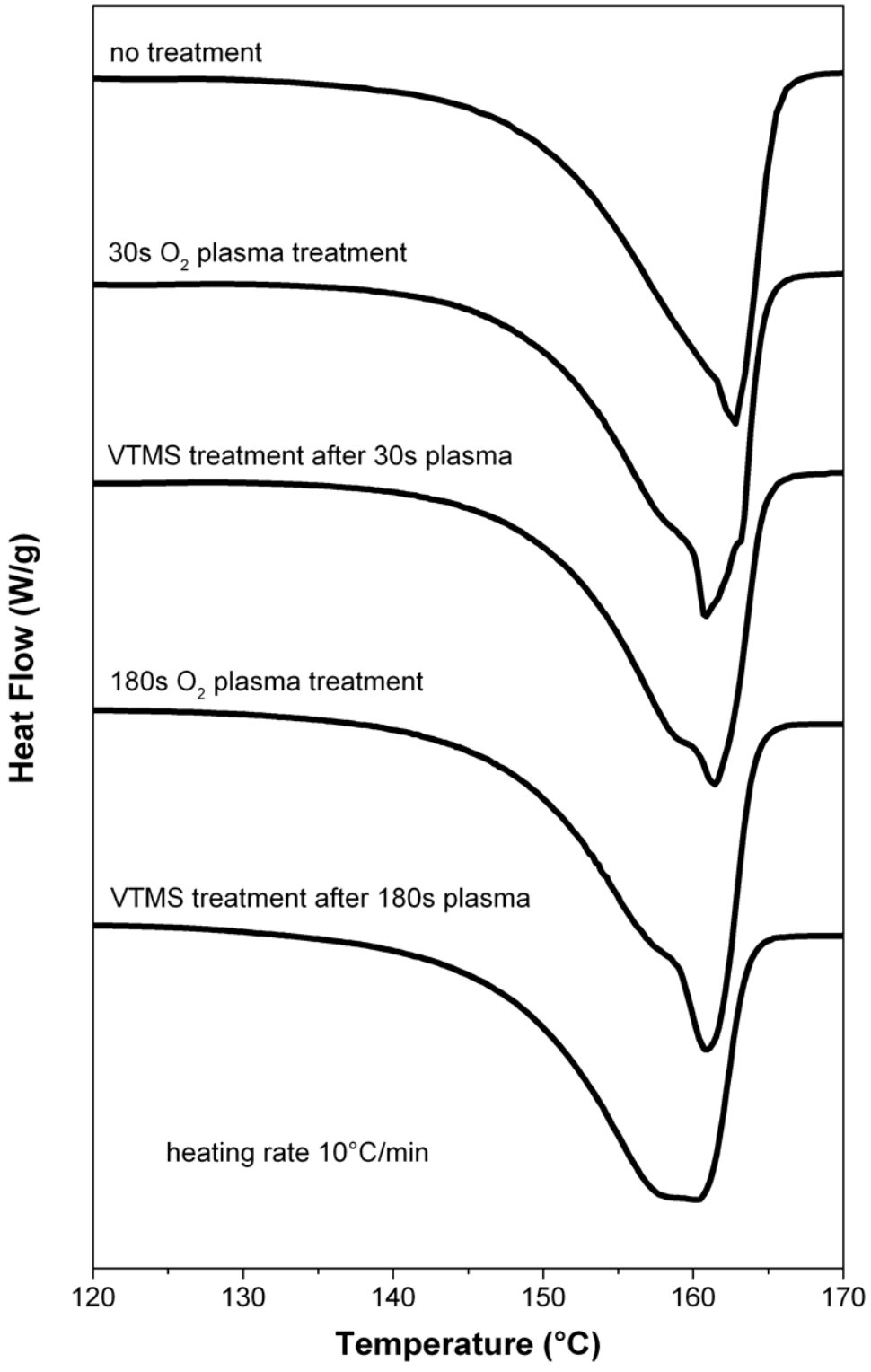

Figure 6.8. DSC thermograms of untreated PP, O_2 plasma treated PP and VTMS-grafted PP showed similar melting transitions.

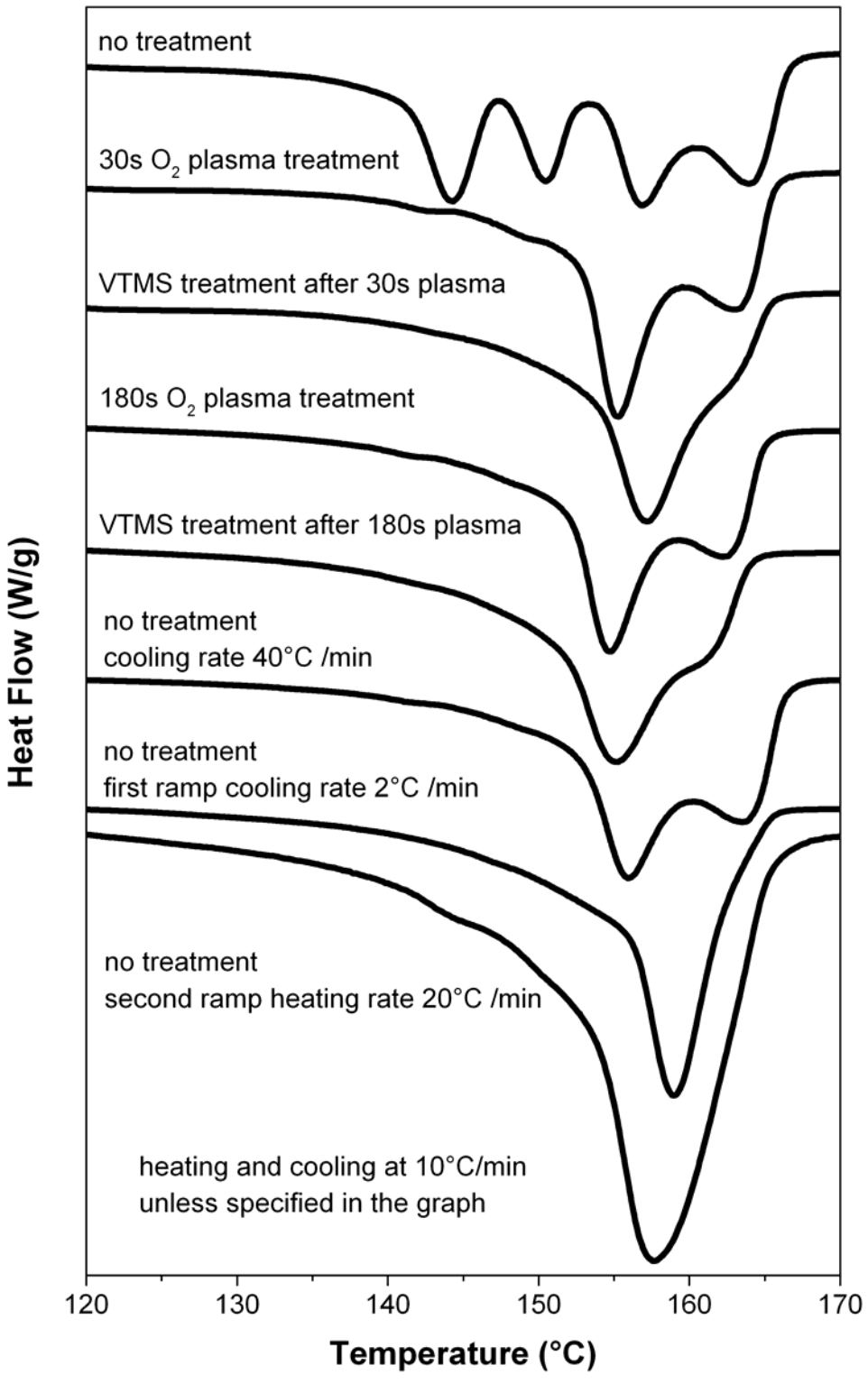

Figure 6.9. DSC thermograms of untreated PP, O_2 plasma treated PP and VTMS-grafted PP at the second heating ramp.

Chapter 7: Toughening Vinyl Ester Resins with Polypropylene Fibers

Vinyl ester (VE) resins have good chemical and mechanical properties but are brittle, which limits their applications in high performance composite materials. Rubber particles are usually used to toughen thermosetting resins because of their excellent energy absorption capacity, but they also greatly reduce mechanical properties. Rigid thermoplastics have been used as toughening materials while limiting the loss of mechanical properties. In this chapter, small diameter polypropylene (PP) fiber meshes were used to toughen commercial thermosetting resins via fiber encapsulation. As-received PP fibers and surface-treated PP fibers with oxygen-plasma or VTMS were compared for their toughening ability associated with the interface. Thermal, thermomechanical and mechanical properties were used to characterize the resin systems. Failure mechanism was discussed based on the fracture surface morphology.

7.1. Experimental

7.1.1. Materials

The commercial vinyl ester resin used in this work was Derakane® 411-350 Epoxy VE Resin (Ashland Specialty Chemical Co), which contains approximately 45% styrene as a reactive diluent. Commercial polypropylene (PP) fibers were obtained from Hills Inc. These fibers were melt-blown using ExxonMobil PP3746G granular homopolymer with a melt flow index (MFI) of 1500 and diameter of 1-2 μm. The fiber mats were composed of randomly oriented PP fibers with an average aerial density of 26 g/m^2. The free radical initiator used was Trigonox 239A (Akzo Nobel Polymer

Chemicals). This initiator contained 45 wt% Cumyl hydroperoxide, 45 wt% carboxylic ester and 10 wt% cumyl acid, as specified by the manufacturer. Cobalt Napthenate (CoNap) (OMG Americas) containing 6 wt% cobalt was used as an accelerator to enable room temperature cure. Heptane (99%, Sigma-Aldrich) was used in the density measurements.

7.1.2. Surface Treatment of PP Fibers

A Sigma Technologies large scale atmospheric plasma system was used for the plasma treatment. Oxygen (O_2) was the desired treating gas to increase the hydrophilicity of the surface. Helium (He) was used to initiate and generate the plasma at atmospheric pressure before O_2 was introduced to the system. O_2 and He were injected into the electrode at atmospheric pressure and allowed to diffuse through a porous metallic layer to form a uniform glow discharge. The operating frequency was 90 kHz with an operating power of 650 W. A mixed gas flow, which was composed of 1000 sccm O_2 and 10,000 sccm He, was used in this work. Treatment time varied from 1.3 s to 6.5 s.

VTMS-grafted PP fibers were obtained using the procedure described in Chapter 6. The fiber meshes were treated with O_2 plasma for 30 s using a small scale DBD plasma reactor before VTMS grafting.

7.1.3. Resin and Composite Fabrication

Neat VE resin test plaques were fabricated in a metal mold. VE monomer was degassed in a Thinky planetary centrifugal mixer ARE-250 for 15 minutes at a speed of 1500 rpm. Trigonox 239A, cobalt Napthenate and VE monomers were mixed at a weight

proportion of 1:0.12:100 to control the gel time at 1.5 hours. The mixture was degassed for another 4 minutes, poured into a mold, and then sealed. After being precured at ambient temperature for 24 hours, the mold was placed in an oven and allowed to postcure at 125°C for three hours.

PP-VE composites were fabricated via vacuum assisted resin transfer molding (VARTM). PP fiber meshes were cut into 150 mm×150 mm squares and stacked to the desired thickness. After being weighed, the stacked meshes were covered by release cloth and a distributing layer and then sealed in a vacuum bag. VE was mixed with Trigonox 239A and cobalt Napthenate at the same proportion as used in the preparation of neat VE resin test plaques. Once infiltration was complete, the inlet and outlet were sealed. The VARTM setup is shown in Figure 7.1. The composites were precured in the vacuum bag at ambient temperature for 24 hours, and then postcured at 125°C for three hours.

7.1.4. Composite Characterization

Densities of composites were measured based on Archimedes' principle. The density measurement setup is shown in Figure 7.2. Weight in air and weight in a heptane bath were measured for each sample. Density was calculated from weights of the sample and density of heptane. The equation for the density calculation is as follows:

$$\rho(sample) = \frac{\rho(hep\tan e) \times W(sample)_{in-air}}{W(sample)_{in-air} - W(sample)_{in-hep\tan e}}$$

Volume fractions of PP, VE and air were calculated based on density and weight of each component in the composite.

Dynamic mechanical analysis was performed on a TA Instruments DMA 2980 dynamic mechanical analyzer (DMA) with a dual cantilever clamp frame. Loss and storage moduli were recorded from 30°C to 180°C at a heating rate of 2°C/min and an oscillation frequency of 1 Hz. The glass transition temperature (T_g) of each VE system was taken as the temperature corresponding to the peak of the loss modulus curve. The activation energies of α and β transitions were calculated from multiple frequency sweeps (0.1, 0.3, 1, 3, 10 and 30Hz) at 3°C isothermal steps from -50°C to 180°C using DMA. Arrhenius activation energy is defined by the following equation [1]:

$$\log f = \frac{-E_a}{2.303R}\left(\frac{1}{T}\right)$$

where E_a is Arrhenius activation energy, f is frequency, and T is corresponding transition temperature at the frequency. The slope in the plot of log f vs 1/T is used to calculate the activation energy, giving

$$E_a = -2.303R \times slope$$

All samples were tested at an oscillatory-displacement amplitude of 15 μm. Typical sample dimensions in the DMA were 35 mm in length, 12.75 mm in width, and 3.15 mm in thickness.

A TA Instruments DSC Q2000 differential scanning calorimeter (DSC) was used to determine the glass transition temperature (T_g), melting temperature (T_m) and heat of melting (ΔH_m) of each VE system under N_2 flow. Sample sizes were about 3 mg. Temperature scans were performed from -70°C to 200°C at a heating/cooling rate of 10°C/min.

Mechanical properties were obtained using an Instron 8872 universal testing instrument. Data was collected using the Merlin software. Three-point single-edge notch

bend (SENB) specimens were used for plane-strain fracture toughness measurements. ASTM 5045-99 [2] specifies sample dimensions of 50.84 mm (span) × 12.71 mm × 6.35 mm to assure plain-strain conditions. An initial crack was made by first sawing a notch with length half the sample width, and then using a sharp razor blade to initiate a crack at the base of the notch. The samples were tested in flexural mode at a crosshead speed of 10 mm/min. Three-point bend specimens were used to measure flexural strength and modulus of elasticity in bending. Typical specimen dimensions were 50.84 mm (span) × 12.71 mm × 3.17 mm specified according to ASTM 790-03 [3] standard. The samples were tested in flexural mode at a crosshead speed of 1.3-1.5 mm/min calculated according to the actual sample dimension. Tests were stopped when samples were broken. Tensile strength and modulus of elasticity were measured according to ASTM D638-03 [4]. Dog-bone shaped specimens were machined according to dimensions of specimen type V. An extensometer was used to indicate the strain with the initial gage length set at 12.5 mm as shown in Figure 7.3. Samples were tested to failure at a crosshead speed of 1 mm/min. All tests were performed at ambient conditions. Fracture surfaces of composites were examined with ESEM using an acceleration voltage of 10 keV in high vacuum mode.

7.2. Results and Discussion

The density of PP-VE composite fabricated by VARTM was found to be about 1.1 g/cm^3. Since the density of PP is about 0.90 g/cm^3 and the density of cured VE resin was found to be 1.148 g/cm^3, the measured composite density is reasonable. For PP-VE composites, the calculated volume fractions of PP fibers and air were 20% and 0.3%,

respectively. The densities and volume fractions for neat VE resin and PP-VE composites using untreated PP (PP-VE), oxygen-treated PP (OPP-VE) or VTMS-treated PP (VPP-VE) are listed in Table 7.1.

PP used in this work has a melting temperature of 161°C and a flexural modulus of 2 GPa. In comparison, the amorphous VE thermoset has a modulus of 3.3 GPa and a T_g of ~115°C. Therefore, incorporation of PP fibers is expected to influence modulus and softening behavior. Plasma treatment roughens the PP fiber surface and the VTMS functional groups are expected to react with VE, so the modulus and softening behavior may also be affected by PP surface treatment.

7.2.1. Toughening VE Resins Using Untreated and Oxygen-Treated PP Fibers

Neat VE resin and PP-VE composites using untreated or oxygen-treated PP fibers were tested for flexural properties. Typical load-deflection curves in flexural testing for the three VE systems are shown in Figure 7.4. Flexural strength and modulus of elasticity in bending for all samples are included in Table 7.2. Neat VE resin had higher flexural strength and modulus of elasticity than PP-VE composite, with almost double the flexural strength of the composite using untreated PP fibers. Additionally, PP-VE composite using untreated PP showed better flexural properties than composite using oxygen-treated PP. The flexural strength of PP-VE composite was reduced by 1/3 while the flexural modulus was reduced by 20% after oxygen-plasma treatment of PP. The significant decrease of flexural properties for OPP-VE composite may be attributed to the degradation of the plasma-treated PP fibers under VE curing conditions. The degradation

of oxygen plasma-treated PP by oxidization was also observed during the suggested VTMS treatment conditions as discussed in Chapter 6.

ESEM micrographs of composite fracture surfaces were used to gage interface integrity. Analysis of the fracture morphologies showed obvious interfacial discontinuities between PP fibers and VE resin as seen in Figures 7.5a. Plasma surface modification to PP was used with the intent of improving interfacial discontinuities. However, oxygen treatment of PP fibers did not diminish void formation at the interface as shown in Figure 7.5b. The discontinuity may contribute to the significant reduction of flexural strength. Better flexural strength may be obtained with higher interfacial strength.

7.2.2. Toughening VE Resins using VTMS-Grafted PP Fibers

As discussed in Chapter 6, stable vinyl functional groups were grafted onto PP after VTMS treatment. The vinyl groups were expected to react with VE during curing to form covalent bonds between PP and VE so as to improve the interfacial strength. Additionally, oxidized carbon groups greatly decreased during VTMS treatment so PP would not degrade during composite fabrication.

7.2.2.1. Thermal and Thermomechanical Properties

Figure 7.6a shows storage modulus (E') as a function of temperature as measured by DMA for VE, PP-VE and VPP-VE systems. It was observed that neat VE polymer possessed a higher storage modulus than PP-VE and VPP-VE below the T_g of the VE resin. At temperatures between the T_g of VE resin and T_m of PP, PP-VE and VPP-VE

displayed higher storage moduli than the VE resin, with PP-VE possessing the highest storage modulus. This indicated that PP could increase the modulus of softened VE below its melting temperature. Above the melting temperature of PP, VE and PP-VE had similar storage moduli. However, VPP-VE showed slightly higher storage modulus than PP-VE below 105°C and above 150°C. The higher modulus may be a result of covalent bonds between PP and VE introduced by VTMS, while the lower modulus near the melting transition of PP may be related to surface damage of PP as observed by ESEM. Figure 7.6b gives the loss modulus (E") as a function of temperature at a frequency of 1 Hz. The T_g values of neat VE and composites were taken as the peak of the loss modulus curves. For comparison T_g was also measured using DSC as shown in Figure 7.7. These data are included in Table 7.3 and show that the composites possessed slightly higher T_g using both measurement methods. The T_g of PP-VE composite was 3°C higher than that of VE resin, and surface treatment did not affect T_g. These changes might be associated with the reinforcing nature of PP fibers. DSC scans also showed a melting peak at 161°C associated with PP for composites, and the heat of melting was about 9.7 J/g in the first ramp. Given that 20 v% (about 16 wt%) PP was in the composites, the equivalent ΔH_m of PP inside VE is 60 J/g, which is lower than that of PP before being embedded in VE. In an attempt to distinguish the annealing effect on PP fibers during post-curing of composites from potential interfacial effects, DSC scans were taken for PP fibers (virgin and treated) after isothermal conditioning at 125°C under N_2 flow for three hours to mimic composite cure conditions. The results are shown in Figure 7.8. An annealing step was observed around 130~135°C for all PP fibers in the first ramp. Otherwise, the

melting transition and the heat of melting in both ramps were similar to the controls (no annealing) shown in Figure 6.8 and 6.9.

The shape of the melting peaks of PP fibers confined by VE were found to be slightly different than observed for free PP fiber mats in the first ramp. It is possible that reorientation and recrystallization behaviors are affected by imposing predefined submicron structure. The second DSC ramps of VE and VE composites showed a 7°C increase of T_g. In contrast to free PP fibers, DSC thermograms of PP-VE and VPP-VE exhibited similar shapes of the melting transition in the second ramp where only two melting peaks at 156 and 163°C appeared. This also could be the result of PP and VTMS-PP fibers being confined to the submicron tunnels of the rigid VE matrix during recrystallization. Additionally, the heterogeneous interface could also be responsible for orienting crystallite growth [5]. It should be noted that free cross-linked VTMS-PP behaves similarly to the constrained fibers.

The thermal properties of VE systems after being tested in DMA (Figure 7.7) were also evaluated. The first heating ramp of all VE systems after DMA tests showed thermal properties closer to the second heating ramp of VE system before DMA tests, with the significant exception that crystalline character was significantly degraded as shown by a decrease in ΔH_m from 9.7 J/g to 3.5 J/g. All PP fibers and VE composites after being tested in DSC were examined using ESEM. Representative micrographs are given in Figure 7.9. The fibers inside the VE matrix during DSC testing maintained a fibrous morphology even at a heating rate as low as 2°C/min (Figure 7.9a, b) although fibers on the surface lost their original morphology (Figure 7.9c, d). In comparison, free

fiber mats almost completely lost their fibrous structures following DSC runs (Figure 7.9e, f).

Loss modulus curves as a function of temperature and frequency were obtained as described in the experimental section and shown in Figure 7.10. This data was used to determine the activation energy (E_a) associated with major transitions. VE showed one large transition around 114°C (1Hz) and the corresponding activation energy was 604 kJ/mol, which indicates it is the α-transition of VE. PP-VE and VPP-VE showed a large transition at about 116°C (1Hz) and a small transition near -5°C (1Hz). E_a for the major transition was 597 kJ/mol and that for the minor transition was 219 kJ/mol for PP-VE. Following VTMS treatment of PP, E_a of the major transition increased slightly to 607 kJ/mol and E_a of the minor transition at 1°C (1Hz) increased to 271 kJ/mol. The major transition for the composites is attributed to the T_g of the VE matrix. E_a for the minor transitions observed for the composites are higher than 100 kJ/mol, which means that they are α-transitions of PP instead of β-transitions of VE [1]. This is consistent with the T_g of PP reported to be in the range of -10~0°C. Surface modified PP-VE composites had higher activation energy than untreated PP-VE composites, possibly because of interfacial bonding between PP and the VE matrix via VTMS.

7.2.2.2. Mechanical Properties

The fracture toughness, tensile properties and flexural properties of VE resin, PP-VE and VPP-VE composites were obtained. Critical stress intensity factor (K_{IC}), critical strain energy release rate (G_{IC}) at fracture initiation, tensile strength (σ_M), modulus of

elasticity (E), flexural strength (σ_{fM}), and modulus of elasticity in bending (E_B) are given in Table 7.4.

The critical stress intensity factor for PP-VE composite was about 1.6 times that of VE resin, while the critical strain energy release rate for PP-VE composite was more than twice that of VE resin. Thus, fracture toughness is improved significantly by encapsulating PP fibrous mats in VE resin. After VTMS-grafting on the PP surface, a further increase in fracture toughness was observed. The possible reasons for this might be the change of the failure mode and improved stress/energy transfer between fibers and matrix after fiber-matrix coupling. The fracture morphology is discussed in the next section.

Neat VE resin had higher flexural strength and modulus of elasticity than both PP-VE composites, with almost double the flexural strength of the composites (Table 7.4). The experimentally measured flexural modulus of the PP-VE was approximately 2.92 GPa in comparison to 3.22 GPa for the neat VE matrix, which was slightly lower than a predicted modulus of 2.99 GPa based on the Voigt model (upper bound) [6]. This indicated that the upper bound model of the combining rule could reasonably fit the PP-VE system. The upper bound model can be applied because the moduli of both components were of similar magnitude, i.e. 3.22 GPa for the VE and 2 GPa for the PP, and the stiffer phase occupied over 80 v% in the composites [6]. The predicted modulus of 2.99 GPa for VPP-VE using the same model was slightly lower than the measured flexural modulus of 3.06 GPa. The difference between PP-VE and VPP-VE may be attributed to the greater interfacial strength created by covalent bonds between VTMS-modified PP and VE resin. Nevertheless, VPP-VE composites did not show a significant

difference in flexural properties compared to PP-VE composites, possibly because the weak nature of PP itself. The tensile modulus results match flexural properties well. Typical load-deflection curves in tensile testing for these systems are shown in Figure 7.11.

7.2.2.3. Fracture Surface Morphology

ESEM micrographs of composite fracture surfaces were used to analyze the dominant failure mode. Fracture surface morphologies of PP-VE showed obvious interfacial discontinuities as seen in Figures 7.12a and b. In contrast Figures 7.12c and d show that such discontinuities are reduced substantially in composites with VTMS-grafted PP fibrous mats. Fiber pullout and fiber breakage were the dominant failure modes in the toughening phase for the composite using untreated PP. The weak interface led to relatively easy fiber pullout at small loads. The increased fracture toughness of VE systems after encapsulating PP fibers might be the energy absorption from voids, fiber pullout and fiber breakage. However, for VTMS-treated PP, fiber breakage was the dominant failure mode in the toughening phase because the strong bonding at the fiber-matrix interface restrained the fiber pullout. Stronger interfacial interactions provided increased load-bearing capability by transferring load from the brittle matrix to the thermoplastic fiber. In addition, mechanical interlocking resulting from the rougher fiber surface might also contribute to improved fracture toughness. However, the PP fiber used in this work has weak tensile properties due to the low molecular weight (high melt flow index). This curtailed the ability of the thermoplastic phase to absorb energy

through deformation mechanisms. The use of higher strength PP fibers would probably increase fracture toughness.

7.3. Chapter Summary

Composites containing micron-sized PP fibers and VE matrices were fabricated using VARTM. The resulting composites contained approximately 20 volume percent PP fibers due to the relatively low aerial density of the PP mats. PP fibers showed good wetting characteristics in VE monomer; but, void discontinuities were generated at the interface of VE and PP fibers during cure. DMA showed the predicted negative contribution of the PP fiber phase on storage modulus, and a minor positive effect on the softening transition. Fracture toughness was greatly improved, but flexural strength was substantially decreased upon encapsulation of the PP fibrous phase. The loss in strength was partly due to the poor interface between the PP fibers and the VE matrix.

Plasma surface modification was used with the intent of improving interfacial discontinuities. However, surface treatment with oxygen plasma appeared to damage fibers and did not diminish void formation at the interface.

A two-step surface modification on PP using VTMS improved interfacial discontinuities by forming covalent bonds between matrix and fibers. Because of weak fiber material, mechanical strength and modulus did not show significant increases for the VPP-VE composite. Fracture toughness of the composite was slightly increased after surface treatment of PP, which might be attributed to improved interfacial load transfer via chemical bonding and mechanical interlocking. PP fibers encapsulated in VE matrix showed significantly different thermal behavior compared to unrestrained PP fibers.

Activation energies at the glass transitions were different for the three VE systems. The VPP-VE composite exhibits slightly higher activation energy at both glass transitions than the PP-VE composite.

List of References

1. Ferry JD. Viscoelastic Properties of Polymers, 2nd edition. New York: Wiley, 1970.

2. Standard Test Methods for Plane-Strain Fracture Toughness and Strain Energy Release Rate of Plastic Materials. Annual Book of ASTM Standards, Designation: D 5045-99. ASTM International, June 1999.

3. Standard Test Methods for Flexural Properties of Unreinforced and Reinforced Plastics and Electrical Insulating Materials. Annual Book of ASTM Standards, Designation: D 790-03. ASTM International, April 2003.

4. Standard Test Method for Tensile Properties of Plastics. Annual Book of ASTM Standards, Designation: D 638-03. ASTM International, January 2004.

5. Karger-Kocsis J. Polypropylene: Structure, Blends and Composites, Volume 1: Structure and Morphology. London: Chapman & Hall, 1995.

6. Whitney JM, McCullough RL, editors. Delaware Composites Design Encyclopedia, Volume 2: Micromechanical Materials Modeling. Pennsylvania: Technomic, 1990.

Table 7.1. Densities and volume fractions of VE systems.

	Density (g/cm^3)	Volume Fraction of PP	Volume Fraction of Air
VE	1.142±0.003	—	0.0059±0.0025
PP-VE	1.096±0.007	0.197± 0.019	0.0031±0.0005
OPP-VE	1.094±0.001	0.203±0.000	0.0034±0.0005
VPP-VE	1.097±0.005	0.196±0.021	0.0029± 0.0003

Table 7.2. Flexural properties of neat VE resin, PP-VE and OPP-VE composites.

Flexural Properties	VE	PP-VE	OPP-VE
σ_{fM} (MPa)	130±2	71±4	47±4
E_B (GPa)	3.22±0.07	2.92±0.07	2.33±0.07

Table 7.3. Thermal and thermomechanical properties of neat VE resin, PP-VE and VPP-VE composites.

	DMA		DSC (first ramp)		
	E' at 35°C	T_g	T_g	T_m	ΔH_m
	GPa	°C	°C	°C	J/g
VE	3.35	118	111	—	—
PP-VE	2.93	121	114	161	9.7
VPP-VE	2.97	121	114	161	9.5

Table 7.4. Mechanical properties of neat VE resin, PP-VE and VPP-VE composites.

	Fracture Toughness		Flexural Properties		Tensile Properties	
	G_{IC}	K_{IC}	σ_{fM}	E_B	σ_M	E
	J/m^2	$MPa \cdot m^{1/2}$	MPa	GPa	MPa	GPa
VE	231±41	1.08±0.15	130±2	3.22±0.07	89±2	3.44±0.13
PP-VE	596±27	1.77±0.06	71±4	2.92±0.07	47±3	3.25±0.16
VPP-VE	651±22	1.81±0.12	66±4	3.06±0.11	48±3	3.23±0.17

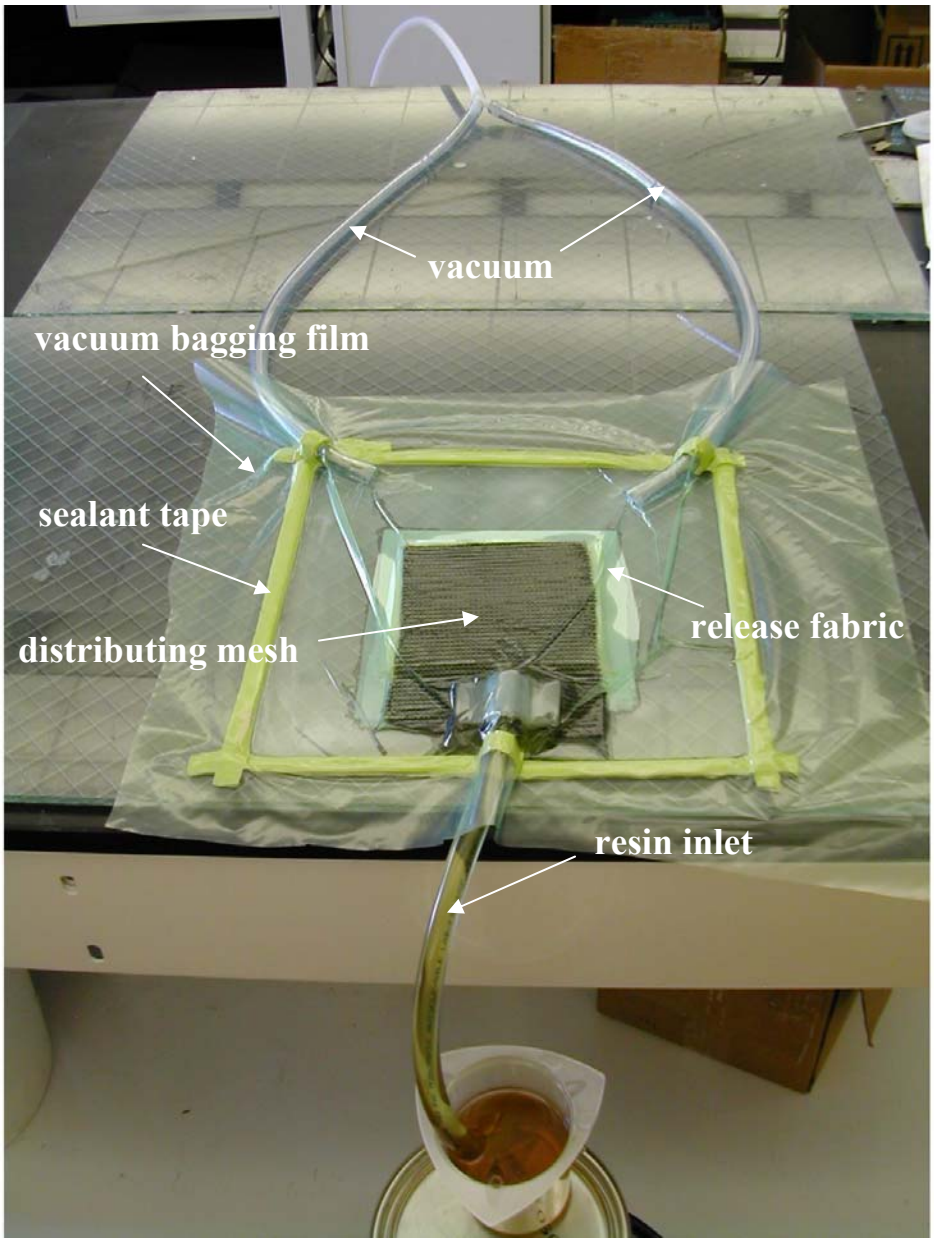

Figure 7.1. Vacuum assisted resin transfer molding setup in composite fabrication.

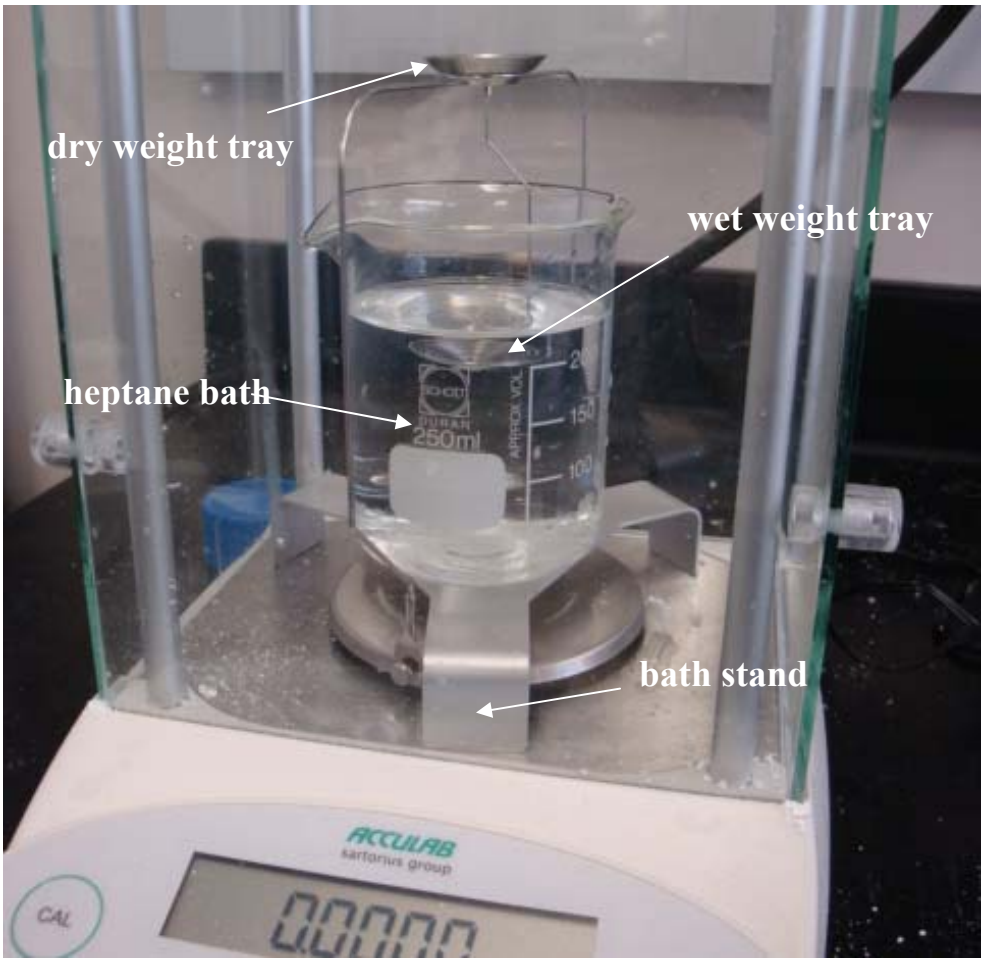

Figure 7.2. Density measurement setup.

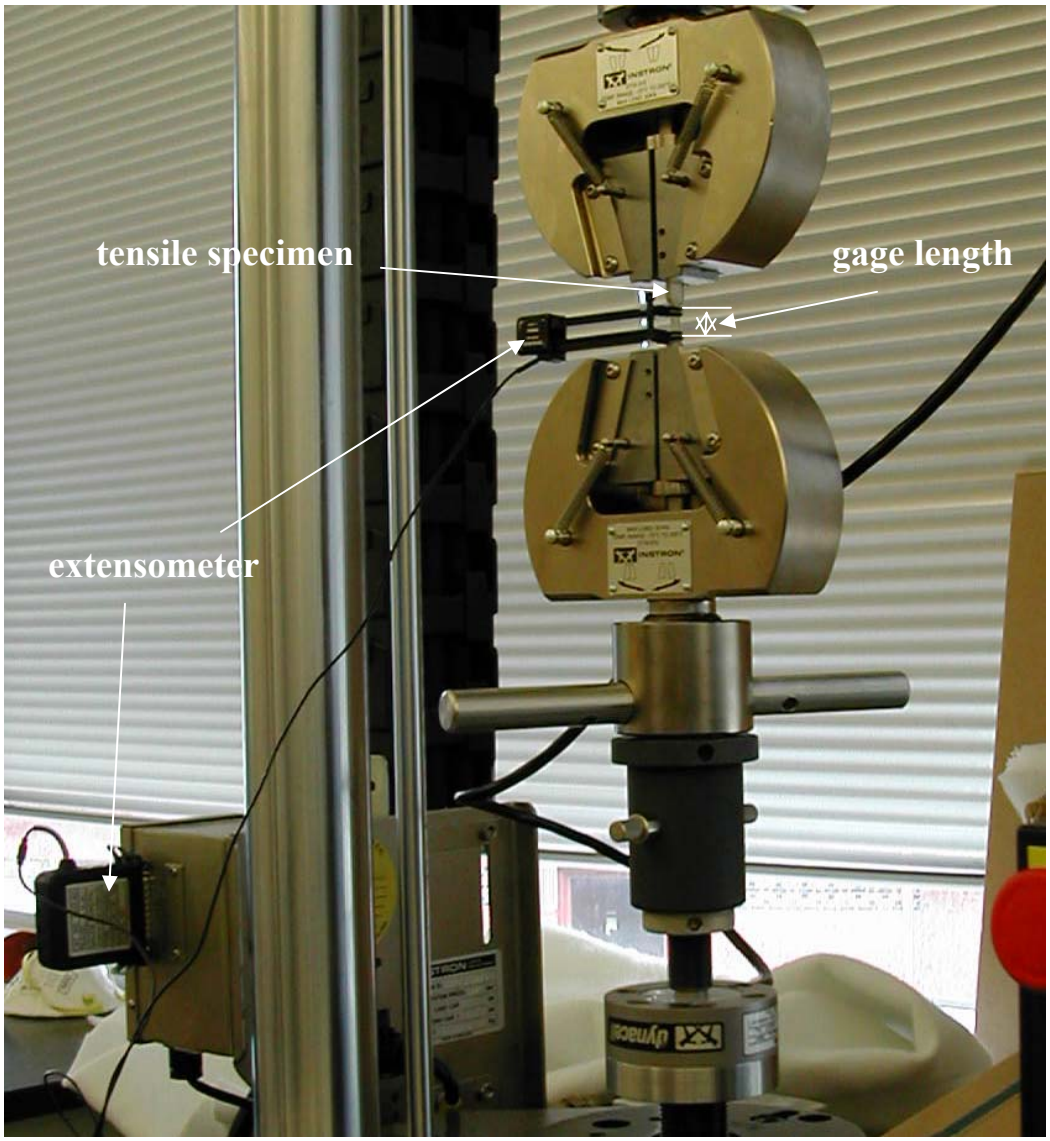

Figure 7.3. Instron setup for measuring tensile properties of rigid plastics.

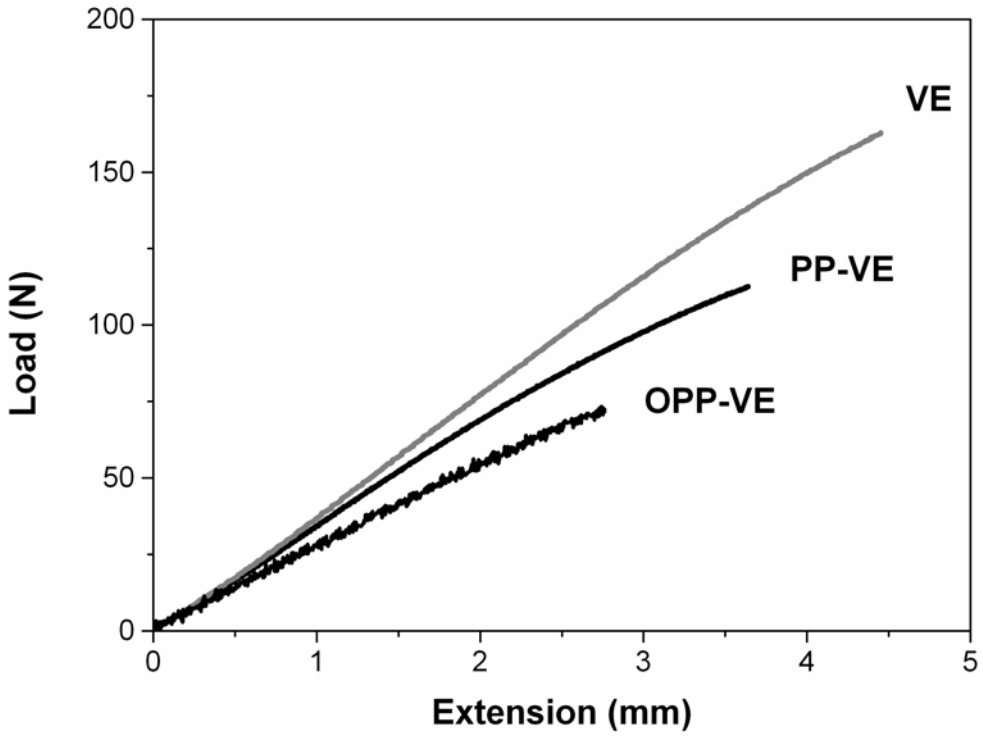

Figure 7.4. Load-deflection curves in flexural tests for neat VE resin and PP-VE composites using untreated PP or oxygen-treated PP fibers.

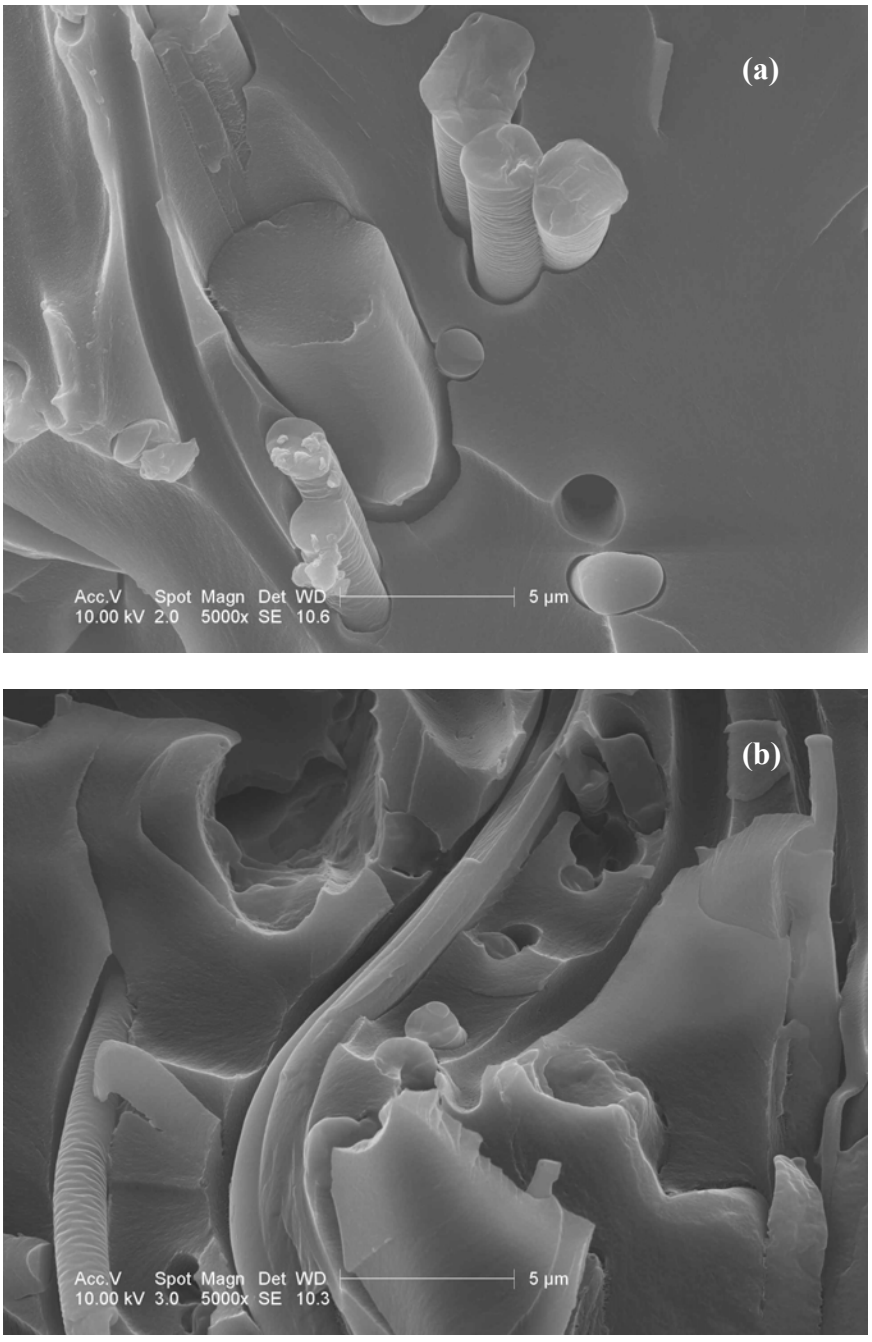

Figure 7.5. ESEM micrographs of fracture surface of the PP-VE composites using (a) untreated PP and (b) oxygen-plasma treated PP.

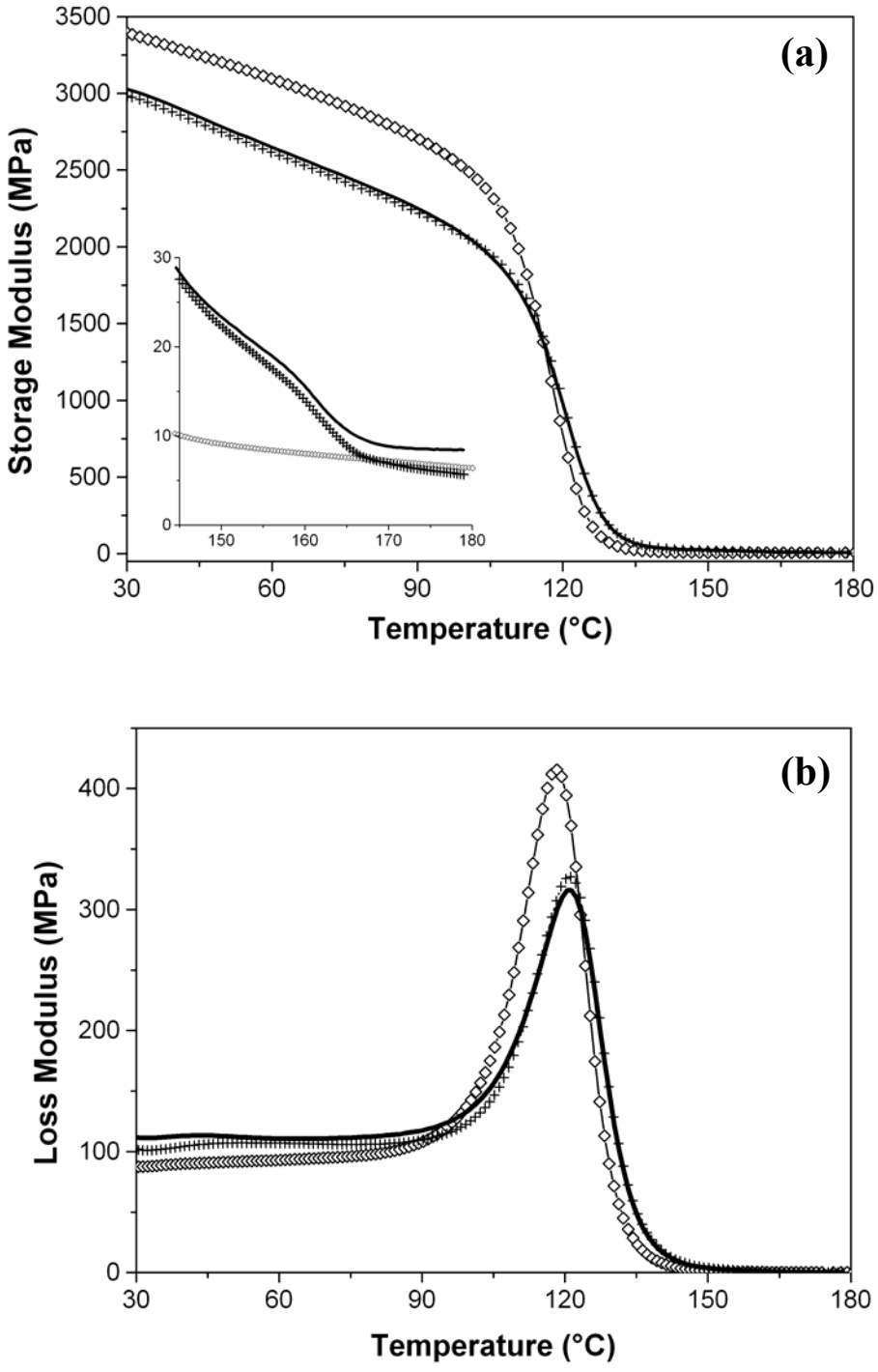

Figure 7.6. DMA temperature scan of (a) storage modulus and (b) loss modulus for neat VE resin and VE composites. ◇— VE, —+— PP-VE, —— VPP-VE

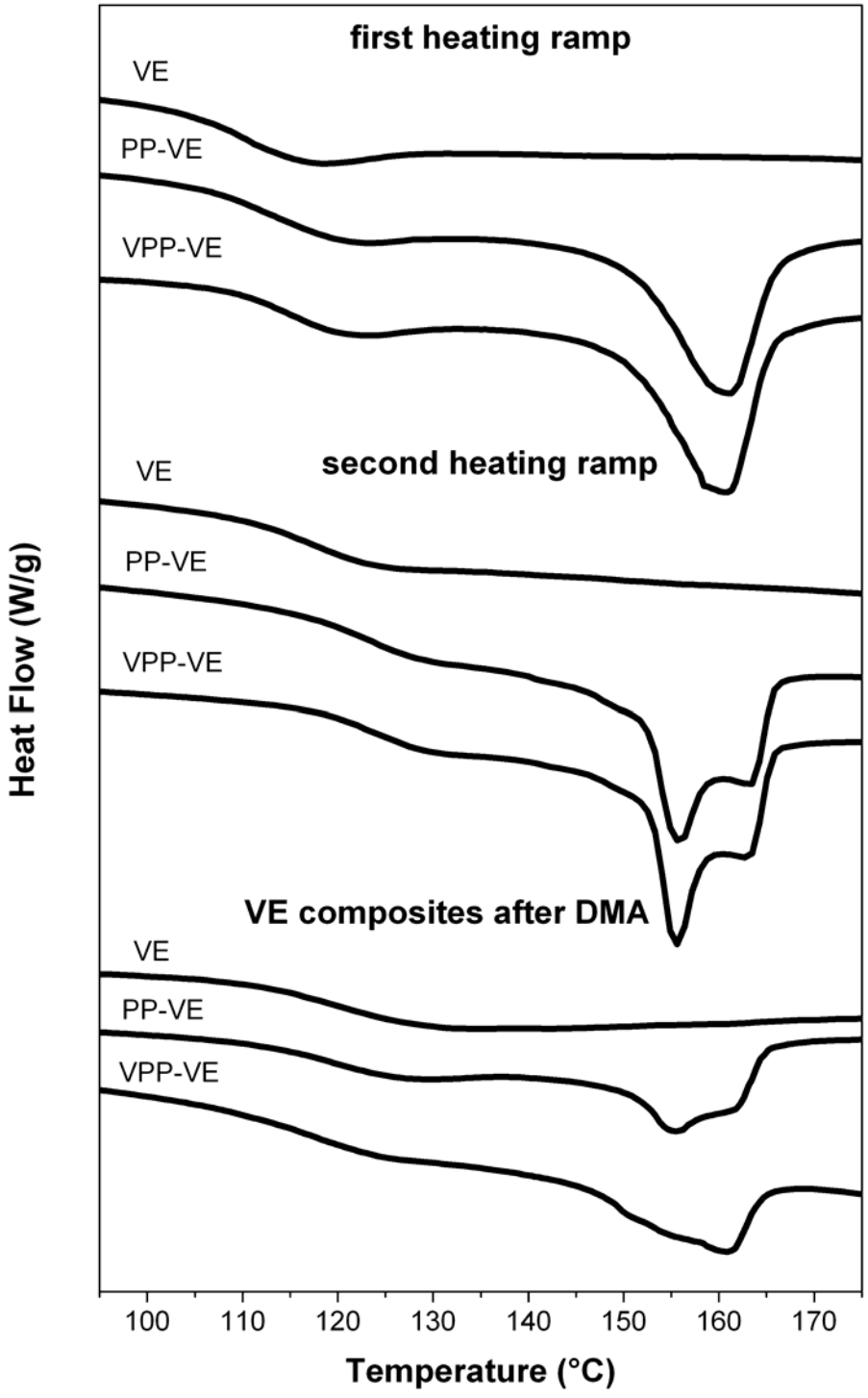

Figure 7.7. DSC thermograms of neat VE resin, PP-VE and VPP-VE composites at the first and second heating ramps and also at the first heating ramp after being tested in DMA.

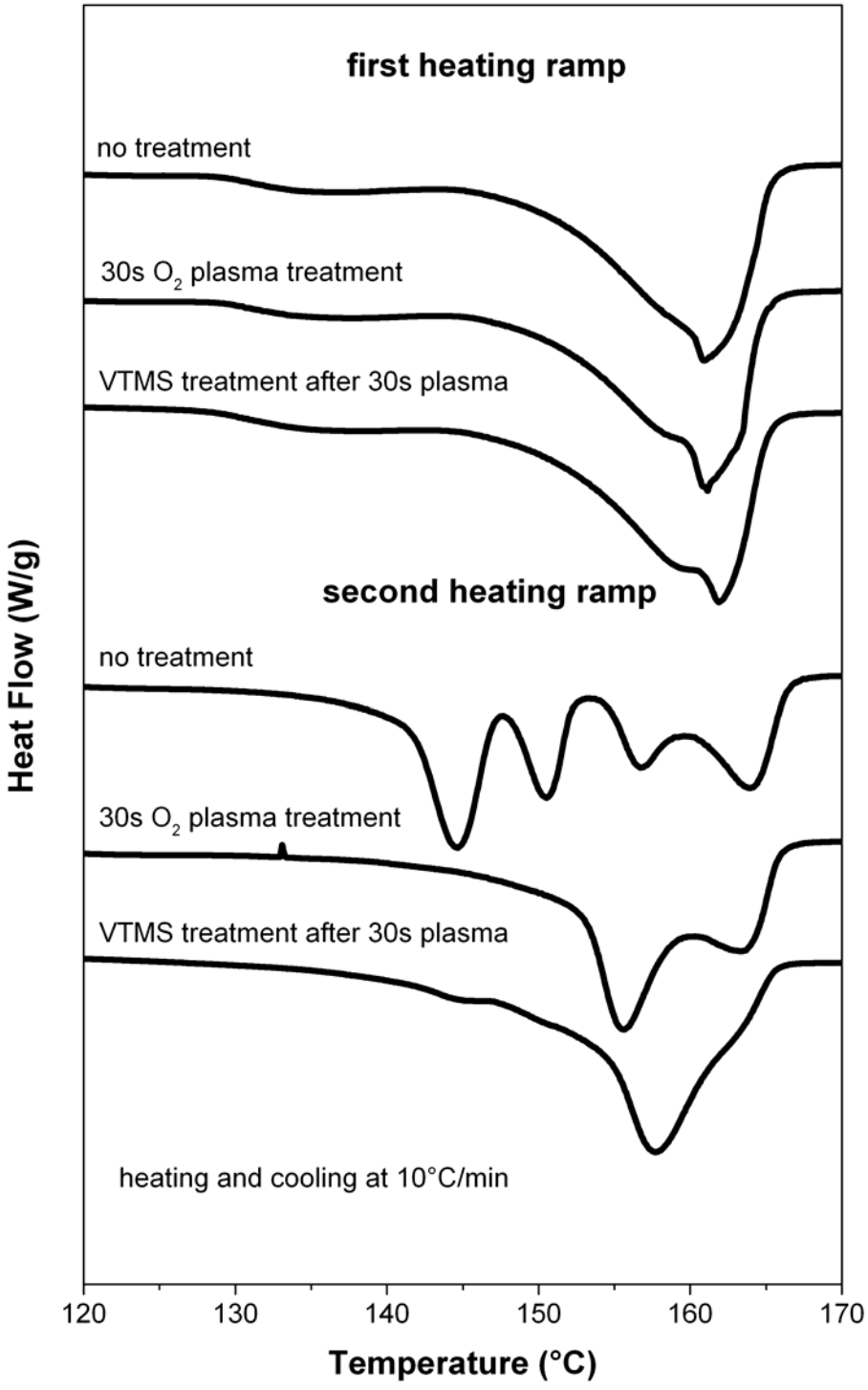

Figure 7.8. DSC thermograms of untreated PP fibers, O_2-PP fibers and VTMS-PP fibers at the first and second heating ramps after isothermal annealing at 125°C under N_2 flow for three hours.

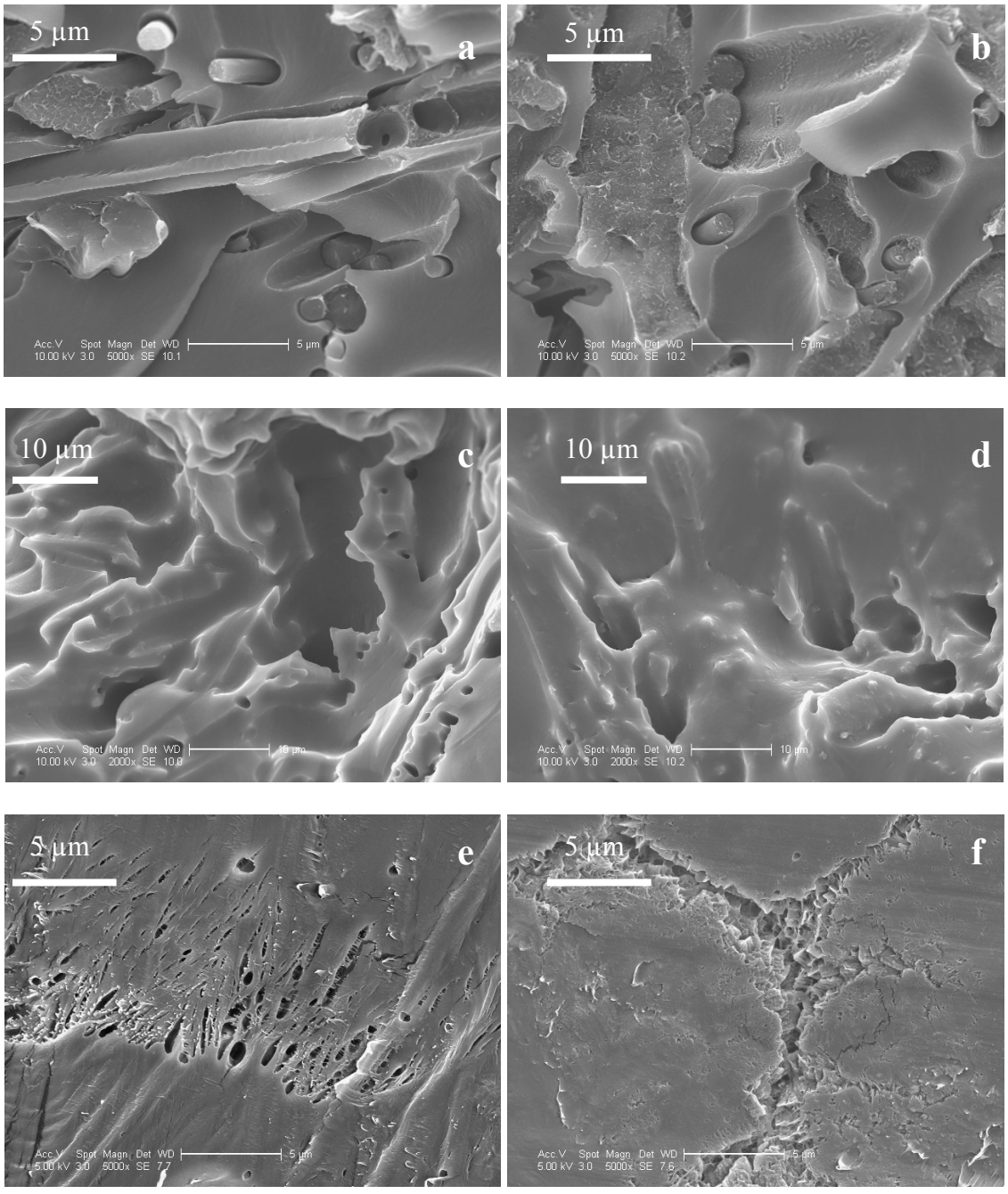

Figure 7.9. ESEM micrographs of VE composites and PP fibers after DSC testing. (a) inside of PP-VE DSC specimen, (b) inside of VPP-VE DSC specimen, (c) outside of PP-VE DSC specimen, (d) outside of VPP-VE DSC specimen, (e) untreated PP fibers, and (f) VTMS-PP fibers.

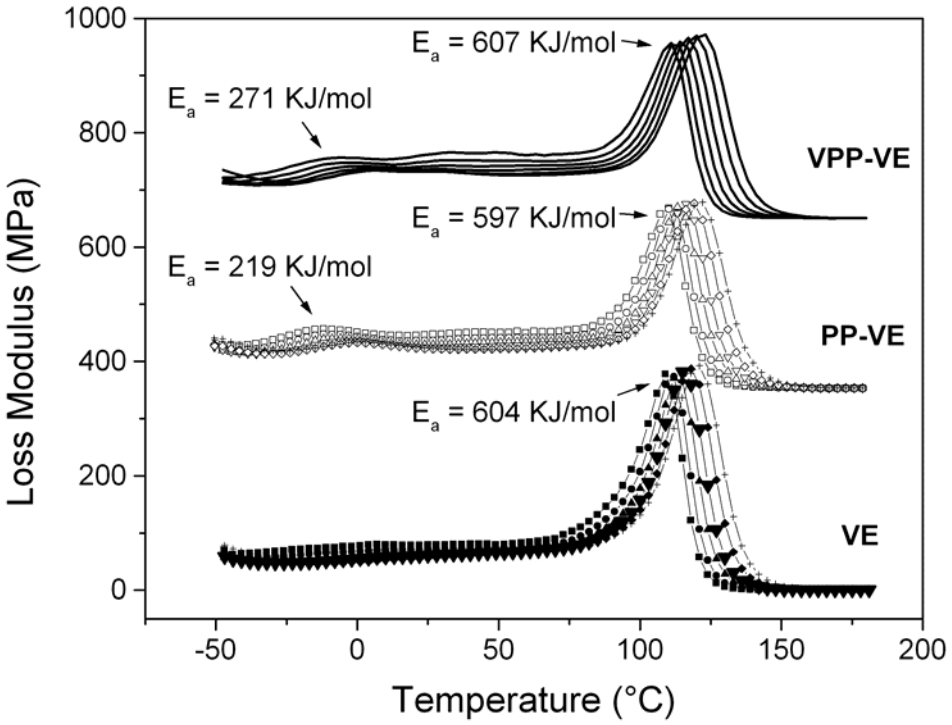

Figure 7.10. Multiple frequency sweep of VE, PP-VE and VPP-VE. For each material, curves shift from left to right when frequency increases from 0.1 Hz to 30 Hz.

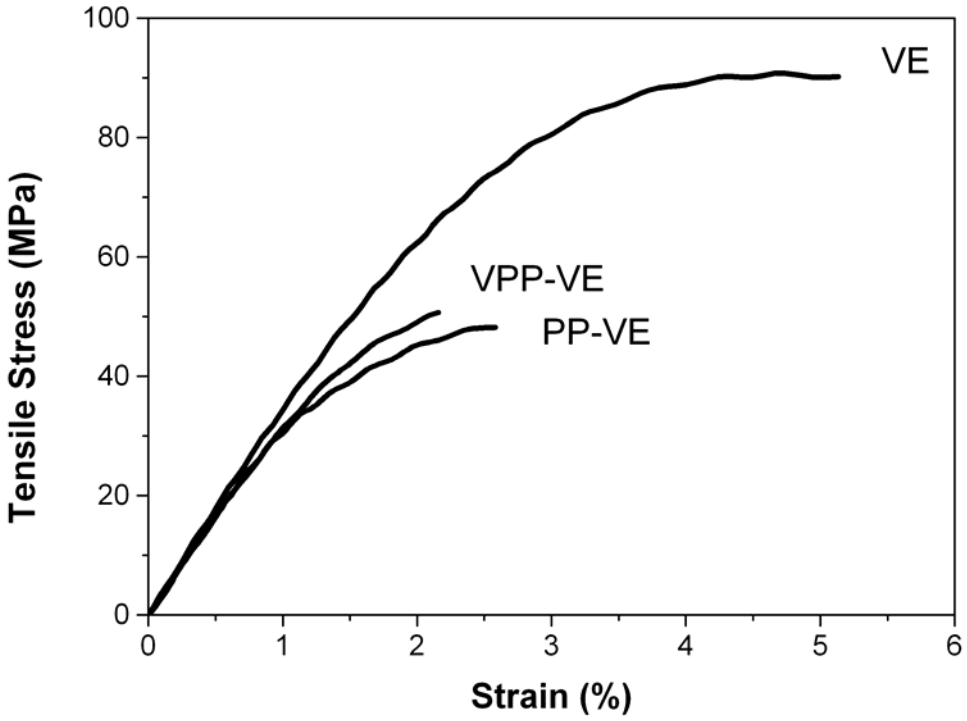

Figure 7.11. Load-deflection curves in tensile testing for neat VE resin, PP-VE and VPP-VE composites.

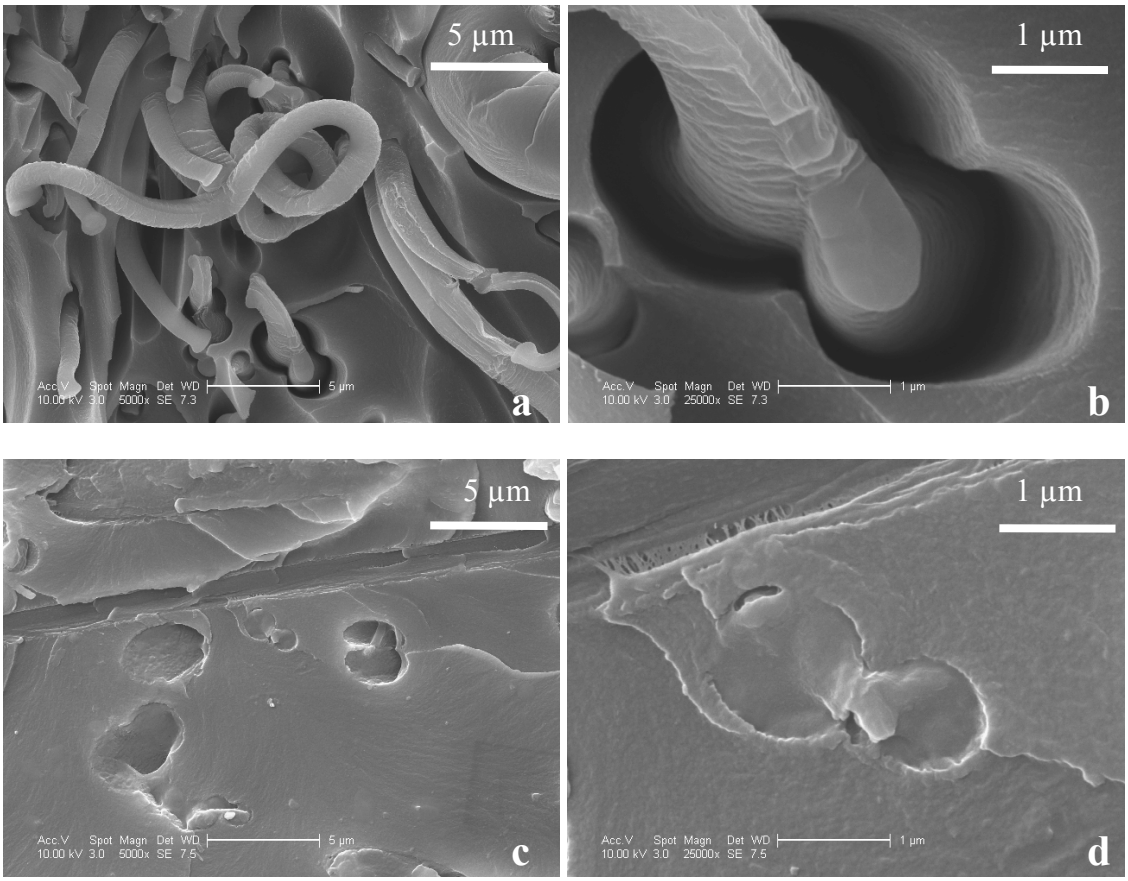

Figure 7.12. ESEM micrographs of fracture surface of (a, b) PP-VE and (c, d) VPP-VE.

Chapter 8: Polymer Toughening in High Performance Composite Applications

Delamination is a major cause of failure in laminated composites. Interlaminar failure can occur when the interfacial strength between matrix and fibers is greater than the matrix cohesive strength, especially when the matrix is very brittle. Most research has been focused on matrix toughening. Polymer toughening can be applied to fiber-reinforced high performance composites to toughen the brittle matrix. Interlayer toughening can toughen just the interlayer without affecting the mechanical strength of each layer. Since the fracture toughness of VE resins was improved by PP fiber encapsulation, we are interested in using PP fiber mats as interlayers to toughen glass fiber-VE composites. In this chapter, interlayer toughening of the glass fiber-VE (GF-VE) composite using PP fibers is evaluated through mode I and mode II interlaminar fracture toughness.

8.1. Experimental

8.1.1. Materials

A 9.64 oz/yd^2 E-glass fabric (Fibre Glast Developments Corporation) was used. This fiberglass fabric is a style 7500 with plain 0-90° weave, and has less than 0.4 wt% organically bound silane. Diameters of these glass fibers are near 10 μm. A 25 μm-thick perfluoroalkoxy fluorocarbon (PFA) film (McMaster) was used as a spacer in the composite fabrication to create an initial crack. FM® 94 film adhesive (Cytec Engineered Materials Inc.) was used to adhere the aluminum piano hinges to the composite specimens in the mode I interlaminar fracture toughness test. The adhesive is

a modified epoxy film adhesive designed for bonding metallic and composite materials. It has a 104°C service temperature.

8.1.2. Composite Fabrication and Testing Specimen Preparation

Composites with an initial crack were fabricated by inserting a 25μm-thick PFA film in the middle of the plies. PP fiber mats were placed where the initial crack was located to obtain the interlaminar fracture toughness of the GF-VE composites with PP interlayer. The layout of the composite and the two fracture modes are sketched in Figure 8.1. The glass fiber composites were fabricated via VARTM as described in Chapter 7. Trigonox 239A, CoNap and VE monomers were mixed at a weight proportion of 1:0.2:100 to control the gel time to 0.5 hours at room temperature. Pre-cure and post-cure procedures were the same as those for VE resins.

Double cantilever beam (DCB) specimens were used in the mode I interlaminar fracture toughness test. Specimen preparation followed ASTM D5528-01 standard [1]. Piano hinges were adhered on the specimens using FM® 94 film adhesive. Approximately 40 psi was applied to the adhered parts using a pair of pliers before the specimens were placed in an oven. The oven was then heated from 20°C to 120°C stepwise at a 10°C increment every four minutes and held for 60 minutes at 120°C. Specimens were slowly cooled to the ambient temperature before releasing the pressure.

End notch flexural (ENF) specimens were used in the mode II interlaminar fracture toughness test. Specimens were precracked to create a sharp starter crack using the method described in the Delaware Composites Design Encyclopedia, Volume 6 [2]. The specimen was clamped across the width at some short distance ahead of the insert

and then the crack was wedged open to propagate a sharp crack until arrested at the clamp.

8.1.3. Interlaminar Fracture Toughness Measurements

Interlaminar fracture toughness measurements were performed on an Instron 8872 universal testing instrument using Merlin software for data acquisition. Experimental setups of the mode I and mode II interlaminar fracture tests are shown in Figure 8.2 and Figure 8.3, respectively.

Mode I interlaminar fracture toughness tests were conducted in tensile mode at a crosshead speed of 2 mm/min. The thickness of DCB specimens was between 4-5 mm, the width was 22-24 mm, and the total length was near 150 mm. Testing procedures followed the ASTM D5528-01 standard [1]. The initial delamination (crack) length was about 50 mm and the test was stopped when the delamination propagated for 50 mm. Mode I interlaminar fracture toughness (G_{IC}) of all tested composites were calculated according to the data reduction method, modified beam theory method, discussed in the standard [1].

Mode II interlaminar fracture toughness was tested in three-point bending flexural mode at a crosshead speed of 2.5 mm/min. The thickness of ENF specimens was between 3-4 mm, the width was 22-24 mm and the span length was four times the initial crack length. The initial delamination length was 38 mm or 40 mm. Detailed testing procedures of mode II interlaminar fracture toughness followed the Delaware Composites Design Encyclopedia [2]. The ENF specimens were preloaded to less than 60% of the maximum load at 2.5 mm/min and then the load was released at the same speed. The

resulting hysteresis loop was used to calculate the friction energy in bending. The typical load-extension curve in the hysteresis loop is given in Figure 8.4. Friction energy in bending was determined by integrating the area between the load and unload cycle of the load-extension curve in the hysteresis loop. Unit friction energy on crack surfaces was calculated to compare with the interlaminar fracture toughness G_{IIC}. The mode II fracture test was stopped when the load showed the first maximum value. Mode II interlaminar fracture toughness (G_{IIC}) of all tested composites were calculated using the equation [2] below,

$$G_{IIc} = \frac{9a^2 P\delta}{2b(2L^3 + 3a^3)}$$

where **a** is the delamination length, **P** is the load at cracking, **δ** is load displacement, **L** is the half span length, and **b** is the width of the specimen.

8.2. Results and Discussion

8.2.1. Influence of Different Interlayers

Interlaminar fracture toughness of GF-VE composites with one-layer PP or one-layer VPP as the interlayer was investigated, using GF-VE composites without an interlayer as a control. The typical load (P) - displacement (extension, δ) curves of the three GF-VE composites in mode I interlaminar fracture test are presented in Figure 8.5. G_{IC} of GF-VE composites without an interlayer, with one layer of PP or VPP, were plotted as a function of the delamination length **a** (Figure 8.6). At the delamination start, GF-VE composite without a PP interlayer seemed to have the highest G_{IC}. GF-VE composites using untreated PP or VTMS-grafted PP as an interlayer possessed similar G_{IC}. After delamination propagated for about 10 mm, G_{IC} of composites with a PP

interlayer became highest and G_{IC} of the composite with a VPP interlayer seemed the worst.

Friction between the crack surfaces may exist during the mode II test. Friction opposes the relative sliding deformations of the crack surfaces in the delaminated region and is an energy dissipating mechanism. When friction energy is significant compared to fracture energy, friction should not be ignored. The typical load - displacement curves of the three GF-VE composites in the mode II interlaminar fracture test are presented in Figure 8.7. Mode II interlaminar fracture toughness and friction energy in bending of all three GF-VE composites are summarized in Table 8.1. It is obvious that the friction energies of all three composites had similar values and were comparable to the standard deviation of G_{IIC} values. Therefore, the friction energy was negligible when G_{IIC} of different GF-VE systems were compared. The influence of various interlayers on G_{IIC} was similar to their influence on the initial G_{IC}. PP interlayer greatly reduced G_{IIC} of the GF-VE composites. GF-VE composites using untreated or VTMS-grafted PP fibers as an interlayer had similar G_{IIC}.

8.2.2. Influence of Interlayer Thickness

Influence of the interlayer thickness on interlaminar fracture toughness was also investigated. G_{IC} as a function of delamination length was plotted in Figure 8.8 for GF-VE composites using one layer or two layers of PP fiber mats as interlayers. The thickness of one PP fiber mat is about 0.11 mm. It is clear that G_{IC} greatly decreased with the increasing interlayer thickness. G_{IIC} and friction energy of GF-VE composites with one or two layers of PP mats are included in Table 8.2. Again, the friction energy

was negligible compared with G_{IIC}. The results were consistent with G_{IC}. A thicker PP interlayer further reduced G_{IIC} although the decrease was not as big as that from zero to one PP layer.

8.2.3. Failure Mechanism

The fracture surfaces of tested specimens were examined using ESEM. The fracture surface morphologies of DCB specimens for four GF-VE composites discussed above are shown in Figure 8.9. It is clear that the dominant failure mode was glass fibers debonding from the VE matrix during the mode I test. Few PP fibers were observed at the fracture surface, so one would expect that PP fibers had little contribution to the energy absorption. Part of the energy absorption capacity came from the microcrack formation in the matrix. Upon inserting the PP interlayer, PP fibers could arrest the growth of microcracks in the matrix and result in decreased energy absorption capacity. When two PP layers were added at the interlayer, the thickness of the interlayer was not doubled. Therefore, the neat resin region was probably reduced by adding more PP layers, which could further limit the microcrack formation. G_{IC} of composites using VPP as an interlayer was close to those using untreated PP at the beginning of delamination due to their similar microcrack suppressing ability. Variation at a longer delamination length might be a result of unstable crack growth. The fracture surface morphologies of ENF specimens for GF-VE composites using one layer or two layers of PP mats are shown in Figure 8.10. Failure mechanism in mode II tests was similar to that in mode I tests since all fiber debonding from the matrix along with some matrix cracks were observed at the fracture surface. Visual observation of the fracture surface after the mode

I test (Figure 8.11a) and mode II test (Figure 8.11b) proved our hypothesis about the failure mechanism. There were almost evenly distributed resins on either fracture surface for GF-VE composites without the PP interlayer. Upon inserting a PP or VPP interlayer, the resins were predominantly distributed on one side of the fracture surface. This became more obvious with thicker PP layers. The weak interfacial strength between GF and VE resin suppressed delamination, so the measured interlaminar fracture toughness did not increase upon inserting PP interlayer.

8.2.4. Using Freshly Received Glass Fiber Fabrics

As discussed in the previous section, the fiber-matrix interfacial strength was weaker than the matrix cohesive strength for the studied GF-VE composites. If good bonding at the fiber-matrix interface can be obtained, the actual interlaminar fracture toughness can be measured to evaluate the interlayer toughening. One possible reason for the weak fiber-matrix bonding is that the sizing on those glass fibers may be expired. Therefore, freshly received glass fiber fabrics were used for the interlaminar fracture toughness study. Previous study has shown that G_{IC} and G_{IIC} were consistent, so only mode II interlaminar fracture toughness was investigated. Results of mode II tests for GF-VE composites without an interlayer or with two layers of PP mats are listed in Table 8.3. GF-VE composite without an interlayer possessed higher $G_{IIC,}$ although the difference in G_{IIC} between the two composites decreased by half. The fracture surface morphologies were examined using ESEM and included in Figure 8.12. Slightly better fiber-matrix interface was observed although fiber debonding from the matrix could also

be noticed. For the GF-VE composite with a thick PP interlayer, obvious delamination in some region was observed.

8.3. Chapter Summary

Untreated and VTMS-grafted PP fiber mats were used as interlayers in GF-VE composites in an effort to increase interlaminar fracture toughness. Mode I and mode II interlaminar fracture toughness was used to evaluate the interlayer toughening. G_{IC} and G_{IIC} of GF-VE composites were found to decrease upon inserting the PP interlayer. Those values further decreased with increasing interlayer thickness. The reason is that the fiber-matrix interfacial strength is weaker than the matrix cohesive strength, so that the tougher interlayer facilitates the debonding by limiting microcrack formation in the matrix. The thicker interlayer magnifies the negative influence on G_{IC} and G_{IIC}.

List of References

1. Standard Test Method for Mode I Interlaminar Fracture Toughness of Unidirectional Fiber-Reinforced Polymer Matrix Composites. Annual Book of ASTM Standards, Designation: D 5528-01. ASTM International, June 2007.

2. Gillespie JW, Carlsson LA. 6.3. Interlaminar fracture of laminated composite materials. In: Gillespie JW, Carlsson LA, editors. Delaware Composites Design Encyclopedia, Volume 6: Test Methods. Pennsylvania: Technomic, 1990: 113-160.

Table 8.1. Mode II interlaminar fracture toughness of GF-VE composites with various interlayers.

Interlayer	a, mm	b, mm	d, mm	P_{max}, N	G_{IIC}, J/m^2	Friction Energy* J/m^2
No PP	38	23.1±0.9	3.43±0.06	240±16	1460±218	80±19
1-ply PP		22.8±0.7	3.43±0.05	217±2	1285±76	107±9
1-ply VPP		23.3±0.5	3.43±0.04	231±7	1283±138	86±5

*Preload to 130N in hysteresis loop

Table 8.2. Mode II interlaminar fracture toughness of GF-VE composites with different interlayer thickness.

Interlayer	a, mm	b, mm	d, mm	P_{max}, N	G_{IIC}, J/m^2	Friction Energy* J/m^2
1-ply PP	40	23.8±0.4	3.63±0.02	224±5	1309±30	22±1
2-ply PP		23.8±0.4	3.66±0.01	221±7	1286±57	23±1

*Preload to 80N in hysteresis loop

Table 8.3. Mode II interlaminar fracture toughness of GF-VE composites using freshly received GF.

Interlayer	a, mm	b, mm	d, mm	P_{max}, N	G_{IIC}, J/m^2	Friction Energy* J/m^2
No PP	40	23.9±0.1	3.30±0.03	179±5	1241±55	13±5
2-ply PP		23.8±0.6	3.48±0.01	185±9	1139±125	18±8

*Preload to 80N in hysteresis loop

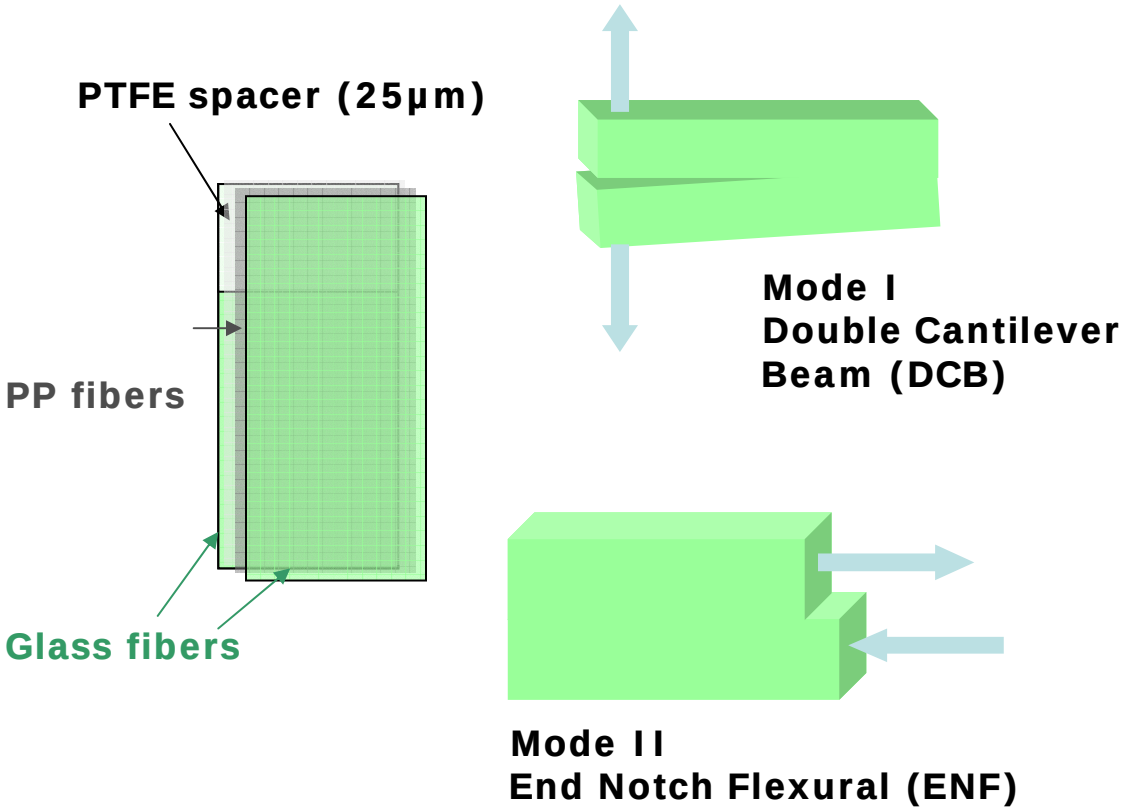

Figure 8.1. The layout of glass fiber-VE composite fabrication with an initial delamination and the sketch of the two interlaminar fracture modes.

Figure 8.2. Mode I interlaminar fracture toughness testing using double cantilever beam (DCB) specimens.

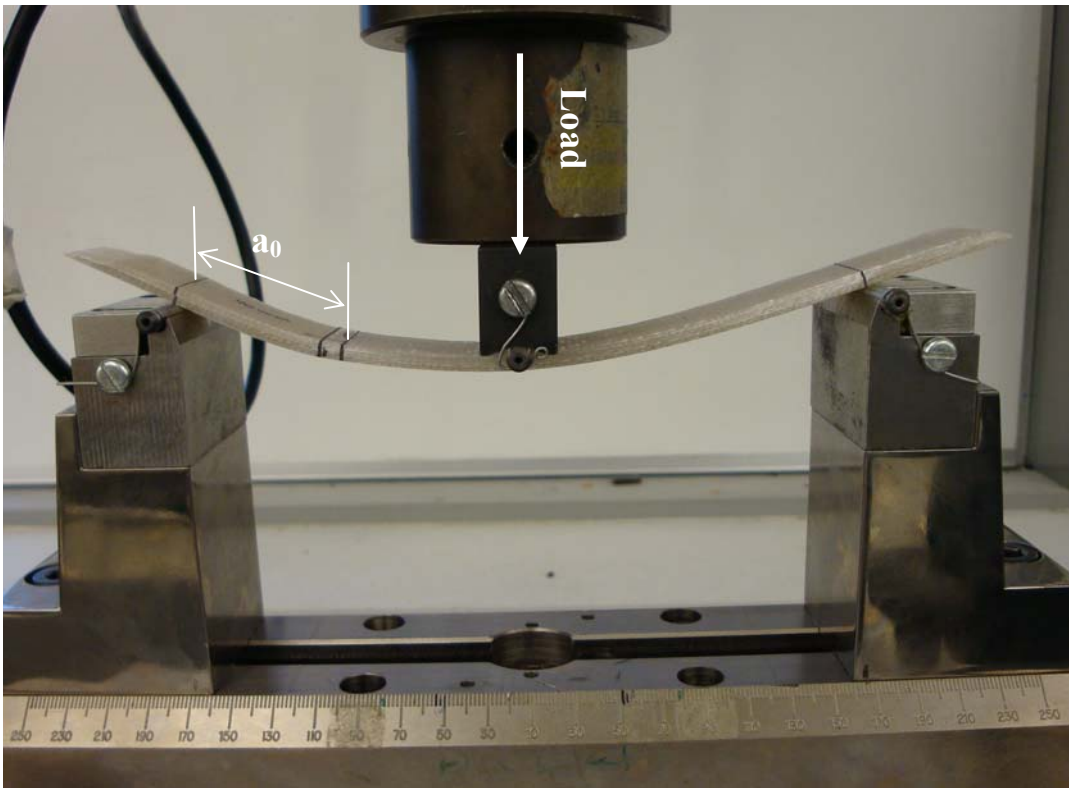

Figure 8.3. Mode II interlaminar fracture toughness testing using end notch flexural (ENF) specimens.

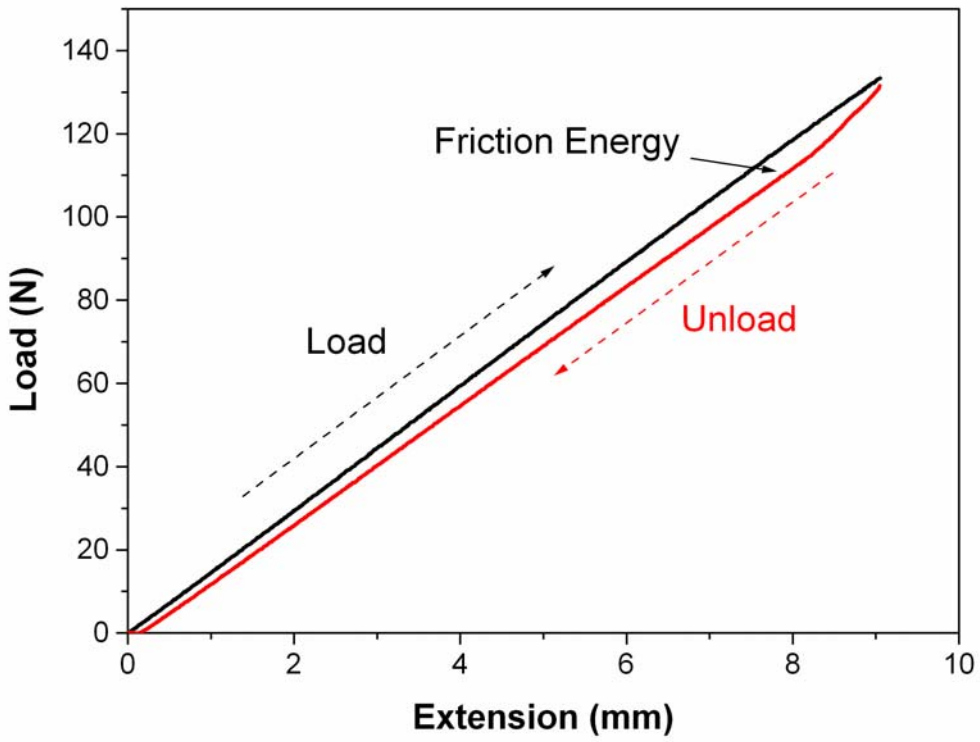

Figure 8.4. Hysteresis loop used to calculate friction energy in bending in mode II interlaminar fracture tests.

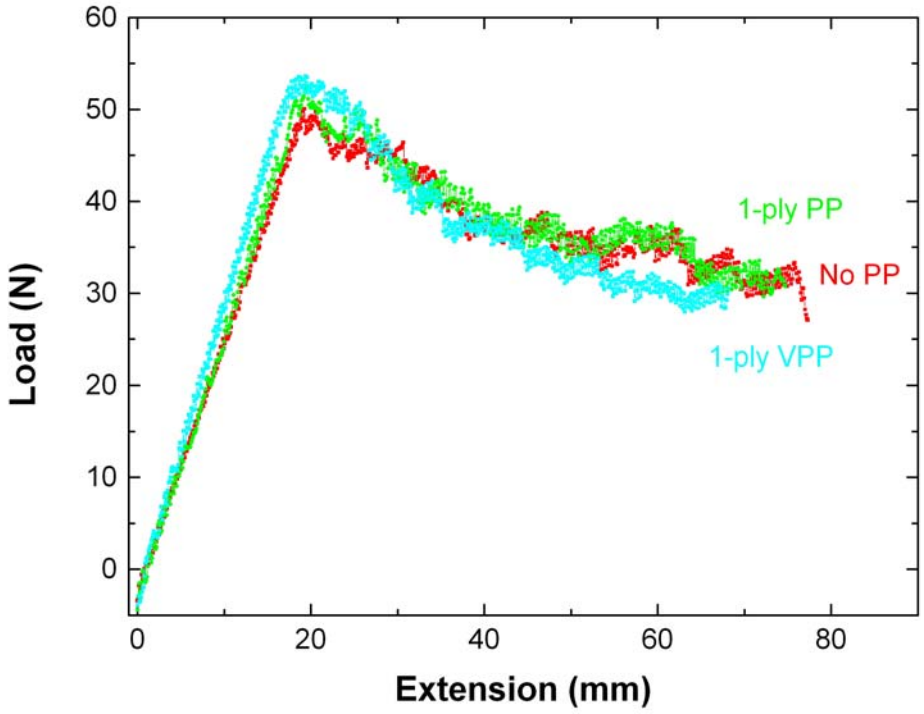

Figure 8.5 Load-displacement curves in mode I interlaminar fracture tests using DCB specimens for GF-VE composites without PP, with one-ply PP or with one-ply VTMS-grafted PP (VPP) as the interlayer.

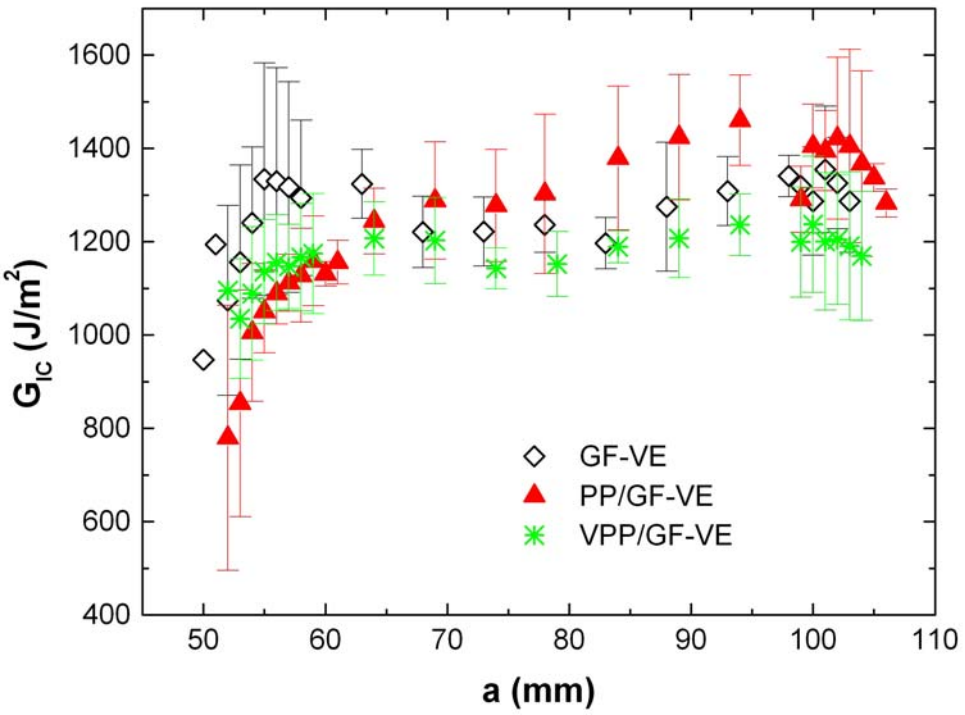

Figure 8.6. Mode I interlaminar fracture toughness as a function of delamination length **a** for GF-VE composites without PP, with one-ply PP or with 1-ply VPP as the interlayer.

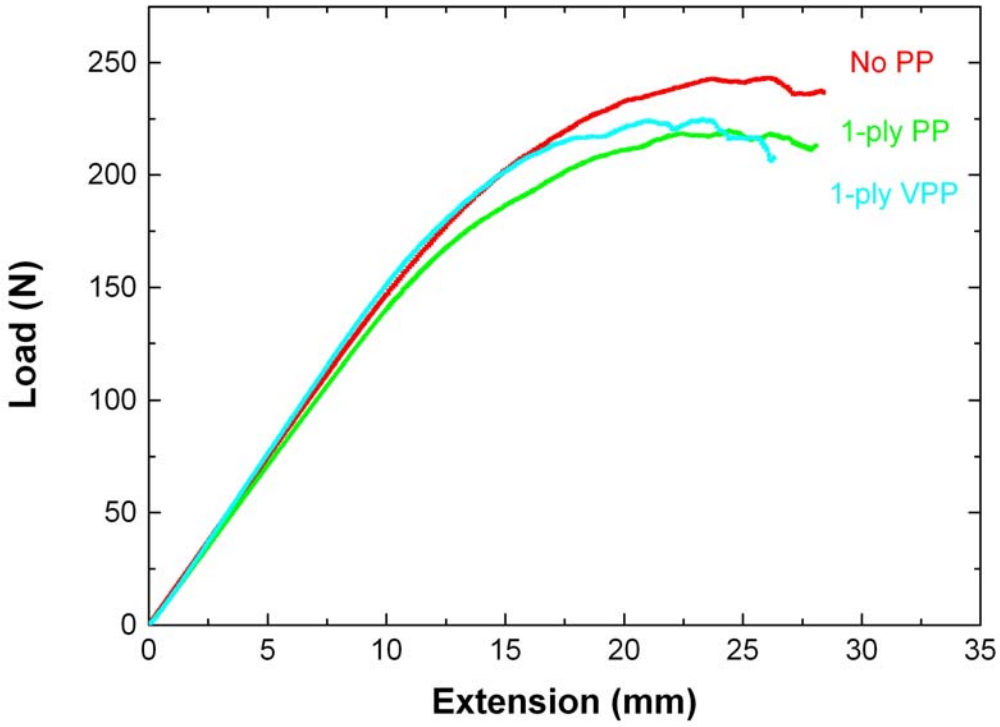

Figure 8.7. Load-displacement curves in mode II interlaminar fracture tests using ENF specimens for GF-VE composites without PP, with one-ply PP or with one-ply VPP as the interlayer.

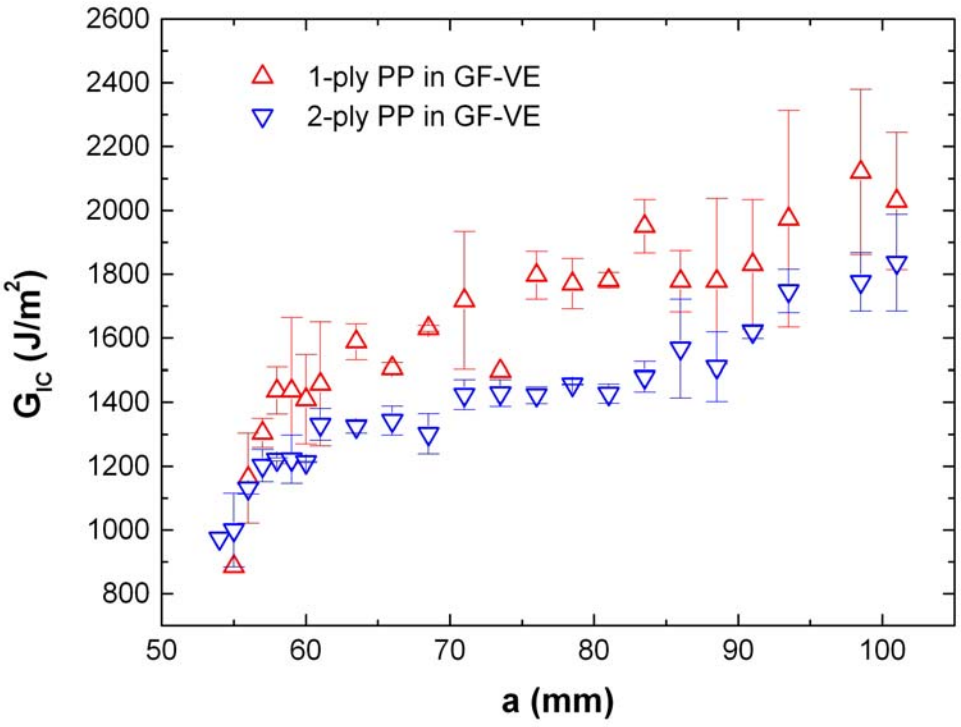

Figure 8.8. Mode I interlaminar fracture toughness as a function of delamination length **a** for GF-VE composites with one-ply or two-ply PP interlayer.

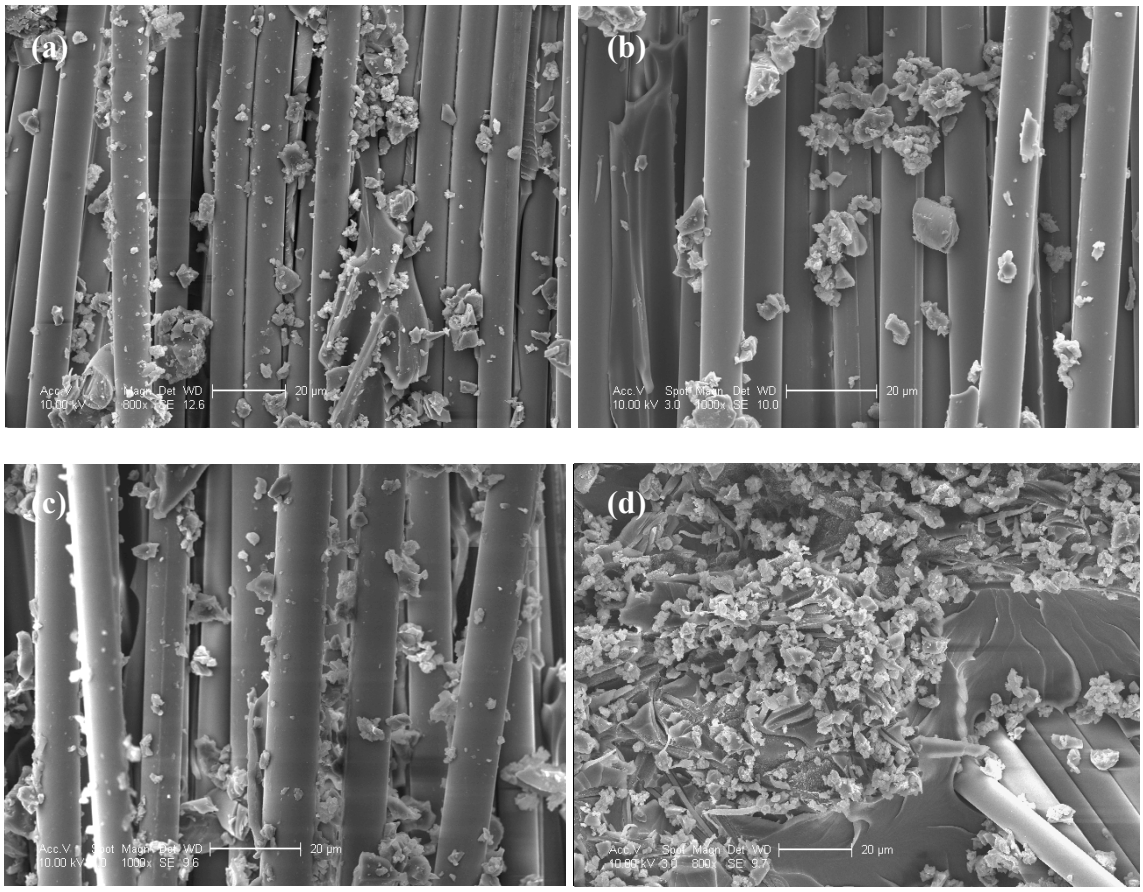

Figure 8.9. ESEM micrographs of fracture surface of GF-VE composites after mode I tests with (a) no PP, (b) 1-ply PP, (c) 2-ply PP, or (d) 1-ply VPP as the interlayer.

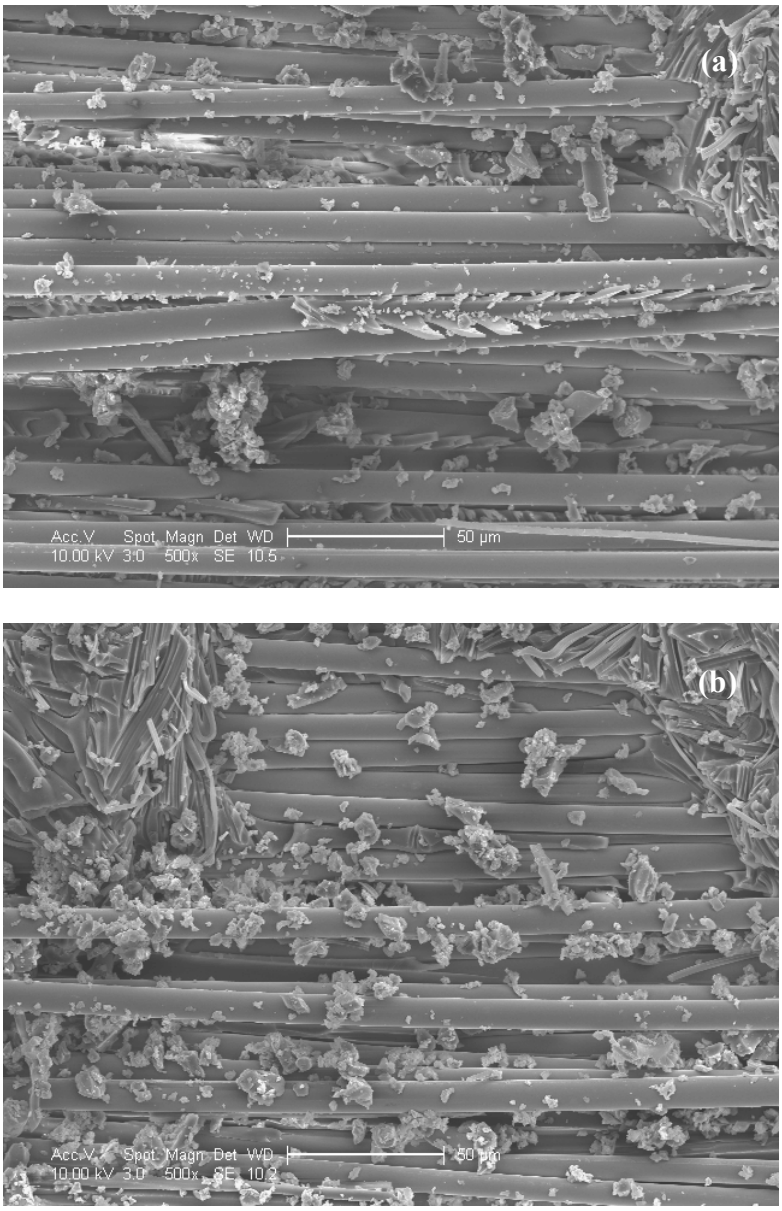

Figure 8.10. ESEM micrographs of fracture surface of GF-VE composites after mode II tests with (a) 1-ply PP or (b) 2-ply PP as the interlayer.

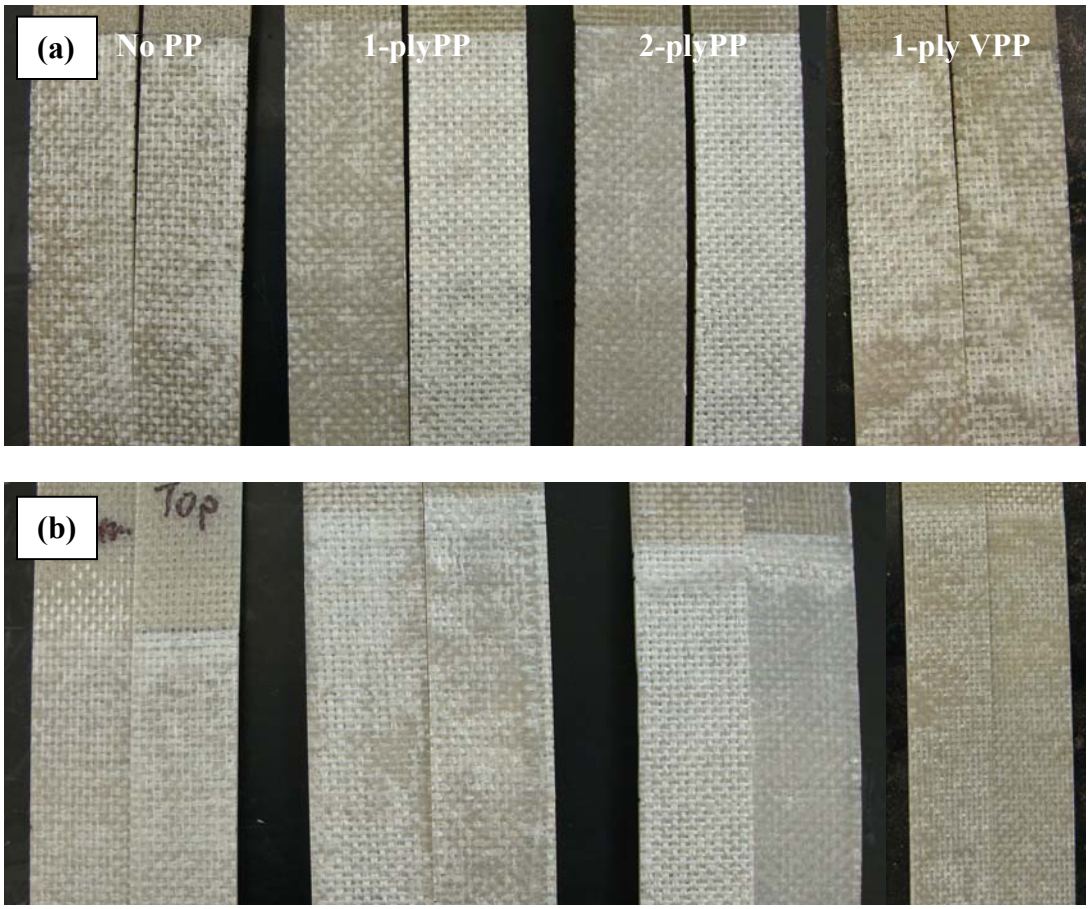

Figure 8.11. Visual observation of fracture surface of GF-VE composites after (a) mode I tests and (b) mode II tests with various interlayer. The color of the glass fibers is lighter than that of the resin.

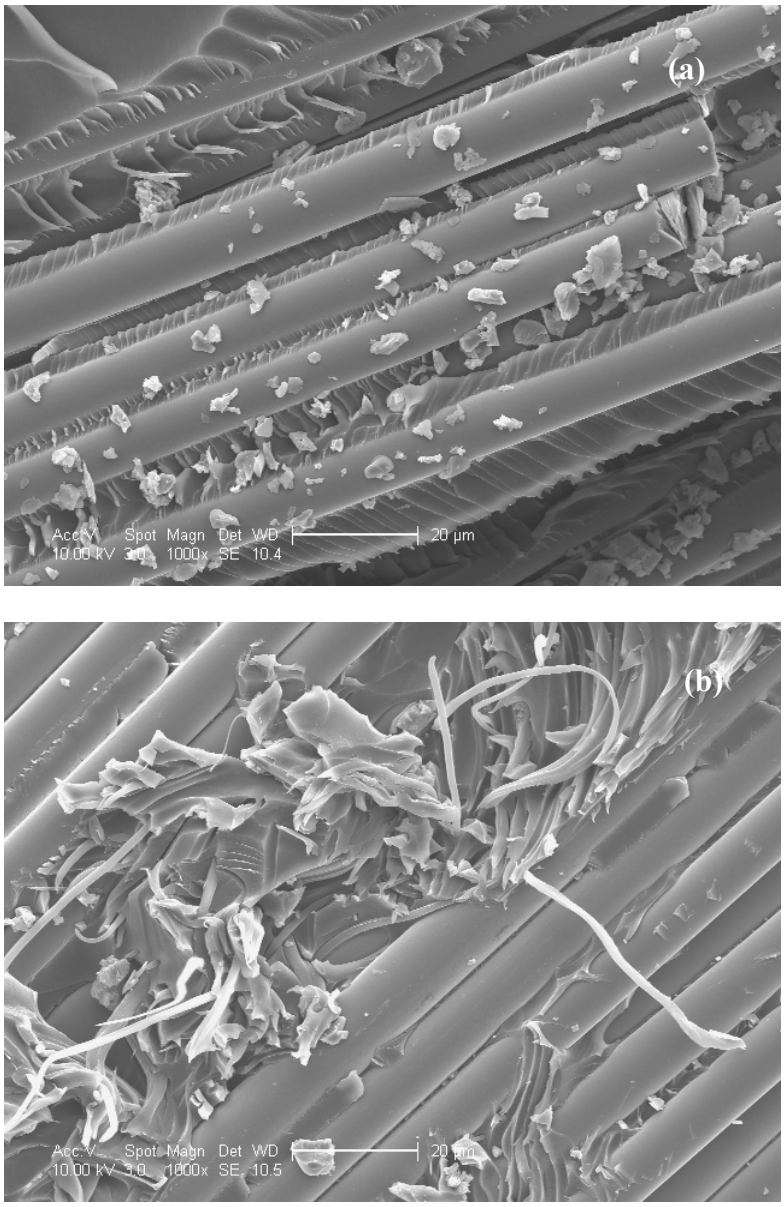

Figure 8.12. ESEM micrographs of fracture surface of GF-VE composites after mode II tests with (a) no PP or (b) 2-ply PP as the interlayer using freshly received GF.

Chapter 9: Conclusions and Recommendations

9.1. PLGA Fiber-PVA Hydrogel Composites

The PLGA fiber-PVA hydrogel composite system has been investigated for drug delivery applications. The work has focused on *in vitro* degradation behavior of PLGA fibers and mechanical properties of the composite during incubation in 37°C PBS buffer at pH 7.4. It was found that the fiber morphology within the range of 100 nm to several microns in diameters and the porous PVA matrix did not have significant effect on the degradation rate of PLGA fibers. Degradation was kinetics-controlled and followed a pseudo-first-order kinetics. The erosion rate of small fibers was nearly constant for different fiber morphologies; therefore it was predictable within a certain dimension range. No initial burst of weight loss was observed for small fibers as it was with thick films. Since the drug release is associated with the erosion rate, the release should also be predictable and free of initial burst. PVA matrix provided good mechanical stability and shape stability for PLGA fiber mats during incubation. Overall, the PLGA-PVA system had a controllable degradation rate and desired mechanical stability for potential applications such as chemotherapy and artificial tissues.

The *in vitro* degradation study was, however, conducted in a simplified environment. Proteins, salts, and other solutes in human body fluids may interfere with the degradation. Enzymatic degradation will accompany hydrolytic degradation, while macromolecules can increase the tortuosity of the diffusion path. Further *in vitro* degradation studies can be conducted in more complex environments by adding proteins and solutes to simulate human body fluids.

Release profile of various model drugs, such as hydrophilic or hydrophobic, small or large molecules, should be investigated to provide some general guidelines about the application range. On the other hand, the incorporated drugs may change the degradation rate of PLGA. A preliminary release study using Myoglobin as a model drug is included in the appendix.

Studies have shown therapeutics could retain their bioactivity after the electrospinning process or the freezing-thawing cycles. However, different drugs have different levels of robustness. Further work can focus on determining the remaining bioactivity of various model drugs after the electrospinning process and after hydrogel fabrication.

9.2. PP Fiber-VE Resin Composites

The random, continuous, small-sized PP fibers have been used to toughen VE resins. Approximately 20 vol% PP fibers were encapsulated in VE using the VARTM technique. Increased fracture toughness and decreased mechanical strength were observed upon encapsulation using PP as the toughening agent compared with neat VE resins. Interfacial discontinuity of composites using as-received PP fibers was observed, but it was improved after surface modification of PP using VTMS. VTMS grafting on PP increased interfacial strength and changed the failure mechanism of composites. However, VTMS grafting of PP fibers did not have significant influence on fracture toughness or mechanical strength due to the weak nature of PP fibers. Mode I and Mode II interlaminar fracture toughness of GF-VE composites decreased when PP fiber mats were used as interlayers. They further decreased with thicker PP interlayers. Overall, the

PP-VE system provided valuable information on the toughening mechanism using thermoplastic fibers as toughening agents and on toughening phase selection.

Stronger PP (lower MFI) fibers can be used in future work to determine if VTMS grafting on PP fibers can improve fracture toughness and mechanical properties. In addition, the influence of the fiber size can be investigated. Bigger fibers are stronger and may show plastic deformation, which can increase mechanical properties and fracture toughness. But the decreased interfacial area can reduce the total interfacial strength and load transfer area. Diameters of PP fibers can be varied to find the optimum diameter range.

Other thermoplastic materials, such as polyethylene (PE) fibers and thermoplastic polyurethane (TPU) fibers, can be used as toughening materials. A preliminary study using TPU fibers has shown promise in toughening VE resins since good interfacial continuity has been observed at the interface of TPU and VE resin.

Interlayer toughening of high-performance GF-VE composites using PP fiber mats has not been successful in this work, possibly due to the weak bonding between GF and VE matrix. Future work can focus on using different VE resins or other thermosetting resins such as Epoxy resins. Results in this work showed that thicker interlayer reduced fracture toughness. Therefore thinner interlayer (less than 0.1 mm) should be studied, if possible.

Vita

Ya Liang was born on December 24, 1975, in Chishui, located in Guizhou Province, China. She received a bachelor's degree in Chemical Engineering and Technology from Tsinghua University, Beijing, China in July 1999. She then joined the graduate program in Tsinghua University with exemption of the admission examinations. However, because she was unsatisfied with the research area and the quality of research education, she decided to pursue an advanced degree in the United States. She joined the graduate program of Louisiana State University in August 2000 and received a master's degree in Chemical Engineering in August 2003. Then she started PhD studies in the Analytical Chemistry Group of the Chemistry Department of Louisiana State University. Shortly thereafter, family obligations required her to discontinue that program and move to Northeastern Pennsylvania. She again pursued her PhD dream by joining the Chemical and Biological Engineering Department of Drexel University beginning September 2004. She worked with Dr. Giuseppe Palmese in the Polymer & Composite Laboratories, and Dr. Anthony Lowman in the Biomaterials & Drug Delivery Laboratories beginning in 2005. In June 2010, she accomplished her studies and received a PhD degree.